Marine Weather Variability, Tropical Cyclone Prediction and Impacts in the Southwest Indian Ocean

Denis Chang-Seng

Environmental Studies Department
Faculty of Science
University of Zululand

Thesis submitted in fulfillment of the requirement for the Degree of Master of Science

June 2005

Abstract

The southwestern Indian Ocean is characterized by significant inter-annual climate variability and numerous tropical cyclones. Long-and short-term variability and associated oceanic and atmospheric fields are analyzed using model-assimilated data. The evolution of monsoon circulations associated with composite tropical cyclones distinguished by track is studied. Case study tropical cyclones are investigated and impacts evaluated through comparison of 'real' and 'model' datasets.

The seasonal variability of intense TC is studied through composite, statistical correlation analysis, cross-modulus wavelet-filter, hovmoller analysis and multi-variate modeling.

The intense TC index is characterized with biennial to decadal cycles that may be related with the QBO and the ocean thermohaline circulation respectively. The decade 1960-69 was the most active while 1980-89 was the least active in terms of intense tropical cyclone days in SWIO. New predictors are uncovered that significantly improve the seasonal prediction of intense tropical cyclones. The new multivariate models are performing about 42 % better than the previous model of Jury et al (1999) in the period 1960-2002. One predictor is the geopotential height (explaining 31 % TC days variability) in the southeast Pacific. It appears to foretell of downstream oscillations in the sub-tropical jet stream which bifurcates and govern wind shear over the Indian Ocean. A duct pattern seems to promote negative vorticity anomalies of $-2.0X10^{6}s^{-1}$ and convergence anomalies of $+1.2X10^{6}s^{-1}$ over SWIO.

Abstract

The southwestern Indian Ocean is characterized by significant inter-annual climate variability and numerous tropical cyclones. Long-and short-term variability and associated oceanic and atmospheric fields are analyzed using model-assimilated data. The evolution of monsoon circulations associated with composite tropical cyclones distinguished by track is studied. Case study tropical cyclones are investigated and impacts evaluated through comparison of 'real' and 'model' datasets.

The seasonal variability of intense TC is studied through composite, statistical correlation analysis, cross-modulus wavelet-filter, hovmoller analysis and multi-variate modeling.

The intense TC index is characterized with biennial to decadal cycles that may be related with the QBO and the ocean thermohaline circulation respectively. The decade 1960-69 was the most active while 1980-89 was the least active in terms of intense tropical cyclone days in SWIO. New predictors are uncovered that significantly improve the seasonal prediction of intense tropical cyclones. The new multivariate models are performing about 42 % better than the previous model of Jury et al (1999) in the period 1960-2002. One predictor is the geopotential height (explaining 31 % TC days variability) in the southeast Pacific. It appears to foretell of downstream oscillations in the sub-tropical jet stream which bifurcates and govern wind shear over the Indian Ocean. A duct pattern seems to promote negative vorticity anomalies of $-2.0\mathrm{X}10^{6}\,s^{-1}$ and convergence anomalies of $+1.2\mathrm{X}10^{6}\,s^{-1}$ over SWIO.

An anti-phase association between South America monsoon convection and intense TCs is found through the Atlantic Zonal circulation especially in the ENSO years. A mild La Nina type of mode is favorable for more TCs. A westward propagating cyclonic circulation is coupled with a transient ocean Rossby wave in respect of the year-to-year variability in tropical cyclone days in the SWIO.

The fish resources of the SWIO are negatively associated with intense TC days, e.g. more TC implies lower catch rates. The east South African fish catch also responds to the GPH wave three patterns.

The daily variability is investigated through composite, hovmoller analysis, *standard empirical tables and equations.*

Daily sequences of composite conditions for tropical cyclones moving west, southwest and southward are compared. A link is established with the northern sub-tropical jet stream that may influence the intensity and track of cyclones in the SWIO. The temporal and spatial variability of TC rainfall and radial winds is significant. Westward and southwestward-moving TCs have rain bands of rainfall intensity of 30 mm h^{-1} that affect the equatorial region. Southwestward-moving TC maintains its intensity while southward-moving TC endures rapid kinematic and thermodynamic transformation. Westward-moving TC suffers from the blocking effect of Madagascar highlands.

In our case study analysis, it is found that the NCEP model consistently underestimates wind speed by a factor of two within a 300 km radius of tropical cyclones, when compared to QuikSCAT satellite winds. As a consequence swell–

driven storm surges are also underestimated. Infrared and microwave satellite rainfall comparisons are done and results are presented.

Preface

Small islands and coastal countries in the south West Indian Ocean (SWIO) are vulnerable to tropical cyclone (TC) variability. Cyclonic marine-weather systems often impact negatively on resources and natural ecosystems. Abrupt cyclogenesis and high seas increase the risks of marine-environmental hazards and threaten the coasts of the region. Understanding short term marine-weather, cyclone impacts and its prediction will improve mitigation strategies such that there could be a more sustainable use of marine resources and a greater potential for eco-tourism.

The main goals of this research are to describe and investigate the causes and mechanisms of intense tropical cyclone variability and their predictability potential. The circulation climatology surrounding TC distinguished by track and marine-weather related cyclone impacts are analyzed and evaluated in the context of marine resources and environment in the SWIO.

To achieve these goals, the following objectives are considered.

1. Establish causes and mechanisms of seasonal intense TC variability.

2. Develop and improve multi-variate statistical models for the prediction of intense TC days in the SWIO.

3. Understand the daily synoptic circulation surrounding selected TCs, distinguished by track.

4. Understand the link between intense TC variability and marine resources (e.g. fisheries) in the western Indian Ocean.
5. To study short term marine-weather variability and evaluate TC impacts by comparison of direct and indirect methods of observation.

The thesis contains eight chapters.

The first chapter provides an introduction, background of the research problem, motivation, objectives and hypothesis of this study. It also examines current knowledge and findings regionally and globally. Chapter 2 describes the data and methods used to fulfill this study.

Chapter 3 is the beginning of the analysis and is concerned with establishing spatial ocean-climate pattern associated with TC days. Chapter 4 considers the degree of association and physical tele-connection between variables and their stability of association with time series of intense TC days. The temporal characteristics of the TC days index is also studied.

Chapter 5 focuses on developing multivariate statistical models for the prediction of TC days in the SWIO. The models are validated to test their operational reliability. The model temporal characteristics, predictive stability and cross associations are examined. The physical mechanisms and suspected causes of TC variability are examined. Links are established with the marine resources of the region (i.e. fish catch).

Chapter 6 concentrates on the evolution of the daily circulations around selected TCs dependent on track. Important differences in kinematic and thermodynamic processes between TC trajectories are considered for operational forecast and impact evaluation.

Chapter 7 examines marine-weather and cyclonic impacts in the SWIO. An evaluation of impacts is provided by comparing direct and indirect methods of observation.

The last chapter takes an overview of scientific issues addressed in this research. It summarizes the main results and provides a discussion to synthesize the main results. Contributions of this research are highlighted and recommendations are then put forward to improve future research and operational capacities in marine weather, cyclone impacts and prediction in the SWIO.

Acknowledgments

I would like to thank my ex-lecturers, Professor Tomzak, Dr Bennette from *Flinders University of South Australia and Dr S Mason and Cathy Smith of NCEP* Data Center for providing on-line assistance. The National Center for Environmental Prediction (NCEP) and the University of Maryland are acknowledged for providing state internet access to data. Meteo-France Reunion web resources played a role in this study and thanks go to Dr Perron. I thank the staff of the Geography and Environmental Science Department of the University of Zululand for facilitating my study.

Special thanks go to my supervisor Professor Mark R. Jury for his wide and rich expertise, supervision and funding during this research.

The Seychelles National Meteorological Service, Ministry of Environment, Policy Planning and Services and the Government of Seychelles is thanked for providing assistance and my release for this research.

Lastly, I offer deep and special gratitude to Bharaty Chetty, my son Shane, and my family for ensuring that my dream was fulfilled.

Dedication

I dedicate this research to Bharaty Chetty for we have walked the road were few would have dared.

'Obstacles are challenges that make one better'
Denis Chang-Seng

Contents

Chapter 1

Introduction and Literature Review

Chapter 2

Data and Methodology

Chapter 3

Ocean- Atmospheric Circulation For Intense TC Activity

Chapter 4

Statistical Relationships, Tele-connections and Stability of Association

Chapter 5

Prediction of Intense Tropical Cyclone Days, Stability and Associations

Chapter 6

Evolution Of The Circulation For Intense Tropical Cyclones Distinguished by Track

Chapter 7

Extreme Marine Weather and Cyclonic Impacts in SWIO

Chapter 8

Conclusions and Recommendations

Figures

Chapter - Page

Tables

Chapter 1

Introduction and Literature Review

1.0 Introduction

The South West Indian Ocean (SWIO) is the focus of this study, extending from 45-70° E and 5°-20°S (fig 1.1). It has monsoon winds and ocean currents that reverse near the equator. There is significant seasonal and inter-annual variability in the circulation and rainfall of the region. The monsoon is a major system within the earth's climate and its impacts affect billions of people around the Indian Ocean.

The Indian Ocean is the source of about two-thirds of the moisture that accounts for the Indian monsoon (Hasterath and Greischar 1993). The islands south of the equator such as Mauritius, Reunion, Madagascar, Agalega and Comoros are directly affected by the impacts of TCs. The equatorial regions of the study area such as Seychelles are in-directly affected by cyclones via the intensification of the intertropical convergence (Walsh, 1993), and spiral rain bands associated with TC passing south of the islands. Transient convective waves similar to 'easterly waves' sometimes influence the region (Jury & Pathack, 1993).

1.1 Statement of the problem

The region just south of the equator in the western Indian Ocean has received some attention recently despite the poor resolution of conventional observations (Jury & Parker, 1999). Global interest is growing because of the monsoon circulation and the discovery of a dipole-like circulation. Whilst international effort is growing with regard to data collection, it is important to understand past marine-weather and climate variability.

Globally it is clear that during some summers there are numerous TCs, yet in other years there are few. What factors cause years of abundant TC? For example in 1984 there were 22 TC days while in 1994 there were 27 TC days (Jury et al, 1999). The new historical record stands at 2.06 sigma in 2001 exceeding the previous record of the 1971 (1.96 sigma).

Some research has been done on TC variability in the SWIO. Jury (1992) identified notable climatological features and forecast indicators similar to Gray (1984) to explain why certain summers experience more TC's. More recently Jury et al., (1999) formulated and conceptualised statistical algorithms with three predictors for the months from July to November period which accounted for 59 % of the variance over the 1971-92 period. The same statistical model; using QBO, southern Indian Ocean pressure and meridional difference in pressure over the NW Indian Ocean as predictors, now accounts for only 20% of intense TC variability. This implies the model has lost some of its ability to explain inter-annual variability of TC days. Perhaps the decadal variability was in-sufficiently represented. Therefore, *further updating and a new conceptual* framework is needed to collectively explain the underlying causes.

In one of the more recent studies, Rakotondrafara (2001) investigated the variability in the SWIO TCs with the hypothesis that the large-scale slowly varying circulation anomalies determine the climatological basic state such that conditions are more favourable at certain times than others for TC formation. The principle objective of the study was to answer how the inter-annual variation of TC frequency is related to the environmental thermodynamic and kinematic parameters using National Centres for Environmental Prediction Atmospheric Research Reanalysis data. The main important findings are elaborated in the literature review section. The constructed TC time series index was based on data from US Navy/ NCDC Global Tropical / Extra tropical Cyclone Climatic Atlas CD-Rom which is compiled data from Joint Typhoon Warning Centre (JTWC) and regional specialised Centres (RSMC) Reunion and Mauritius Island. The 32 years TC index from 1966 to 1998 used in the study is for named tropical storms (greater than 34 knots) only. In this study we are looking at intense tropical cyclone rather than named TCs. The interest in intense tropical cyclone is because of their possible strong signal and related impacts. In addition, the study raised questions regarding the issue of the reanalysis data converging to climatology in data poor regions. It was seen that upper-level relative vorticity at 200 hPa correlated negatively with TC frequency in the cyclone development area, indicating less anti-cyclonic flow with more TCs. The contradiction may indicate a spurious effect of the upper level data due to the scarcity of upper-air-sounding station in the Indian Ocean. The same feature is observed in the analysis of vertical wind shear which was observed to be positively correlated with TC frequency, adding more suspicions to the accuracy of the upper level data. In addition, the study is limited to the in-season analysis in the Indian Ocean region only. In this study, thermodynamic and kinematic potentials signals are analysed from the Indian to the Pacific Ocean before and during the TC season.

A detailed knowledge of the daily synoptic thermodynamic and kinematic fields surrounding intense TC is lacking. TC climatology in the SWIO is limited to estimates of tracks, intensity and overall frequency. Detailed aircraft surveys on the structure and dynamics of TC have not yet been attempted in the SWIO. The evolution of the spiral rain band (Asnani, 1993), strong winds and swell-driven storm surges associated with TCs is well studied in other ocean basins, however there are only few studies for the SWIO.

The socio-economic impacts of extreme weather and climate have not been investigated in the region except in the case of the Bay of Bengal (Flierl and Robinson, 1972; Das et al., 1974; Ghosh (1977). Very few studies have compared and evaluated the impacts of TC using high resolution satellite data (QuikSCAT scatterometer winds, tropical rainfall measurement (TMI)).

The ocean-climate interaction with natural resources such as fisheries has recently gained much interest among scientist because of the potential economic benefits, but few studies have considered the relation between TC frequency and fisheries.

1.2 Motivation and Objectives of the study

Marine weather systems often impact negatively on resources and natural ecosystems. Countries in the region and the world have recognized that the Indian Ocean profoundly influences the lives of at least 1.5 billion people. Although floods, droughts, strong winds and storm surges have always been an

integral part of human existence and has influenced people's experiences, our collective coping strategies have so far been limited by the complexity of human responses to marine weather systems. This has led to the development of conservative management that fails to capitalise on the up-sides of weather variability and only poorly buffer against the down-sides. Being small islands and coastal countries scattered in the wide expanse of the Indian Ocean, most of the economies are largely dependent on fisheries and tourism. In addition, almost one-third of the world's total petroleum production and over half of the world's sea-trade in crude oil pass through these waters, mostly transported from the Middle Eastern countries.
Sudden cyclogenesis and high seas increase the risks of marine-environmental hazards and coastal degradation which poses the most immediate threat to the coastal regions of the SWIO. The tourism sector, the fishing industry and the environment are all vulnerable to TC impacts in the region. It is therefore necessary to understand and predict year to year and long-term trends in the frequency of intense TCs within the context of risk assessment by insurers and the need for public protection.

It is important to outline the problems in order to assist in the process of establishing a more formal approach. The knowledge of marine weather variability and its socio - economic impacts in the SWIO will help to better predict climate variability and develop management criteria for sustainable use of marine resources and eco-tourism.

The specific objectives of the study are:

1. Establish how seasonal TC activities relate to the large scale ocean and monsoon circulation structure.
2. Develop and improve multi-variate statistical models for the prediction of intense TC days in the SWIO through composites and statistical analyses.
3. Establish causes and mechanisms of seasonal intense TC variability.
4. To study the daily synoptic circulation surrounding TCs and the rain band pattern distinguished by their track.
5. Evaluate the performance between numerical weather predictions (NCEP) and spaceborne scatterometers (QuikSCAT) around the TC centre in SWIO.
6. To show short term marine-weather variability and evaluate swell and storm surge impacts of TC in the SWIO by comparison of various equations and input data, e.g. satellite vs. model.
7. Compare infra-red and micro wave estimations of rainfall in the spiral rain band of TC for impact assessment.
8. Understand the link between intense TC variability and marine resources (e.g. fisheries) in the southwestern Indian Ocean.

1.3 Hypothesis

The following hypotheses are tested:

- Vertical wind shear controls the seasonal frequency of TCs in the SWIO (more than thermodynamic effects) through the southern hemisphere subtropical jet stream both locally and upstream (eg. to the west).

- The decadal component of seasonal TC frequency in the SWIO is controlled by the Atlantic circulation (revealed through anti-phase conditions over South America and Indian Ocean).

- Coupled transient Rossby waves (heat content and surface fluxes) play a role in modulating the interannual component of TC frequency.

- TC impacts (e.g. wind speed, rainfall, swell heights and storm surges) are underestimated by a factor of two using current numerical weather prediction assimilated products.

- There are substantial thermodynamic and kinematic differences distinguishing the track and intensity of SWIO TCs (eg. the northern hemisphere subtropical jet stream and equatorial outflow).

- Monsoon flow to the north of Madagascar and trades winds to the southeast help determine the intensity of TCs and their impact.

1.4 Literature review

1.4.1 Interannual-Seasonal Variability

The SWIO is recently gaining some attention though data is relatively scare compared to other oceans. The understanding of the atmospheric circulation and synoptic scale variability is gradually improving in the Indian Ocean due to recent studies related to the uniqueness of the Indian Ocean monsoon and dipole circulation. Dennet (1978) indicated that alterations in the circulation in the region have implications for the WIO. In recent years a number of studies have shown that climate variability in the Indian Ocean has direct consequences for tropical African rainfall (Ogallo, 1988; Arpe et al., 1998; Makarau and Jury, 1997, Reason and Mulenga, 1999; Walker, 1990; Mason, 1995).

Studies by Reverdin et al., (1986), Meyers (1996), Webster et al., (1999), Saji et al., (1999) and Camberlin et al., (2001) have suggested that strong seasonal ocean-atmosphere interaction modes are unique to the Indian Ocean climate system. Behera et al., (1999) and Vinayachandran et al., (2000) showed that there are internal dynamic and thermodynamic processes that lead to basin-scale air-sea interaction in Indian Ocean. It has been claimed that an east-west dipole mode exists in SST in the tropical Indian Ocean which is independent of the El Nino signal. This condition can lead to increased equatorial easterly flow and excess rainfall in the western Indian Ocean and eastern Africa.

SST variability in the Indian Ocean is important because it determines moisture in the summer monsoon (Hastenrath & Greischer, 1993). In a study on inter-annual variability in sea surface temperature (SST) in the tropical Indian Ocean, Murtugudde and Busalacchi (1999) indicated that the SST variability is determined largely by thermocline variability in the SWIO through the process of Ekman pumping, entrainment through vertical advection.

In a recent study (Yeshanew, 2004) showed that the first EOF mode of heat content anomaly in the Indian Ocean accounts for 32 % of total variance (fig 1.2) of which 73 % is inter-annual. The EOF1 of HCA was linked with the first

EOF of the wind stress (fig 1.3), which together comprises the Indian Ocean dipole.

El Nino events have been shown to be associated with TC in the Atlantic basin (Gray 1984 a, b; Shapiro, 1987). The physical link between ENSO and cyclones is the alteration of tropospheric flow patterns and upper ocean heat content. In warm episodes (El Nino) increased westerlies at 200 hPa causing shear and reduced TC in many areas (Schroeder and Yu, 1995).

On an inter-annual basis, the El-Nino alters SST and the global circulation such that Sahel rainfall is reduced (Palmer et al, 1992, Ward, 1992). The more intense and frequent El Nino events in the 1980's and 1990's caused decreased Sahel rainfall and lowered Atlantic basin hurricanes. On a multi-decadal time scale a warmer southern and cooler northern hemisphere SST contributed to Sahel drought (Folland et al., 1986, 1991). A strong association has been established between increased (decreased) rainfall over the West Sahel and increased (decreased) Atlantic TC basin activity. Intense hurricanes show a strong downward trend during the 1980s. The Sahel drought which began in the late 1960's was a temporary condition. Thus, it was expected that the ending of the Sahel drought will bring an increase in intense hurricane activity associated with abundant Sahel rainfall similar to what happened in the late 1940's and 1950' (Landsea and Gray, 1992).

The seasonal link between Sahel rainfall and Atlantic hurricane activity is mainly due the upper tropospheric circulation which brings changes in the monsoon structure and strength of the easterly waves produced over North Africa. Sahel drought years are associated with upper level westerly and shear over the tropical Atlantic

In another independent study Glodenberg and Shapiro (1995) confirmed that the main physical mechanism for both these associations is an equatorially–confined Walker-Cell-circulation which acts to modify the vertical wind shear over the Atlantic cyclogenesis region. Jury, Enfield and Melice (2003) also found the subsequent decrease in West African rainfall, and the Sahel drought to be consistent with the acceleration of the direct circulation.

The global sea surface temperatures (SSTs) have a strong influence on the hurricane activity in the Atlantic. Figure 1.4 is the correlation of the anomalous SST in August - October (ASO) and the number of Atlantic hurricanes in this period. Hurricane activity has a high correlation with the local sea surface temperatures in the tropical Atlantic. The negative correlation in the South Atlantic could be part of the Atlantic dipole pattern, which is related to the rainfall variability in the Sahel (Folland et al., 1986), and Sahelian rainfall variability (Gray 1984). The correlation pattern on the North Atlantic has been related to a multidecadal variability of the Atlantic hurricane activity (Goldenberg et al. 2001). *On the Pacific, an ENSO pattern appears,* which influences the Atlantic hurricane activity indirectly, mainly by changes in the upper tropospheric winds in the tropical Atlantic (Gray 1984). The Pacific pattern is possibly a mixture of ENSO and the PDO.

In a study on climate trends associated with multi-decadal variability of Atlantic hurricane activity Gray, Sheaffer and Landsea (1997) concluded that the preeminent effect dominating all factors such as regional SST's and trends in global pressure is decadal variations in the Atlantic thermohaline circulation. Similar results were also obtained by Christoph et al., (1998) and Cai et al., (1999). It was found through decadal variations of intense hurricane activity is one effect of variations of heat transport by the thermohaline circulation that helps to connect the south Atlantic and southern Indian Ocean.

The Antarctic circumpolar wave (ACW) impact on global climate is of some importance. It has a unique ability to transport ocean-atmosphere anomalies around the southern ocean. The ACW has been investigated by White and Peterson, (1996), Jacobs and Mitchelle (1996). In 1997, Qiu and Jin found that a preferred zonal wave number 3 occurred around Antarctica. The mechanism suggested for maintaining ACW is through air-sea interactions. Cai and Baines (2001) suggested the presence of both zonal wave numbers 3 and 2 in the ACW structure in the last 20 years. Carill and Navarra (2001) found a dominant wave number 2 structure on interannual time scales likely modulated by inter-decadal variability.

The association of the Antarctic climate with ENSO was also investigated. Carleton (1988) was the first to point out the association between El-Nino events and Weddell Sea ice pack. His results were confirmed by Simmonds and Jacka (1995), Gloersen (1995), Ledley and Huang (1997), Yuan and Martinson (2000). Peterson and White (1998) suggested that the ENSO signal is transmitted through the troposphere into the ocean in the subtropics to the high latitudes, where it becomes a source of ACW. In a recent study, Cai and Baines (2001) suggest a tele-connection between ENSO and ACW through the atmospheric Pacific–South American pattern in the southern high latitudes.

Recently, Venegas (2003) confirmed the existence of the two significant signals with different temporal and spatial characteristics in the southern ocean. The first signal having a zonal wave number 3 structure has a period of around 3 years driven by air-sea interactions. The second signal is a zonal wave number 2 structure with periodicity of 5 years. It is found to be remotely forced by ENSO phenomena. It involves large-scale patterns and is more confined to eastern Pacific sector. Venegas suggested possible linear combinations of the two signals and a link to its fluctuations of the ACW on the interannual timescale.

The temporal and spatial variability of jet streams in the northern hemisphere have been investigated by a couple of researchers. However, there are still a number of issues which are not clear and are still a debatable. Why the polar front jet (PFJ) in some years runs well to the north/south or becomes blocked? In northern hemisphere during warm ENSO phase the entrance trough is weaker. Therefore, jet seems to split into a subtropical and poleward jet over eastern Pacific in winter, thus storm tracks become elongated, enhancing more cyclones to enter the US from SW compared to its north west entry in normal years. In the ENSO cold phase, the eastern ridge is enhanced causing storm track to be deflected further polewards. Therefore, baroclinic eddy generated in the bifurcation has important consequences on storm track variability (Lau 1985; Held et al., 1989; Orlanski 1998).

In a very recent study White and Tourre (2003) investigated global SST and sea level pressure waves during the 20th century. It is argued that a discrete number of global signals (SST and SLP) dominated climate variability from 40° S to 60° N during the last hundred years. Quasi-biennial (2.2 year period), inter-annual (3-7 year period), quasi-decadal (~11- year period) and inter-decadal (~17-year period) signals were identified. These global waves exhibit standing and travelling modes. The travelling waves propagate eastward and are thought to be useful for climate prediction.

Recent studies show that during the El Nino of 1997/98, anomalous easterlies developed in the tropical south Indian Ocean, forcing a westward-propagating downwelling wave and positive SST anomaly. This is associated with more rain due to cyclonic circulation in the surface wind flow. This coupled Rossby wave is important on ocean-climate in the WIO. Xie et al., (2002) tested this by compositing the number of TC days when the SWIO thermocline achieves a threshold deviation of 0.75. It was found that there were 10 such cases of deep and 10 cases of shallow thermocline. The difference between the deep and shallow years attains a difference in TC frequency at maximum about 60° E, 15°S, a 66 % increase (figure 1.5).

In a study of climate variability in the SWIO, Jury and Pathack (1991) showed that the trend of cyclone genesis was from ENE-WSW, paralleling a similar pattern in the SST and ITCZ (OLR minimum). Increasing SSTs to the NE Madagascar in the preceding spring (October) creates conditions for the development of more TC (Jury, 1993). In the same study it was shown that transient convective waves exist between 10-20°S band during the summer and that the waves contribute to SWIO summer rainfall.

In another study regarding climatological pattern associated with TC in the SWIO, Jury (1993) found that more TC favoured upper easterlies and lower westerlies over the equatorial zone north of Madagascar. Sub-tropical easterly winds increased while mid-latitude westerlies retreated polewards such that the southern Hadley circulation strengthens. In the same study, statistical analysis showed cyclone spectral peaks at 2.2 - 2.85, 4 and 10 years. QBO was modulating the occurrence of TC in the SWIO, hence explaining the first spectral peak. More cyclones form in the east phase of the QBO (when stratospheric equatorial winds are from the east). The west phase (+U component) suppresses TC frequency. It was also indicated that cyclone frequency tends to increase one year prior to a global El-Nino (-SOI).

The variations in the number of intense tropical cyclones (central pressure below 945 hPa) in the south-west Indian Ocean was studied over the last thirty years by Hoarau (1999). The intensity of cyclones was estimated through the interpretation of satellite pictures. It was found that the number of intense tropical cyclones has a tendency to increase especially in the case of the extreme systems (pressure below 920 hPa) for which a stronger increase in frequency occurred over the period 1990-99. This increase is not steady: a slight decrease in the number of intense cyclones took place over the decade 1980-89. There was no increase in intense TC associated with the 1980's ENSO. In contrast, the decade 1990-99 shows the greatest number of intense cyclones. Figure 1.7 shows the decadal variations in the number of intense TCs for different categories according to the Dvorak classification in the SWIO. It indicates an increase in intense TCs in the SWIO: 27 for the decade 1970-79 and 34 for 1990-99. Similar trend in intense TCs is observed with the north Atlantic, and northeast Pacific cyclone basin (fig 1.8). The annual average of intense TC are 2 for north Atlantic, 3 for SWIO and five for northeast Pacific basin.

One of the most related findings on the internnual variability of SWIO named TCs using similar but shorter data set was investigated by Rakotondrafa (2001). In general it was found that TCs are generated slightly poleward and more eastward during active years. Correlation analysis indicated small positive correlation between SST and cyclones in the TC development area while significant correlation between TCs and sea level pressure are found in the mid-to-late season. During active years TC frequency from November to February is twice that during inactive years while the differences are not substantial in the late season. An early start of TC indicates high TC frequency, but characterised with short active season. In contrast, low TC count shows late season surge in April with March being quite. Only SST, low-level vorticty and wind circulation showed differences comparable to their respective average interannual standard deviation. The most notable differences between active and inactive years occur in the mid-latitudes which is characterised with an anomalous anticyclone located south of Madagascar from surface to 200 hPa. The anticyclone seems to generate anomalous southerly flow in the channel area. Several studies have linked the south Indian Ocean subtropics to different regional or remote forcing such as the Indonesian through flow, the Antactic Circumpolar current on the basin (Hist and Godfrey 1994, Allan et al 1995). One of the interesting finding is a local minima approximately every 30 days in the 6-day running average between December and early May suggesting a possible link with the Madden Julian oscillation (MJO) signal.

1.4.2 Marine-Weather Variability and Impacts

Sadler (1976) found that the position of the upper troposphere trough relative to the centre of a TC centre is important for intensification of TC. Holland and Merrill (1984) explained that an approaching upper level westerly trough acted to enhance upper level divergence for the outflow of TC. Molinari and Vollaro (1989) documented the rapid intensification of Hurricane Elena due to large inward eddy momentum flux in the outflow layer caused by the passage of a mid-latitude trough north of the hurricane. The numerical studies conducted showed that the sudden intensification of Florence's inner core was correlated *with the position of the upper tropospheric westerly jet.*

Many researchers (Reihl, 1950; Pfeller and Challa, 1981; Molinari and Vollaro 1989; 1990) have concluded that the interaction between upper level troughs and TCs are positively associated. In one study (Kaplan, 1987) showed the interaction between hurricane Emily and an upper level trough enhanced the vertical circulation described by Molinari and Vollaro (1990). Beven (1993) illustrated how the proximity of a trough leads to track changes and delayed re-curvature.

The scarcity of fine resolution data has surely limited the study of cyclone circulation both in its surrounding and outside environment in the SWIO. However, Jury and Parker (1999) investigated the synoptic environment of composite TCs in the SWIO for westward and re-curving cyclones using ECMWF model data. The results indicated that westward cyclones tend to be associated with declining intensity while poleward recurving TC undergo vortex development. In addition, it was recognized that the presence of strong westerly winds in the upper troposphere was a condition for TC re-curvature. Westward-moving TCs were thermally driven while south-recurving TC was dynamically driven.

Naerra and Jury (1997) investigated the interaction between TC and the background circulation. It was uncovered that a long zonal ridge suppressed the subtropical jet south of 25°S in 1994. Winds at upper levels suggested strong equatorward outflow near the tropopause consistent with the findings of Nassor (1995). The background flow was conducive to maintain the intensity of TC.

Many studies have concluded that local environmental factors affect storm intensity. Internal forces has been investigated by a couple of researchers (Barnes et al., 1983) suggesting rain band affecting TC intensity through thermodynamic modification of low-level inflow. Convectively active rain bands are regions having significant reduction in radial inflow to the TC core. Winds in the lower troposphere become much more tangential, such that it delays the arrival of the inflow air.

In other ocean basins many spiral rain band studies have been carried out using mesosynoptic observation (Wexler, 1947; Simpson, 1954; Ligda, 1955; Fujita et al., 1967). More quantitative studies and dynamical explanations including numerical simulations of the spiral bands have been carried out by Abdullah (1966), Kurihara (1976), Mathur (1975). However little is known about the SWIO cyclone spiral rain band especially the equatorward band, which is often associated with the ITCZ.

Tokyo University (1969) has reported rainfall in excess of 30 mm per hour in rain band. Along a rain band there are patches of heavy cloud separated by relatively clear skies. It is unclear if the rain band movement is inward or outward (Willoughby 1977, 78; Kurihara, 1976). Spiral rain bands can last for days while the individual convective cells of the spiral rain band have a life span of half an hour. Maximum vertical velocity occurs behind a pressure minimum. New convective cells form on the upwind (inner) side of the band and travel through the band to dissipate on the downwind (outer) side of the band. The convective rain is normally accompanied by gusts of wind. All previous studies confirm the existence of some axial asymmetry of a TC. Two bands are observed spiralling in with a width of the order of 50 km near the outer periphery and contracting inwards. The angle of inflow is of the order of 15 degrees.

Studies on marine weather variability and its impacts are gradually emerging in the region. In a study on intra-seasonal climate variability of Madagascar, Nassor and Jury (1997) showed unstable thermodynamic conditions shift eastward from SE Africa coupled with surges of monsoon northwesterlies and upper level easterlies. These are the key features of flood producing systems over NW Madagascar. In another study Jury and Naerra (1997) analysed the impacts of TC on eastern Madagascar during 1994. Floods inundated 300000 hectares of plantations on the coastal plains while a 6 m storm surge and waves of 10 m thrashed the eastern coast of Madagascar.

Recent work on inter-comparison and validation of QuikSCAT scatterometer generated wind field has gained much interest and attention. The measurement and accuracy of scatterometer winds has been studied widely by Freillich and Dunbar (1999) and Freilich and Vanhoff (2001). It was found that the error in wind speed is less than 1 m s^{-1} over the full range of the wind speeds, while the directional uncertainty decreases rapidly with increasing wind speed. Kelly et al., (2001) showed that regions of strong Ocean current produce differences of 1 m s^{-1}.

It is well known that the details of the circulation of TC are poorly resolved in surface wind analyses and forecasts produces by NWP centres. This shortcoming is addressed by applying a process of "bogussing" within a specified radius of the TC centres using solutions of simple parametric models. Cox et al., (1992) and Thomson et al., (1996) describe an operational system used for modelling tropical wind fields. Wide swath satellite scatterometer data make it possible to fit the model with QuikSCAT winds though there are some problems with rain contamination. The result indicated a close statistical match between QuikSCAT derived model winds and the HRD aircraft derived winds.

In a recent validation study (Chelton, 2000) used vector correlation developed by Jupp and Mardia (1980) to provide a measure of the agreement between the ECMWF and NCEP wind data sets. A vector correlation of 1 means the two vector data sets differ by only a constant multiplication factor in speed and constant offset in direction. Global maps of the vector correlation between operational analyses of 10 m winds by NCEP and QuikSCAT over the period July 1999 through June 2000 were produced. Both NCEP and ECMWF indicated poor low vector correlation in the tropics. The low correlations were related to light and variable flows. Largest errors are in the tropical regions, southern hemisphere and in the ITCZ where the sigma exceeds 2 m s^{-1} for each orthogonal component. The limitations of the ECMWF and NECP model were due to the spatial resolution of model, inadequacies in the model parameterisation of the atmosphere boundary layer and inaccuracies in the SST boundary condition.

In another interesting verification and application study Hsu (1995) demonstrated that accurate estimates of TC intensity over data sparse ocean regions are attainable by using a planetary boundary layer model that relates the pressure gradient to the surface winds observed by the scatterometer. Thus, an estimate of the surface pressure is possible, which is one of the indicators of the intensity of TC. Comparison between ECMWF and scatterometer derived winds were favourable near the TC centre. It was *concluded that scatterometer data could be used to resolve the circulation of* TC not shown in ECMWF, and therefore can be further used to derive the surface pressure.

More recently Liu et al., (2000) showed how the high spatial resolution of QuikSCAT data provides a detailed description of TC. The 12.5 km data resolution reveals the delineation of surface wind convergence associated with the multiple rain bands of Hurricane Floyd.

1.4.3 Synthesis of literature reviewed

The above studies agree that ocean-atmosphere interaction, ENSO, QBO, Indian Ocean dipole and Rossby wave propagation have relevance to the seasonal to interannual oscillations in weather in the Indian Ocean. Many papers have been put forth by Gray (1968), Gray and Landsea (1992), and Gray et al., (1992, 1993) on the Atlantic hurricanes while few papers have studied causes of SWIO TC variability (Jury and Pathack (1991), Jury (1993) and Jury et al., (1999).

The study by Rakotondrafa (2001) revealed many important causes and mechanism of TC variability in SWIO during the cyclone season, however some results were contradictory such as the upper level vorticty being less anticyclonic in the active years and the positive correlation between vertical wind shear and TCs in the development area. Further considerations about the mechanisms of TC frequency variability require a longer TC index and environmental data set for covering a larger study region. It is also expected that the recent improvement in TC observational techniques will be of much of an advantage. In this study there is need to study the thermodynamic and dynamic potentials not only during the season but also prior to the peak TC season.

An updating of multivariate statistical models is needed similar to Gray's Atlantic hurricane statistical models. In addition a revised conceptualised framework is needed to collectively explain both the underlying causes and mechanisms driving the variability of intense TC days.

Few detailed information is available on the circulation structure and climatology surrounding the TC and its spiral rain band and its impacts in the SWIO. Past studies on cyclone impacts were focused on Madagascar (Naerra and Jury (1997)). Studies by Parker and Jury (1999) were quite detailed in investigating synoptic environment of composite TC, however the numbers of TC cases used to construct the composite were small and the TC impacts were not an issue. This study will examine the daily synoptic circulation and rain band surrounding TCs distinguished by their track in the SWIO.

Many researchers have focused on intercomparison and validation of high resolution data with model estimated and in-situ data around the world. However, impact assessments using high resolution data compared to model estimated and observed fields are limited. Therefore, high resolution data provides a unique opportunity for comparison with the operational models and to evaluate the impacts of TC in the SWIO.

Overall it is expected that the use of a range of data sets including model – assimilated and new high resolution data sets will bring new insights and understanding to marine weather variability, cyclonic impacts and prediction in the SWIO. Therefore, such research is needed. Figure 1.6 is a composite of TC tracks in the SWIO that illustrates the main TC zone as 50°-75°E, 10°-20°S. Fig 1.9 is the research path in this study. It shows that the intense tropical cyclone days variability and its prediction forms the central part of this research. The short term marine weather variability is examined by analysing the surrounding circulation associated with intense TC by track while impacts (swells, storm surges, and intense rain) in the SWIO are evaluated by comparing direct and indirect methods of observation. Applications of this research is geared mainly towards operational real time forecasting (aviation, marine and public), fisheries management and in helping to develop mitigation guidelines, strategies and planning.

The next chapter discusses the data and methods used to study marine-weather variability and cyclone impacts and prediction in the SWIO.

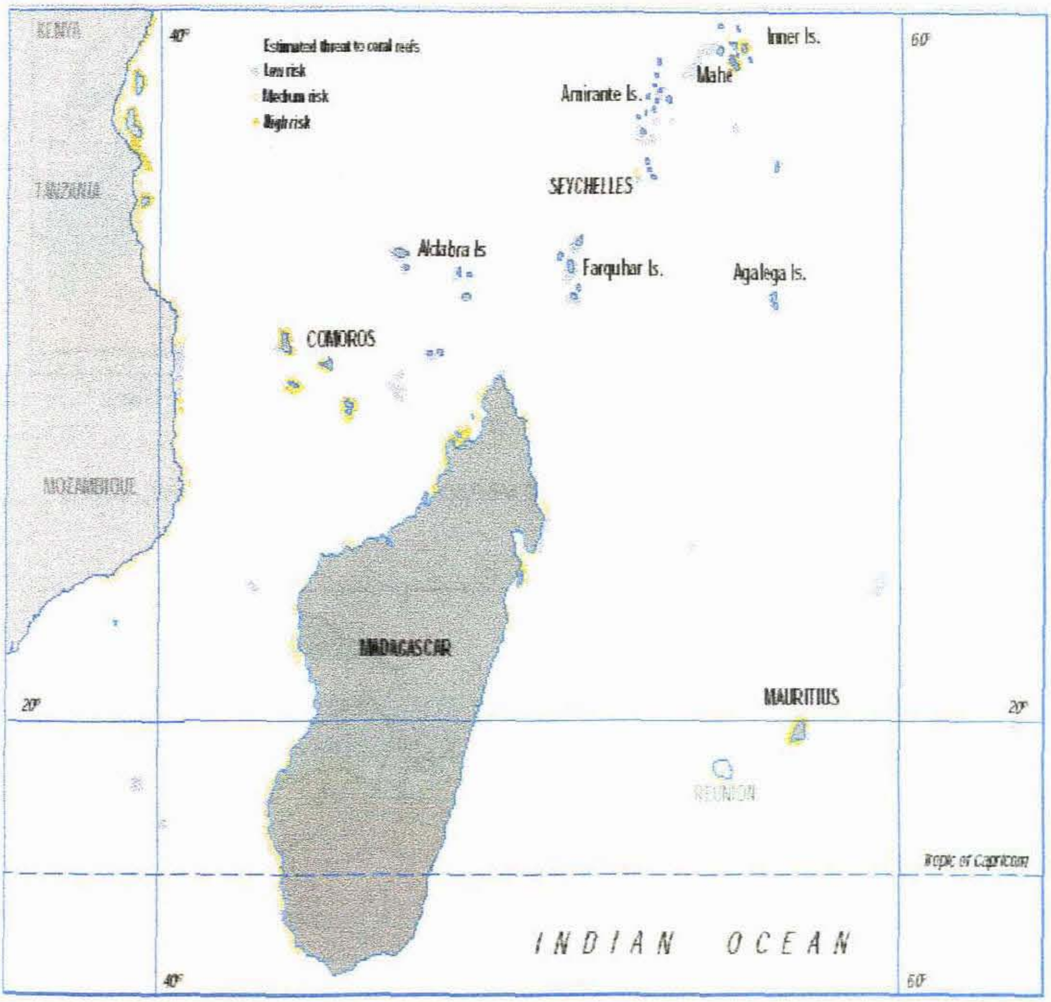

Fig 1.1: Map of the study area (Source: UNESCO)

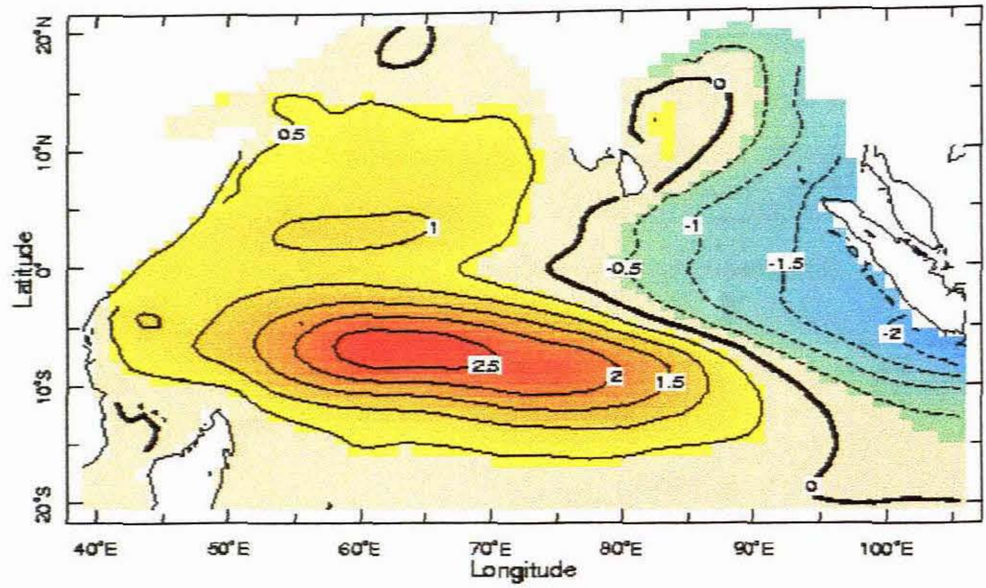

1
Fig 1.2: EOF 1 of HC 125 in IO (32% of variance) (Source: Yeshanew, 2004)

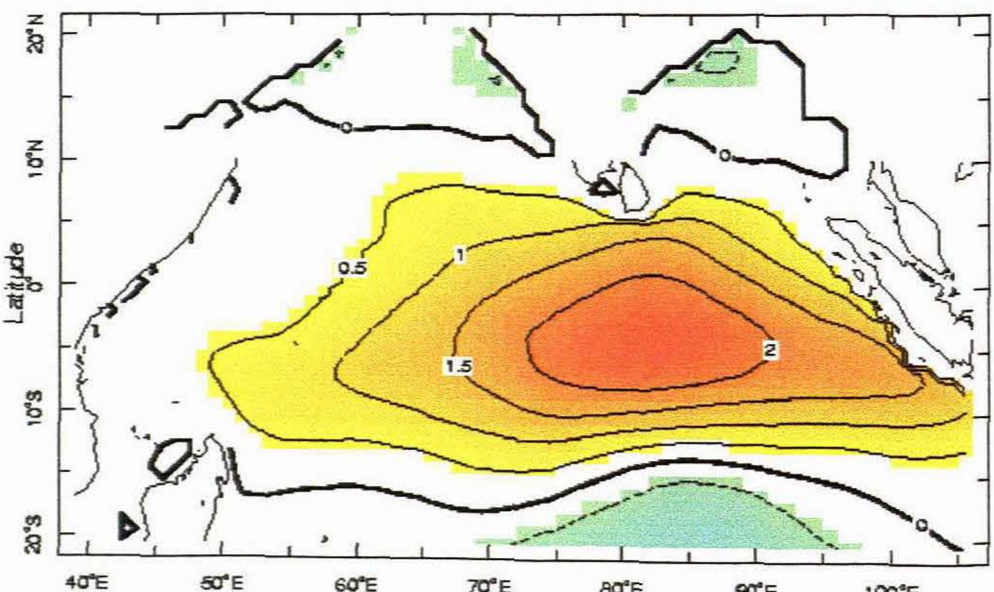

Fig 1.3: EOF 1 of wind stress in IO (22% of variance) (source: Yeshanew, 2004)

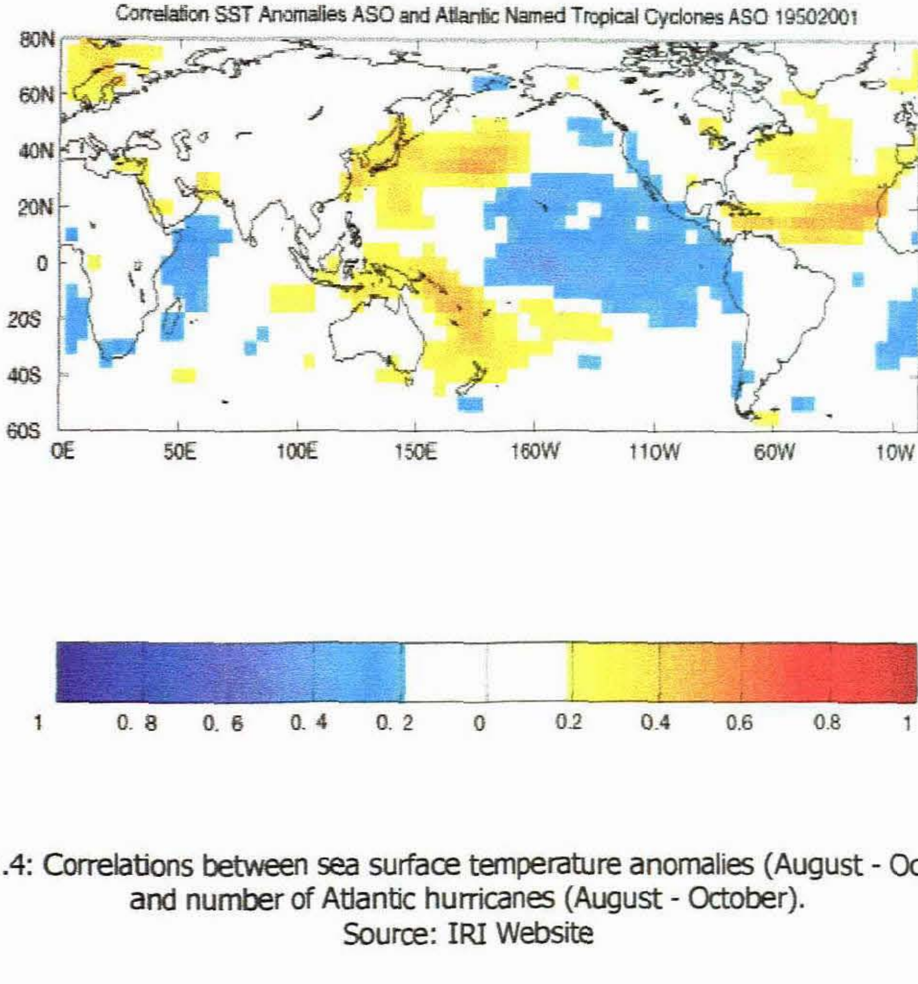

Fig 1.4: Correlations between sea surface temperature anomalies (August - October) and number of Atlantic hurricanes (August - October).
Source: IRI Website

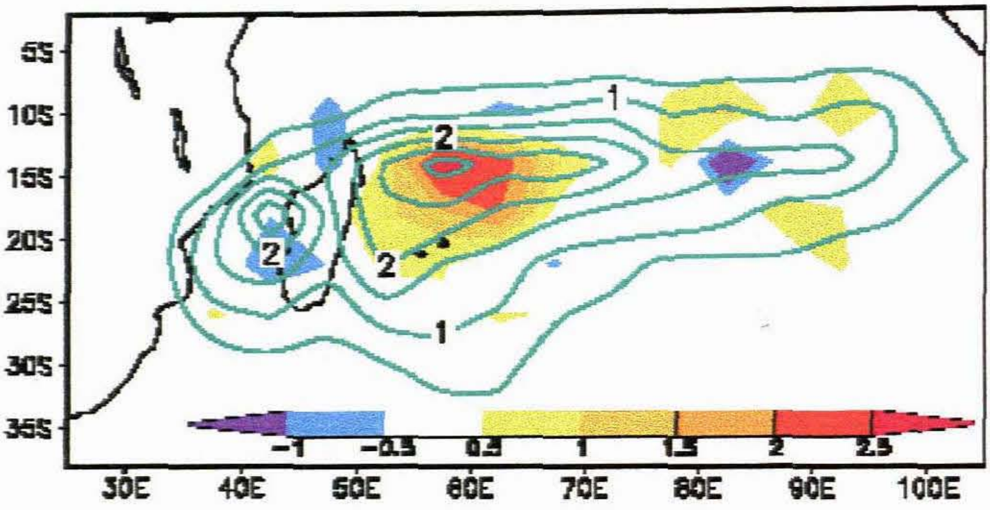

Fig 1.5: Climatological-mean TC days (contours) in December-April, and the difference (color shade) between years of anomalously deep and years of anomalously shallow thermocline in 50°-70°E, 8°-12°S (source: Xie et al., 2001)

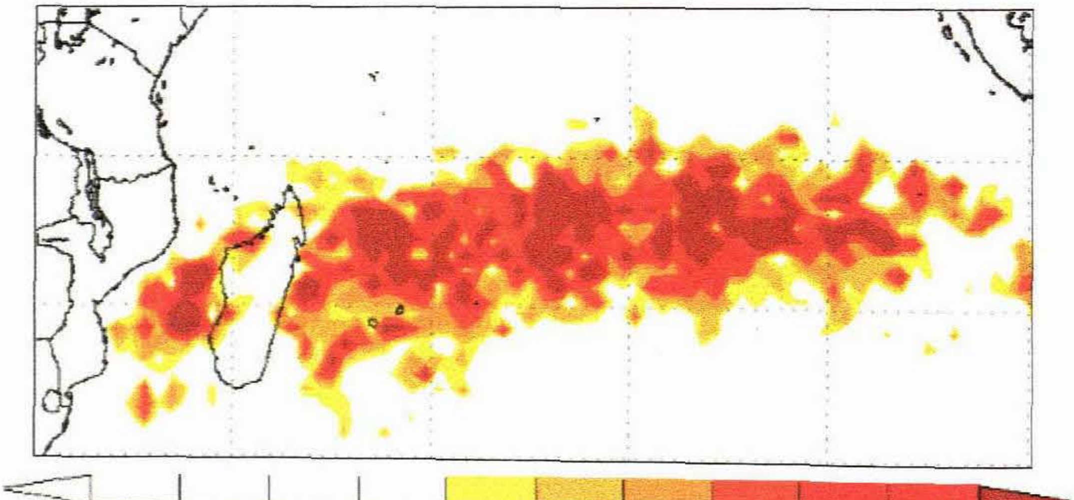

Fig 1.6: Composite TC in southern Indian Ocean: Number of positions passing through 1 x 1 degree bins and best track positions with an intensity of 25 kts or greater.(Source: Naval Pacific Meteorology and Oceanography Centre, JTWC).

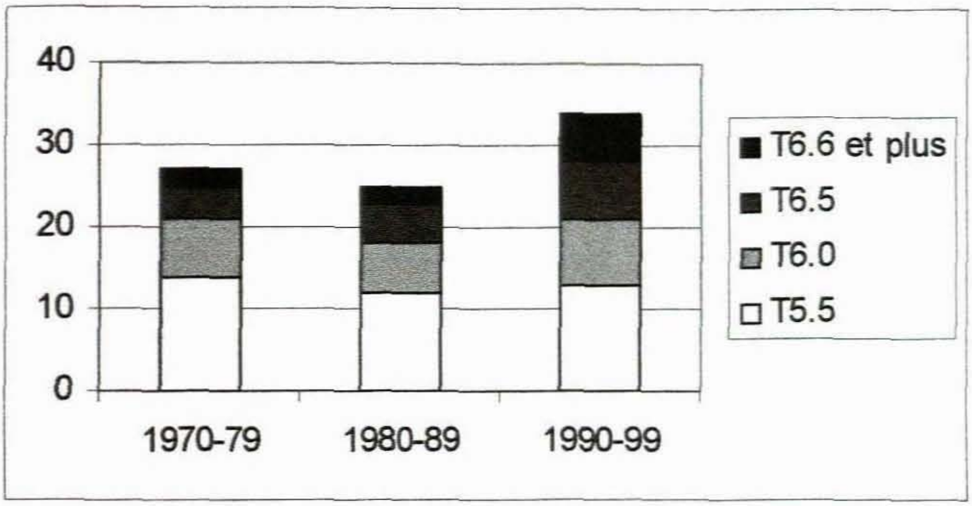

Fig 1.7: The decadal distribution of the number of intense TCs for different categories (Dvorak classification) in the SWIO
(Source: NCDC, 1999).

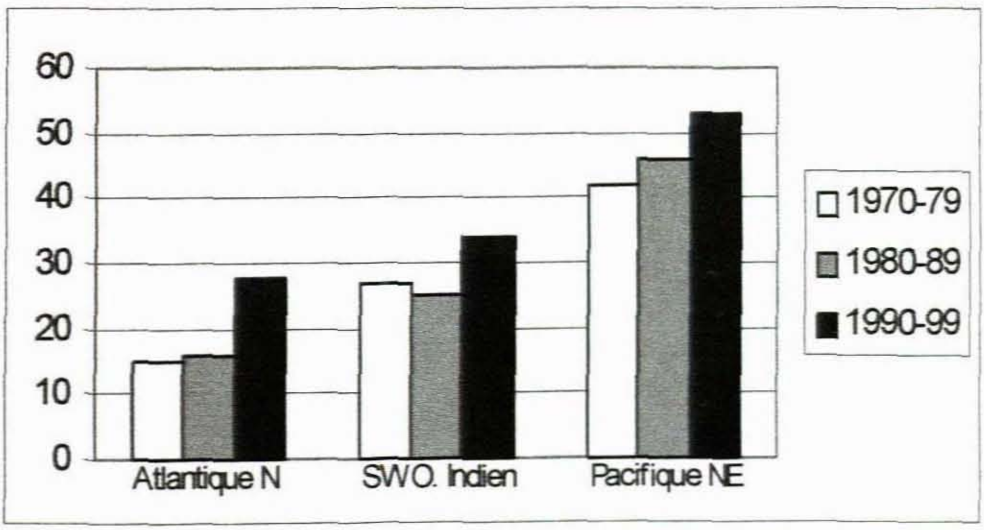

Fig 1.8 : The decadal distribution for the number of intense TCs (>T 5.5) in North Atlantic, SWIO and Northeast Pacific Ocean
(Source: NCDC, 1999; NHC, 1999)

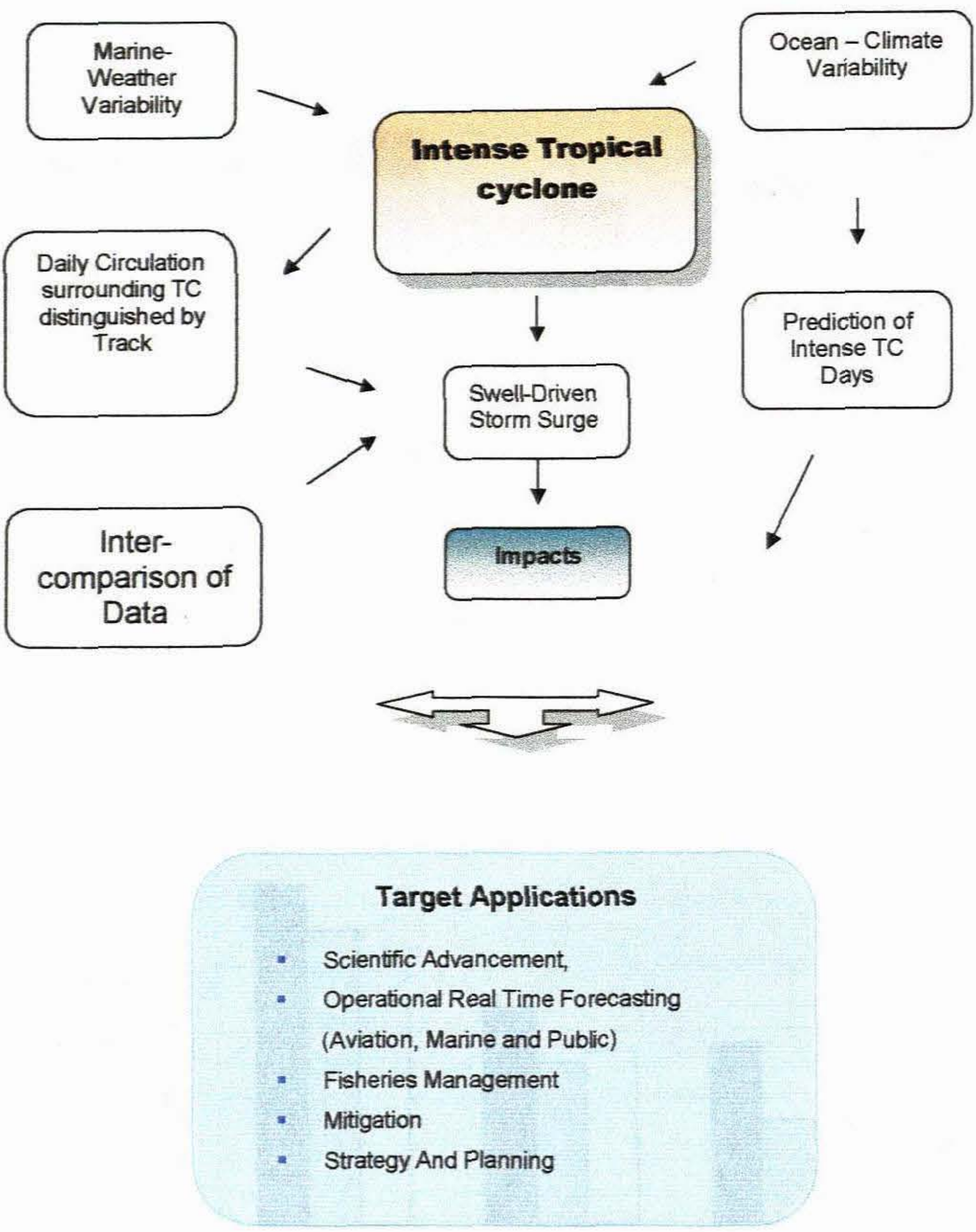

Fig 1.9: Research path of the study on Marine weather, tropical cyclone prediction and impacts in the SWIO

Chapter 2

Data and Methodology

2.1.0 Data

To study the inter-annual variability of TC, daily circulation surrounding intense cyclones, marine weather and their associated impacts required a range of data sets from diverse sources to be used. Annual data on intense TCs was obtained from Meteo-France (Reunion) and the Mauritius meteorological services which spans the period from 1960 to 2002. Historical advisories of TC positions and intensity were drawn from the US Navy archived at the Australian Bureau of Meteorology (BOM) website. Most atmospheric data are from NCEP (National Center for Environmental Prediction). All ocean sub-surface data: heat content, temperature, etc are from the University of Maryland ocean reanalysis data set. To evaluate the impacts of TC scatterometer (QuikSCAT) wind and TRMM (Tropical Rainfall) data were extracted from NASA's Earth Science Enterprise (ESE). Satellite–derived rainfall data were available from the GLOBE website managed by the University Corporation for Atmospheric Research (UCAR). Station observed rainfall was made available from the national meteorological services in the region, while fish catch data were made available from the FAO (Food and Agriculture Organization) data base. Disaster data are extracted from annual TC review publications of Mauritius, Madagascar and Meteo-France, Reunion.

2.1.1 TC Data

The TC days index is a merged data set from Mauritius (1961-1969) and Meteo-France (Reunion) (1969 - 2002). The time series consist of 41 years of data from the TC season of 1960 - 1961 to 2000-2002 for the southwestern Indian Ocean. The TC days index is an estimate of the total number of days an intense TC is located in the area 10 - 20°S, 50 - 70°E in the months December to March. The number of intense TC days is defined as the total days a cyclone has an eye surrounding the cloud vortex in satellite imagery, coupled with a surface wind speed in excess of 45 m s^{-1}. The accuracy of the TC index is perhaps less so prior to 1970's due to poor observational and satellite coverage in the SWIO (Vermulen and Jury (1992), Jury (1993) and Rakotondrafara (2001)). Historical TC position, track and intensity were drawn from the Meteo-France-Reunion website while historical predicted TC intensity and track were drawn from the US Naval Research archived at the Australian BOM website in the period 1996-2004. The addresses of the websites are as follows:

http://www.meteo.fr/temps/domtom/La_Reunion/#

http://australiasevereweather.com/cyclones/

2.1.2 NCEP Re-analysis Data

NCEP (National Center for Environmental Prediction) has developed monthly reanalyzed data sets using all recovered data (land surface, ship, radiosonde station, aircraft, satellite) from 1948 to the present using a highly advanced numerical analysis and data assimilation system. The re-analysis project is a joint effort between NCEP and NCAR (Kalnay et al, 1996) to produce a 40 year record of global climate fields. This re-analysis data is consistent and eliminates artificial (model) discontinuities in observed climate. The NCEP data has been used by many researchers such as (Hastenrath, 1994; Webster et al., 1999; Rakotondrafara, 2001). In this study analyses of zonal wind (U), meridional wind (V), velocity potential (VP), stream function, OLR (out going long wave radiation), specific humidity, precipitable water, precipitation rate, potential temperature, geopotential height (GPH), sea level pressure (SLP), air temperature and sea surface temperature (SST) were used.

2.1.2.1 Spatial Density And Temporal Characteristics Of NCEP Reanalysis Data

The properties of the data used to assimilate NCEP modeled data are briefly investigated. The sources of the data originate from ship and buoy observations, radiosonde observations, land surface and satellite. Here an examination of the spatial density and temporal characteristics of NCEP data mainly in the Indian Ocean are of interest.

Satellite Derived winds and Radiosonde Observation

Space-based observations have become important in deriving variables such as wind speed. The spatial coverage has increased in most regions, however satellite gaps still remain. Figure 2.3 shows the time series data density for upper satellite derived winds in the SWIO. The average observation per grid box (2.5X2.5) from January 1980 to 1998 was 2.7 per month in the area between 50-70°E, 10-20°S (SWIO region). There is an increase in satellite wind observation density to 18.5 in 1997. This improvement in satellite observation is the result of the repositioning of the meteosat into the central Indian Ocean in sustenance of the Indian Ocean Experiment (INDOEX). Note that cloud-tracked (satellite) winds are almost absent until 2000.

Figure 2.4 shows a time series of Sonde density observation in the same region per month. The monthly average count observation is 5 per grid box. There is a slight increase to 7.5 in the 1990's. This implies that there is less than one Sonde observation per day per grid box.

Ship and Buoy Observations

Ship and buoy observations are important data input to the NCEP models however ship observation are confined to shipping lanes of the voluntary Observing Ships (VOS) of the World Weather Watch. In contrast buoys are much lacking in the deep ocean of the equatorial Indian Ocean.

Figure 2.5 shows the spatial coverage of ship and buoy observation in January 1990. The major ship observation extends from southern Africa along the eastern coast of Africa to the Arabian Seas. The other major observation path runs diagonally near Mauritius and Reunion islands towards Australasian seas. The maximum ship and buoy observation is about 30 per day per grid box just south of Africa and southeast Madagascar. So on average, only in these areas is observations done once per day.

The time series of ship and buoy density observation in figure 2.6 were averaged at 7 per grid box per month in the SWIO. There was a sharp increase in ship density observation in 1970 but then declined. This means that there is less than 1 Ship and Buoy observation per day per grid resolution. In the United

States region, observation density per grid box per month is over 30. This implies that observation is made once each day per grid resolution.

2.1.3 Ocean Reanalysis Monthly Data

In this study use of ocean sub-surface data consisting of 125 meters vertically integrated heat content anomaly, thermocline (20°C isotherm) depth, 50 m and 100 m Ocean temperature were analyzed from the University of Maryland ocean reanalysis monthly data set.

Upper ocean heat content fields (mean temperature in the top 234 m) for the period 1958-1998 have been derived from an ocean data assimilation system operated at COLA as outlined in Huang and Kinter (2002). The data assimilation uses a variational scheme (Derber and Rosati 1989) to combine temperature observations in an ocean general circulation model (oGCM). The analysis uses all observations available in a moving 10-day assimilation window. The observations are inserted into the first guess field of the oGCM and discrepancies are iteratively minimized. It is forced by monthly averaged surface wind stress from NCEP reanalysis available at an irregular grid with a variable resolution of around 2° near the equator. The solar flux is prescribed (Oberhuber 1988), surface heat and long-wave fluxes are parameterised (Philander et al 1987, Rosati and Miyakoda 1988).

Ocean temperature observations are assimilated from in situ SST measurements from the COADS archive (Slutz et al., 1985), temperature profile (XBT, MBT, CTD, etc.) measurements (Conkright et al 1998) and, since 1981, with satellite-blended weekly SST fields (Reynolds and Smith 1994). The number of temperature profiles is generally 3000-9000 per year within the square between 30° E-120° E, 30° S-30° N during the 41 years (see figure 2.7 a, b). In 1967, 68, and 79, it surpassed 15000 profiles. In situ SST measurements exceeded 90,000 per year, reaching a maximum of 270,000 per year. However, many of these observations, especially the subsurface data, are concentrated along the coasts. There are more observations along key lines from Perth to the NW, from Madagascar to the NE, from Mauritius to the north, and from Mombassa to the east (Masumoto and Meyers 1998), which are important for our present study. However, some of these, especially in the South Indian Ocean, were established with TOGA in 1985. Figures 2.7 a, b show the spatial distributions of the temperature profiles per degree-square for the years 1958-1980 and 1981-1998. It is evident that measurements on major ship tracks were enhanced in the later period in the South Indian Ocean. Even after this enhancement, the distribution of the subsurface temperature observations was still sparse. Therefore, the assimilated product is inevitably strongly affected by the ocean model and the surface forcing fields. The model-derived results are considered in this light and we therefore employ analysis techniques that highlight repetitious patterns (eg. EOF, composite).

2.1.4 Station Rainfall Data

Daily rainfall data originates from the Seychelles, Madagascar, and Mozambique National Meteorological services for comparison of rainfall in case study TCs. The observed data are of quality according to WMO standards.

2.1.5 Fisheries Data

The fish catch data used are for Seychelles, Madagascar, Mauritius, and southeast Africa. The data spans from 1960-1999 and was obtained from Food and Agriculture Organization data base. The fish data is the total coastal fish catch managed by the fishing authority in the respective countries. However, the fish catch does not only represent changes in local concentration but also its catchability. Other problems include the reporting of fishing activities. Therefore, the results are interpreted with caution.

2.1.6 Scatterometer (QuikSCAT) Data

Scatterometers are satellite based microwave radars that infer surface winds from the roughness of the sea surface. The Sea Winds scatterometer on the NASA QuikSCAT satellite is a conically scanning antenna that samples the full range of azimuth angles with each scan cycle of 3.33 seconds during which the satellite moves 22 km along the ground track. These radar measurements when processed estimate winds with 25 km resolution over a single broad swath of 1600-km width centered on the satellite ground track. Special products with 12.5 km resolution are also available for selected regions. The Sea Winds scatterometer on the NASA QuikSCAT satellite started in July 1999 and covers 93% of the global ocean in a single day. Space bome scatterometers provide realistic detailed information as compared to numerical weather reanalysis models. The wide swath coverage of QuikSCAT is suitable for a synoptic view of wind fields over the global oceans. The 25 km resolution of its data enables a detailed description of small weather systems such as TC (Liu et al., 2000).

QuikSCAT is sensitive to wind variations from sea roughness except at rainfall rates above 100 mm h^{-11}. Improvement in winds for rain effects come with a polarimetric radiometer, but the TC eye wall still remains an obscure area. QuikSCAT wind is compared with NCEP modeled wind in the 300 km radius of TC and for impact evaluation (winds, swells, storm surge). Various website offers scatterometer data. These can be obtained from the following address: ttp://www.ssmi.com/qscat/

2.1.7 TRMM Data

The monitoring of rapid developing marine weather systems such as the spiral rain band of TCs is often difficult especially where there are few rain gauges and poor radar coverage. The Tropical Rainfall Measuring Mission (TRMM) is a recent satellite capability that can alleviate some of these difficulties. It provides an accurate estimate of the daily spatial precipitation rate in substitute of rain-gauge network (Rouault, 2001). The TRMM microwave imager is a joint project by the US and Japan to give a quantitative rain rate daily over a swath width of 760 km. Figure 2.8 shows the characteristic orbits for one day of the Tropical Rainfall Measuring Mission (TRMM) satellite. It should be noted there are five swath width intersections in the SWIO. The swath intersects over Seychelles, northwest Madascar, Mauritius and Reunion, south Madagascar and one in the central SWIO Indian Ocean at about 10°S / 70° E. Therefore this technology should be useful for studying rapid changing weather in the SWIO. TMI has an extra channel (10.7 GHz) compared to SSM/I designed to estimate tropical rainfall at a ground resolution ranging from 5 km for the 85.5-GHz channel to 45 km for the 10.7–GHz channel. The TMI measures the tiny amounts of microwave energy radiated by the earth and its atmosphere and is able to *quantify the water vapour, cloud and rain rate intensity in the atmosphere.* The limitation of TMI signal is its sensitivity to sea-surface roughness, whereas the infrared images are not. It is noted that infrared radiometers provide high spatial resolution and very good time sampling (every 30 minutes), however infrared brightness temperature do not have a direct physical relationship with rain rate since it is measured at the top of the cloud, which is indirectly related to the surface rate. In this study, TMI data are used to study the structure of spiral rain band of TC. TRMM data can be obtained from the following address: http://www.ssmi.com/qscat/

2.1.8 Satellite-Modelled Rainfall

Satellite-derived (NCEP model) rainfall data were extracted from the GLOBE website which is managed by University Corporation for Atmospheric Research (UCAR). Comparison is made between satellite derived and other methods of rainfall measurement for selected TCs in the SWIO. The website address is indicated below: http://www.globe.gov/

2.1.9 Disaster Data

Meteo-France Reunion is the TC Warning Center responsible for annual review publications on the cyclone season in the SWIO. Their publication largely focuses on the technical aspect of TC movement and structure, while the disaster statistics are rather patchy. Although the publications have improved tremendously from this centralization, disaster data for the RA1 region (SWIO) is lacking. There are several challenging problems in this respect including poor benchmarks regarding the cost evaluation of disasters. Nevertheless, the disaster data were extracted from the cyclone season publications to develop case study cyclones such that impacts can be assessed in the SWIO (see appendix). These include wind gusts; swell heights, floods, injuries, deaths, infrastructure loss, etc.

2.2.0 Methodologies

This section focuses on the various methods that have been employed to understand climate and marine weather variability and predictability at inter-annual and daily time scales respectively. Many are standard methods which have been utilized by other researchers typically like Rakotondrafara (2001). Some methods have been adapted to capture specific causes of daily weather associated with TCs. The study of seasonal variability of TC activity was principally undertaken by creating a standardized intense TC index for the SWIO (eye of cyclone visible on satellite image and wind speed of over 45 m s^{-1}. The seasonal composite analysis technique was extensively used to study the spatial patterns and temporal characteristics associated with high and low TC days. Daily composite analysis was also used to understand the synoptic evolution of the monsoon circulation surrounding TCs moving in westward, southwestward and southward direction. Hovmoller (longitude-time and latitude-time) analysis was used to study the ocean-atmosphere variables with time, while longitude-height and latitude-height plots were useful to study variables in the vertical profile. Correlation analysis was used to establish the relationship and association between ocean-climate variables. Cross-wavelet spectral modulus techniques were used to understand the time evolution of the common spectral energy of the tropical circulation indices associated with intense TC and to establish stability of association among potential predictors of

TC activity. The forward stepwise linear regression technique was the method adopted to create seasonal multivariate statistical models to enable the prediction of intense TC days. Digitization of spatial data from maps was also carried out to enable comparison between QuikSCAT and NCEP winds in case study cyclones. The US Navy wave model in tabular form was used to estimate swell properties while a 2-D numerical storm surge model equation was employed to estimate and compare the storm surge (growth of sea level) forced by QuiKSCAT and NCEP winds.

2.2.1 Standardizing Data And Selection of Extreme Events

Standardizing was done to most time series. When comparing time plots all variables should be represented by similar scale. Otherwise, variables with large values can dominate the display. The creation of the standardized intense TC index involves using the following equation:

$$TC_i = \frac{1}{k}\sum_{i=1}^{k}\frac{X_i - U_i}{\sigma_i} \qquad \textbf{(1)}$$

Where TC_i is the annual standardized departure, x_i is the observed individual seasonal value, U_i is the long term seasonal mean and σ_i is the long term standard deviation over 42 (k) years. The TC index is used to select years (December to March) with high and low TC days according to the following criteria:

High Intense TC season: $\frac{x_i - u}{\sigma} \geq 1$ **(2)**

Low Intense TC season: $\frac{x_i - u}{\sigma} \leq -1$ **(3)**

The years identified with high TC days are 1962-63, 1967-68, 1969-70, 1970-71, 1972-73, 1993-94, 2001-2002 and the years selected with low ITC days are 1966-67, 1973-74, 1980-81, 1982-83, 1984-85 and 1986-87, 1997-98. It is important to note at this stage that there are significant differences in the active and inactive years between this study and the investigation of Rakotondrafara (2001). The difference in active and inactive years is simply due to the different categories of TC considered in the two studies.

2.2.2 Seasonal Composite Analysis

Composite analysis is used to study common features and patterns in selected fields. It is carried out using NCEP seasonal data to study the causes and mechanisms leading to the variability of intense TC days. To simplify and facilitate analyses the difference in composite fields for high minus low intense TC cases were calculated. The composite method has the advantage in creating a richer data field for events with similar characteristics. The main disadvantage of using composite analysis is that it tends to smooth the data field such that the details of individual events can be removed. Rakotondrafara (2001) used similar method of analysis to study the interannual variability of SWIO TCs.

2.2.3 Daily Composite Analysis

The composite structure and evolution of the monsoon circulation associated with intense TC with different trajectories is analyzed using NCEP daily data. Compositing various events with similar characteristics have the advantage of creating a richer data field and helps generalize results (Parker and Jury 1999). Selected groups of westward, southwestward and southward moving TC in the region 45-70° E and 8-20° S are used to construct fixed system composites of intense TC four days before to two days after maximum intensity. The day of maximum intensity T- 0 is defined as the day the cyclone reaches maximum surface wind speed following official declaration (Meteo-France Reunion) of TC strength (eye visible from satellite imagery) while sustaining a wind speed greater than 45 m s^{-1}. Cyclones should also reach peak intensity before 20° latitude. The procedure for compositing intense TC is to average the spatial field of selected cases by grid point per pressure level each day and to divide by the sample size. The composite criteria are similar to Parker and Jury (1999) but the composite technique uses a fixed geographical system unlike the system-following grid adopted by the above researchers. The geographical system is similar to Naeraa and Jury (1997) used to study case study impacts over Madagascar in 1994. The fixed coordinate system is suitable to study the synoptic features of TC provided they are relatively co-located. Composite cyclones are constructed when the eye is not more than 400 km from a central point at maximum intensity (T- 0). The daily positions of the TC were extracted from the Meteo-France Reunion website. Composites for the westward, southwestward and southward moving TC are used to study the structure and evolution of the monsoon circulation surrounding the cyclones. Parameters showing interesting features are presented. The structural evolution of the TC circulation is analyzed for 7 days between T-4 to T+2, and comparisons of kinematic and thermodynamic patterns are made with regard to different trajectories. This study employs case studies for recent TCs to enhance the quality of the analysis and results.

Westward - Moving TC: θ > 247.5 □

Southwestward -Moving TC: 247.5 □□< θ<202.5 □

Southward-Moving TC: θ≤202.5 □

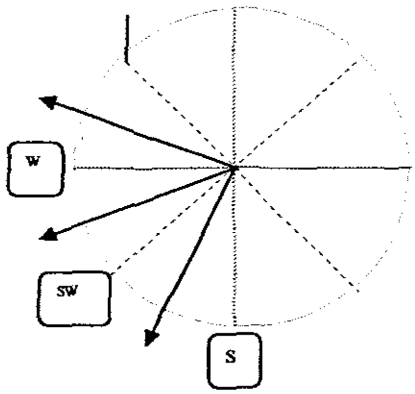

Fig 2.1: Selection criteria for West, Southwest and Southward-Moving TC's

2.2.4 Key Areas

Key ocean-atmosphere signals modulate the climate of a particular region. To understand climate variability and its predictability the key area selected must be large enough to capture the ocean-atmosphere signal. The signal must also be reasonably stable throughout prediction months (MJJ, JAS and SON). Various methods such as principle component analysis (PCA), canonical analysis, composite, correlation and singular spectrum analysis can be used to define key areas. In this study a combination of composite and correlation analysis techniques were adopted to define the key areas.

2.2.5 Correlation Analysis

The relationship or degree of association between variables can be tested using correlation analysis both in time and space. In Chapters 4 and 5, correlation analyses are used to establish the tele-connection between TC variability and ocean-atmosphere parameters and to explore ocean - atmosphere coupling. Since TC days index extends from 1961 to 2002, the number of degree of freedom (df) is 40 and a correlation coefficient is statistically significant at 95 % at a value > 0.23. Significantly correlated fields will provide potential predictors for the development of multivariate linear regression models to predict intense TCs at various lead times. The correlation equation is as follows:

$$R = \frac{S_{xy}}{S_x S_y} \qquad \textbf{(4)}$$

Where $S_x S_y = \frac{\sum\left(X - \bar{X}\right)\left(Y - \bar{Y}\right)}{N-1}$, N is the sample size, $\bar{X}$ and $\bar{Y}$ are the average of the independent and dependent data respectively.

2.2 .6 Hovmoller and Cross Section Analysis

Hovmoller analyses are useful in the investigation of transient or standing ocean-atmospheric phenomena. In this study this technique is principally used to study the formation, propagation and intensification of the ocean Rossby wave in the Indian Ocean using the 125 m vertically integrated heat content anomaly (HCA). Cross- section analysis is useful to view phenomena with an interesting pattern in the vertical atmosphere or ocean depths. It was used to locate the level and latitude / longitude of maximum signal in moisture flux, zonal and meridional wind, and potential temperature. Similarly this technique was used to understand the depth showing strongest temperature signal and its temporal and spatial variability.

2.2.7 Stream Function, Velocity Potential and Vorticity

This section provides mathematical definitions of some of the important derived parameters used in this study to help understand the circulation patterns. These include stream function, velocity potential and vorticity.

2.2.7.1 Stream Function and Velocity Potential

A horizontal wind vector V can be decomposed into a non-divergent part(rotational) and an irrotatinal part (divergent)

Thus according to Helmholts theorem:

$$V = k^* \nabla \psi + \nabla \chi \qquad \textbf{(5)}$$

Where V= [u v]

ψ = horizonatal stream function (non-divergent part),

χ = horizonatl velocity potential (divergent part) and k is unit vector.

Positive values of stream function(rotational component) indicates cyclonic circuation and negative values shows anticyclonic circulation. Negative/positive velocity potential is associated with divergence/convergence.The velocity potential(irrotational component) are impotant in identifying sources and sinks of atmospheric moisture an convection. Large convergence flows may be indicated by tight contour gradients.

2.2.7.2 Vorticity

Vorticity is the rate of spin experinced by a circular vortex of air around vertical axis. In the southern hemisphere, negative/positive charaterizes cyclonic/anti-cyclonic voticity. Anticyclonic vorticity is linked with divergence and cyclonic vorticity is assocaited with low level convergence.The vorticity equation is given by:

$$\zeta = \frac{\partial v}{\partial x} - \frac{\partial u}{\partial y} \qquad \textbf{(6)}$$

Where u= wind component in the zonal direction

V= wind component in the meridinal direction

X= zonal distance (longitude), y =meridionl disatnce (latitudinal)

The relationship between stream function and vorticity is described mathematicaly by these equations below:

$$\zeta = \nabla \psi \qquad \textbf{(7)}$$

2.2.8 Continuous Wavelet Transform (CWT)

Earth science phenomena often display rhythmic variations. Both spectrum and wavelet transform are methods that can be used to detect multi-scale signals and to determine the variability. The wavelet transform is a powerful and superior technique compared to the spectral energy method. Spectral analysis uses Fourier Transform to describe the integrated characteristics of the signal over time (frequency). Wavelet analysis localizes variations of power within a time series in time-frequency mode. The main difference between the two methods is that CWT the individual wavelet functions are localized in space and can be represented graphically in 2-D. One is able to determine dominant modes of variability and how those modes vary in time (Torrence and Compo, 1997). The signal x(t) is mathematically decomposed in terms of wavelets. The scale of the signal is represented by the wavelets created. The wavelet algorithm can resolve cycles at various frequencies (low, high,) such that gross or fine features are detected. A complete description of applications can be obtained in Foufoula-Gergiou and Kumar (1995) while detailed theoretical explanations can be read from Daubenchies (1992). The CWT of a signal x (t) is defined as

$$W_x(b,a) = \frac{1}{a}\int_{-\infty}^{\infty} x(t)\psi^*\left(\frac{t-b}{a}\right)dt \qquad \textbf{(8)}$$

Where a and b are real parameters representing the dilation (scale) and the translation parameter respectively. The 1/a is the normalization chosen rather than $1/\sqrt{a}$ (Delprat et al, 1992) to filter the data in the CWT and * denotes the complex conjugate. In 1993, Morlet developed a continuous complex wavelet that is localized in frequency space. The Morlet wavelet is defined as:

$$\psi(t) = \pi^{\frac{1}{4}}\, e^{\frac{-t^2}{2}}\, e^{iw_0 t} \qquad \textbf{(9)}$$

Where $\iota = \sqrt{-1}$ and ω_0 = 5.4 is large enough such that φ satisfies the condition:

$$\int_{-\alpha}^{\infty} \varphi(t)dt = 0 \qquad \textbf{(10)}$$

For the Morlet wavelet the inverse of the scale to frequency is required. The relation between the scale a and the usual frequency f is given by (Meyers et al, 1993):

$$f= \frac{\omega}{2\pi}\left(\frac{\omega_0}{a}+\frac{\sqrt{2+\omega^2}}{\omega_0}\right) \qquad \textbf{(11)}$$

The Morlet wavelet acts as a band pass filter of weight 1/a centered around $\omega_0=\omega_0/a$ and is complex. The wavelet transform coefficient $W_x(b,a)$ is also complex and can be expressed in terms of real and imaginary parts, modulus and phase. The CWT maps the original signal into a 2-D time–frequency image. Important information such as periodicity of the local signal can be revealed from the ridges of the CWT.

2.2.8.1 Cross-Wavelet Transform (CWT)

The cross-wavelet transform of two series x (t) and y (t) is given by:

$$W_{xy}(b,a) = w_x(b,a)w^*_y(b,a) \qquad \textbf{(12)}$$

Where $w_x(b,a)$ and $w_y(b,a)$ are the CWT of x(t) and y(t) respectively and where * denotes the complex conjugate. The CWT coefficient $W_{xy}(b,a)$ is therefore a complex number.

2.2.8.2 Local Phase Difference

From above, the local phase difference $\Delta\phi(b,a)$ between the two time series for each point of the (b, a) time-frequency space. The local phase difference does not depend on the amplitude of the signal. On this premise an estimate of the instantaneous phase difference ($\Delta\phi(b)$) between the signal x(t) and y(t) can be obtained. The details can be obtained from the following papers (Jury et al 2002). Therefore, the instantaneous time-lag between the two time series x(t), y(t) is as follows :

$$T(b) = \frac{\Delta\phi(b)}{2\pi F(b)} \qquad \textbf{(13)}$$

Where F(b) is the instantaneous frequency defined as the normalized moment. The CWT and the local phase difference technique will be applied mainly to study the interactions and stability between environmental variables in the time and frequency domain as done by (Jury et al., 2002, Yeshanew, 2004). It will be used mainly to investigate the decadal variability of TC, ENSO transmission into the IO, ocean - atmosphere coupling and assessment of the stability of association (e.g. predictors). However, there exists edge effect in this technique on the spectral character of the signal. There is some ambiguity for the first and last 3-4 years of the record and is less reliable when the cross-wavelet amplitude is small.

2.2.9 Multiple Linear Regression Model

In reality, forecasting problems require more than one predictor. Here use is made of the multiple linear regression model. In a multiple regression model, a single predictand, Y, has more than one predictor variable, X.

The model for multiple linear regression is:

$$\mathbf{Y} = \beta_0 + \beta_1 \mathbf{x}_1 + \beta_2 \mathbf{x}_2 + \beta_p \mathbf{x}_p + \varepsilon \qquad \textbf{(14)}$$

Where Y is the dependent variable to be predicted (i.e. TC days), x is the independent variable (i.e. QBO), and the β's are the regression coefficients that adjust to provide "best fit".

2.2.9.1 Model Development

In summary, research was first undertaken through composite and area correlation analysis to reveal which physical parameter offers potential skill for the seasonal prediction of TC based on their historical relationship. Pair-wise correlation analysis at 3, 6 and 9 months lag prior to the cyclone season was used to isolate predictors. A maximum of 13 candidate predictors for each season (MJJ, JAS and SON) was extracted for consideration.

2.2.9.2 Forward Stepwise Regression

In this study linear multivariate models are developed using forward stepwise regression. The forward stepwise method starts with zero parameters in the model and then interactively selects and adds parameters into the model with the aim of obtaining a model with a high degree of fit to the predictant. In the forward stepwise technique the predictors are added to the regression equation progressively starting with the one that explains the highest variance. A maximum of three predictors are permitted in the model to eliminate the dangers of co-linearity. The stepwise method also allows predictors to be removed from the model through manual interaction. For each model fit an evaluation of adjusted R^2, the standard error of the estimate, and an ANOVA table for assessing the fit of the model is performed.

2.2.9.3 Co-Linearity Test of model predictors

Co linearity can be problematic in multivariate regression models. Independent predictor variables should be relatively uncorrelated. So tests are done once a model is developed to see if each predictor makes a unique contribution. A rejection criteria of $r>0.23$ is applied.

2.2.9.4 Validation and Verification of the Model

Validation determines the skill of the forecast. Any forecast verification method involves comparison between matched pairs of forecasts and the observations to which they pertain. Cross-validation is performed by successfully omitting groups of years from the training period. In doing so, the prediction is now based on a model for the remaining years. The withdrawn years play no part of the prediction. The predictor data for the withheld years are then projected onto the model, and predictand values are generated and verified against observed data for the withheld years. In this study the predictive models were tested for reliability by excluding the first and the last 10 years and predicting the outcome based on a model for the remaining years. Similar to work has been done by Hastenrath et al., (1995); Mason, (1998); Jury et al., (1999);

Mwafulirwa and Jury (2002). To explore instabilities in the model equations one model is allowed to 'freely' select predictors from the candidate pool of predictors of the remaining years, while the other method 'freezes' the predictors (Mwafulirwa and Jury 2002) so that the same predictors are found in the model for the test period. The results from both validations are then compared. Model performance is evaluated using normalized data in a tercile category scheme (Barnston, 1992).

Below shows the tercile category developed for TC verification in SWIO:

Below Normal: < - 0.5

Normal : -0.5 to + 0.5

Above Normal: >0.5

2.3.0 Comparison Between NCEP And QuikSCAT Wind Field Across TC center

A number of TC's were selected in the period 1999-2002 to compare NCEP and QuikSCAT wind speed. The wind speeds were digitized from the maps in a north- south and east-west cross-section across the TC center. A composite of similar fields was developed to calculate the difference between NCEP and QuikSCAT winds within 300 km of the TC center using a simple area approximation method.

2.3.1 Area Approximation

The area average wind field is calculated by summing up the area under QuikSCAT and NCEP graph from 100 to 300 km radius for N-S and E-W cross-sections as shown in figure 7.1 (e) of chapter 7. The factor difference between the two is simply calculated as follows:

$$\sum_{i=1}^{n}\frac{a_{QScat_i}}{a_{NCEP_i}}=\frac{a_{QScat_1}+....+a_{QScat_n}}{a_{NCEP_1}+....+a_{NCEP_n}} \qquad \textbf{(15)}$$

2.3.2 Swell Computations

Calculating wave properties near TC is often difficult. The primary difficulty is that the wind speeds increase from the outer limits of the TC to the eye wall. It is also difficult to find an area were the winds are constant in speed and direction. The fetch area for NCEP and QuikSCAT are also spatially different. Nevertheless, best estimates of cyclone generated swell, wave set-up and storm surge heights are crucial for the evaluation of coastal impacts. The practical application of studying swells is to know when the first swells are expected to arrive and what their direction will be. Other critical information include wave period and most importantly the wave height. In this study wave properties generated by QuikSCAT and NCEP winds are compared via a set of criteria: The fetch area represents winds with similar direction facing the landfall station and the wind speed is an area average over the fetch. A combination of duration times and unlimited duration time and fetch length based on US Navy wave model was applied to calculate significant wave height and period for given wind speeds. The fraction of the swell reaching the forecast point compared to seas present at the downwind edge of fetch was computed using decay curves. The speed of the TC was not considered in these calculations.

2.3.3 Basic Swell properties

In swell computation, the group velocities of individual sinusoidal wave components are important to propagate wave energy. The wavelength (L) and group wave speed (C) is given by the following equations:

$$L=\frac{gT^2}{2\pi} \quad \textbf{(16)}$$

$$C=\frac{gT}{2\pi} \quad \textbf{(17)}$$

Where g is the acceleration due to gravity, T is the wave period in seconds. The travel time of the swell from the generation area to a given point in that same direction is given in equation below.

$$t_s = \frac{R_p}{c_g} = \frac{R_p}{1.515T} = 0.660* \frac{R_p}{T} \quad \textbf{(18)}$$

Where t_s is the travel time, T is the wave period; R_p is the distance from the front edge of the fetch to point P (Landfall station).

Wave components with maximum period are the first to arrive at a given point because they travel faster. These components continue to arrive over a period D_p h until they disappear. Meanwhile, slower wave components arrive and also last for a period of D_p h. The slowest wave component starts to arrive as the fastest wave is disappearing. D_p is the duration of wave generation in the direction of P. The swell heights in table 7 of chapter 7 are decayed swells calculated from the TC fetch area for a given distance away from the landfall location.

2.4.0 Storm Surge Computations

When the TC makes landfall a rise of sea level occurs, followed by a rush of sea water inland. This inland-moving water often causes devastating damage to coastal property and also loss of life along the coast. A number of factors operate together to produce storm surge. These include: inverted Barometric effect (sea surface rises at a place as atmospheric pressure is low), open sea waves (wind generated waves), fetch of water (water displaced towards the coast in which the winds are on-shore), slope of the coastal shelf (a shallow shelf causes a rise in sea level near the coast), local coastal topography (shape and structure of coast) and astronomical tides (rise and fall of water level depending on the phase of the moon and sun) .

2.4.1 2-D Storm Surge Analytical Model

A 2-D analytical model of storm surge is employed to estimate the sea level rise for selected cyclones driven by scatterometer (QuikSCAT) and NCEP winds when making landfall over Madagascar and Mozambique. Here the total storm surge is computed by considering the effect of the surge (wave-set-up from on-shore wind), astronomical tidal values and inverse barometric effect. Frictional effects at the surface and at the sea bed are not included and it is assumed that the amplitude of the surge is small compared to the depth H of the sea.

Further, it is assumed that the horizontal scale of the surge is large compared to H, such that hydrostatic assumptions are valid. The depth of the sea is assumed constant from the coast. The storm surge is calculated by solving the three equations of motion (19), (20) and (21). It is noted that the stationary solution of the equations is in interest. Therefore, the storm surge (sea level growth) due to the wind is given in equation (22). The horizontal wind stress (τ_x) of the wind is given by equation (23) and directed perpendicular to the water mass movement (M_x).

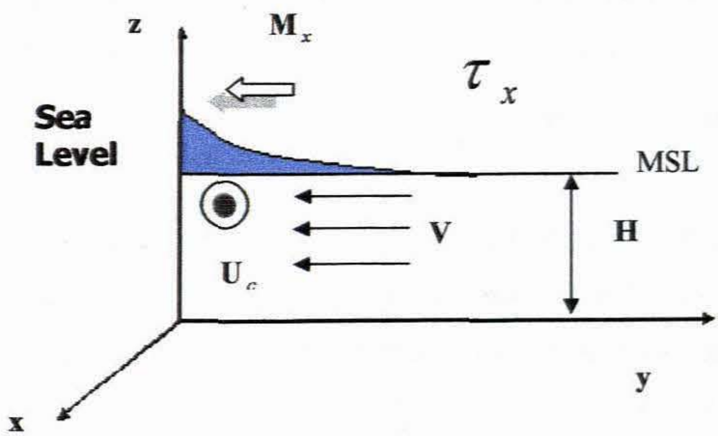

Fig 2.2: Diagram of 2-D storm surge model

$$\frac{\partial u}{\partial t} - fv = \frac{A\partial^2 u}{\rho\partial^2 z} \quad \textbf{(19)}$$

$$\frac{\partial v}{\partial t} + fu = -g\eta_y \quad \textbf{(20)}$$

$$\frac{\partial u}{\partial x} + \frac{\partial v}{\partial y} + \frac{\partial w}{\partial z} = 0 \quad \textbf{(21)}$$

$$\frac{\partial \eta_s}{\partial t}\bigg|_{y=0} = \frac{\tau_x}{\rho f R_d} = \frac{\tau_x}{\rho\sqrt{gH}} = \frac{\rho_a C_d U^2}{\rho_w \sqrt{gH}} \qquad \textbf{(22)}$$

and

$$\tau_x = \rho_a C_d U^2 \qquad \textbf{(23)}$$

Where $C_D \approx 1.4 \times 10^{-3}$ (drag coefficient, τ_x is the horizontal wind stress, f is the coriolis effect, R_d is the Rossby radius, ρ_a is the density of air, ρ_w is the density of sea water, U is the average wind in the fetch area in m s^{-1} , H is the depth of the sea in meters, t is the time variable, y is the horizontal distance of the TC from landfall, and η_s is the sea level.

The sea level growth estimation was done from 0 hours to +3 hours only. The 3 hours represents the time taken for the sea level to grow before TC landfall. The 3 hours cut-off is chosen because frictional effects at the surface and at the sea bed are ignored and horizontal scale of surge is large compared to the ocean depth.

2.4.2 Wave Set Up

The cyclone tide caused by the shoreward water mass transport and the effect of breaking waves yields a wave setup. The wave set up is dependent on the height H and period T of the breaking waves (Simpson and Riehl, 1981). This equation was also employed by Naerra and Jury (1997) to estimate storm surge in Madagascar. The wave set up is added as a component of the total storm surge.

$$S = 0.19\,H\,[(1 - 2.82(H / g\,T^2)^{\frac{1}{2}}] \qquad \textbf{(24)}$$

2.4.3 Astronomical Tide

The astronomical tide (η_t) was computed by considering the typical tides at TC landfall position. The average astronomical tide is then presented as error bars to indicate the potential total storm surge height ($\overline{\eta_t}$).

2.4.4 Inverse Barometric effect

In estimating the storm surge, a further condition is applied to include meteorological effects of atmospheric pressure. At deep water boundaries the inverse barometric effect (Bowden, 1983) is used. This correction is obtained by assuming static conditions. The inverse barometric effect is given by the following equation:

$$n_i = -\frac{(P_c - P_0)}{\rho g} \quad \textbf{(25)}$$

Where P_0 is the mean sea level atmospheric pressure (MSL) calculated east of Madagascar (12-25°S, 47-55° E) eg. 1010.8 hPa and 1013.5 hPa in February and April respectively and P_c is the central atmospheric pressure of the TC.

2.4.5 Total Storm Surge

The total storm surge (η_T) is therefore the combination of the inverse barometric effect, astronomical tides and surge effects.

$$\eta_T = \eta_i + \eta_s^* \pm \overline{\eta_t} \quad \textbf{(26)}$$

Where η_s^* also includes the wave setup. It should be noted that effects of TC movement were not considered here.

2.5 Oceanic Upwelling (ω_E)

The thermocline sea-saw is forced by wind stress and is much related to the transient Rossby wave. The following equations explain the relation between wind stress, divergence and upwelling.

$$\textbf{Div} = \nabla \bullet M = \frac{\partial m_x}{\partial x} + \frac{\partial m_y}{\partial y} \tag{27}$$

$$\approx \frac{1}{\rho} \left[\frac{\partial}{\partial x}\left(\frac{\tau_y}{f}\right) - \frac{\partial}{\partial y}\left(\frac{\tau_x}{f}\right) \right]$$

$$\approx \frac{1}{\rho f} \left[\frac{\partial \tau_y}{\partial x} - \frac{\partial \tau_x}{\partial y} \right]$$

Where m_x and m_y are the water mass transport in the x and y direction respectively

$$\omega_E \approx \frac{1}{\rho f} \text{ Curl } \vec{\tau} \tag{28}$$

Where ω_E is the vertical speed (upwelling)

f is the coriolis force

$\vec{\tau}$ is the wind stress curl.

The link between thermocline oscillations, TC days and fish catch is examined in this study. Decrease TC days may be associated with a shallower wind mixed layer, raised thermocline and increase nutrients in the euphotic zone (light layer), thus better fish catch.

2.6 Summary

In this chapter data type, sources and general methods of data analysis have been covered. A range of data sets ranging from monthly to daily are used to study the variability of intense TC, cyclonic marine weather and impacts in the south west Indian Ocean. The main methods of analyses are composite, correlation, hovmoller, continuous wavelet transform (CWT), forward stepwise multivariate statistical analyses, digitization, and the use of empirical tables and model equations.

The next chapter examines the dominant spatial ocean-climate signals of high and low TC days through the composite analysis method.

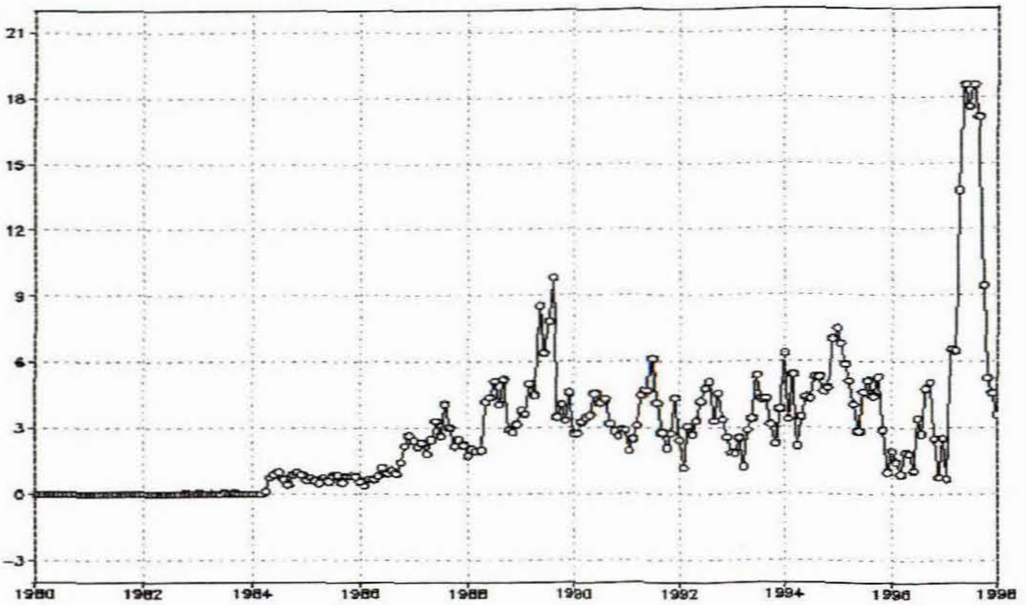

Fig 2.3: Time series of satellite wind observation density (per 2.5X2.5 grid box) in the SWIO (10-20°S, 50-70°E)

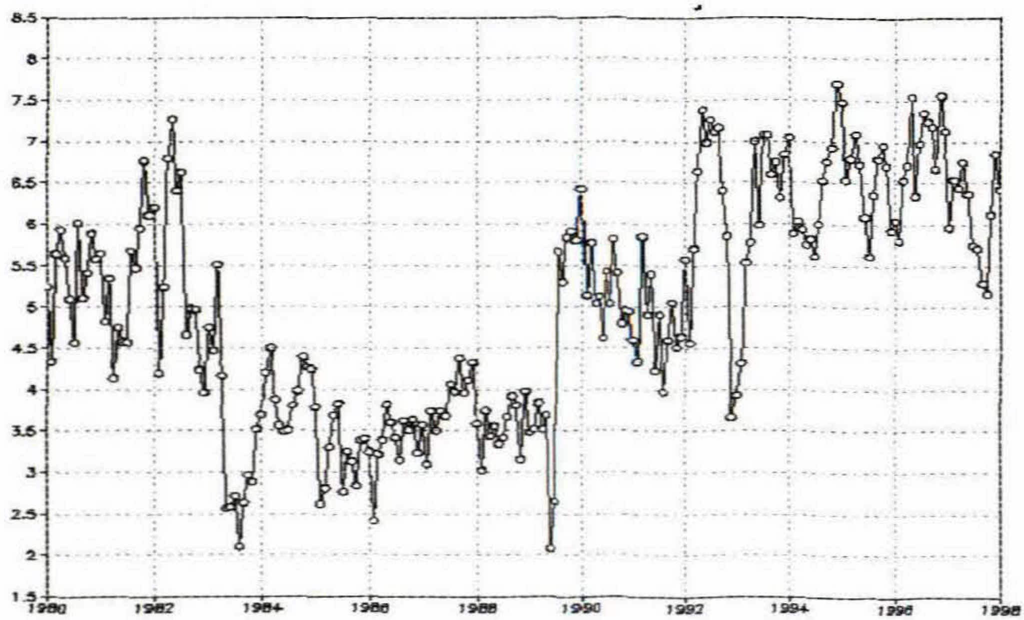

Fig 2.4: Time series of Radiosonde observation density (per 2.5X2.5 grid box) in the SWIO (10-20°S, 50-70°E)

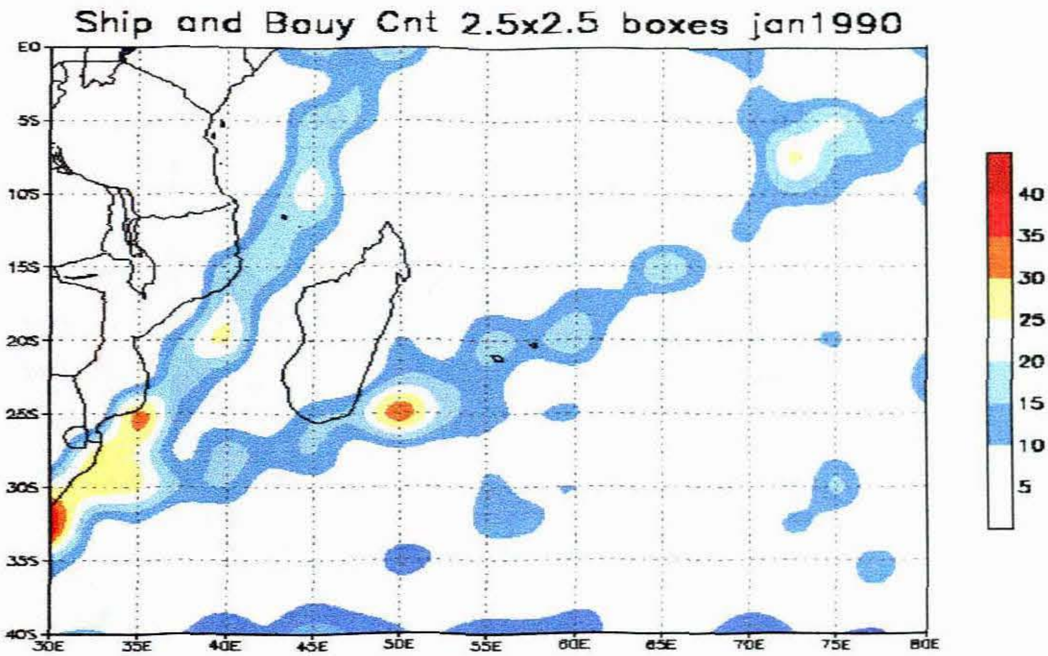

Fig 2.5: Ship and buoy count per grid box in the southern Indian Ocean

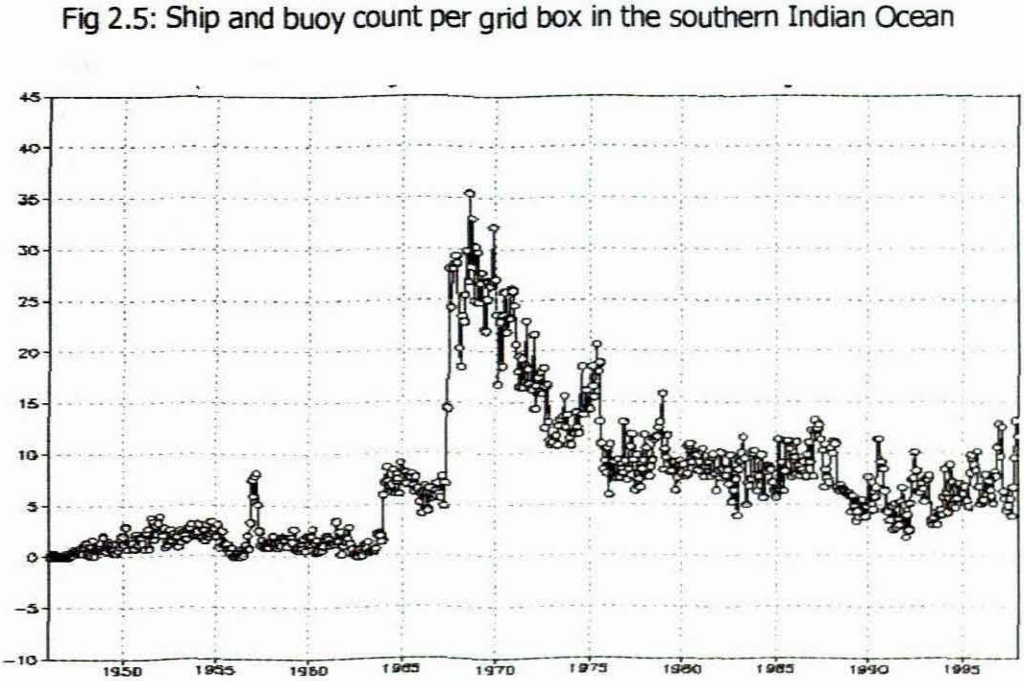

Fig 2.6: Time series of ship and buoy count per grid box in the SWIO (10-20°S, 50-70°E)

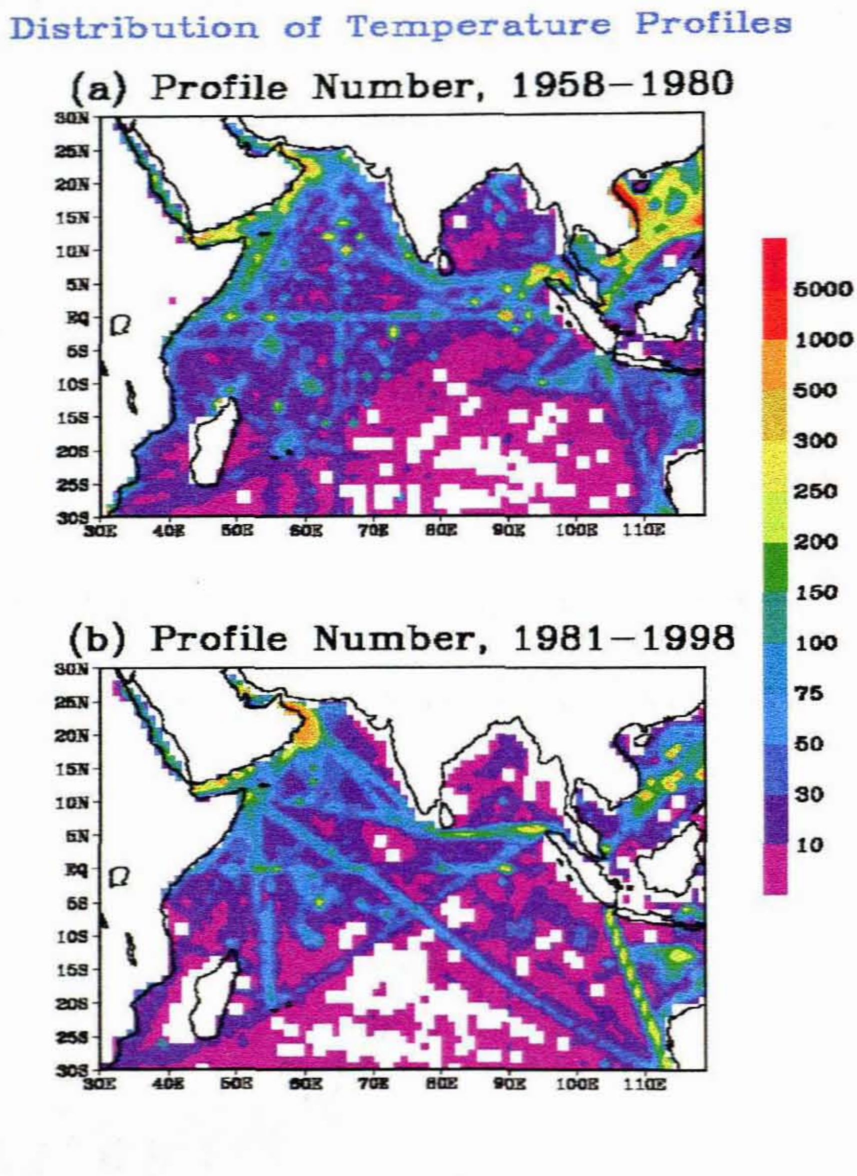

Fig 2.7: The spatial distribution of profile measurements on 1° lat X 1° long grid within 30° S-30°N, 30°E-120°E during (a) 1958-1980 and (b) 1981-1998
(Source: Jury et al)

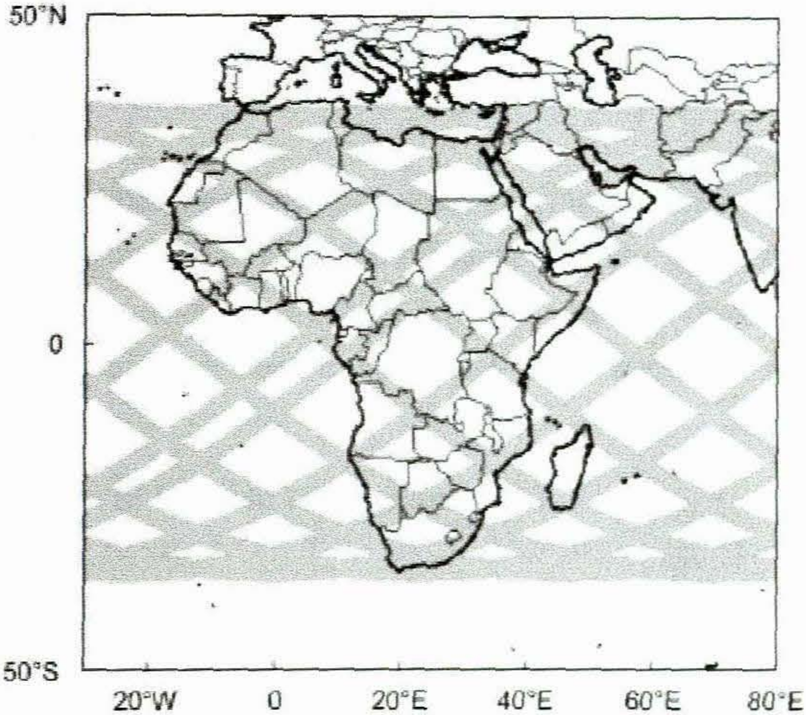

Fig 2.8: Characteristic orbits for one 24-h period of the Tropical Rainfall Measuring Mission (TRMM) satellite. The width of the lines indicates the extent of the footprint (Source: Rouault)

Chapter 3

Ocean- Atmospheric Circulation For Intense TC Days

3.0 Introduction

The ocean and atmosphere fields associated with the variability in the intense TC days are investigated in this chapter. An intense TC index is created as discussed earlier. Maps are generated for high and low years to reveal the dominant signals. The key target variables and areas are determined.

3.1 Time Series of Intense TC Days In SWIO

The dependent variable used to define seasonal TC activity is the total number of days in the season in which disturbances had radial wind >45 m s^{-1} and an eye visible on satellite imagery. The standardized intense TC days index for the SWIO is shown in figure 3.1. The time series consists of 41 years of data from the TC season of 1960 -1961 to 2001 - 2002. The average standardized TC days for the decade 1960-69,1970-79,1980-1989 and 1990-99 are 0.3, 0, -0.7 and 0.1 respectively. This shows that the decade 1960-69 was the most active while 1980-89 was the least active in terms of intense tropical cyclone days.

3.2 High And Low Intense TC Years

High TC years occur in the 1960's to early 1970's and in the early 1990's and 2001. In contrast, low years are observed in the mid 1970's up to the early

1990's. The years identified with high TC days (standard deviation >1) are 1962-63, 1967-68, 1969-70, 1970-71, 1972-73, 1993-94, 2001-2002 and the years selected with low TC days (standard deviation < -1) are 1997-98, 1966-67, 1973-74, 1980-81, 1982-83, 1984-85 and 1986-87.

3.3.0 Seasonal Composite of Ocean-Atmosphere Anomaly Fields

The composite fields of the Atmospheric-Ocean surface variables such as vector winds, geopotential height, sea level pressure, velocity potential, stream function, specific humidity, OLR, potential temperature and SST are mapped using the NCEP–Climate Diagnostic Centre (CDC) data for the JJA, SON and DJFM season. For presentation simplicity and whenever appropriate, composite maps for June to November season are presented. Variables showing interesting features with height are analyzed through pressure cross-section analysis with respect to longitude or latitude.

3.3.1 Vector Wind

Composite wind fields are analyzed to find the kinematics responsible for the extreme mode of variability in TC days in the SWIO. The levels 700 and 200 hPa are considered. A westerly wind anomaly extends across the tropical Atlantic at 700 hPa in JJA (fig 3.2 a) and SON (fig 3.3 a) season. The westerly wind anomaly at 700 hPa weakens in the DJFM season (fig 3.4 a). On the other hand, there is a significant increase in northwesterly flow north west of Madagascar. The in-season pattern in vector wind agrees well with earlier results of Rakotondrafara (2001). At 200 hPa there are anomalous easterlies over the Atlantic Ocean in the months JJA (fig 3.2 b) and SON (fig 3.3 b). The easterlies die out significantly in DJFM season (fig 3.4 b). A burst of easterlies is seen in the Indian Ocean in SON only. The Atlantic zonal overturning is further examined through cross section analysis from June to November season. Figure 3.5 (a) confirms the zonal overturning with westerly winds peaking from 50° W - 60° E while easterly winds peak in the layer 100-300 hPa. The height-latitude cross section of zonal wind (fig 3.5 b) when averaged from 80° W to 100° E shows maximum upper level easterlies along the equator.

Another important climate feature observed on the 200 hPa wind field is a southern hemisphere subtropical jet stream and an eastward propagating trough from the South Atlantic Ocean to southeast Africa during the season. The jet stream pattern has important links to the variability of TC days in the SWIO as will be studied later.

3.3.2 Velocity Potential

The kinematic feature that represents convective outflows and vertical motion is velocity potential, the divergent (irotational) component of the wind. Strong convection is associated with areas of negative velocity potential at upper levels. Two opposing centers of action are identified, over South America and a relatively weaker signal over the east Indian Ocean (fig 3.6 a). The pattern weakens during the SON season (not shown). In the cyclone season the negative velocity potential intensifies and displaces further north of Australia causing steep gradient at 80 E (fig 3.6 b).

3.3.3 Potential Temperature

To assess the thermodynamic role of the atmosphere, the potential temperature field is analyzed at 500 hPa. Anomalous positive temperature is detected in the Indian Ocean centered over Mauritius before the season. The potential temperature is below normal in the south eastern Atlantic Ocean (fig 3.7 a). During the cyclone season, the potential temperature signal in the SWIO weakens slightly but is much enhanced over West Africa. Simultaneously there is significant decrease in potential temperature along the eastern equatorial Indian Ocean (fig 3.7 b).

3.3.4 Geopotential Height

Geopotential height (GPH) indicates atmospheric structure in zones of thermal gradients. The long waves in the GPH field constitute the most energetic and longest time-scale phenomena in the atmosphere. Rossby waves cause deviations of the circumpolar jet. Synoptic-scale cyclones and anticyclones with length scales of the order of 1000-3000 km and time scales 5-10 days are embedded within these large Rossby wave loops. In the high minus low TC composite map (fig 3.8 a) center of deep low GPH signal is observed in the southeast Pacific Ocean and another slightly weaker low GPH center in the southern tip of South Africa. In between are positive anomalies which together constitute a "wave train" of circumpolar number three. In the cyclone season (fig 3.8 b) the GPH wave three patterns is less coherent. The deep low GPH displaces from the south east Pacific into the South Atlantic Ocean. The positive GPH center in the Atlantic Ocean propagates to the southern tip of Africa, while a negative anomaly resides in the SWIO in the peak cyclone season. The GPH has an approximate wavelength of 10,000 kilometers in the period from June to November. Propagation of the GPH signal from the Pacific to the Indian Ocean is an important climate signal related to intense TC and wind shear. Therefore, further work will be carried in the coming chapters to establish associations and links.

3.3.5 Outgoing Long Wave Radiation (OLR) and Specific Humidity

OLR is the outgoing long wave radiation measured by satellite, and is a key element in identifying regions of convection. Negative OLR indicates convection regions while positive OLR are warm and cloud free regions. For the TC composite, a strong and stable positive signal is observed over the Amazon suggesting suppressing convection and clouds there. In contrast, negative OLR is found over equatorial Africa and the Indian Ocean region in the June - November season (fig 3.9 a) associated with the near equatorial trough (NET). Interestingly OLR is negative over the Sahel in JAS season (not shown). Hence increased rainfall there leads to more TC days in the SWIO, just as for Atlantic hurricanes. The OLR signal over the Amazon becomes stronger in SON season while in the Indian Ocean the OLR weakens (not shown). During the cyclone season both the Amazon and Indian Ocean signal weakens (fig 3.9 b). A negative anomaly in OLR develops between latitude 5-12°S in the Indian Ocean associated with a strengthened intertropical convergence zone (ITCZ). The OLR is also another important climate signal to be investigated in the following chapters.

Similar pattern is reflected in the specific humidity fields in the 600 hPa (fig 3.10 a). The maximum moisture around 30°S, 70°E during the season (fig 3.10 b) suggests the area where the TCs dissipate and transfer energy polewards.

3.4.0 Seasonal Composite of Ocean Anomaly Fields

The composite fields of ocean-subsurface variables were mapped using the University of Maryland reanalysis data. Variables such as heat content anomaly (HCA), sub-surface temperature and, thermocline composites were explored for both the Atlantic and Indian Ocean. The Indian Ocean basin reveals a strong signal. Cross-section analyses with longitude were performed on the sub-surface temperature, while hovmoller or time-longitude analysis was carried out on the heat content anomaly.

3.4.1 Sea Surface Temperature

A notable signal in SST is a persistent cooling (up to peak of -1.6° C) in the east Pacific Ocean. The signal is stronger in DJFM season (fig 3.11 c). This resembles a La Nina mode (Meyers et al., 1986). In the Indian Ocean significant warming in SST's is observed between 5-25°S and 70 to 100° E (Fig 3.11 a, b). The evolution of the warm pool (peak +0.5°C) from the South East Indian Ocean to the central IO resembles a propagating 'Rossby' wave. Similar pattern in SST were obtained by Rakotondrafara (2001).

3.4.2 Heat Content

The Indian Ocean HCA is characterized by the west being below normal and the east being above (fig 3.12). The center of positive HCA is shown to displace westward from a mean center of 80°E to 72°E from JJA to DJFM season. This characterizes the slow westward propagation of the Rossby wave in the Indian Ocean.

3.4.3 Time Longitude (Hovmoller) of 125 m vertically Integrated HCA

An investigation is carried out to study the Rossby wave propagation using Hovmoller analysis of vertically integrated HCA. Figure 3.13 (a), 3.13 (b) and 3.13 (c) are time-longitude section for high, low and high minus low TC days respectively.

For High TC days (fig 3.13 a) the dominant structure is composed of the Rossby wave propagating from 85° E to near 70° E from JJA to SON. The Rossby wave amplifies in magnitude in the central Indian Ocean basin. Below normal HCA is seen to gradually develop west of 65° E during the cyclone season DJFM. Overall the composite for high TC clearly shows the East–West gradient in HCA.

In the Low TC days the east is characterized with negative while to the west there is positive HCA especially in June-August months. The pattern weakens towards January. This pattern is opposite to the high intense TC days HCA structure and pattern.

The remarkable feature in the difference field (high- low) is the dipole like pattern in the early season. In the longitudes 50 - 60° E there is negative HCA and between 75-85° E it is positive HCA. This suggests ocean indices such as SST and HCA may help in TC prediction from the early season.

3.4.4 Subsurface Temperature

The maximum negative subsurface temperature amplitude is centered at 40-140m deep and between 50-60°E while the positive center is having similar depths to the east at 75-85° E in JJA (fig 3.14 a). In SON (fig 3.14 b), it is observed that the warming spreads deeper. This intuitively suggests that the Rossby wave penetrates deeper as it propagates westward. Though, the structural pattern modifies and slightly weakens, the dipole structure is maintained. In the cyclone season (fig 3.14 c) the sub-surface centers have tighter temperature gradient and are seen to maintain their maximum amplitudes above 100 meters depth. The zero contour line separating the warm and cool centers shifts between 70°E to 60°E from July to January. The composite subsurface temperature structure with respect to TC days resembles an east- west mode recently found by Yeshanew (2004).

3.4.5 Low Level Wind field And HCA In The Indian Ocean

The wind field at 1000 hPa shows an interesting cyclonic circulation positioned at 15-30° S, 80-90° E in SON (fig 3.15 a) with strong easterlies to the south. The cyclonic circulation displaces to the west IO without suffering much change to 55-65° E in DJF (fig 3.15 b). This circulation helps drive the propagation and downwelling of the Rossby wave indicated by the shaded contours. At this time the easterly wind anomaly to the south is observed to decrease but simultaneously there is a marked increase in northwesterly wind anomaly to the immediate north of Madagascar. The increased north westerly anomaly is of paramount importance to the development and intensification of intense TC in the region indicated by a dashed box.

3.5.0 Key Target Areas

Key target areas are identified from the ocean and atmosphere composites fields on the basis that the parameters have a strong stable *and spatially widespread* signal three to six months prior to the peak cyclone season (Table 3.1).

3.6.0 Summary

The average standardised TC days shows that the decade 1960-69 was the most active while the decade 1980-89 was the least active. The ocean and atmospheric fields associated with the variability of intense TC in the SWIO has been analyzed via the composite method using high minus low cases. The difference field reveals potential climate signals. Table 3(b) summarizes the identified strong signals and their location. There is a strong easterly wind anomaly at upper levels over the Atlantic Ocean while opposing westerly flow occurs at low levels. The composite analyses reveal a centre of action over the Amazon in velocity potential, and OLR. The South America signal is stronger than the Indian Ocean signal. Another important finding is the south east Pacific geopotential height which shows a global wave three pattern particularly in SON. In the following chapters the dipole between South America and Indian Ocean and the south east Pacific geopotential height wave three patterns will be investigated further.

Oceanic parameters such as HCA and subsurface temperature reveal the important role of the coupled Rossby wave propagating from the eastern to central Indian Ocean. In phase with the Rossby wave is a westward-moving cyclonic circulation comprised of increasing easterly trade winds in the subtropics and north westerly winds near Madagascar.

The next chapter considers statistical relationships, tele-connection and stability of association between TC days and ocean-atmosphere variables uncovered here.

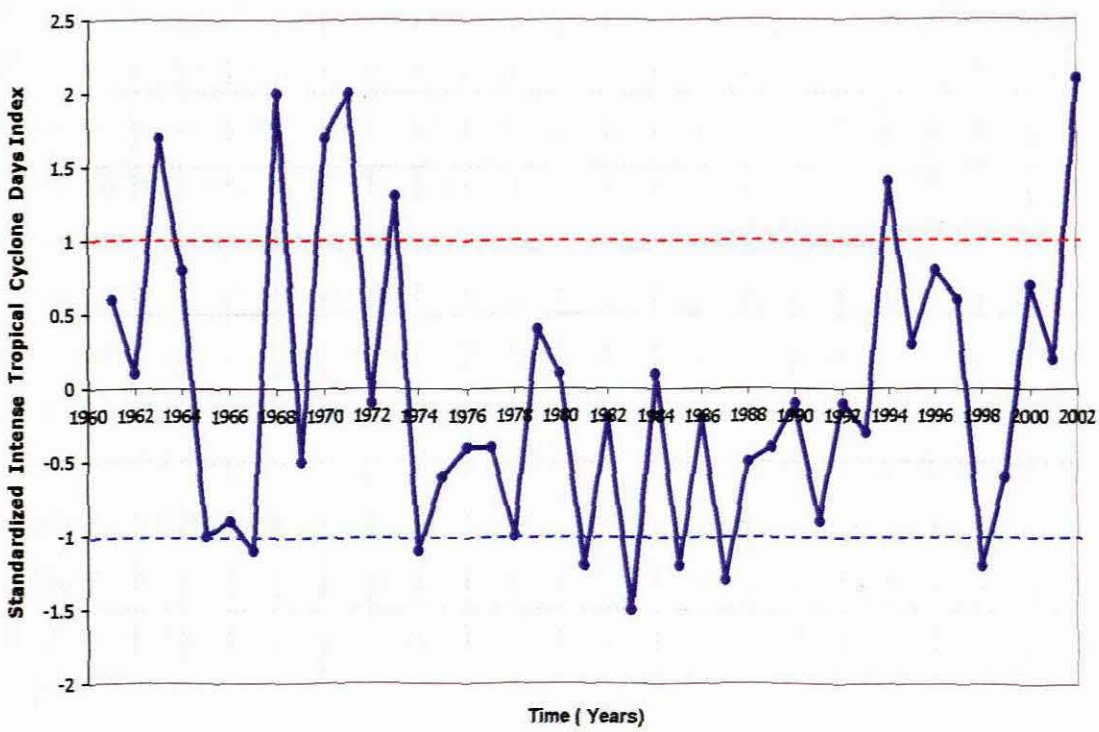

Fig 3.1: Standardized time series index of intense TC days in SWIO

Fig a

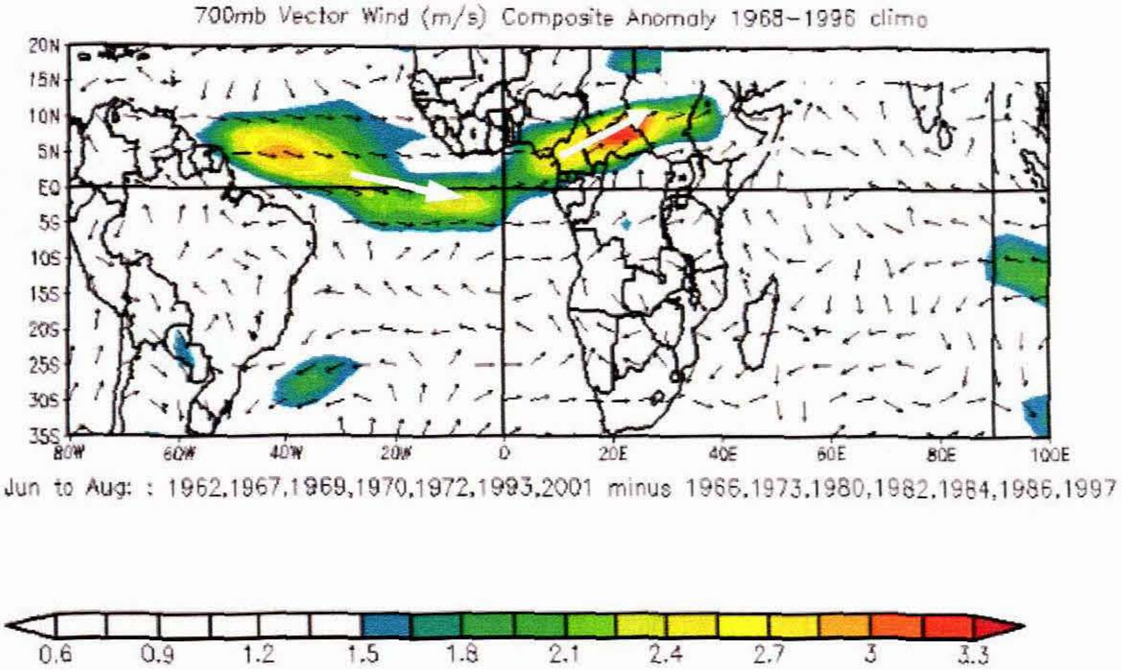

Fig b

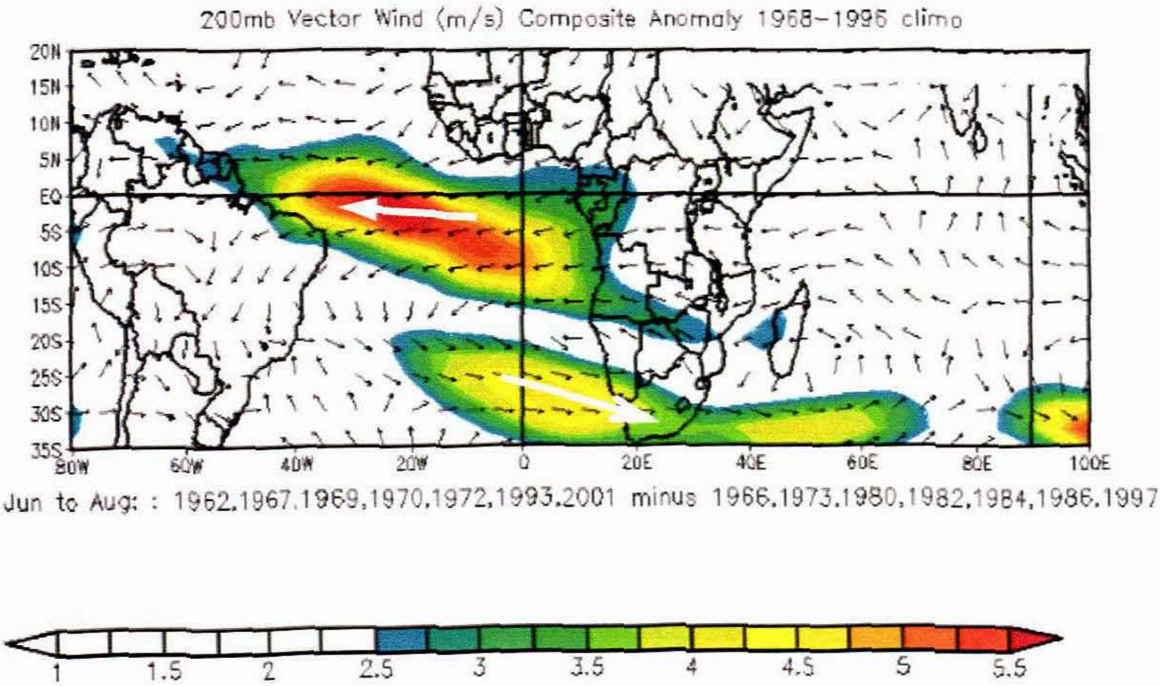

Fig 3.2: High - Low vector wind at 700 hPa (a) and 200 hPa (b) from June to August

Fig a

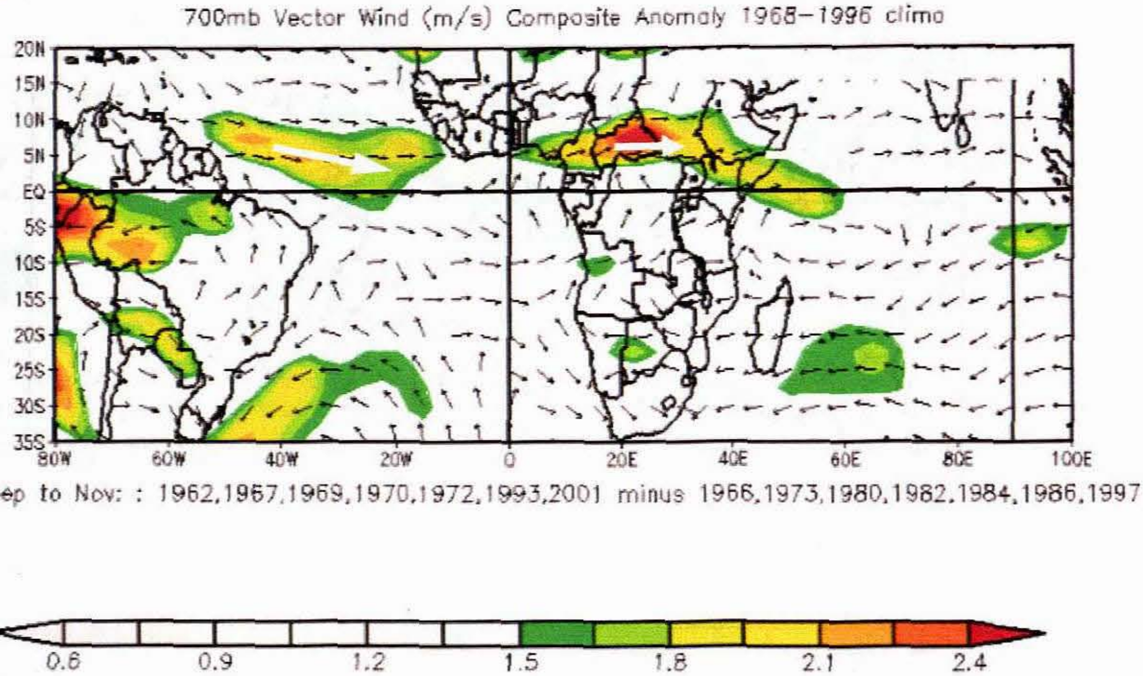

Fig b

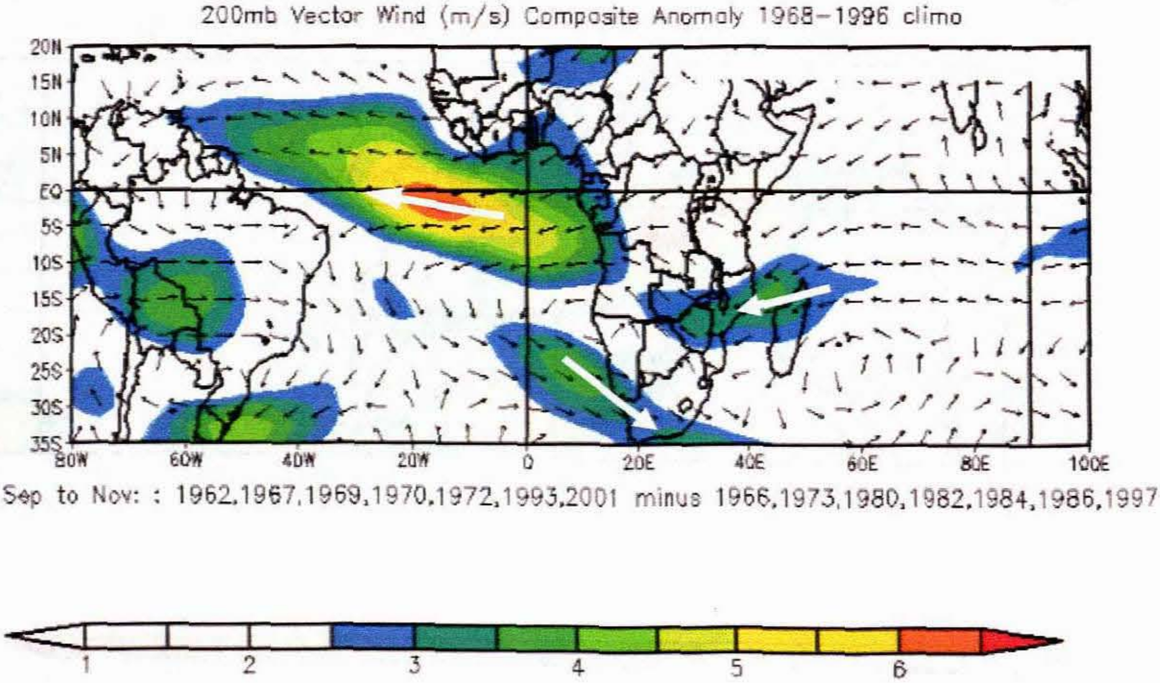

Fig 3.3: High - Low Vector wind at (a) 700 hPa and (b) 200 hPa from Sep to Nov

Fig a

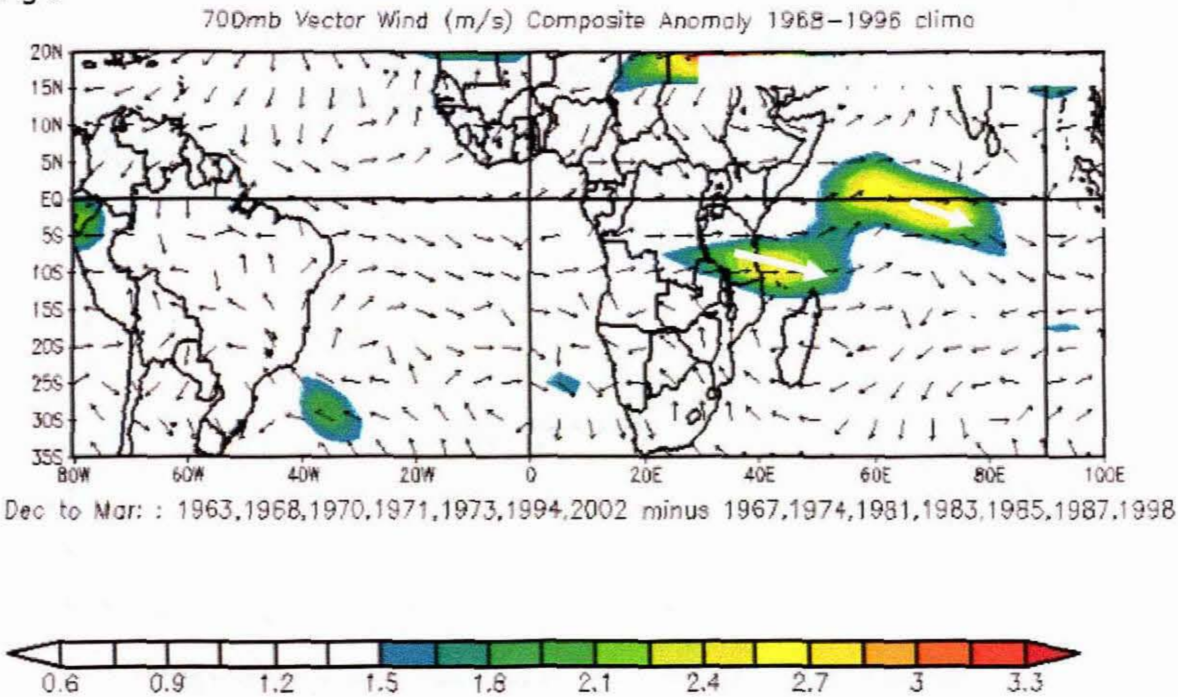

Fig b

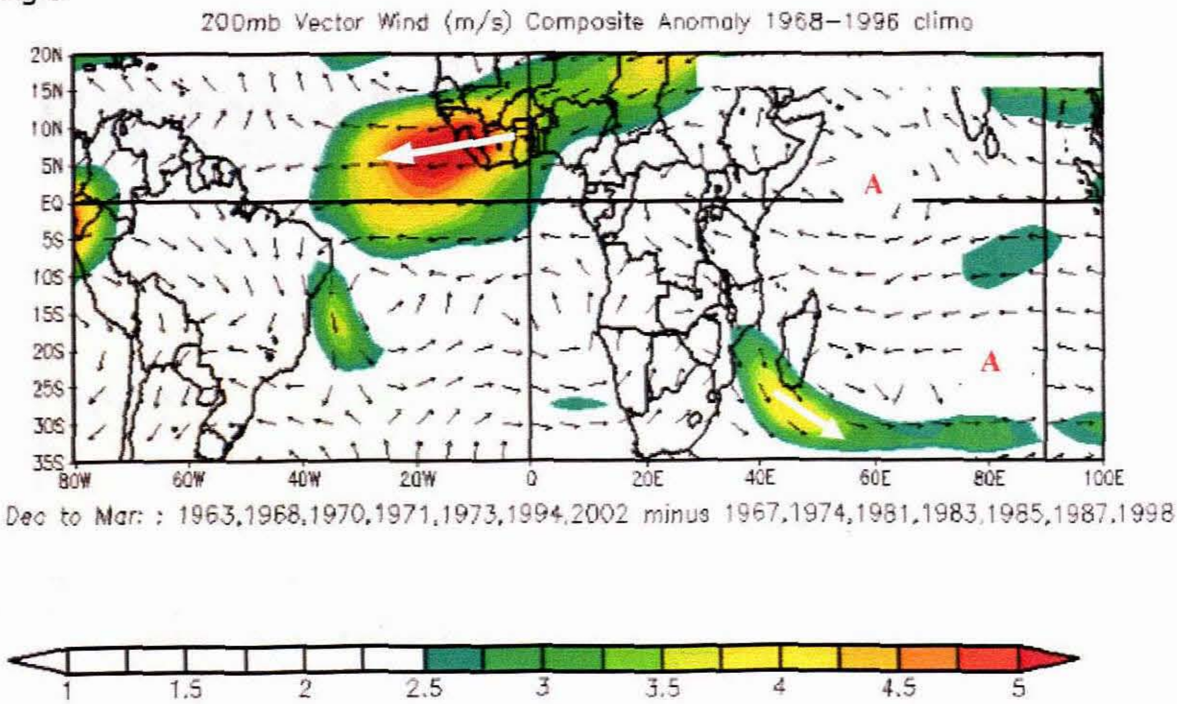

Fig 3.4: High - Low vector wind at 700 hPa (a) and 200 hPa (b) from Dec – Mar

Fig a

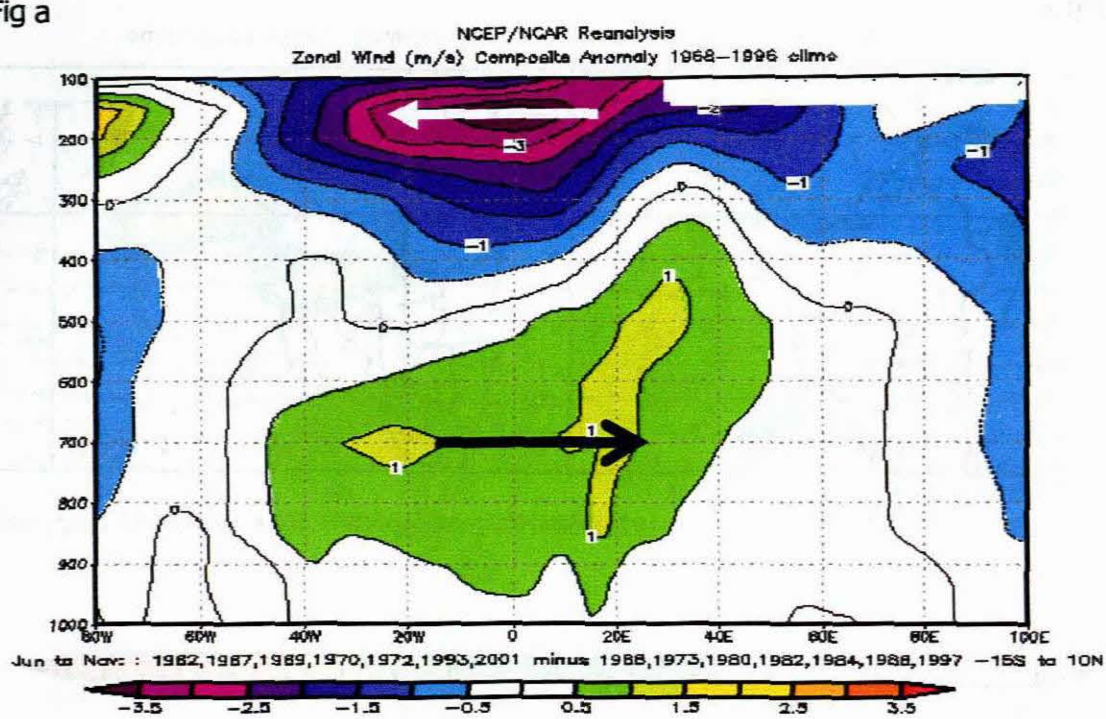

Fig b

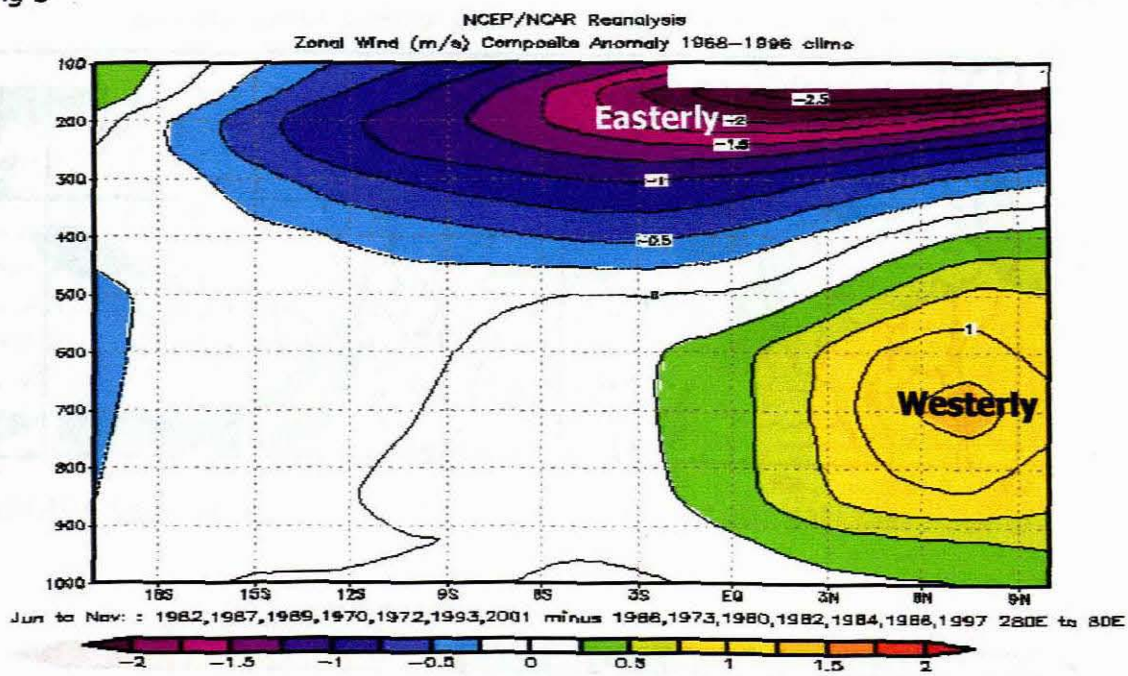

Fig 3.5: Pressure-Longitude (a), pressure-latitude cross-section (b) of zonal wind from Jun-Nov

Fig a

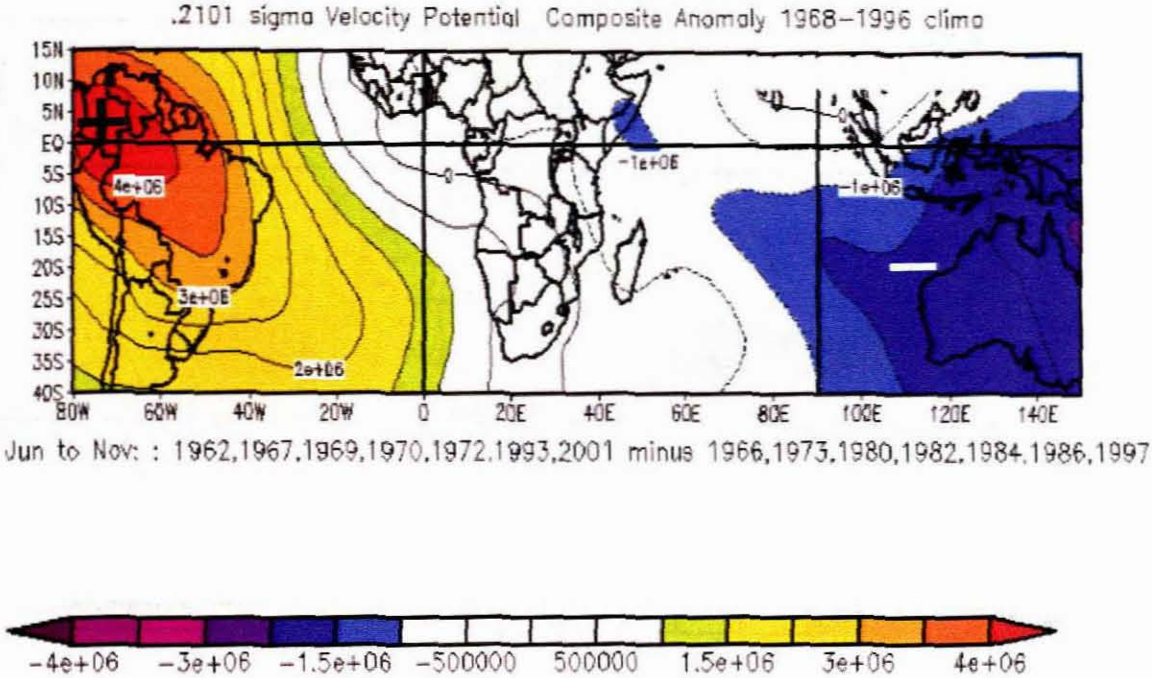

Fig b

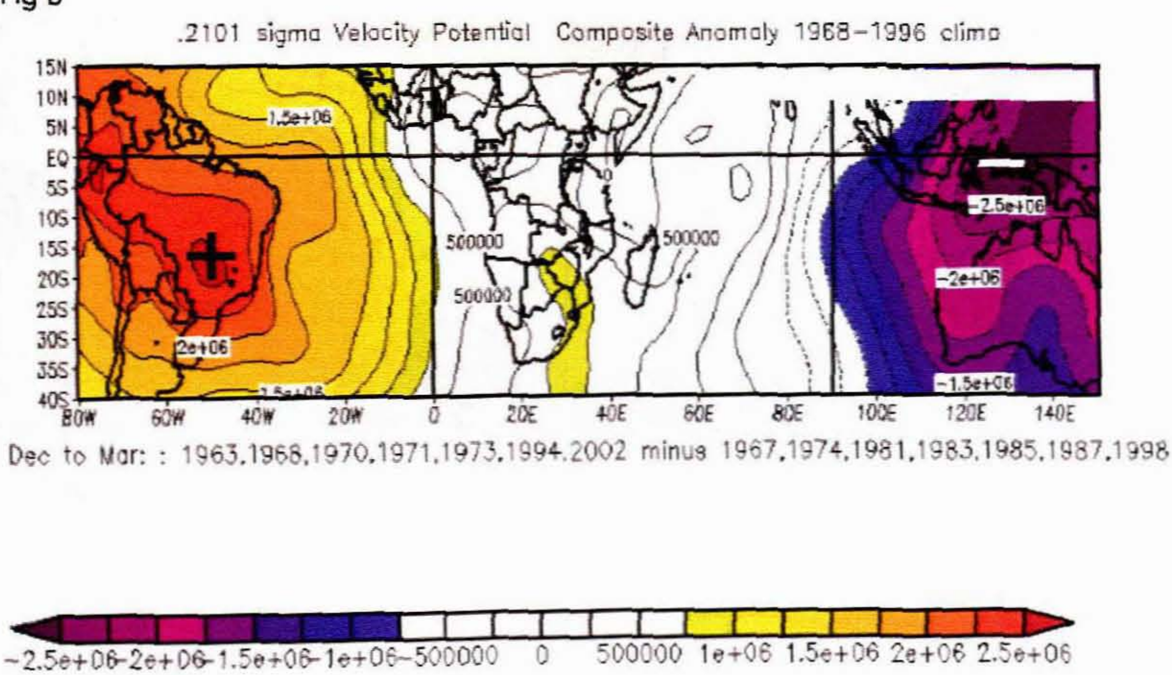

Fig 3.6: High-Low 0.2101 sigma velocity potential for (a) Jun- Nov and (b) Dec-Mar

Fig a

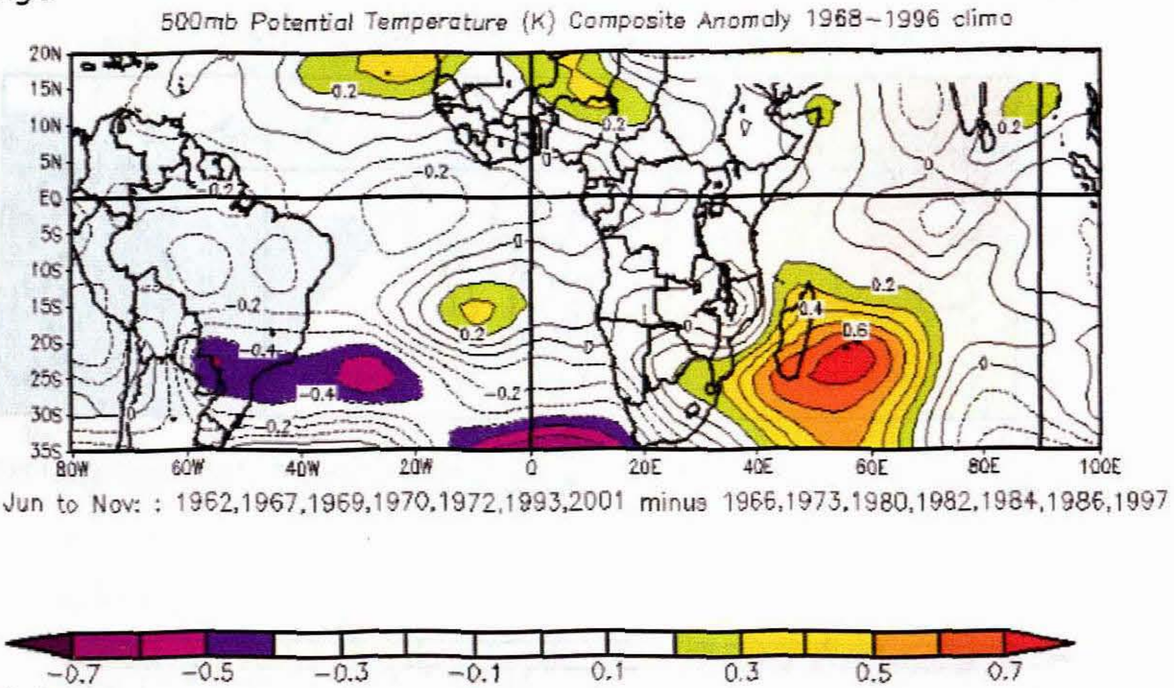

Fig b

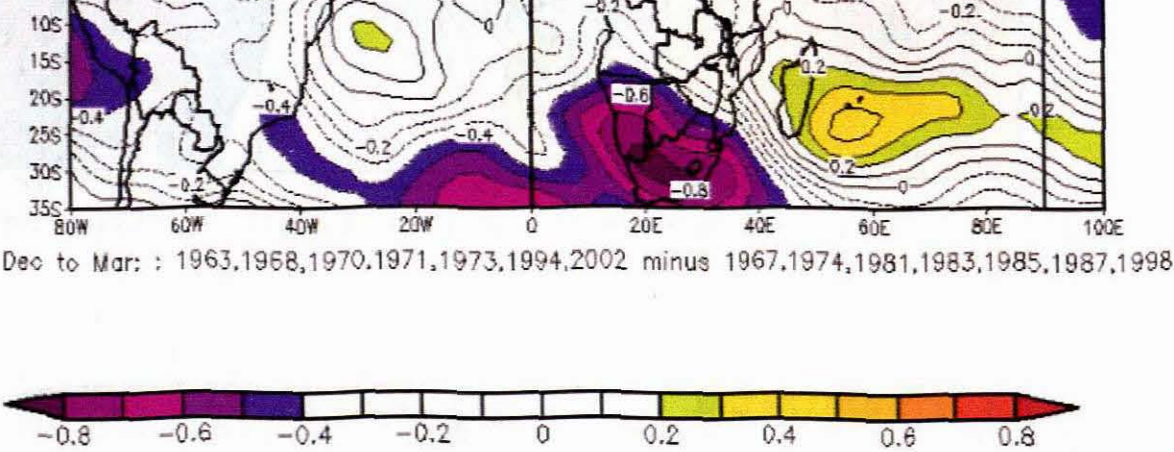

Fig 3.7: High-Low potential temperature for (a) Jun-Nov (b) Dec-Mar

Fig a

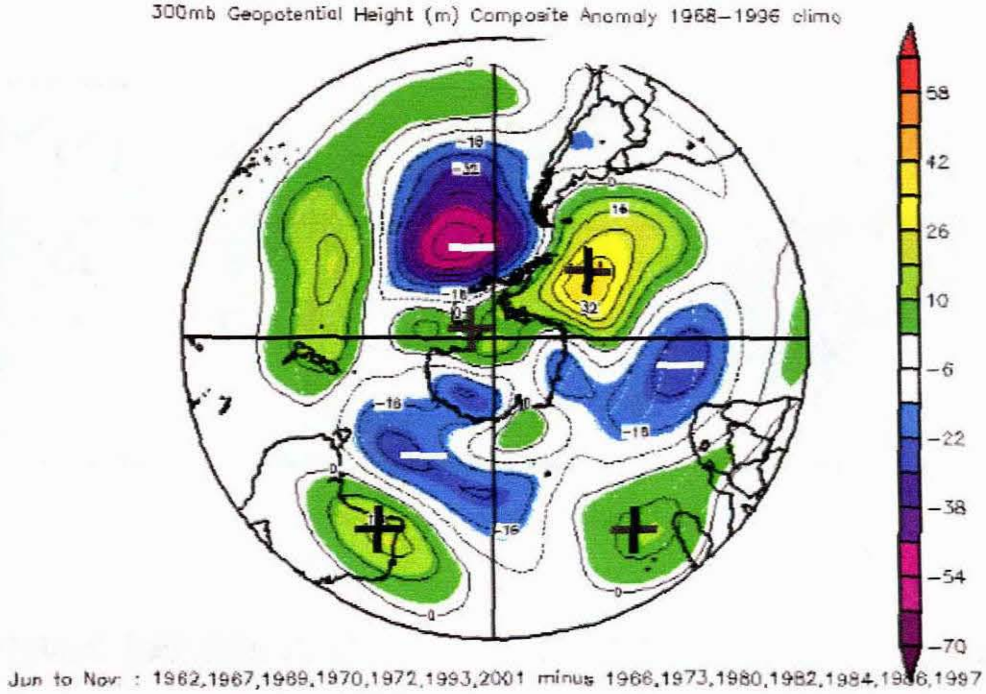

Fig b

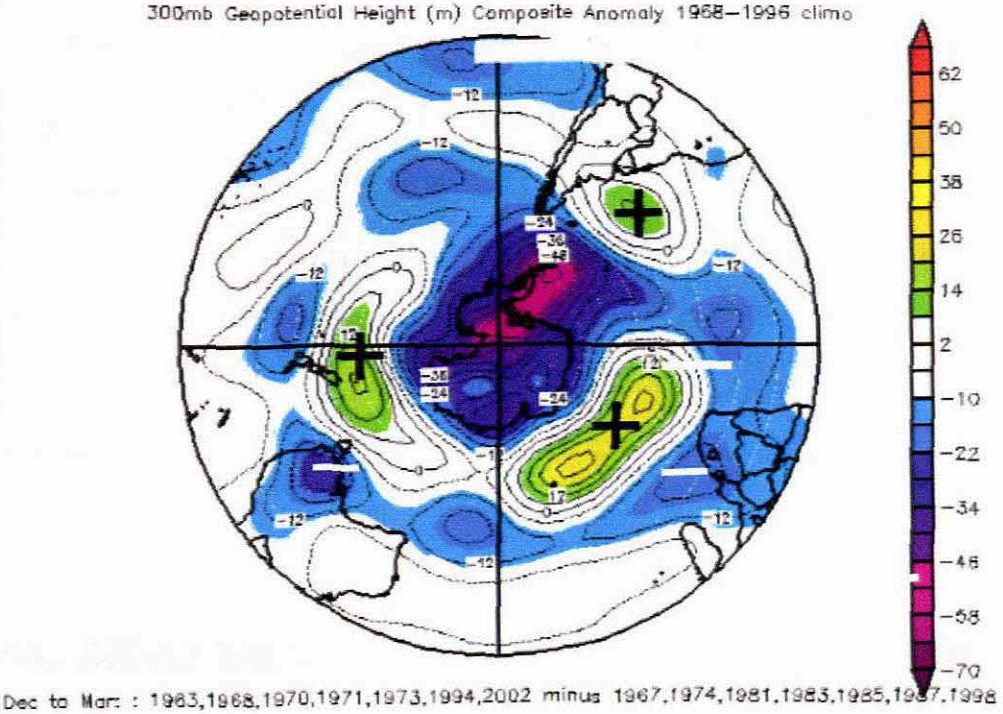

Fig 3.8:High-Low geopotential height anomaly at 300 hPa for (a) Jun-Nov (b) Dec-Mar

Fig a

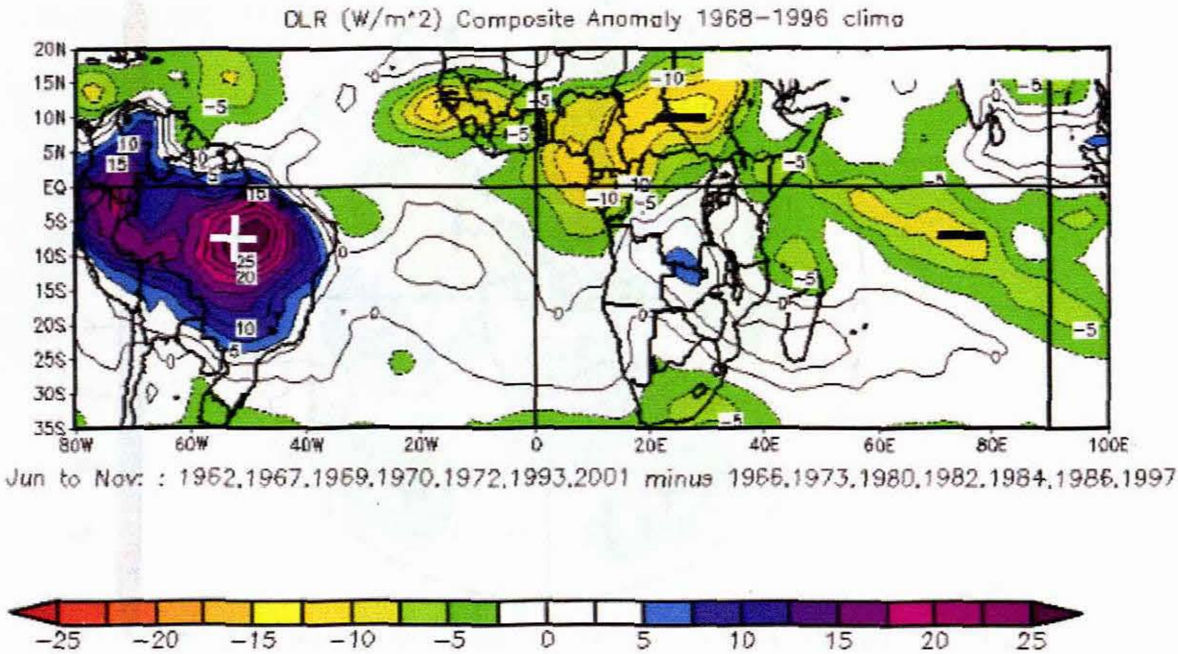

Fig b

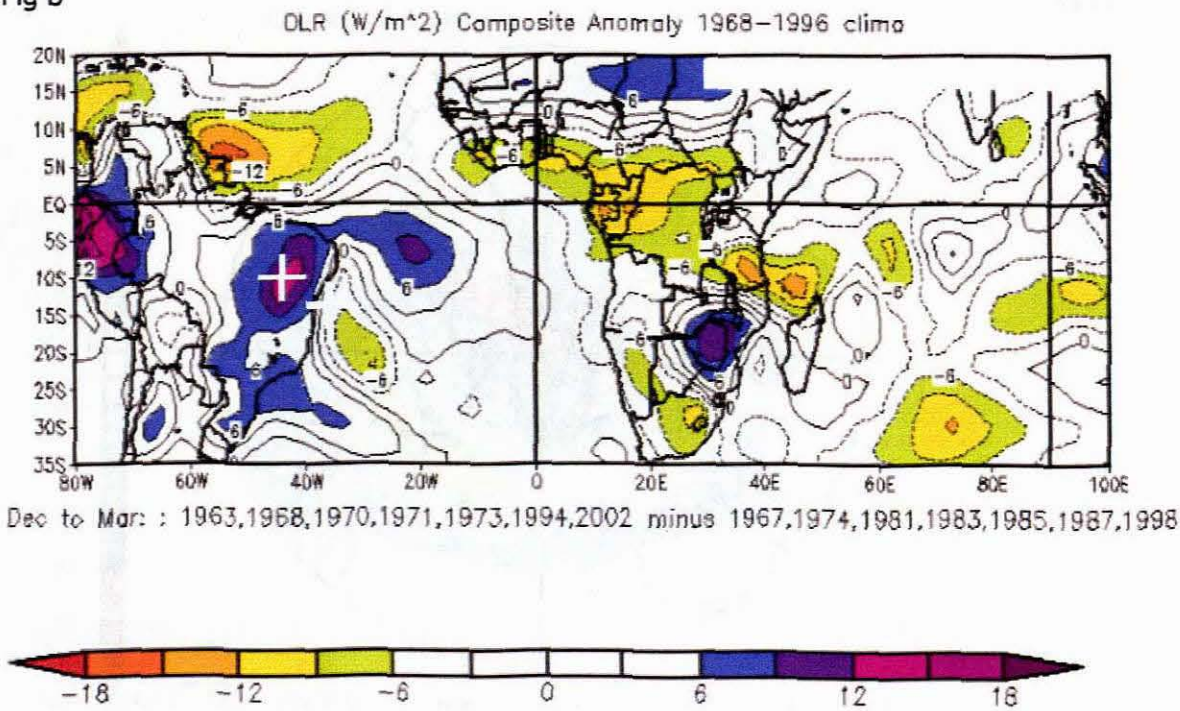

Fig 3.9: High - Low OLR from (a) Jun- Nov (b) Dec-Mar

Fig a

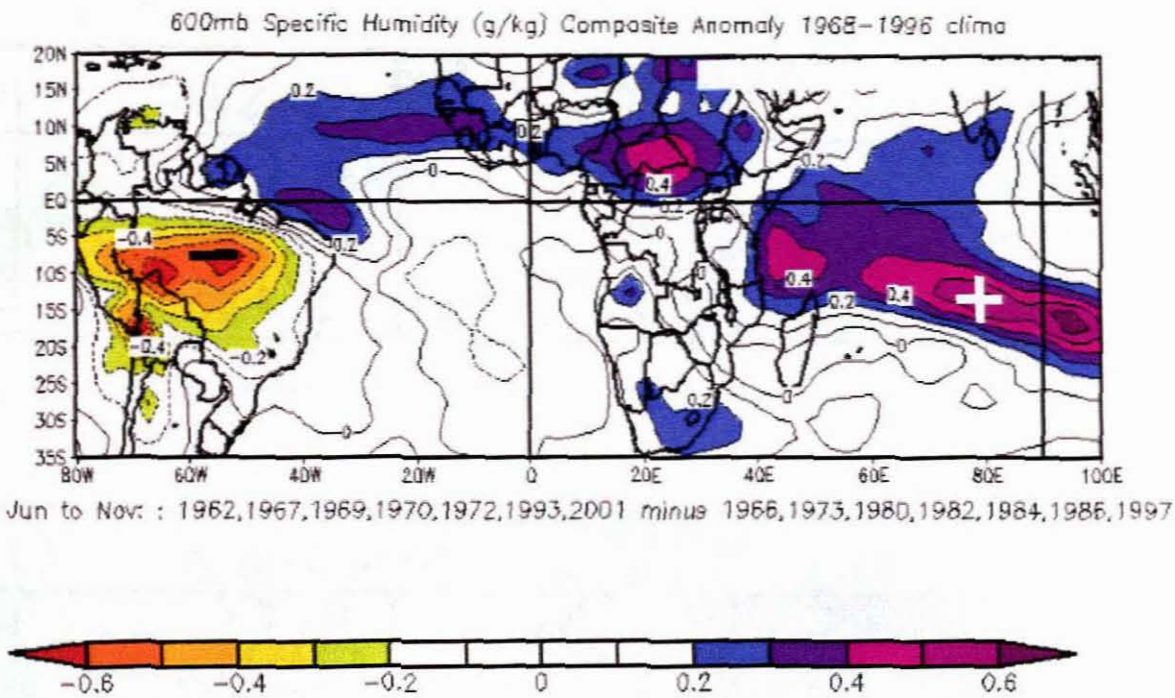

Fig b

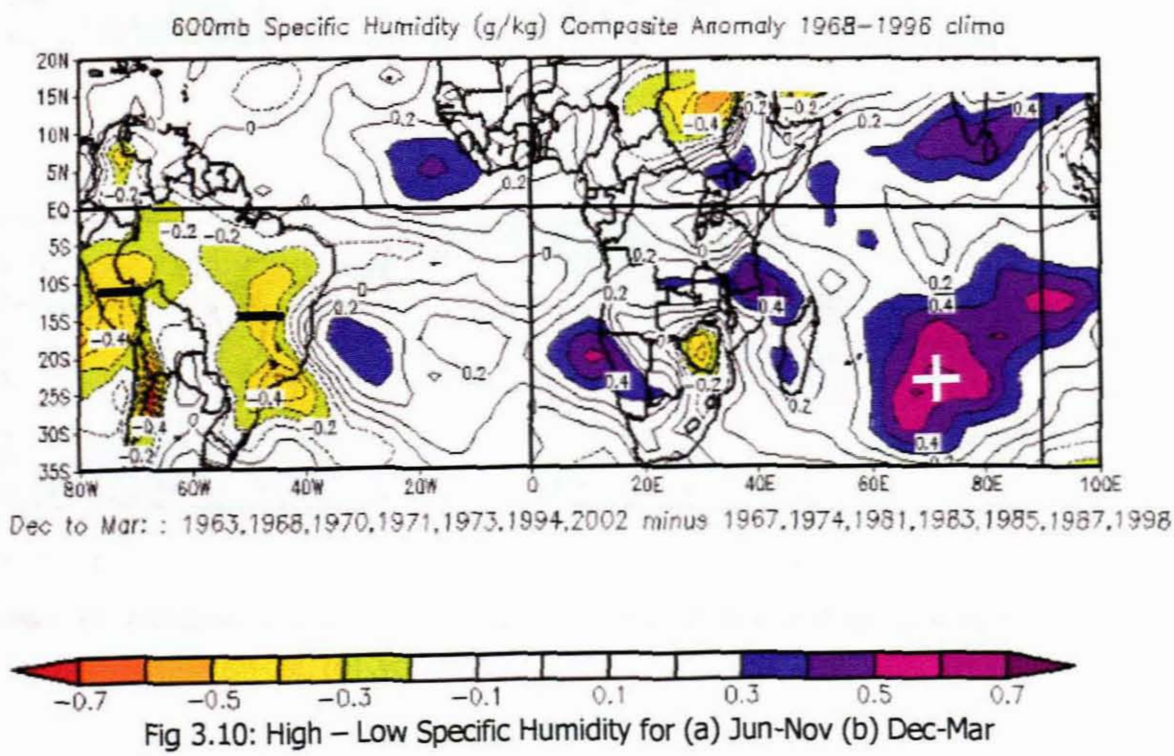

Fig 3.10: High – Low Specific Humidity for (a) Jun-Nov (b) Dec-Mar

Fig a

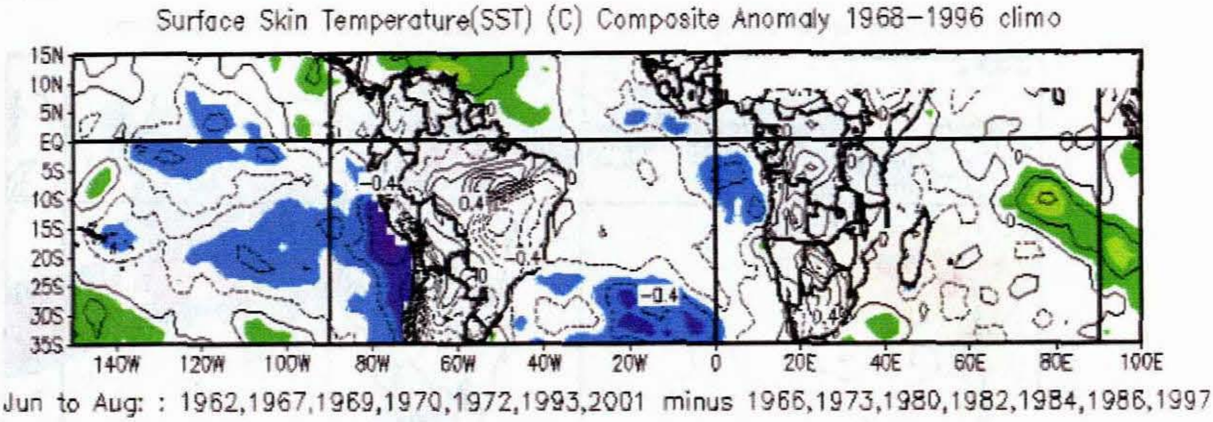

Fig b

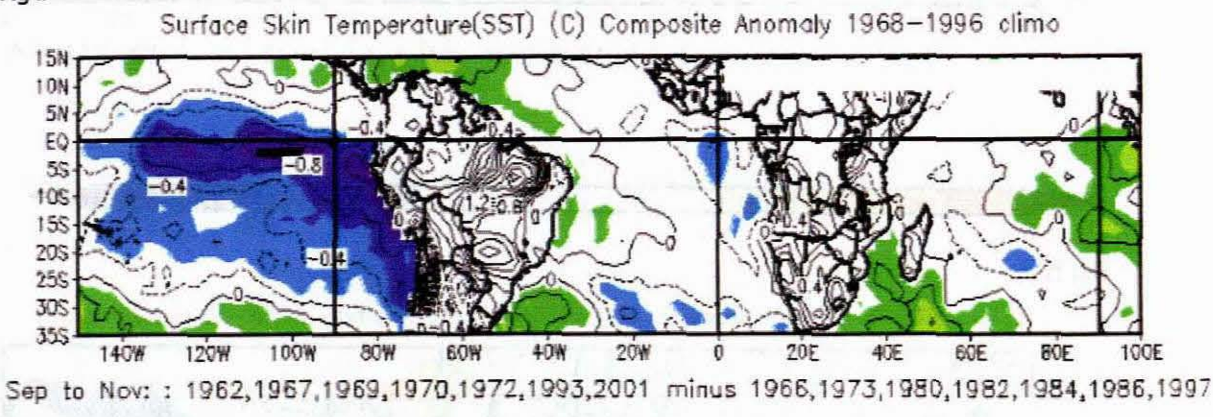

Fig c

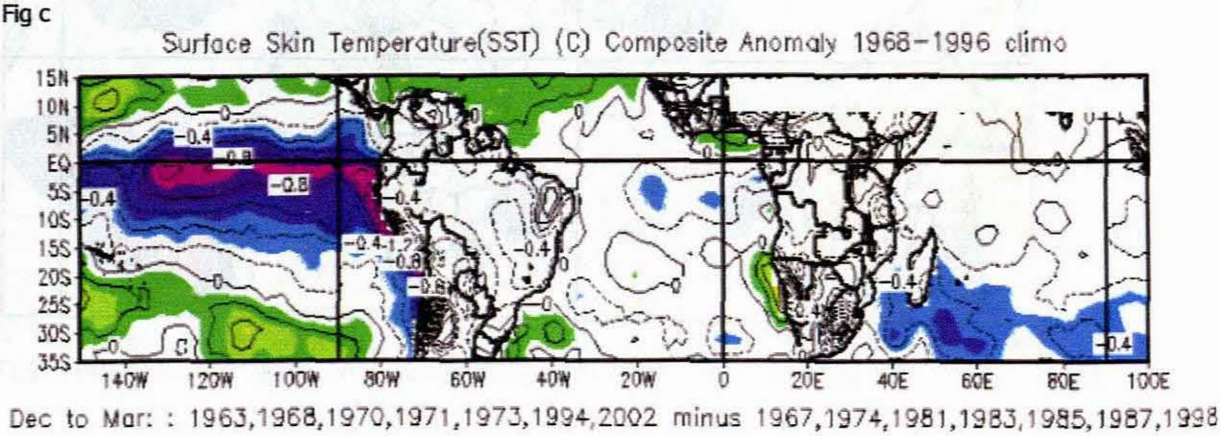

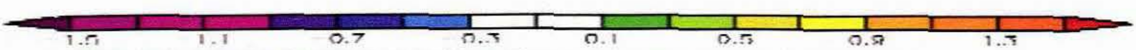

Fig 3.11: High - Low SST (a) Jun–Nov, (b) Dec-Mar

Fig a

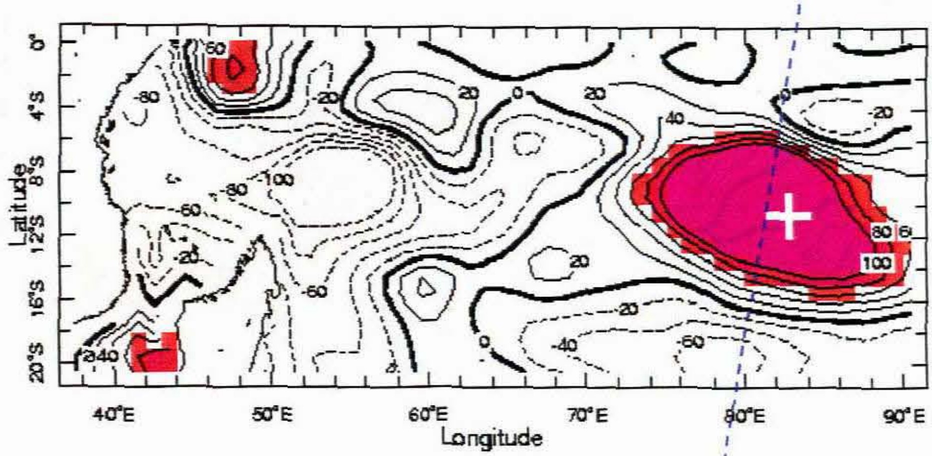

Fig b

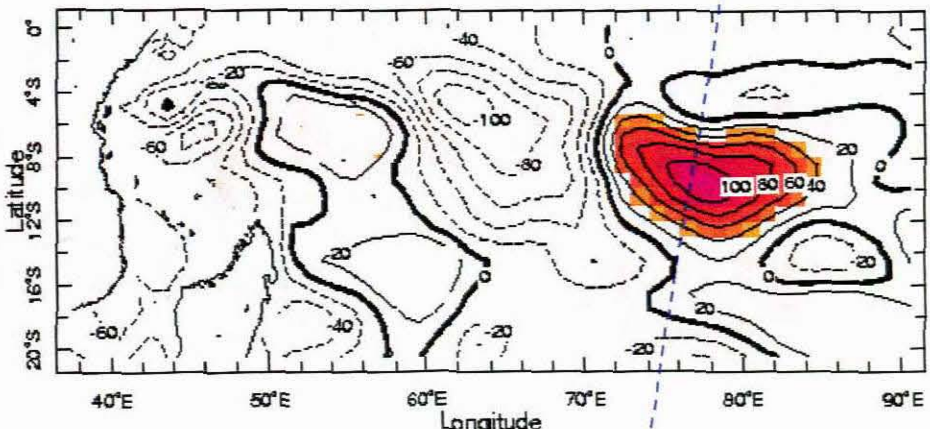

Fig c

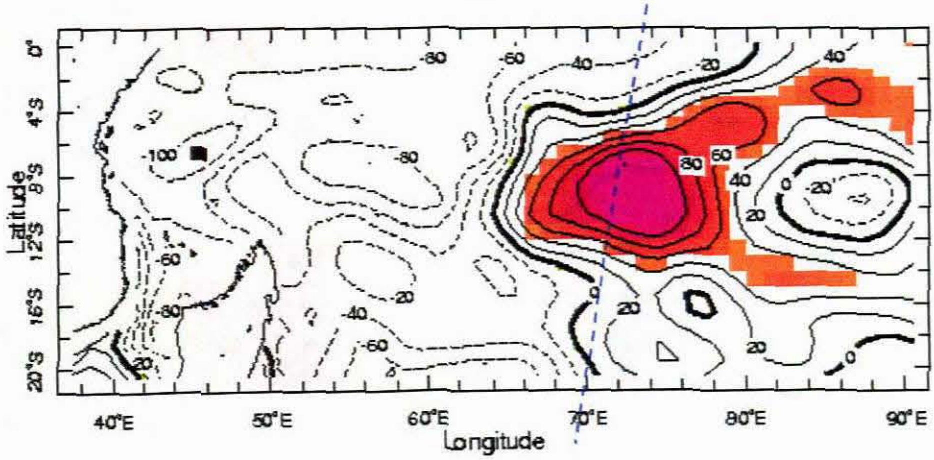

Fig 3.12: 125 meters vertically integrated HCA composite for high minus low TC days (a) JJA (b) SON (c) DJF season in the equatorial Indian Ocean

Fig a

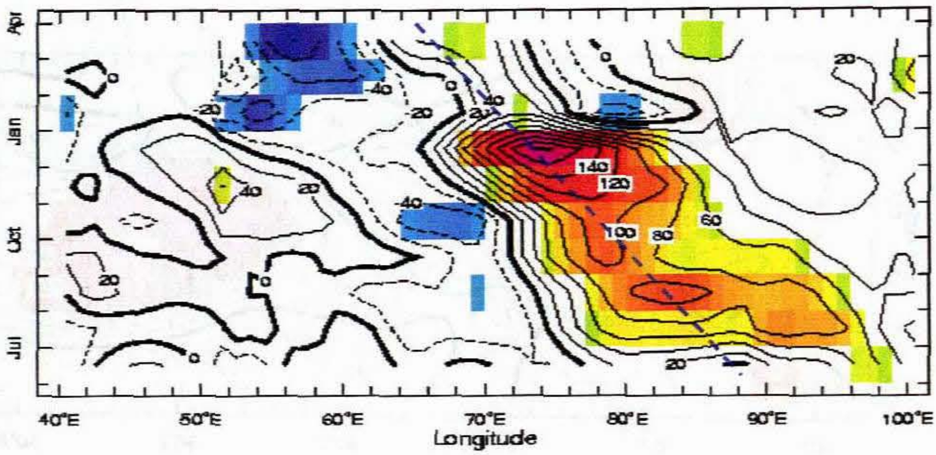

Fig b

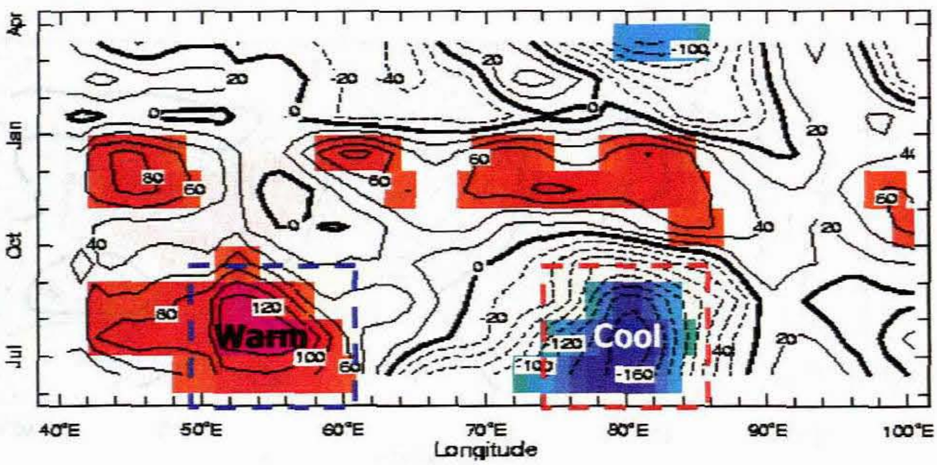

Fig c

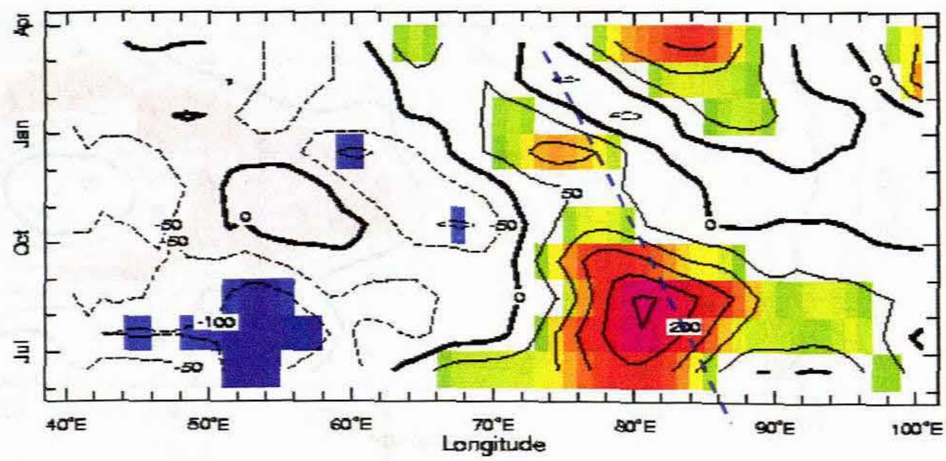

Fig 3.13: Hovmoller analysis of HCA for (a) high (b) low and (c) high minus low TC days in the Indian Ocean

Fig a

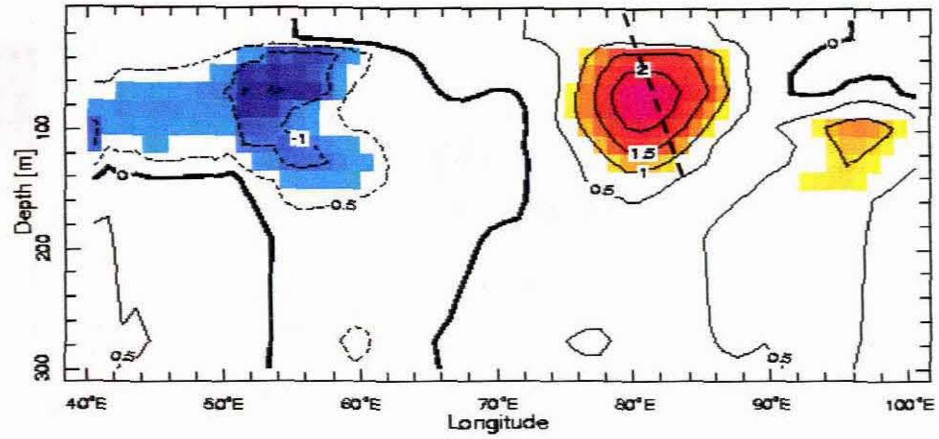

10.5S

Fig b

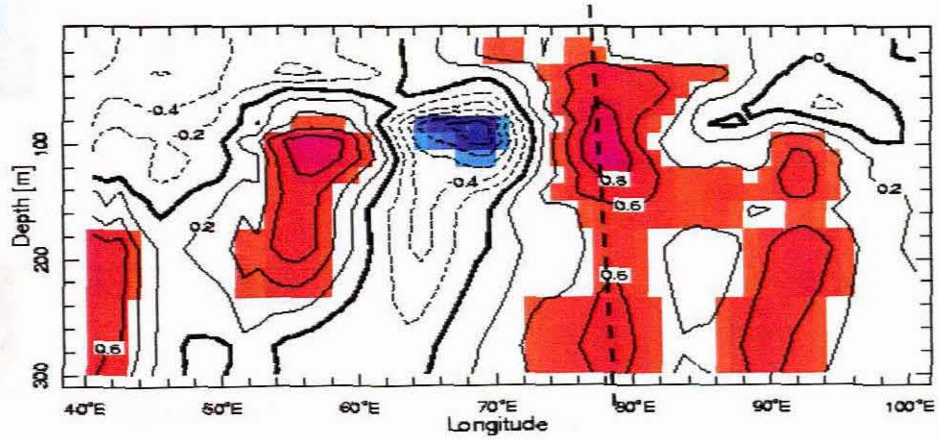

10.5S

Fig c

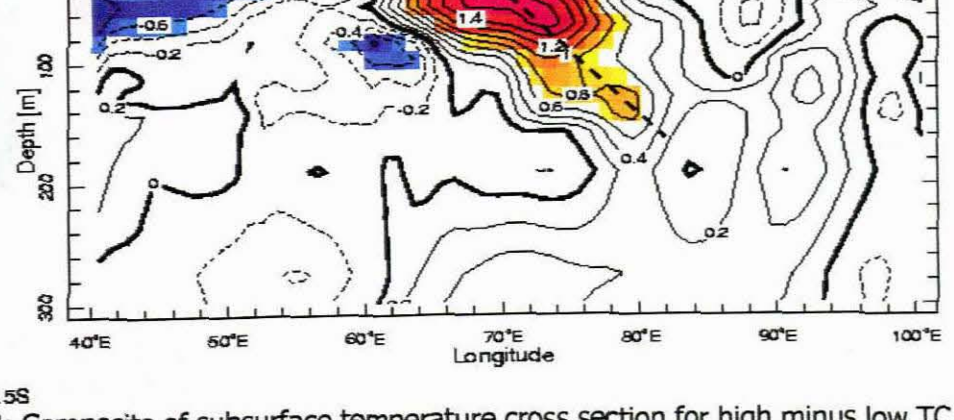

10.5S

Fig 3.14: Composite of subsurface temperature cross section for high minus low TC days during (a) JAS, (b) SON and (c) DJF seasons in the Indian Ocean.

Fig a

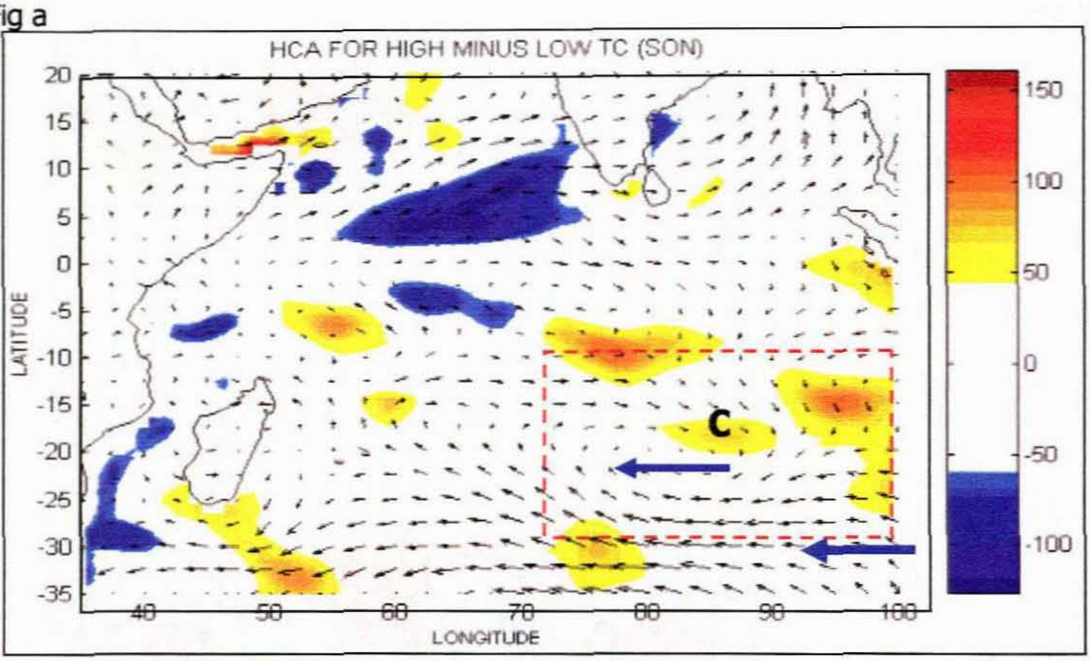

Fig b

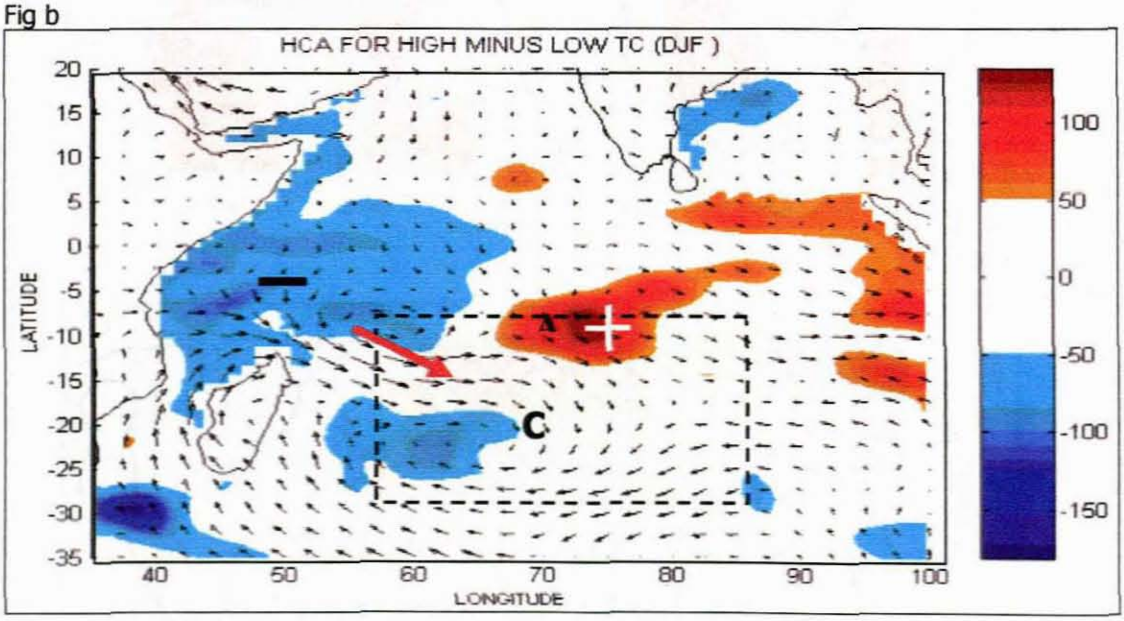

Fig 3.15: HCA and low level winds (1000 hPa) for high minus low TC during SON (a) and DJF season (b) showing cyclonic circulation propagating west, the development of strong westerlies north of Madagascar and the HCA dipole

Parameter	Key Area	Level	Key Area location
Zonal Wind	Equatorial East Indian Ocean	700 hPa	0 - 25° S / 45 E - 100° E
Zonal Wind	Equatorial Atlantic + Equatorial Indian Ocean	700 hPa	10 N - 2.5° S / 60 W -60° E
Zonal Wind	South Atlantic Ocean + South Indian Ocean	200-100 hPa	20 S - 35° S / 20 W - 100° E
Zonal Wind	East Atlantic Ocean + Indian Ocean	200-100 hPa	15 N - 10° S / 60 W -80° E
Meridional Wind	South Atlantic Ocean	200 hPa	0 - 20° S / 40 W- 0° E
Meridional Wind	WIO	200 hPa	10 S - 30° S / 30 E - 50° E
Meridional Wind	WIO	200 hPa	10 S - 30° S / 55 - 75° E
Stream Function	South Atlantic + South Indian Ocean	0.21 Sigma Level	5 S - 30° S / 40 W - 100° E
Velocity Potential	South America	0.21 (300-100 hPa average)	15 N - 20° S / 90 W-40° W
Velocity Potential	South East IO	0.21 Sigma Level	5 S - 35° S/ 60 E - 100° E
Velocity Potential	South America	0.95 Sigma Level	0 - 35° S / 80 W - 30° W
Potential Temperature	South America	500 hPa	15 S – 30° S / 60 W - 20° W
Potential Temperature	Indian Ocean	500 hPa	15 S - 35° S / 40 - 60° E
Pressure	South Atlantic Ocean	Surface	20 S - 35° S/ 40 W - 0° E
Geopotential Height	South Atlantic Ocean	300 hPa	30 S -70° S / 50 W- 10° W
Geopotential Height	South East Pacific Ocean	300 hPa	35 S - 70° S /135 W- 80° W
OLR	South America	Surface	10 N - 20° S/ 80 W - 40° W
Specific Humidity	South America	1000 hPa	5 N - 20° S /80 W - 40° W
Specific Humidity	East Atlantic Ocean/ Equatorial Africa/IO	600 hPa	10 N - 10° S /40 W - 100° E
Precipitable Water	South America		10 N - 20° S/ 80 W - 40° W
Precipitable Water	East Atlantic Ocean/ Equatorial Africa/IO	Surface	10 N - 10° S/ 40 W - 100° E

Table 3.1(a): key area, level and location of atmospheric parameters extracted from high minus low TC composite

Parameter	Key Area	Level	Key area location
SST	East Atlantic Ocean	surface	5 N - 20° S / 30 W - 10° E
SST	South Atlantic Ocean	surface	25 S - 35° S / 30 W - 10° E
SST	West Indian Ocean	surface	20 S – 35° S / 50 E - 80° E
SST	South East Indian Ocean	surface	10 S - 25° S / 80 - 100° E
Ocean Heat Content (HCA)	WIO	Subsurface to 125m	0 - 10° S / 50 - 65° E
Ocean Heat Content (HCA)	EIO	Subsurface to 125m	5 S - 15° S / 70 - 90° E
Ocean Heat Content (HCA)	NWIO	Subsurface to 125m	5 N - 15° N / 55 - 70° E
50 m Temperature	WIO	50 m Depth	5 S - 15° S / 50 - 65° E
50 m Temperature	EIO	50 m Depth	5 S - 15° S / 70 - 90° E
100 m Temperature	EIO	100 m Depth	5 S - 15° S / 70 - 90° E
100 m Temperature	WIO	100 m Depth	5 S - 15° S/ 50 - 65° E

Table 3.1(b): key area, level and location of ocean surface and sub-surface parameters extracted from high minus low TC composite

Chapter 4

Statistical Relationships, Tele-connections and Stability of Association

4.0 Introduction

This section studies the degree of associations and physical tele-connection between variables using correlation analysis. In addition to the composite signals of chapter 3, the key climate fields showing significant correlations will provide a candidate pool of predictors for the seasonal prediction of TC days. The stability of association between the potential predictors is investigated through cross wavelet transform (CWT) method. It was shown in chapter 3 that there existed an opposing convective (OLR) polarity pattern between South America and Indian Ocean before and during the TC season. Recent studies have highlighted the importance of the Atlantic zonal circulation are in establishing anti-phase climate regimes in South America and North Africa. Further work will be carried out to investigate how this mechanism relates to SWIO TC variability.

Linear correlation analysis is the method used to describe the relationship between TC days and environmental parameters for the MJJ, JAS and SON months. The degree of association between TC and key area time series indices will indicate the climate variables influencing TC variability in the SWIO. It is recalled that annual statistical correlation coefficient of (r) > 0.23 is statistically significant at 95 % since the degrees of freedom (df) of the TC days index is 40. Therefore, values < 0.23 are omitted in the following tables.

4.1 Association Between Intense TC Days Index With Atlantic Equatorial And Indian Ocean Winds.

The TC days index is negatively correlated with the equatorial Atlantic- western Indian Ocean zonal wind at 200 hPa (peak correlation in SON with -0.29) but positively related with zonal winds at 700 hPa with peak correlation of 0.33 in SON. The equatorial southeast Indian Ocean 200 hPa wind anomalies is poorly associated with the TC days index but is significantly negatively correlated with 700 hPa zonal wind with a correlation of -0.45 in JAS. The results indicate how the Atlantic and Indian Ocean zonal overturning circulations affect TC potential in the SWIO (table 4.1).

Level	Season	(Uaoio) Atlantic & Indian Ocean Zonal Wind (U)	(Ueio) Equatorial East Indian Ocean Zonal Wind (U)
200 hPa	MJJ	-	-
	JAS	-0.27	-
	SON	-0.29	-
700 hPa	MJJ	0.26	-0.28
	JAS	0.27	-0.45
	SON	0.33	-0.28

Table 4.1: Correlation of between TC days index and 200 hPa and 700 hPa zonal wind in east Indian Ocean (Ueio) and Atlantic Ocean (Uaoio)

4.2 Association Between Intense TC Days With Velocity Potential Over South America And Stream Function In South Atlantic - Southern Indian Ocean

A strong positive association of velocity potential at upper levels over South America is observed throughout with TC index. The strongest association is in SON when the correlation is +0.44 (table 4.2). This suggests increased upper level convergence and low level divergence over South America. The South Atlantic and Indian Ocean stream function (sigma 0.21) shows peak negative association of -0.29 with TC days in SON season. Hence upper anti-cyclonic shear favors increased TC days.

Season	**(VPsa)** South America Velocity Potential	**(SFsaoio)** South Atlantic & Indian Ocean Stream Function
MJJ	0.26	-
JAS	0.33	-0.23
SON	0.44	-0.29

Table 4.2: Correlation coefficient between TC days index and south America upper level velocity potential (VPsa) and stream function over south Atlantic & Indian Ocean (SFsaoio)

4.3 Association Between Intense TC Days Index And Southeastern Pacific Geopotential Height And Eastern Pacific Ocean SST.

The geopotential height (GPH) in the southeastern Pacific Ocean is significantly negatively correlated with the SWIO TC index with a peak correlation of -0.56 in SON. Similarly, the eastern Pacific SST is negatively correlated (r= -0.3) with the TC days index (table 4.3). The cooling in SST in the eastern Pacific suggests an association with ENSO phase, eg. La Nina favoring increased TC.

Season	(GPHsp) Southern Pacific Geopotential Height	(SSTep) Eastern Pacific Sea Surface Temperature
MJJ	-0.24	-
JAS	-0.24	-0.27
SON	-0.56	-0.30

Table 4.3: Correlation coefficient between TC days index and southern Pacific geopotential height (GPHsp) and eastern Pacific ocean SST (SSTep)

4.4 Association Between Intense TC Days Index With South America-Indian Ocean Out going Long Wave Radiation (OLR) And Specific Humidity.

The OLR is a proxy of convection. Positive OLR implies poor convection and negative OLR indicates convection. The TC days index is strongly positively correlated with South America OLR with peak correlation of +0.45 in SON (table 4.4). Below normal specific humidity is also observed in the surface layers with TC days (correlation of -0.4). *This implies below normal rainfall or dry conditions prevail over South America during years with high TC.* In contrast, the central-east equatorial Indian Ocean experiences increased convection from MJJ to SON (r= -0.22 in JAS) and increased moisture flux in SON (peak correlation +0.22).

Season	(OLRsa) South America OLR	(OLReio) East Indian Ocean OLR	(SHsa1) South America Specific Humidity	(SHeio) East Indian Ocean Specific Humidity
MJJ	0.30	-	-0.26	-
JAS	0.41	-0.23	-0.39	0.23
SON	0.45	-	-0.40	0.23

Table 4.4: Correlation coefficient between TC days index and OLR over south America (OLRsa), east Indian Ocean *(OLReio) and specific humidity over south America and east* Indian Ocean (SHsa1 and SHeio)

4.5 Association Between Intense TC Days Index With Thermocline Depth

The thermocline depth across the Indian Ocean is surprisingly found in this study not to be statistically significant with respect to the intense TC days index. This result is at odds with the signal and studies such as Xie et al (2001). However, the 100 m sub-surface ocean temperature and SST's in the southeast Indian Ocean in the JAS months provide a useful signal as shown below.

4.6 Association Between Intense TC Days Index With Southeast Indian Ocean SST, Sub-Surface Temperatures and Northwest Indian Ocean HCA

A peak positive correlation of 0.25 exists between the TC days index and South east Indian Ocean SST in SON (table 4.5). The inter-annual variations in SST show significant associations in the months directly before TC season. Warmer SST influences the moisture content and stability of the lower atmosphere. It provides extra energy for cyclone development and intensification. It also induces a lower surface pressure as shown in figure 3.15 of chapter 3.

The 100 m depth temperature in the southeast Indian Ocean is also significantly associated (r= 0.28) with the TC days index in JAS months (table 4.5). Very weak associations between TC days and the SWIO SST and HCA are found at these time lags. The HCA in the northwest Indian Ocean shows a significant negative correlation of -0.27 with the TC during the SON season possibly due to a stronger southwest monsoon. This suggests that a stronger/weaker southern hemisphere winter monsoon could be followed by a decrease/increase in TC days in SWIO governed by tropospheric biennial oscillations (TBO).

Season	(SSTseio) South East Indian Ocean SST	(T100eio) South East Indian Ocean 100 m temperature	(HCAnwio) North Western Indian Ocean Heat Content
JAS	0.24	0.28	-
SON	0.25	-	-0.27

Table 4.5: Correlation between TC days index and southeastern Indian Ocean SST (SSTseio), southeast Indian Ocean 100 m temperature and north western Indian Ocean heat content anomaly (HCAnwio).

4.7 Association Between Intense TC Days Index With Global Indices

Nino3 representing the ENSO signature in the Pacific Ocean is negatively correlated (r=-0.29 in SON) with TC days index (table 4.6). The warm phase of the ENSO (El Nino) in the Pacific Ocean suppresses intense TC days mainly by altering relative vorticity in the lower atmosphere and by increasing vertical shear. The QBO at 30 hPa is negatively associated with the TC index with peak correlation of -0.23 in SON. Gray (1984a) and Shapiro (1989) have shown that the stratospheric QBO modulates Atlantic basin TC activity; enhanced activity is observed during QBO west phase. However, in the IO, it is the east phase of the QBO that enhances TC activity. A detailed mechanism is still to be established. The north Atlantic oscillation (NAO) in positively associated with a correlation of 0.29 with the TC days index in SON months while the Pacific Decadal Oscillation is negatively associated with the TC index (r=-0.29). The Sahel rainfall index is also showing significant relation with a peak correlation of +0.38 in JAS with the SWIO TC index (table 4.6).

Season	(Nino3) SST Pacific Ocean	(NAO) North Atlantic Oscillation	(QBO-1) Quasi-Biennial Oscillation	(SHrf) Sahel Rainfall	(PDO) Pacific Decadal Oscillation
MJJ	-	-	-	0.22	-
JAS	-	-	-	0.38	-0.29
SON	-0.22	0.29	-0.23	0.24	-

Table 4.6: Correlation between TC index, Nino 3 (ENSO Signature), north Atlantic oscillation (NAO), QBO, Sahel rainfall and Pacific decadal oscillation (PDO)

4.8 Summary of Ocean-Atmosphere Relationship with TC

The correlation summary as bar graphs are shown in figures (4.1 a) and (4.1 b). It is observed that few ocean variables are significantly associated with the TC index at these lead times compared with the atmospheric variables. Variables with a correlation > 0.23 are retained as candidate predictors in modeling efforts in chapter 5.There are a total of 9 predictors for MJJ months while 13 for both JJA and SON months.

4.9 ENSO Transmission to the SWIO

We seek to explain ENSO - interactions and transmission with the related climate indices and its influence in the Indian Ocean. Earlier results indicated that negative anomalies of SST in the eastern Pacific and south eastern Pacific geopotential height were possible signatures of cold phases of ENSO (La Nina) that enhance the number of intense TC days in the SWIO. Jury & Pathack (1992) established that El Nino suppress TC by increasing westerly wind shear despite the favorable anomalous warmer SST.

4.9.1 Eastern Pacific SST and Associations With Atlantic Zonal Winds and South America Moisture

The east Pacific SST in MJJ is negatively associated with the JAS Atlantic 700 hPa zonal winds with a maximum negative correlation of -0.33. In contrast, the east Pacific SST has a maximum positive association with Atlantic 200 hPa zonal winds of 0.51 in SON. The correlation of the eastern Pacific SST and South America low level specific humidity (1000 hPa) is statistically significant with correlation of +0.49 in MJJ. When east Pacific SST declines, so does moisture over the Amazon. There is a coupling with the Atlantic, such that lower westerly/upper easterly wind anomalies occur.

4.9.2 ENSO Temporal Relationship And Stability

To understand the interactions and time evolution of the common spectral energy and the tropical circulation indices with the intense TC days in the time and frequency domain the cross wavelet transform (CWT) filtered in the 1.5-16 year time band is used. CWT helps examine the evolution of association that correlations cannot evaluate (Jury et al., 2002). It will indicate the stability and phase relationship between related environmental variables. The Atlantic zonal circulation Index is defined here as the difference in zonal wind at 200 hPa and 700 hPa (U_{200} - U_{700}) over the region stated in table 3 of chapter 3.

4.9.3 Relationship Between Atlantic Zonal Circulation (AZC) And Eastern Pacific SST

The AZC is closely coupled with eastern Pacific SST time series for most of the time between 1950 and 2001 (fig 4.2 a). The instantaneous correlation is significant at +0.63. The cross modulus-spectral energy between the AZC time index and eastern Pacific SST shows common spectral energy from 1967-1974, 1982-1989 and 1993-2001 in the 3 to 4 year band. 28% of total cross-wavelet modulus energy is found in the decadal band (fig 4.2 b). The instantaneous time delay between the two time series is shown in figure 4.2 c. The AZC leads the eastern Pacific SST by an average lead time of 2 to 4 months.

4.9.4 Relationship between Atlantic Zonal Circulation and OLR Over South America

The OLR over South America is positively associated with the AZC (r= 0.38). The overturning of the AZC increases low level moisture divergence over South America and consequently increasing OLR (decreasing convection). The common cross wavelet modulus spectral energy between the two time series shows high energy between 1971 to 1977 and 1995-2001 in the 2-3 year band. Moderate cross-modulus spectral energy is found in the 4 year band from 1983 – 1998 (fig 4.3 b). Weak spectral energy is observed from 1954-1980 in the 10 year band. The time delay analysis shows that the OLR lags the AZC by an average period of 3 to 5 months (fig 4.3 c).

4.9.5 Relationship Between Nino 3 and South West Central Indian Ocean SST

Nino 3 SST index is used as al reference for the ENSO tele-connection from the Pacific region. The result shows that Nino 3 is associated with SEIO SST with a correlation coefficient of 0.47 respectively (fig 4.4 a). The peak co-spectral energy is concentrated during strong ENSO years in the at 2-4 year band (4.4 b). Nino3 consistently leads the IO SST by 4 - 6 months on average (fig 4.4 c). This clearly indicates the ENSO influence on SST variability in the Indian Ocean. This result agrees well with previous findings (Latif and Barnett, 1995; Tourre and White, 1997; Venzke et al, 2000). The mechanisms by which El Nino signal may be transmitted in the Indian Ocean is through some of the Rossby wave motion in the eastern Pacific during El Nino which may penetrate through the Indonesian archipelago and reach Africa, where it causes a deepening of the thermocline, as in Peru. This causes unusually warm water off equatorial eastern Africa, which may result in disruptive floods particularly after the normal end of the wet season. Walker-like circulation cell is responsible for the uplift over eastern Africa and subsidence (severe drought) over Sumatra (Indonesia).

4.10 Coupled Ocean-Atmosphere Interactions

This section explores ocean-atmosphere interactions between the Atlantic and Indian Ocean. The Atlantic Zonal Circulation is correlated with the Indian Ocean SST and sub-surface ocean temperature for the seasons MJJ, JAS, and SON months. A Similar procedure is carried out with the Indian Ocean zonal winds at 700 hPa and the Indian Ocean surface and sub-surface parameters. The temporal associations and stability are studied with the CWT technique.

Ocean - Atmosphere Interactions between Atlantic and Indian Ocean

The Atlantic zonal wind at 700 hPa and 200 hPa in JAS and MJJ has a peak correlation of -0.58 and +0.67 with the JAS western Indian Ocean SST. The east Indian Ocean is less influenced by the Atlantic Zonal Circulation (maximum correlation of -0.39).

The ocean sub-surface temperature at 100 m depth in JAS is positively associated (correlation of 0.34) with the SON 700 hPa Atlantic zonal wind. In MJJ the 100 m temperature has a -0.36 correlation with the JAS 200 hPa Atlantic wind. It is suggested that oscillations of the Indian Ocean thermocline are related to the AZC (Yeshanew, 2004). The east-west oscillation of the thermocline via the ocean Rossby wave propagation (Shukla, 2002) has important consequences in ocean-atmospheric coupling, especially in terms of the Atlantic and Pacific zonal atmospheric circulations in the ENSO time scale which sets the climatic dipole between South America and Africa.

The following section examines the temporal associations and stability between east IO zonal winds and the sub-surface and surface flux using the CWT technique.

4.10.1 Temporal Stability of Atlantic Zonal Circulation and SST in the SWIO

Using monthly filtered (1.5-16 years) time series data from 1950-2001 it is found that the Atlantic zonal circulation anomaly is significantly coupled with SST in the SWIO (r=0.34) (fig 4.5 a).The peak co-modulus spectral energy is located in the known ENSO years (1971-72, 1982-1989 and 1995-2001) in the 2-4 year band (fig 4.5 b). The Atlantic circulation leads the SWIO SST by an average of 8-9 months, but decreases during strong El Nino years to 2-5 months (fig 4.5 c).

4.10.2 Temporal Stability Between Atlantic Zonal Circulation and Sub - Surface Parameters in SWIO

The Atlantic Zonal circulation has a correlation of -0.29 with the sub-surface heat content anomaly in the SWIO. The HCA shows high amplitude variability suggesting the presence of Rossby wave propagation in the IO. A similar but weaker signal is observed in SST and sub-surface temperature. The results suggest a stronger coupling during ENSO events. The time delay graph (not shown) indicates the HCA in the WIO leading the AZC after the 1970's. This could indicate a possible climatic shift related to warming trend.

4.10.3 Ocean - Atmosphere Interactions In The Indian Ocean

The SST during MJJ and JAS in the east IO is significantly inversely associated with the East IO zonal wind (peak correlation = -0.46). Similarly the East IO 100 m temperature is significantly associated with the east IO zonal wind. The following section examines the temporal associations and stability between east IO zonal winds and the sub-surface and surface fluxes.

4.10.4 Temporal Stability Between East Indian Ocean Zonal Wind and Southeastern Indian Ocean SST

The SST in the south east IO is negatively associated with the east IO zonal wind. The instantaneous correlation is -0.27. The time delay averages at 6 months (fig 4.6) (winds leading). The delay decreases to an average of 3 months during warm ENSO events when the coupling is stronger.

4.10.5 Temporal Stability Between East Indian Ocean Zonal Wind and 100 m Temperature in SWIO.

The 100 m ocean temperature in the SWIO is also negatively correlated with the east IO zonal wind(r=-0.34). There is strong co-spectral energy in the 1.5 - 4 year band in the period 1995–2000 (not shown). Zonal Winds lead SWIO 100 m temperature by an average of 8 months.

4.10.6 Temporal Stability Between Meridional Monsoon Wind and SWIO SST

Raw monthly data for the inter-hemispheric monsoon flow of the West Indian Ocean is found to have a strong correlation -0.61 with SST in the SWIO. The cross wavelet transform (CWT) analysis filtered in 1.5-16 years band shows strong spectral energy in 1962-77, 1995-2000 at 2-4 year cycles. Moderate spectral energy is found between 1982-1990. Decadal spectral energy is found in the years 1950-1974 (not shown). The SWIO SST is found to lead the meridional wind by a maximum of 16 months and minimum lead time of 5 months with the exception of the years 1959-68 where SST was lagging the meridional wind by 5-6 months. The time delay between the two signal decreases during the strong ENSO years.

4.11 Temporal Variability of Intense TC Days

Introduction

The temporal character of the intense TC days index is discussed in this section. The wavelet power spectrum analysis of standardized intense TC days reveals the principle temporal mode. The Cross Wavelet modulus spectral analysis with a band pass filter in the 8 -15 years is used to explore possible causes of the decadal cycle in intense TC.

4.11.1 Principle Temporal Mode of Intense TC Days Variability

From chapter 3, it was found that high TC days are found in the 1960's to early 1970's and in the early 1990's and 2002. In contrast, low TC days are observed in the mid 1970's up to early the 1990's. The wavelet power spectrum of the TC index (figure 4.7) shows peak power mainly at 2.4 and 10 year cycles. The 2.4 year cycle was dominant in the years between 1967 and 1972. A weaker 2.4 year cycle is found in the periods 1980-85 and 1996-2002. The ten year cycle is strongest occurred between the 1960's to early 1970's and emerges again in the late 1990's. Therefore the TC days index is characterized with biennial to decadal frequency variability.

4.11.2 Biennial Variability in Intense TC Days Index

The 2.4 year cycle in the TC index has been previously found by Jury et al. (1999) to be associated with the Quasi Biennial Oscillation (QBO) at 30 hPa. In the Atlantic TC activities are also modulated by the QBO (Gray, 1984). The QBO is a major natural oscillation in the equatorial stratospheric zonal wind with a period of oscillation around 26 months (Reed, 1965). The driving force of the QBO is the vertical transfer of momentum from the troposphere to stratosphere by Kelvin and Rossby-gravity waves. The wind regime propagates from 10 hPa down to 100 hPa with maximum amplitude of 40 to 50m/s at 20 hPa. The easterlies are normally stronger. Several studies have shown that the phase of the QBO influences weather events such as the Indian summer monsoon (Mooley et al., 1986) and is proved to modulate ENSO phenomena (Roplewski et al., 1992). It is also an integral part of the Asia-Pacific climate.

4.11.3 Decadal Variability in Intense TC Days

An investigation is carried out to understand the possible forces causing the decadal cycle in TC days, considering the recent findings of White and Toure (2003) on global eastward moving SST and SLP waves. To isolate the decadal variability, a filter in the 8 -15 year band is applied to previously identified parameters exhibiting a decadal cycle using the CWT.

4.11.4 Association Between Atlantic Zonal Circulation and Eastern Pacific SST

The two signals are highly coupled over the entire domain in this decadal filtered analysis. The degree of association is very high at 0.77 (fig 4.8 a).The Atlantic zonal circulation shows higher variability than eastern Pacific SST from 1980 to 1990. Common spectral energy occurs at 11-12 year cycle, especially in the years 1974 to 1990 (fig 4.8 b). It is important to note that the decadal spectral energy is about 25 % of the total. The time delay graph shows that the eastern Pacific SST leads the Atlantic zonal circulation by an average of 10 months at the decadal cycles (fig 4.8 c) unlike the 2.4 year cycle where the AZC leads.

4.12 Summary

The statistical analyses have revealed that the south Pacific geopotential height has the strongest association with the TC days index in the SON season. Other results suggest that ENSO plays a key role in TC variability in the SWIO by transmitting its signal primarily through the Atlantic zonal circulation. The Atlantic zonal overturning (AZO) is an integral part of the global ENSO as indicated in the correlation and CWT analyses. La Nina conditions favour SWIO TC while El Nino suppresses

Anomalous convection (OLR) over the Amazon is linked with SWIO TC variability. The South America climate seems to operate in anti-phase association with Africa and the east Indian Ocean. SST in the southeast Indian Ocean and the sub-surface temperatures at 50-100 m are useful in predicting TC days. However, Ocean-atmosphere interactions in the Indian Ocean play a secondary role. The AZC seems to lead the processes of intense TC variability.

The TC days index displays biennial (2.4) and decadal (~10) cycles. The biennial cycle is modulated by the *stratospheric quasi-biennial oscillation* and southeast Indian Ocean SST and associated ocean Rossby waves. The Atlantic zonal circulation is coupled with the eastern Pacific SST signal in the decadal frequency. The AZC lags eastern Pacific SST in the decadal band, but leads at higher frequencies. Gray, Sheaffer and Landsea (1997) explain that decadal variations in the Atlantic thermohaline circulation are important.

The next chapter assembles the results from chapter 3 and 4 for the development of multivariate models at 3, 6 and 9 month lead time. The models are tested for operational reliability. The temporal characteristics and stability of predictors are assessed.

Fig a

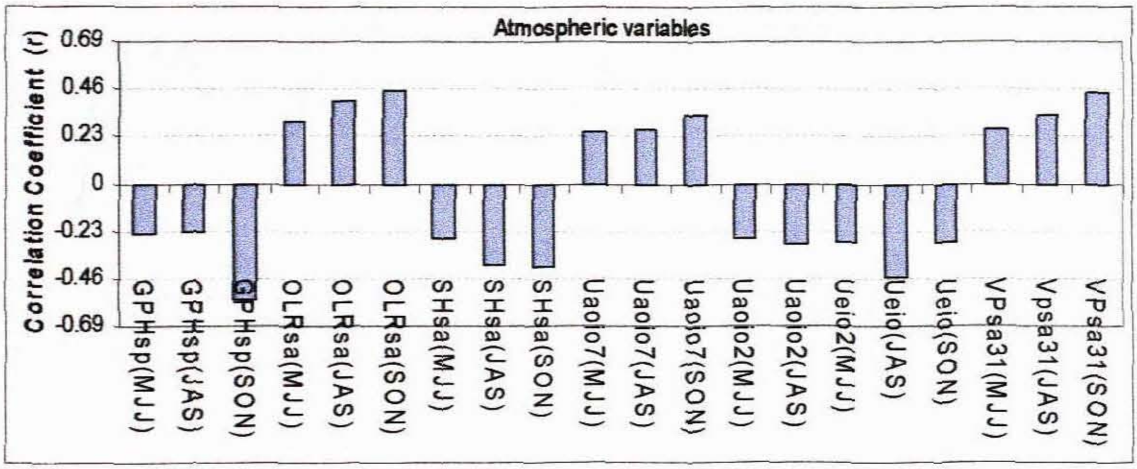

Fig b

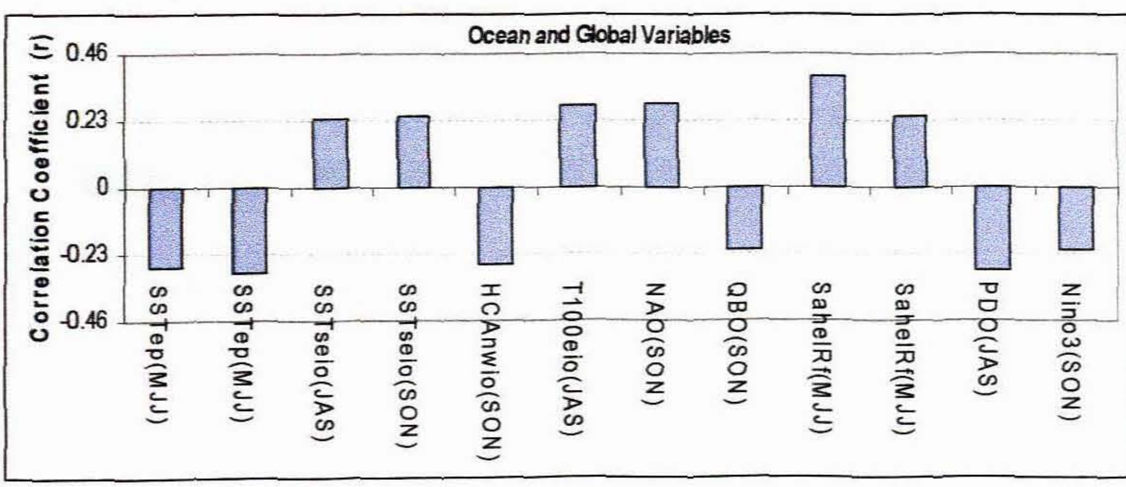

Fig 4.1: Significant correlation graph of TC days index with (a) atmospheric variables (b) Ocean and global variables. Only months (MJJ, JAS and SON) with significant correlations are shown.

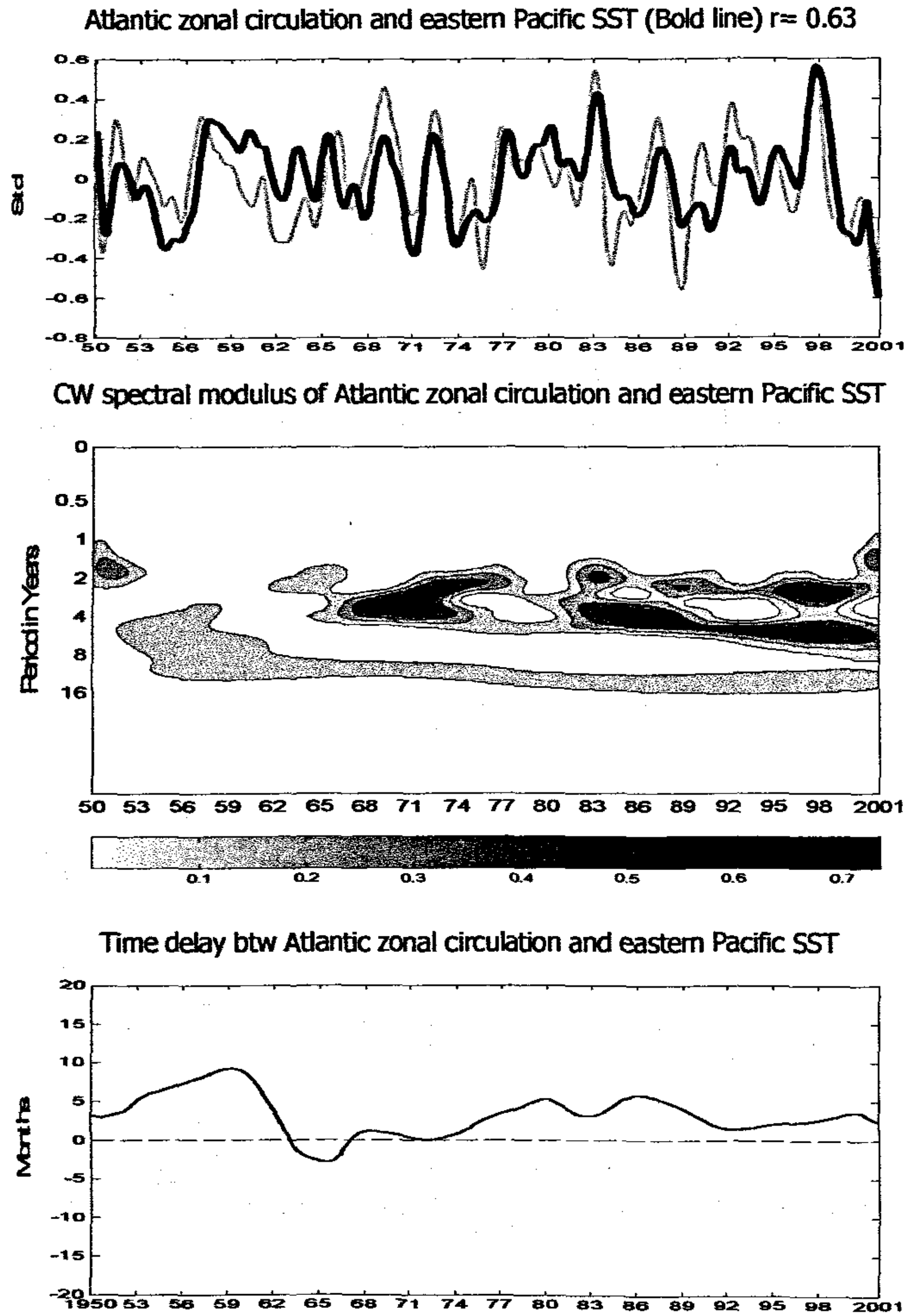

Fig 4.2: (a) Temporal evolution (b) co-spectral power and (c) time delay between Atlantic zonal circulation and eastern Pacific SST:
ENSO Transmission (Low band pass filter 1.5 -16 yrs)

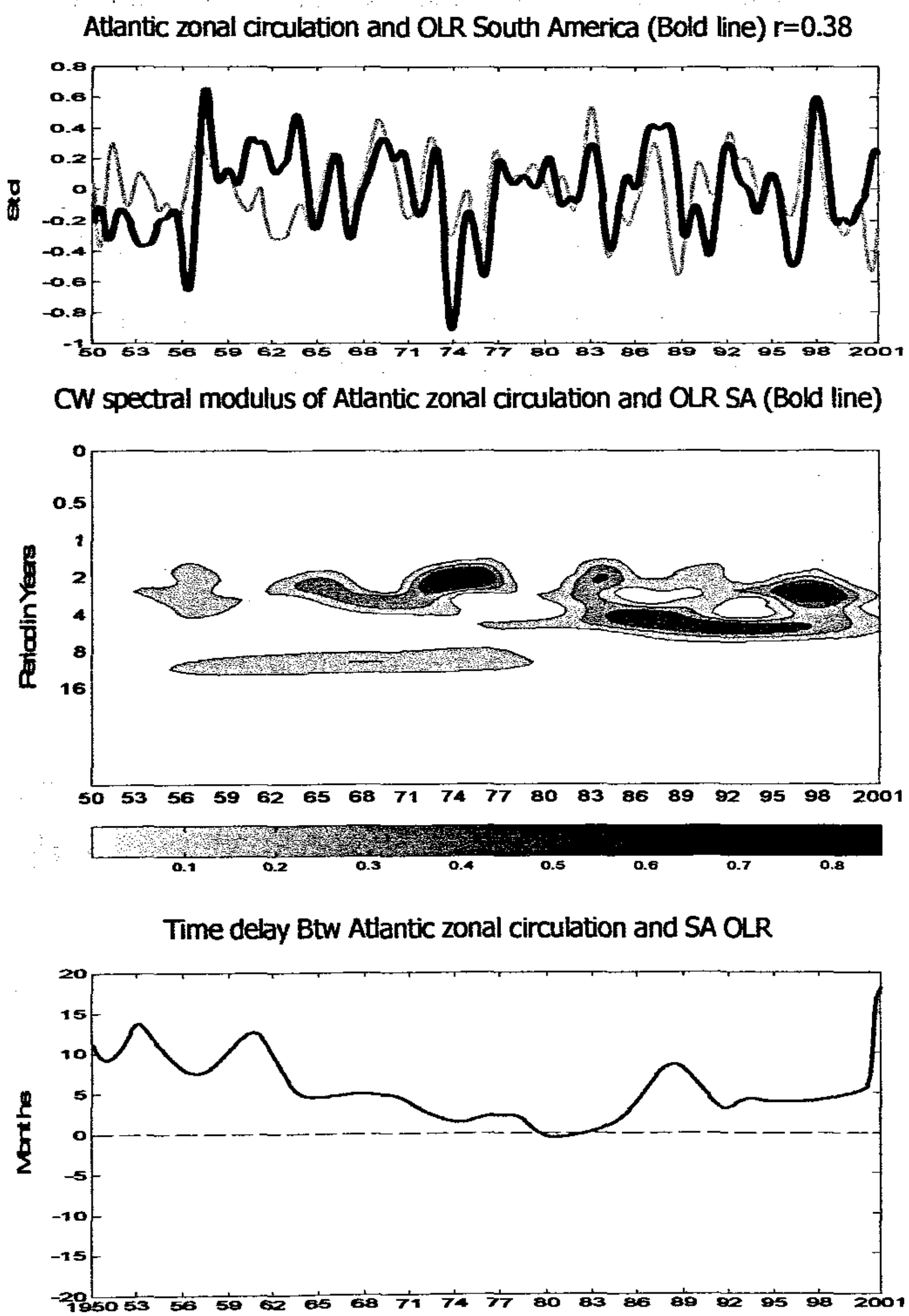

Fig 4.3: (a) Temporal evolution (b) co-spectral power and (c) and time delay between Atlantic zonal circulation and south America OLR:
ENSO Transmission (Low band pass filter 1.5 -16 yrs)

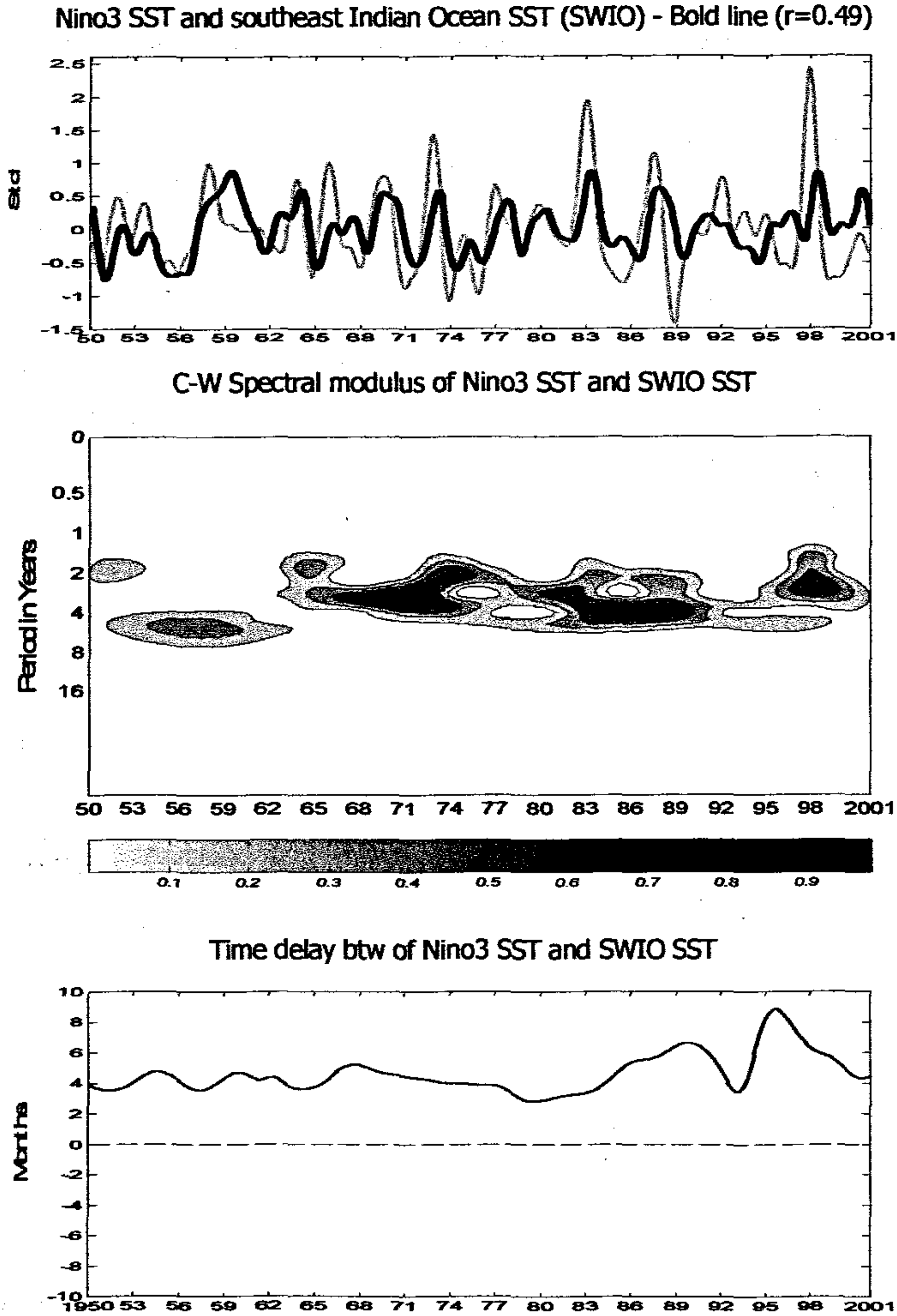

Fig 4.4: (a) Temporal evolution (b) co-spectral power and (c) and time delay between Nino 3 SST and SST southwest Indian Ocean (SWIO):
ENSO Transmission (Low band pass filter 1.5 -16 yrs)

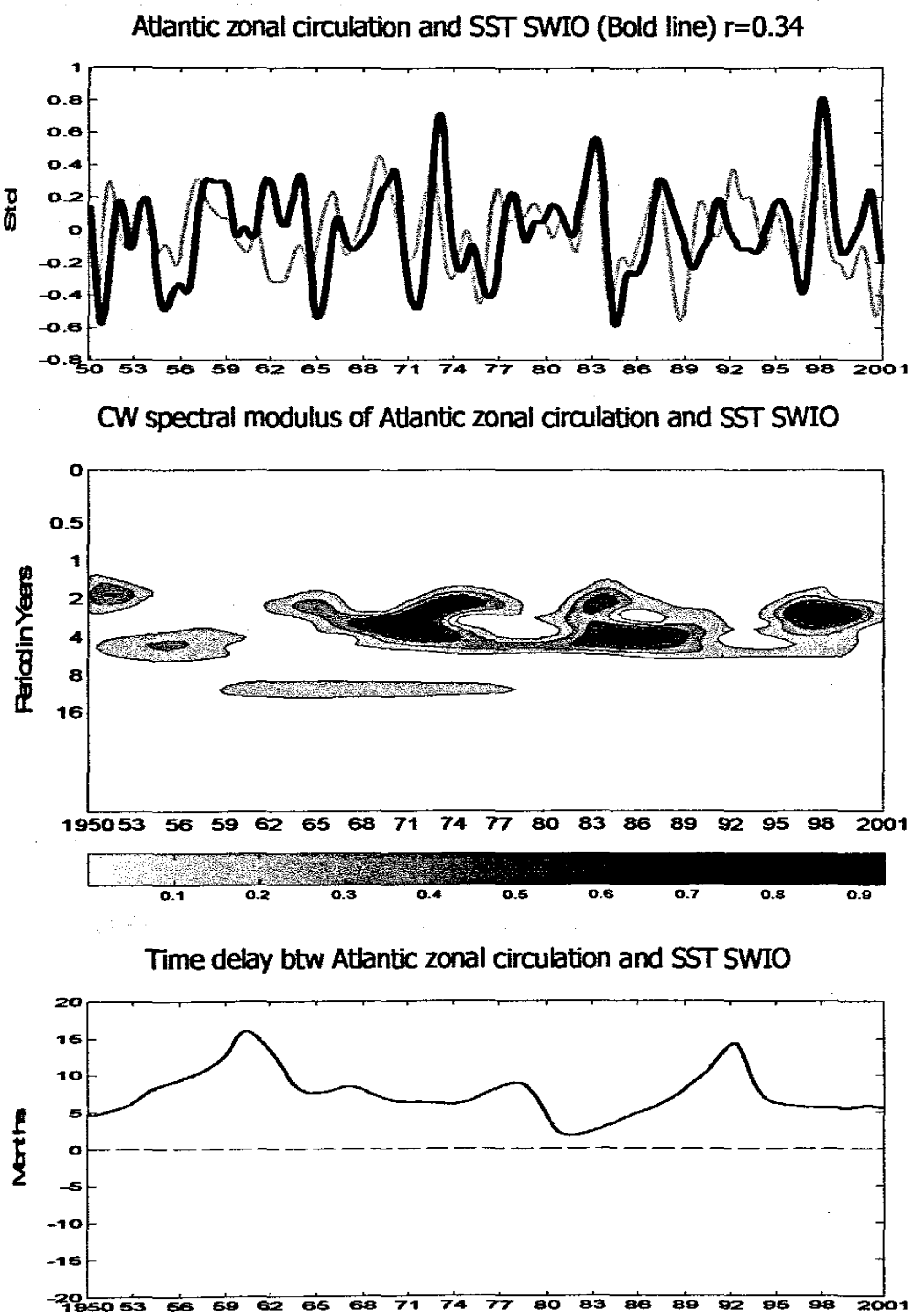

Fig 4.5: (a) Temporal evolution (b) co-spectral power (c) time delay between Atlantic zonal circulation and SST SWIO: **Coupled Ocean-Atmosphere Interaction (Atlantic and Indian Ocean)** (Low band pass filter 1.5 -16 yrs)

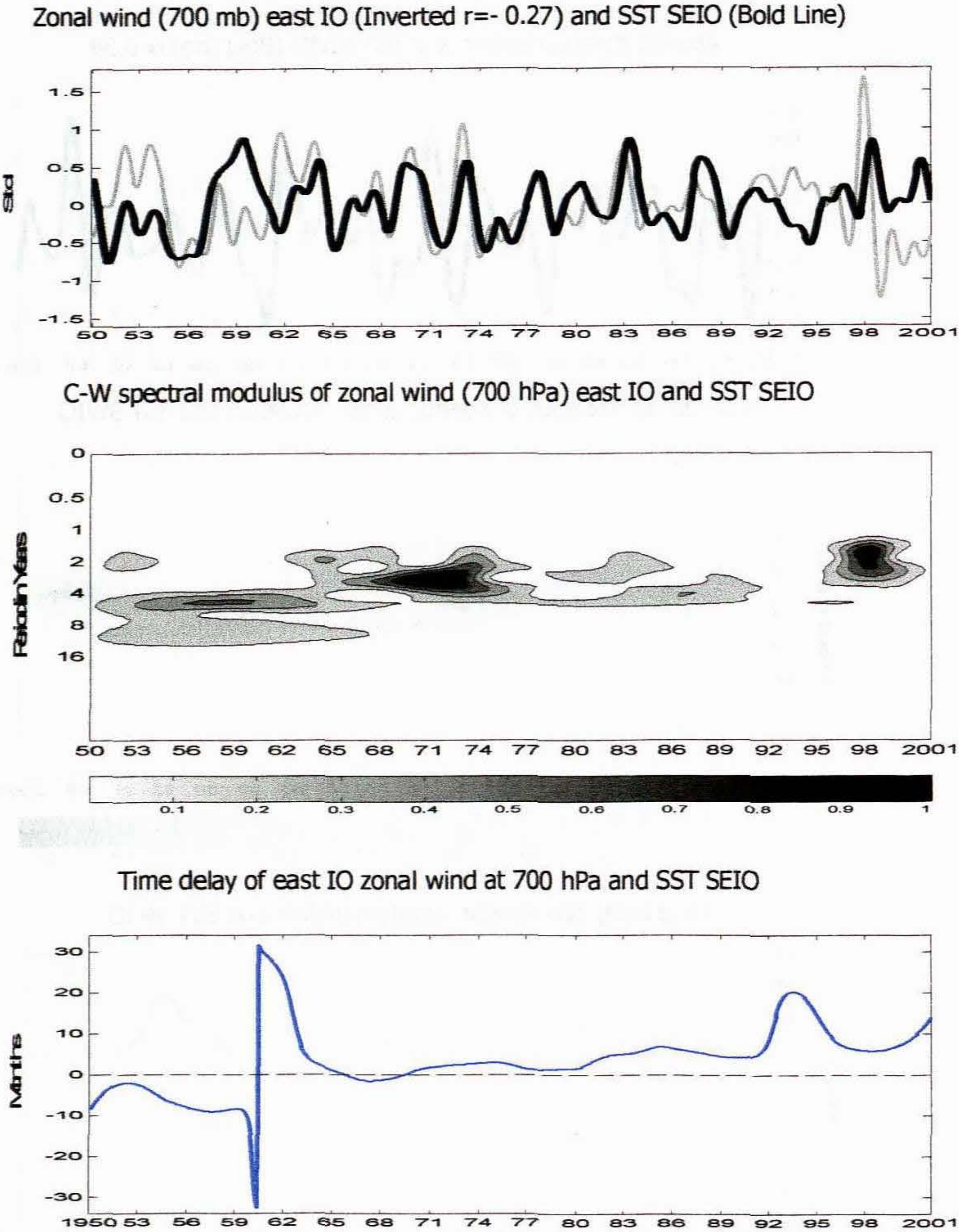

Fig 4.6: (a) Temporal evolution (b) co-spectral power and (c) time delay between 700 hPa zonal wind east Indian Ocean and SST SEIO: **Coupled Ocean-Atmosphere Interaction (Indian Ocean)** (Low band pass filter 1.5 -16 yrs)

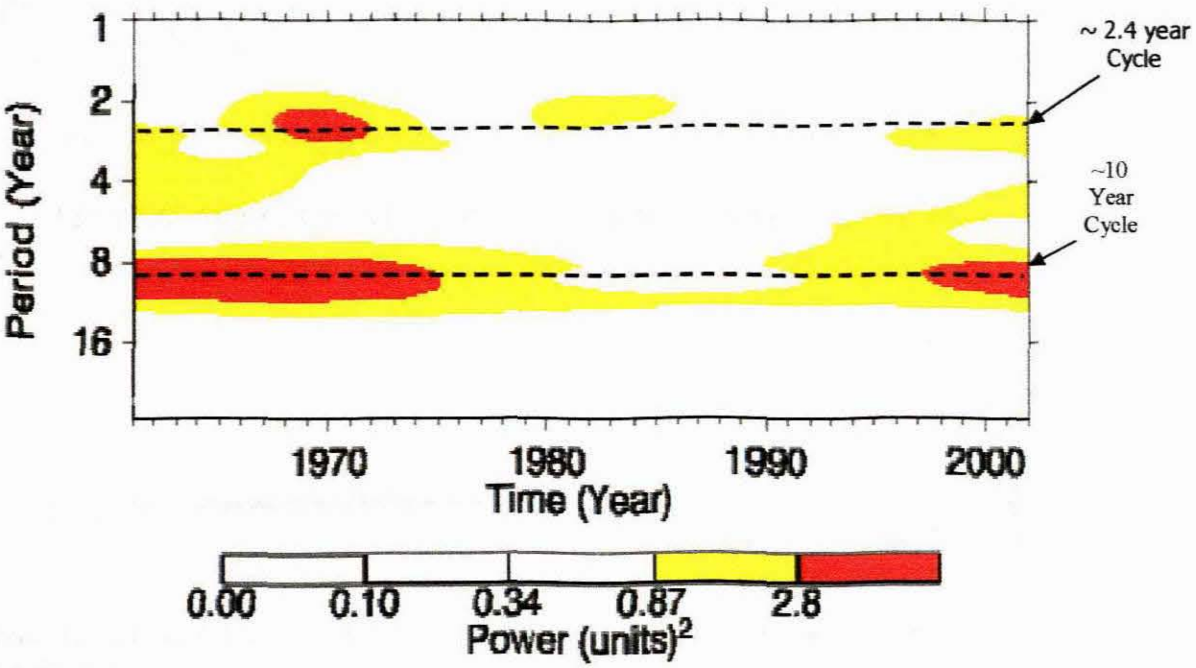

Fig 4.7: Intense TC days time series index and wavelet power spectrum:

Temporal Characteristics

Fig a

Atlantic zonal circulation (Bold) and eastern Pacific SST(r= 0.77)

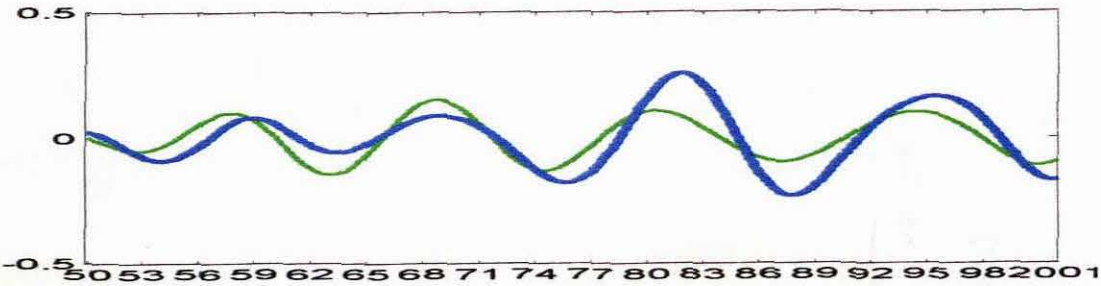

Fig b

CW spectral modulus of Atlantic zonal circulation and eastern Pacific SST

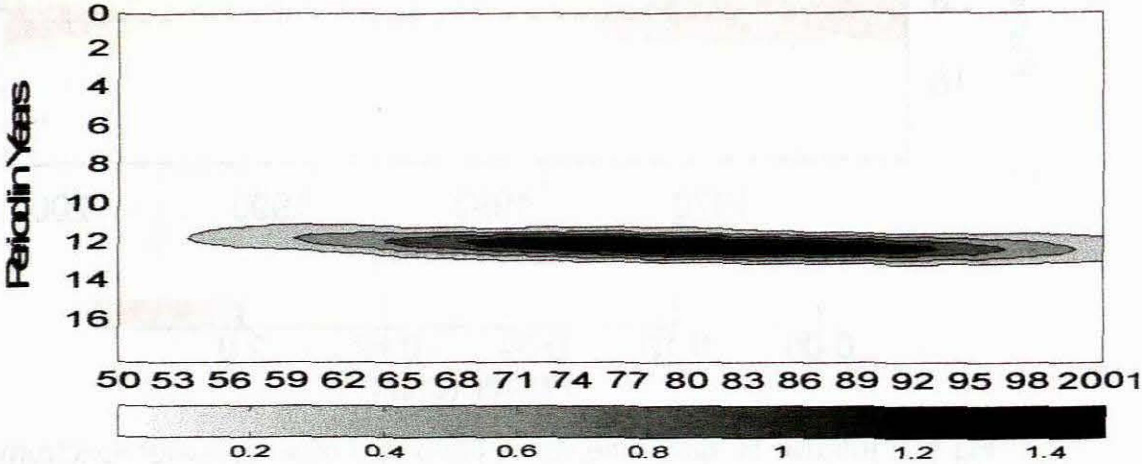

Time delay Btwn Atlantic zonal circulation and eastern Pacific SST

Fig c

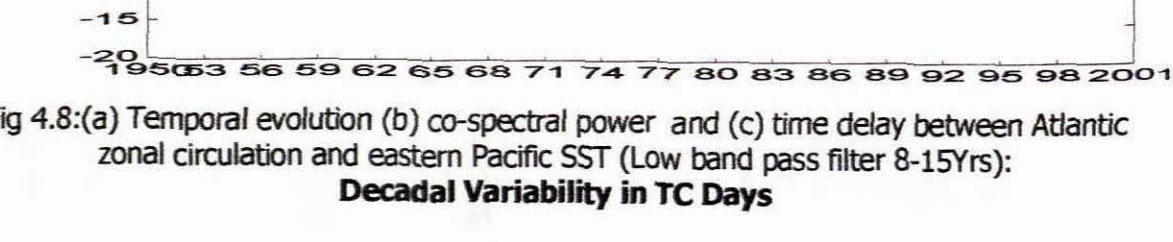

Fig 4.8:(a) Temporal evolution (b) co-spectral power and (c) time delay between Atlantic zonal circulation and eastern Pacific SST (Low band pass filter 8-15Yrs):
Decadal Variability in TC Days

Chapter 5

Prediction of Intense Tropical Cyclone Days, Stability and Associations

5.0 Introduction

The aim of this chapter is to develop multi-variate statistical models for the prediction of intense TC days in the SWIO. The models are validated to test their potential reliability. It is noted that two general methodologies exist for forecasting marine weather regimes: statistical and numerical (Jury, 1993; Jury 2001 b; Mason, 1997). Statistical models are advantageous here because they can "target" TC days, whereas numerical models predict rainfall and temperature.

5.1 Multi-Variate Model Development

In chapter 3, research was undertaken to reveal the potential predictors for seasonal TC days based on their historical relationship. The initial work involved analyzing composite ocean-atmosphere fields for high minus low TC days. The regions showing strong and consistent signal throughout the season were considered for correlation analysis in chapter 4. A pool of 9 candidate predictors was extracted for MJJ while 13 for the JAS and SON months (table 5.1). Predictive linear multi-variate models are developed using the forward stepwise technique. A maximum of three predictors are permitted in the model to reduce problems of co-linearity. For each model equation an evaluation of the statistical performance is done. The model is rejected if a significant ($r>0.23$) correlation between predictors is detected

5.2 Predictors of Intense TC Days in SWIO

Overall the TC statistical multivariate model for SWIO achieves an adjusted r^2 fit of 34 % in MJJ, 38 % in JAS and 48 % in SON months (Table 5.2).

1. The MJJ model equation consists of three predictors: the southeast Indian Ocean zonal wind at 700 hPa, specific humidity at middle levels over equatorial Africa and Sahel Rainfall.
2. The JAS model has the South Amazon OLR as the leading predictor followed by the SST signal from the southeast Indian Ocean. The third predictor is HCA in the northwest Indian Ocean.
3. The SON model has three predictors. The leading predictor is the southeast Pacific GPH followed by SST in the southeast Indian Ocean and the QBO signal.

5.3 Comparison Between Tropical and Non-Tropical Models

The south east Pacific GPH is a high latitude predictor. Therefore, it is important to show its reliability compared to tropical indices. A model is developed for the SON months with tropical predictors only and comparison is made between the two. The model with the GPH from the higher latitude is defined as the 'non-tropical' model.

The 'non-tropical' model for SON has an adjusted R^2 of 48%. In contrast the tropical model consists of three predictors (OLR South America, SST south East Indian Ocean and Heat content anomaly in the northwest Indian Ocean) with an adjusted R^2 of 38 % (table 5.2). The non-tropical model exhibits a higher adjusted R^2 value than the purely tropical model. This implies the non-tropical model with southeast Pacific GPH performs better. From this point the non-tropical model is selected as the best model. It is tested further using the validation and verification techniques. Model predictors are assessed for temporal associations and stability below.

5.4 Validation of Model

Cross validation was used to evaluate how the *model* would have predicted a group of years excluded from 'training': This is done for the first and last ten years of the data and predicting the outcome based on the remaining years.

5.4.1 'Non-Tropical' Model Validation and Verification

The 'non-tropical' model achieves a 70 % tercile hit rate and achieves an adjusted R^2 fit of 38 % (fig 5.1 b) with the last 10 years removed. When the 'non-tropical' model is validated against the first ten years the model achieves an adjusted R^2 fit of 56 % and a hit rate of 90% (fig 5.1 a). It should be noted that validation was also carried out for the tropical model but the details are excluded here. The results confirm its lower level of performance. The tropical model performs poorly with a 40-50 % hit rate in the last period 1993-2002. In the following sections the predictability is analyzed.

5.5 Temporal Variability of Key Predictors

Temporal variability is studied using the wavelet spectral transform method filtered in the 1.5-16 year band. The southeast Pacific GPH (fig 5.2) shows peak spectral modulus energy around 2-3 year cycle particularly in the period between 1960 -1980 and from 1990-2000. Moderate spectral energy in the 5 and 10 year band is found from 1950's to 1960's.

The SST in the southeast Indian Ocean has peak spectral energy in the 3 year cycle band mainly in the period between 1968 -1972 (fig 5.3). A weaker spectral energy is detected in the 1997-2000 in that cycle band. In the mid 1980's the SST exhibited some spectral energy in the 4 year band while significant spectral energy in the period 1955-1962 comes from the 6 year band. The coupled Rossby wave in the Southern tropical Indian Ocean could be playing a significant role in setting the frequency of the SST variability.

The OLR signal from South America (Amazon) has peak spectral energy in the 2 year band between 1971- 1976 period (fig 5.4). A significant 3 year cycle is found in the period 1994 -2000. It is interesting to observe that the OLR signal shows inter-decadal spectral energy in the mid 1950's to early 1980's.

5.6 Inter-annual Stability of Model Predictors

It is sometimes assumed that predictability remains constant and predictand variables are valid under future climate conditions. However, from the model validation experiment it was observed that the models were performing differently when data at the beginning and end are withdrawn. In recent studies similar to Jury et al (2001) climatic relationships are found to change over time. It is known that the Indian Meteorological Services is constantly changing and updating their statistical models based on the stability and change of association. An analysis of the historical stability of association between the predictors gives useful insights to the impact of climate change on future applications.

5.6.1 Association between South Eastern Pacific Geopotential Height And South Eastern Indian Ocean SST

The southeast Pacific Geopotential height time series shows higher frequency variability than the SST in southeast Indian Ocean (fig 5.5 a). The cross-modulus spectral energy between the geopotential height and SST shows peak energy at 2 - 4 year cycle in 1963-1974. There is moderate co-spectral energy in 1980, 1987-1992, 1996-2001. Common spectral energy in the decadal band is found from 1950 to 1974 (fig 5.5 b). SST is seen to lead GPH by 10-15 months before 1962. However, the GPH signal leads southeast Indian Ocean SST by an average of 5 months after 1962 with the exception of 1978 - 1981 and 1987 - 1992 (5.5 c).

5.6.2 Association between South America OLR and SST South Eastern Indian Ocean

SST in the southeast Indian Ocean shows greater amplitude than the South America OLR (5.6 a). The two signals share common spectral energy between 1965 - 1977 and 1995 - 2001 in the 2 to 3 year band (5.6 b). Moderate spectral energy is found between 1984-1995 in the 4 year band. Some spectral energy is also observed in higher frequency cycles from 1950-1982. Most of the time the South America OLR leads the southeast Indian Ocean SST by an average of 3 months with the exception of the years between 1990-1995 (5.6 c).

5.7 Monthly Stability and Predictability of Model Predictors

The results of studying the stability of the model predictors at inter-annual time scale concluded that the model have a reasonably stable relationship although there are a few occasions where the phase changes. This section will examine the monthly stability and predictability of the leading model predictors (GPH southeast Pacific, SST southeast Indian Ocean, OLR South America).

Firstly, the result shows stability in the above predictors prior to the cyclone season (fig 5.7). Secondly, the leading predictor displays increasing predictability in the months of SON depicted by the increasing difference between high and low TC composites (0.3 in September to 2.0 in November fig 5.7 a). The southeast Indian Ocean SST and South America (Amazon) OLR also confirm their high predictability in these similar months (fig 5.7 b, c).

5.8 Geopotential Height Wave Three Pattern, Subtropical Jet Stream, And Wind Shear Modulation

From earlier results a strong association was found between geopotential height in the southeast Pacific and intense TC in the SWIO. This high latitude association deserves a detailed examination. How is the high latitude GPH related to the variability in TC? The low GPH center in the southeast Pacific progresses to the south western Atlantic from June-Nov months to Dec-March months.

The dependence of TC with the southeast Pacific GPH suggests links with the Antarctic Circumpolar wave (ACW). The influence of ACW variability on climate lies in its unique ability to transport oceanic anomalies into the three major ocean basins – Pacific, Atlantic, and Indian, by the Atlantic circumpolar current. Recent research by Venegas (2003) has found the zonal wave 3 has a period of around 3.3 years across the southern ocean involving self-sustaining fluctuations and driven by coupled air-sea interactions in which the atmosphere and the ocean interactively force each other. In contrast, the zonal wave number-2 signal has a period of around 5 years and has a signature mainly in the eastern Pacific sector. It is linked by the forcing of tropical ENSO phenomena and is a manifestation of a larger-scale pattern. The ENSO periodicity seems to set the time scale of this oscillation. The tele connection between ENSO and the south eastern Pacific has been suggested to occur via the Pacific-South American (PSA) pattern (Cai and Baines 2001), the Southern Hemisphere counterpart of the Pacific-North American pattern (Karoly, 1989). Latent heat release associated with ENSO-related anomalous precipitation in the Equatorial Pacific triggers the PNA and PSA. It was first suggested by Peterson and White (1998) that the ENSO signal is transmitted through the troposphere into the ocean in the subtropics to the high latitudes, where it becomes a source of the ACW.

5.9 GPH Pattern In The Indian Ocean

Figure 5.8 (a) is a close up illustration of the zonal wave three pattern in GPH and its effect on the Indian Ocean in December-March months for high minus low TC days. Negative GPH anomalies occur in the subtropics (15-40°S) and positive GPH anomalies occur further south in the mid latitude at 50°S. The GPH pattern suggests a bifurcation of polar front jet and subtropical jet. The implications of the bifurcation will be elaborated in the discussion section of chapter 8.

5.10 Zonal Wind Variability In The Indian Ocean

The climatological mean of zonal wind with height-latitude consist of strong westerlies between 18-50° S at most levels in figure 5.8 (b). Peak westerlies are located at 250-300 hPa at 45° south.

However, in the difference in field for high and low TC days in figure 5.8(c) westerly winds are reduced in the latitudes 35-50°S and enhanced between 55-75°S. A core of westerly wind anomalies are observed between 25-35°S over southern Africa. This pattern confirms the bifurcation of the jet stream into the STJ overlying southern Africa and polewards retreat of the PFJ.

5.11 Relationship Between TC And Fishery Resources In SWIO

The relationship between TC and climate regimes in other basins has been studied. Nutrient enrichment is due to many factors such as entrainment by upwelling and wind mixing by monsoons and TC. The North Australian Large Marine Ecosystem (LME) is an example where the continental shelf and coastal marine ecosystem is influenced by TCs. The rainfall that accompanies cyclonic weather systems can be a significant source of freshwater to the region influencing temperature and salinity. Cyclones are driven by strong winds, and the nutrient levels in sea water are controlled by wind-driven upwelling. *Upwelling and a shallower thermocline is often associated with good fish catch*

Figure 5.9 (a) shows the total fish catch for Mauritius and Madagascar and TC days index from 1960 to 1998. Figure 5.9 (b) represents Seychelles and East S Africa fish catch. The Mauritius fish catch shows downward fish catch trend in the period between 1960-1980, 1990-1998 and increased fish catch in the 1980-1990. The Madagascar fish catch also follows similar trend but the main difference is there was increased fish catch in the period between 1960 -1970. The Seychelles fish catch increased in the period 1970-1980 and 1990-1998 while decreased in the period between 1980-1990. The east South African fish catch is characterized by large positive and negative fluctuations. There was decreased fish catch from 1964-1972, 1984-1994 and increased catch between 1972-1984 and 1994-1998. The temporal variability characteristics would be interesting to investigate in its own right, however in this study only the link between fishery resources and TC days is of interest.

Statistical correlation analysis suggests fish catch is inversely correlated with TC days. Seychelles is showing a negative correlation of -0.28. There is a decrease in fish catch when TC days are high. Eastern South Africa exhibits a significant correlation before, during and after. Highest negative correlation occurs during the season (T-0) with a value of - 0.35 (table 5.3). This suggests that fish catch also decreases/increases for eastern South Africa when there is an increase/decrease in intense TC in the southwestern Indian Ocean basin.

5.12 Relationship Between Related TC variables and Fish Resources in SWIO

The fish catch for Madagascar and Mauritius is merged into a single time series index based on their related association (r =+0.57). E.S. Africa and Seychelles fish catch time series indices are also correlated with the ocean-climate variables. Table 5.4 shows the results. Mauritius and Madagascar fish catch are significantly positively related with the September to November 50 m sub-surface temperatue in the east IO.

The Seychelles fish catch shows positive relationship of around +0.43 with the SST in southwest Indian Ocean in September to November season. The HCA in the North West Indian Ocean has a negative correlation of -0.4 with the Seychelles fish catch. The East South African fish catch is showing some different association compared to the SWIO islands. The GPH in the south east Pacific exhibits a peak correlation of +0.41 in September to November months with the east South African fish catch. Other variables showing significant association with E.S Africa fish catch is Nino 3 SST, North Atlantic Oscillation and low level winds in the equatorial Atlantic Ocean. It is again observed that the HCA in northwest Indian Ocean is related with the E.S. African fish catch.

5.13 Summary

In this chapter the forward stepwise regression method was used to develop multivariate statistical models to predict TC days in the SWIO at various time lags before peak TC season. The models hindcast fit at 3, 6 and 9 months lead time are 48 %, 38 % and 33 % respectively. The new predictors have significantly improved the seasonal prediction of TC in the SWIO. The new predictors are the southeast Pacific geopotential height, SST in the southeastern Indian Ocean and the OLR over South America. Cross- validation was applied to test model reliability by removing the first and last decade of data. The results shows high level of performance in these prediction experiments with 90 % and 70 % tercile hit rates for the first and last decade. The southeast Pacific GPH has a dominant 2-3 cycle and weaker variability at 5 and 10 years. The Amazon OLR predictor shows 2-3 and 10 year cycles. The south East Indian Ocean has 3-4, and 6 year cycle and is associated with the coupled transient Rossby wave of the IO. The Cross Wavelet modulus spectral analysis reveals the south east Pacific GPH leading the eastern Pacific SST by around 5 months. However, the eastern Pacific leads the Amazon OLR. The South East Indian Ocean SST lags the predictors in the Pacific region, but on few occasions the Indian Ocean SST leads. The coupling between predictors is stronger during ENSO years. The inter-annual phase lag analysis has shown that stability is not always guaranteed. The monthly analysis of individual predictors (GPH, SST, and OLR) for high and low TC days for the JAS and SON model suggests a phase-locking of predictability with respect to the seasonal cycle.

The results indicate an anti-phase association between South America and the east Indian Ocean particularly during ENSO years. Low convection over Amason is associated with increased TC days in SWIO and vice versa.

The propagation of the zonal wave three pattern in GPH helps determines the downstream oscillation of the subtropical jet stream in the SWIO. A shift in the sub-tropical jet stream polewards reduces westerly wind shear locally such that there is an increase in TC days.

The coastal fish resources of the countries are negatively associated with the TC days in the SWIO. An increase in TC days implies decrease fish catch. Statistical analysis shows that the Mauritius and Madagascar fish resources are significantly influenced by sub-surface temperatures in the east IO. The Seychelles fish catch is also dependent on SST in the SWIO and HCA in the northwest IO. Southeast Pacific GPH in Sep-Nov months is significantly related with the S.E. African fish catch with peak correlation of +0.41.

The forthcoming chapter examines the daily evolution of circulation around intense tropical cyclones distinguished by track. Important kinematic and thermodynamic differences are considered for operational forecasting and impact evaluation in the SWIO.

Table a	Potential Predictors and Location	Abbreviations	(MJJ) CCoeff
1	Geopotentiall Height up to 300mb (Southern Pacific)	**SSTsp**	-0.243
2	OLR(South America)	**OLRsa**	0.304
3	Surface Specific Humidity (South America)	**SHsa1**	-0.261
4	700mb Zonal Wind (Equatorial Atlantic+ Equatorial Indian Ocean)	**Ueaoio7**	0.256
5	700 mb Zonal Wind (South East Indian Ocean)	**Useio7**	-0.28
6	600mb Specific Humidity (Equatorial Atlantic +Equatorial West Indian Ocean)	**Sheaowio6**	0.273
7	Sahel Rainfall	**SHrf**	0.390
8	South America Velocity Potential (300-100 Average)	**Vpsa31**	0.264
9	50 m sub-surface Temperature (west Indian Ocean)	**T50wio**	-0.247

Table 5.1: Pair Wise Correlation of the TC index with the Potential Predictors for the (a) MJJ months

Table b	Potential Predictors and Location	Abbreviations	(JAS) CCoeff
1	SST (Eastern Pacific Ocean)	**SSTep**	-0.273
2	Geopotentiall Height up to 300mb (Southern Pacific)	**GPHsp**	-0.236
3	OLR(South America)	**OLRsa**	0.407
4	Surface Specific Humidity (South America)	**Shsa1**	-0.39
5	SST South East Pacific	**SSTsp**	-0.273
6	200mb Zonal Wind (Equatorial Atlantic+ Equatorial Indian Ocean)	**Ueaoio2**	-0.265
7	700 mb Zonal Wind (South East Indian Ocean)	**Useio7**	-0.448
8	600mb Specific Humidity (Equatorial Atlantic +Equatorial West Indian Ocean)	**Sheaowio6**	0.262
9	Sahel Rainfall	**SHrf**	0.381
10	SST(Equatorial South East Indian Ocean)	**SSTseio**	0.237
11	100 m sub-surface Temperature (East Indian Ocean)	**T100eio**	0.283
12	Pacific Decadal Oscillation	**PDO**	-0.289
13	South America Velocity Potential	**Vpsa31**	0.329

Table 5.1: Pair wise correlation of the TC days index with the potential predictors for the (b) JAS months

Table c	Potential Predictors and Location	Abbreviations	(SON) CCoeff
1	SST (Eastern Pacific Ocean)	**SSTep**	-0.296
2	Geopotentiall Height up to 300mb (Southern Pacific)	**GPHsp**	-0.557
3	OLR(South America)	**OLRsa**	0.448
4	Surface Specific Humidity (South America)	**Shsa1**	-0.4
5	*700mb Zonal Wind (Equatorial Atlantic+ Equatorial Indian Ocean)*	**Ueaoio7**	0.334
6	200mb Zonal Wind (Equatorial Atlantic+ Equatorial Indian Ocean)	**Ueaoio2**	-0.289
7	*700 mb Zonal Wind (South East Indian Ocean)*	***Useio7***	-0.278
8	600mb Specific Humidity (Equatorial Atlantic +Equatorial West Indian Ocean)	**Sheaowio6**	0.319
9	SST(Equatorial South east Indian Ocean)	**SSTseio**	0.247
10	100 m depth integrated Heat Content (North west Indian Ocean)	**HCAnwio125**	-0.269
11	North Atlantic Osillation	**NAO**	0.285
12	Quazi Bienal Osillation(30mb)	**QBO30**	-0.219
13	South America Velocity Potential	**Vpsa31**	0.438

Table 5.1: Pair wise correlation of TC days index with the Potential Predictors for the (c) SON months.

Time Lag	Model Algorithm	Statistical Test
MJJ	**TC Days = $-0.29*(\text{Useio}_7)$ + 0.39*(SHsaoio) +0.46* (SHRf)**	R^2 = 34% DW= 2.4
JAS	**TC Days = 0.52*(OLRsa) +0.39*(SSTseio) - 0.38*(SSTep)**	R^2 =38% DW=2.034
SON	**TC Days = -0.65*(GPHsp) + 0.39*(SSTseio) -0.27*QBO** **'Non-Tropical Model'**	R^2 = 48% DW= 1.64
	TC Days =-0.53*(OLRsa) +0.38*SSTseio -0.37*HCAnwio **'Tropical Model'**	R^2 = 38% DW=1.834

Table 5.2: Statistical multivariate linear models for the MJJ, JAS and SON months (Max 3 predictors with threshold colinearity $\leq$23%).DW: Durbin-Watson Statistics.

Fig a

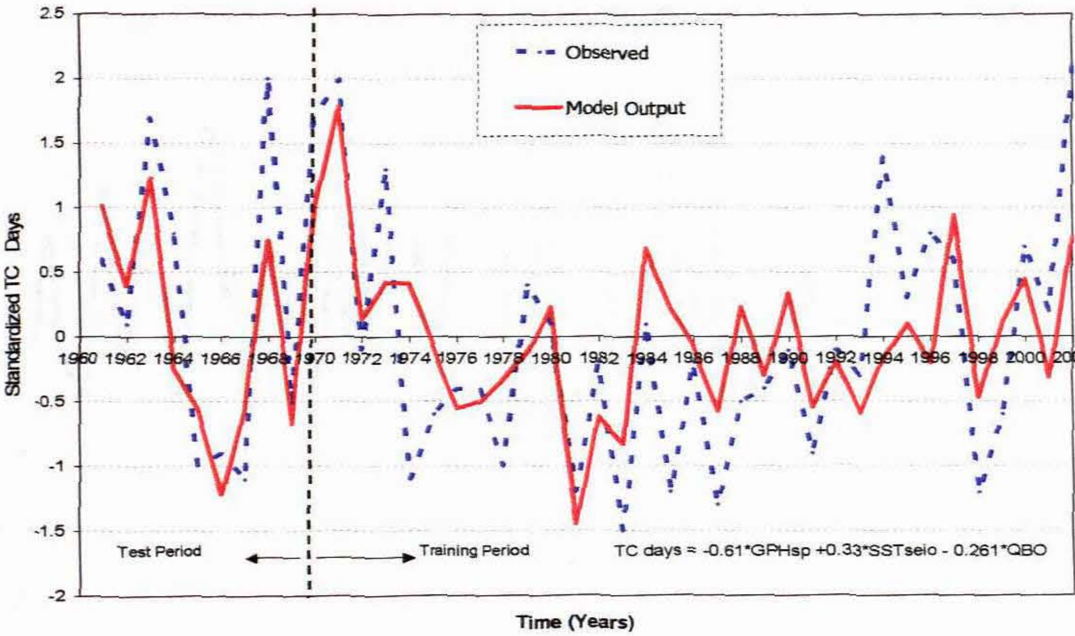

Fig b

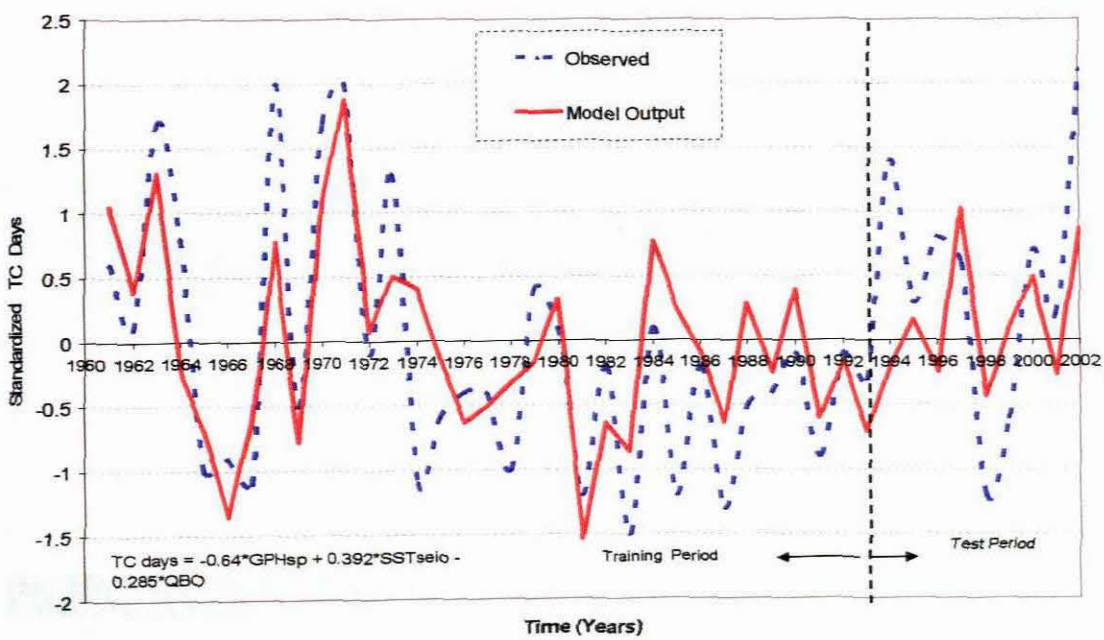

Fig 5.1: Non-Tropical Model (SON) (a) Test period first 10 Years (b) Test period last 10 Years: **Validation of TC days.**

Fig a

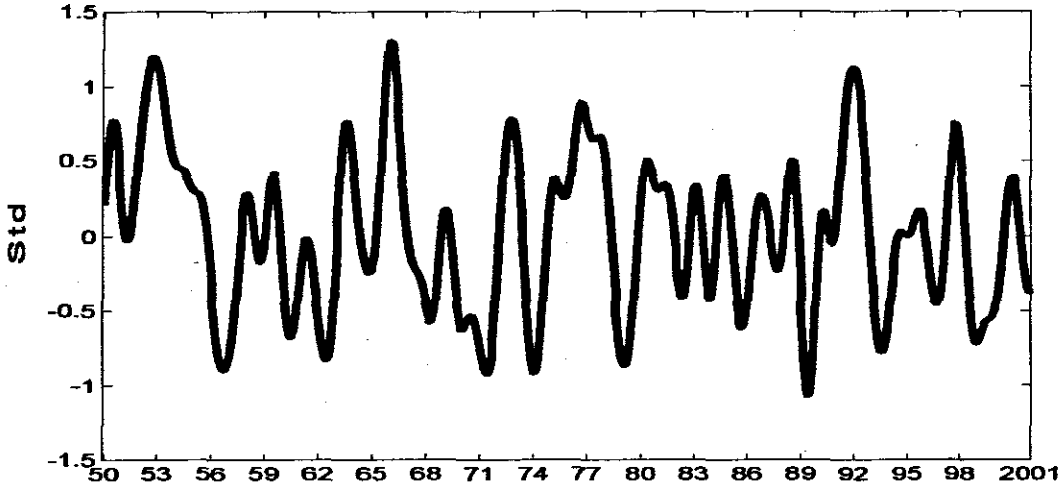

Fig b

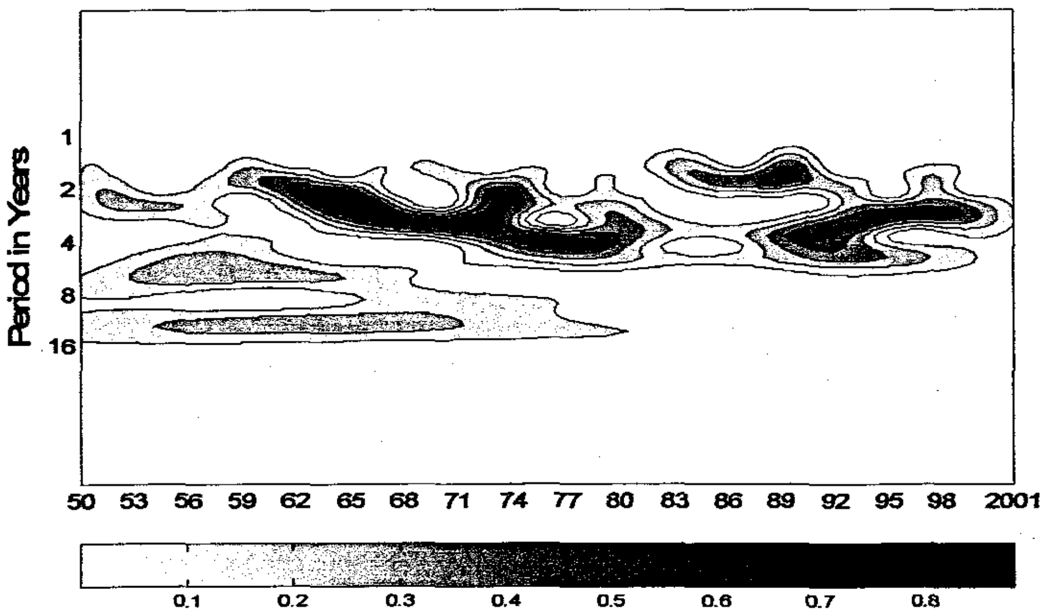

Fig 5.2: (a) GPH South East Pacific Ocean and (b) Wavelet Spectral Modulus (Low Band pass filter 1.5 - 16 Yrs):
Temporal Variability of Predictors

Fig a

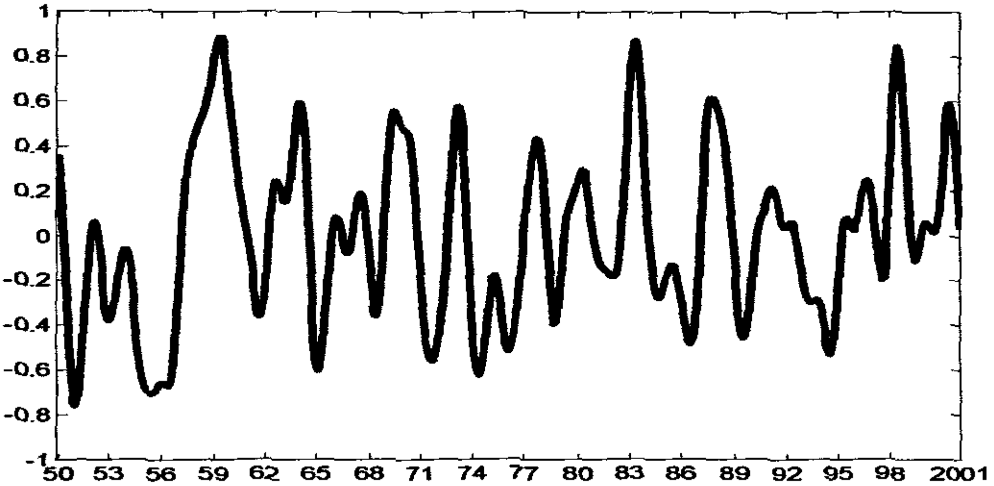

Fig b

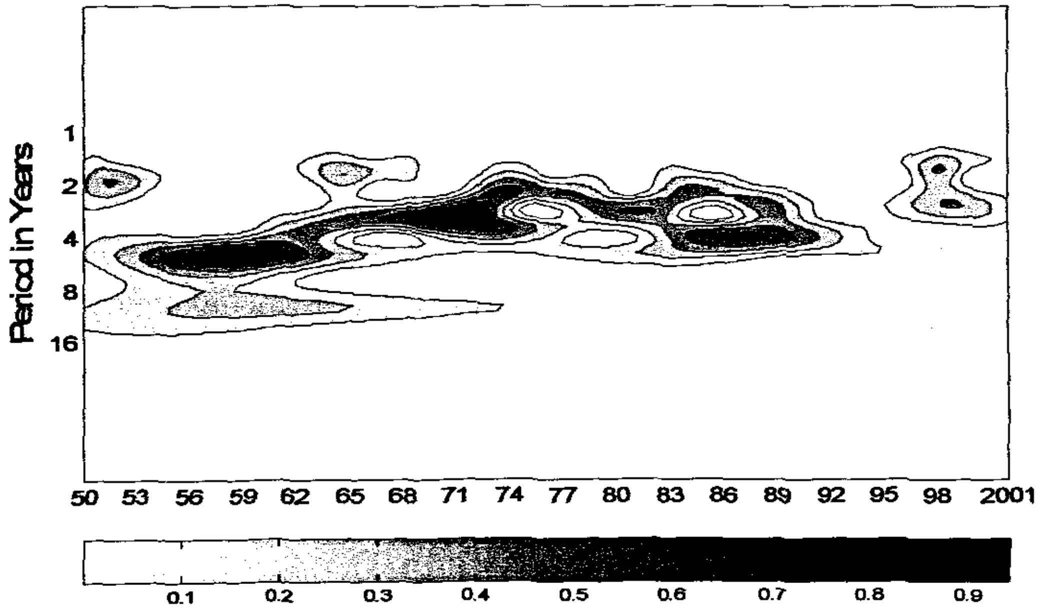

Fig 5.3: (a) SST South East Indian Ocean and (b) Wavelet Spectral Modulus (Low Band Pass filter 1.5 - 16 Yrs):

Temporal Variability of Predictors

Fig a

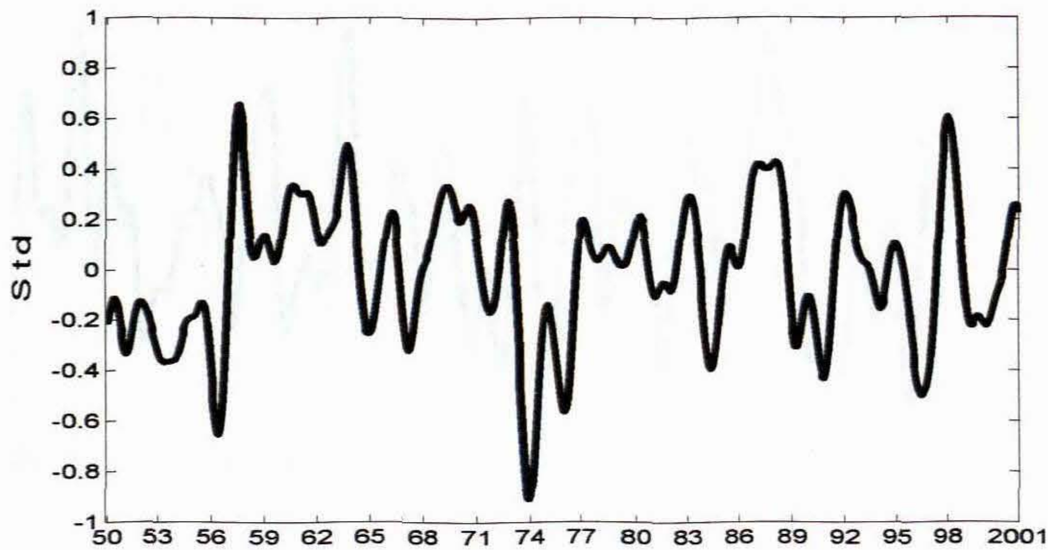

Fig b

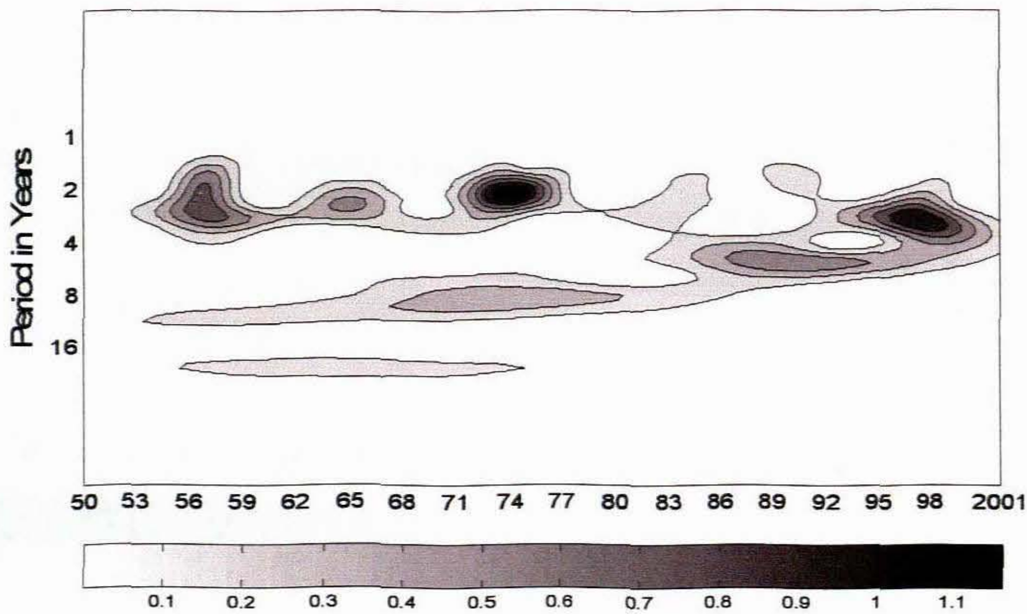

Fig 5.4: (a) OLR South America (Amazon) and (b) Wavelet Spectral Modulus
(Low band filter 1.5 - 16 Yrs):
Temporal Variability of Predictors

(a) South East Pacific Ocean Geopotential Height (Bold Line) and SST SEIO

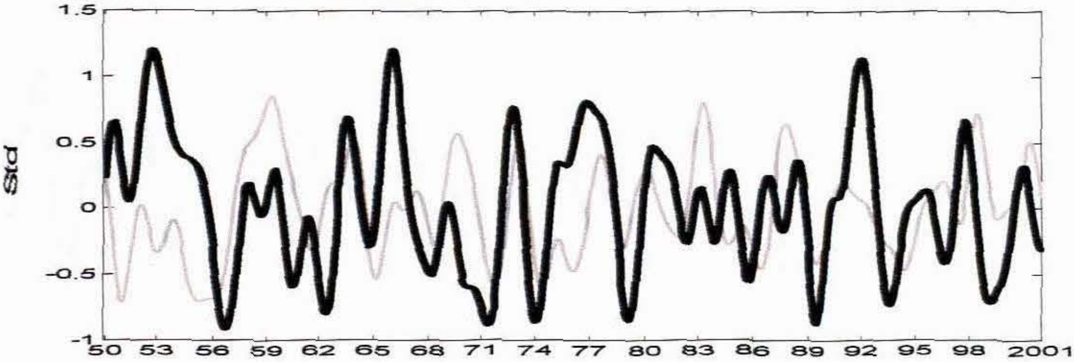

(b) C-Wavelet Spectral Modulus of South East Pacific GPF and SST (SEIO)

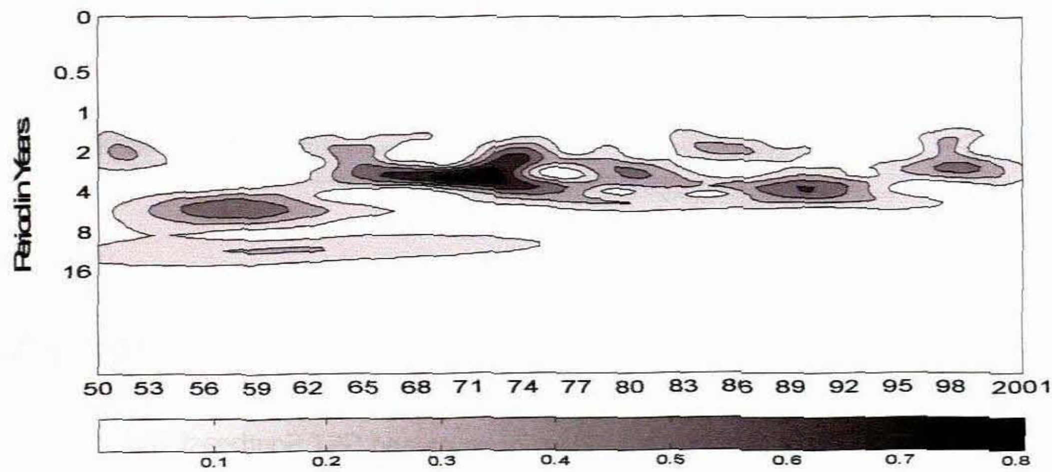

(c) Time delay between GPH south Pacific and SST South East IO

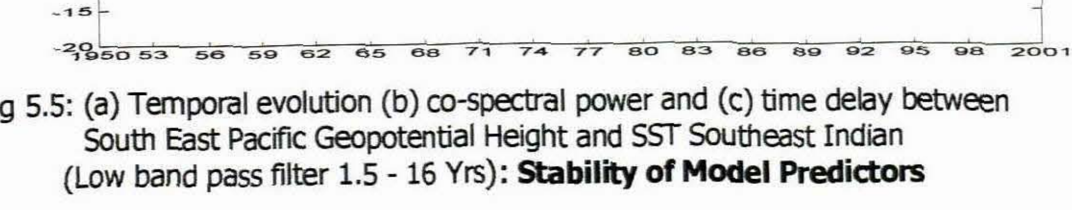

Fig 5.5: (a) Temporal evolution (b) co-spectral power and (c) time delay between South East Pacific Geopotential Height and SST Southeast Indian (Low band pass filter 1.5 - 16 Yrs): **Stability of Model Predictors**

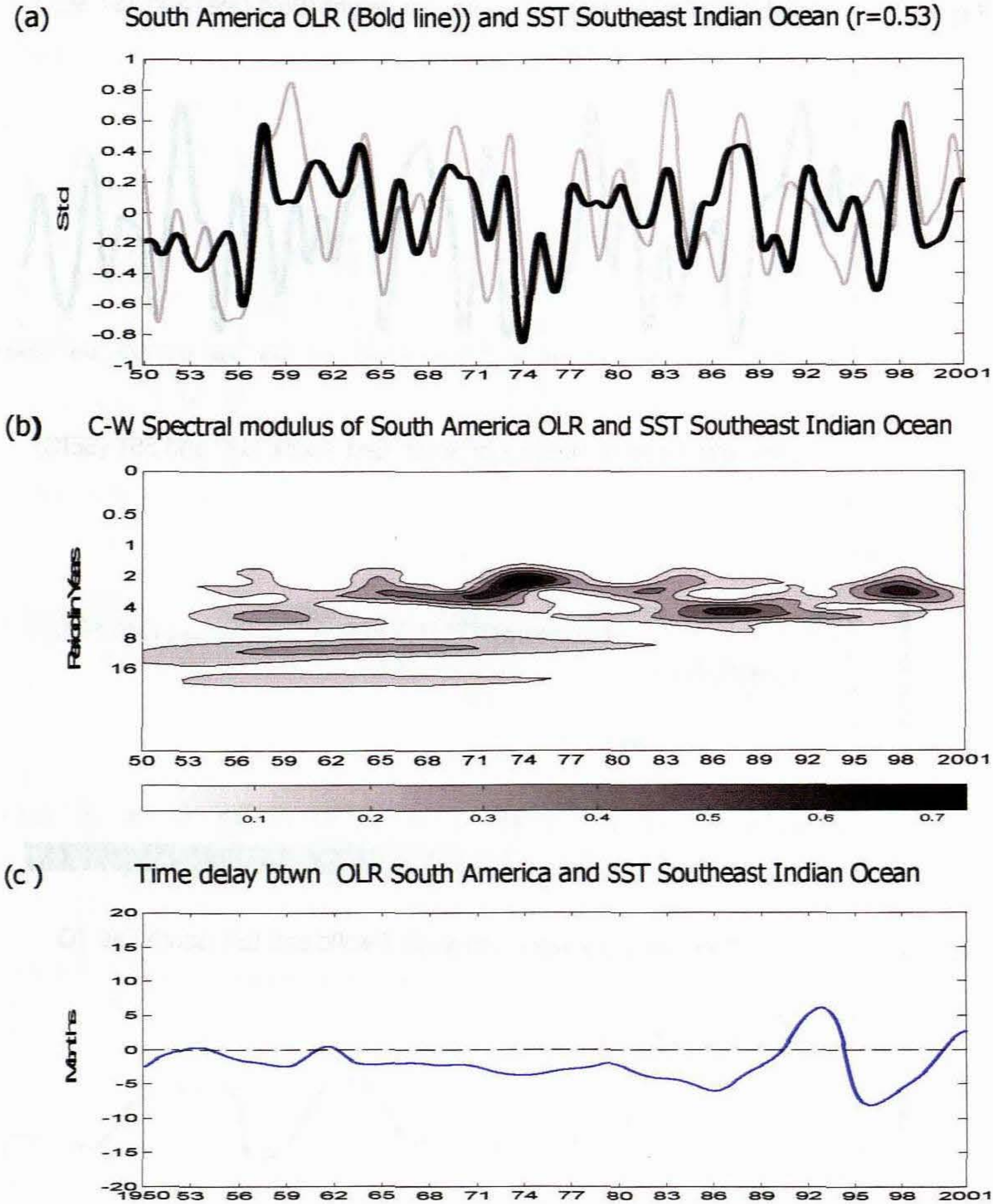

Fig 5.6:(a)Temporal evolution (b)co-spectral power and (c) time delay between OLR South America and SST Southeast Indian Ocean (Low band pass filter 1.5- 16 Yrs): **Stability of Model Predictors**

Fig a

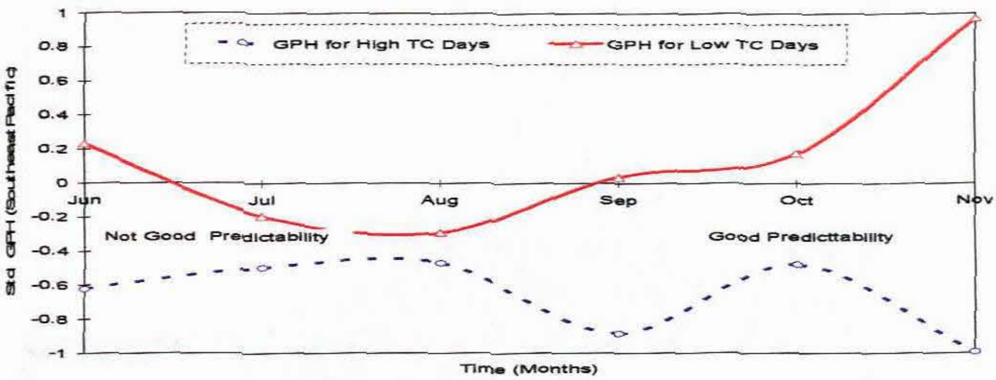

Fig b

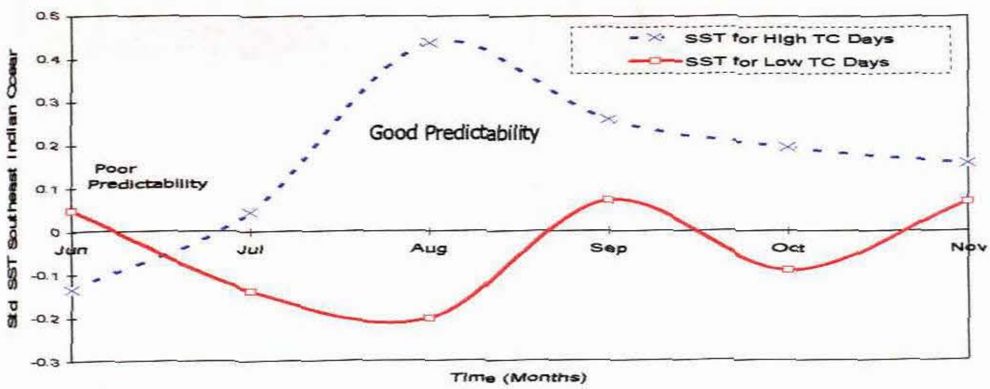

Fig c

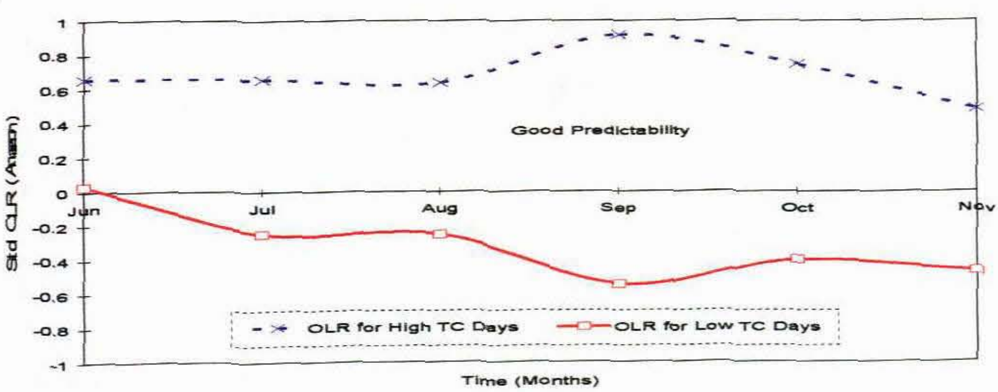

Fig 5.7: Monthly stability and predictability of leading JAS and SON model predictors for high and low TC Days (a) GPH South East Pacific Ocean (b) SST Southeast Indian Ocean (c) OLR over Amazon

Fig a

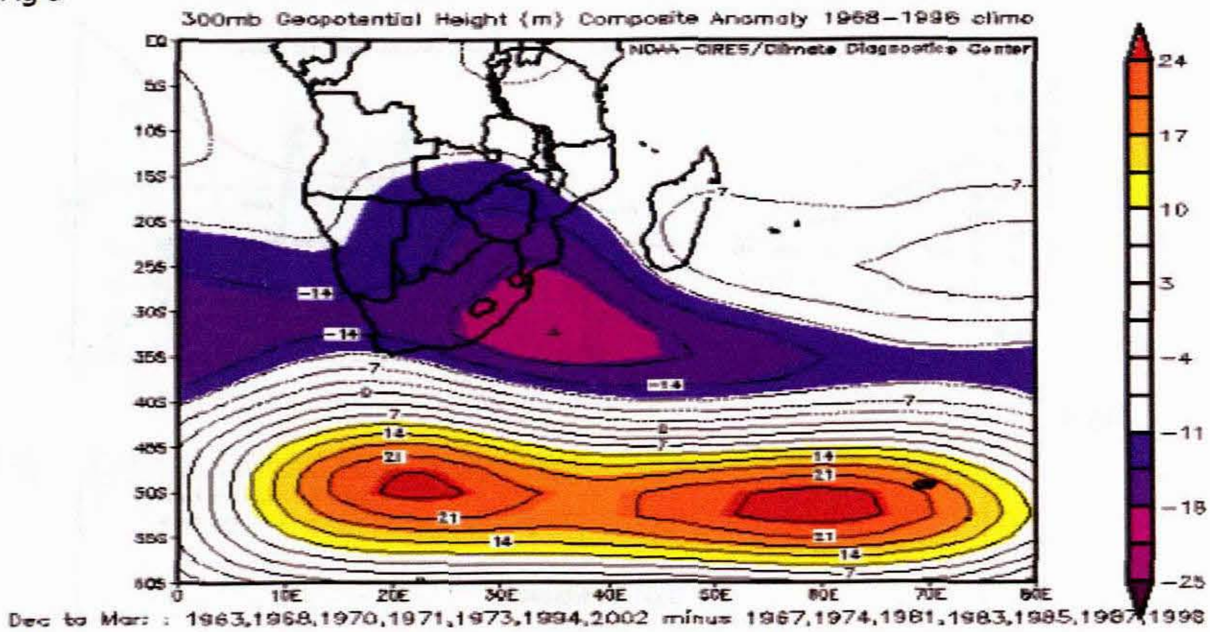

Fig 5.8: High - Low TC Days of (a) GPH (300 hPa) anomaly

Fig b

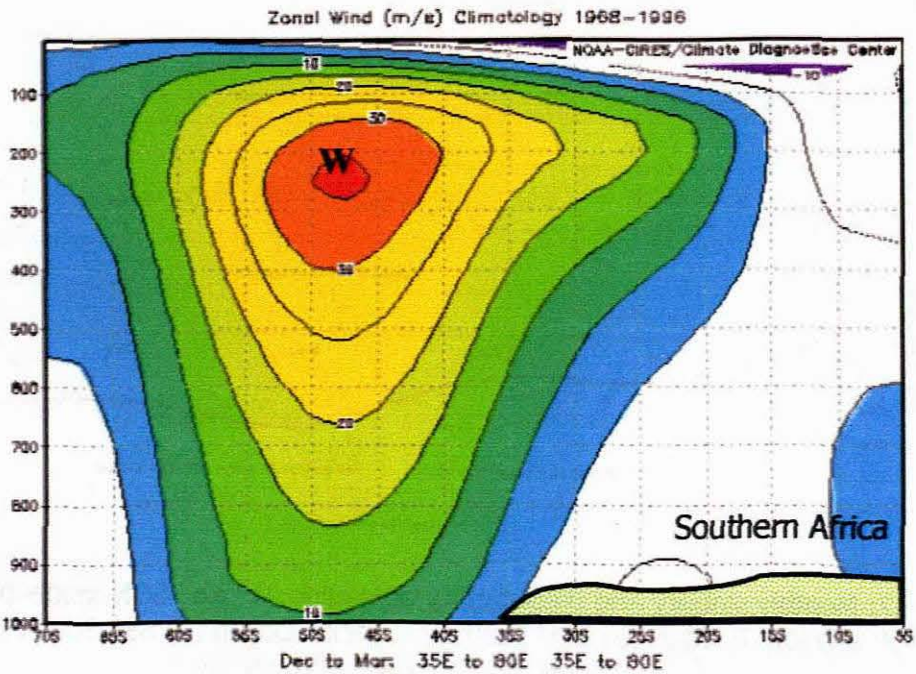

Fig 5.8: Height-Latitude cross-section of zonal wind for (b) climatology

Fig c

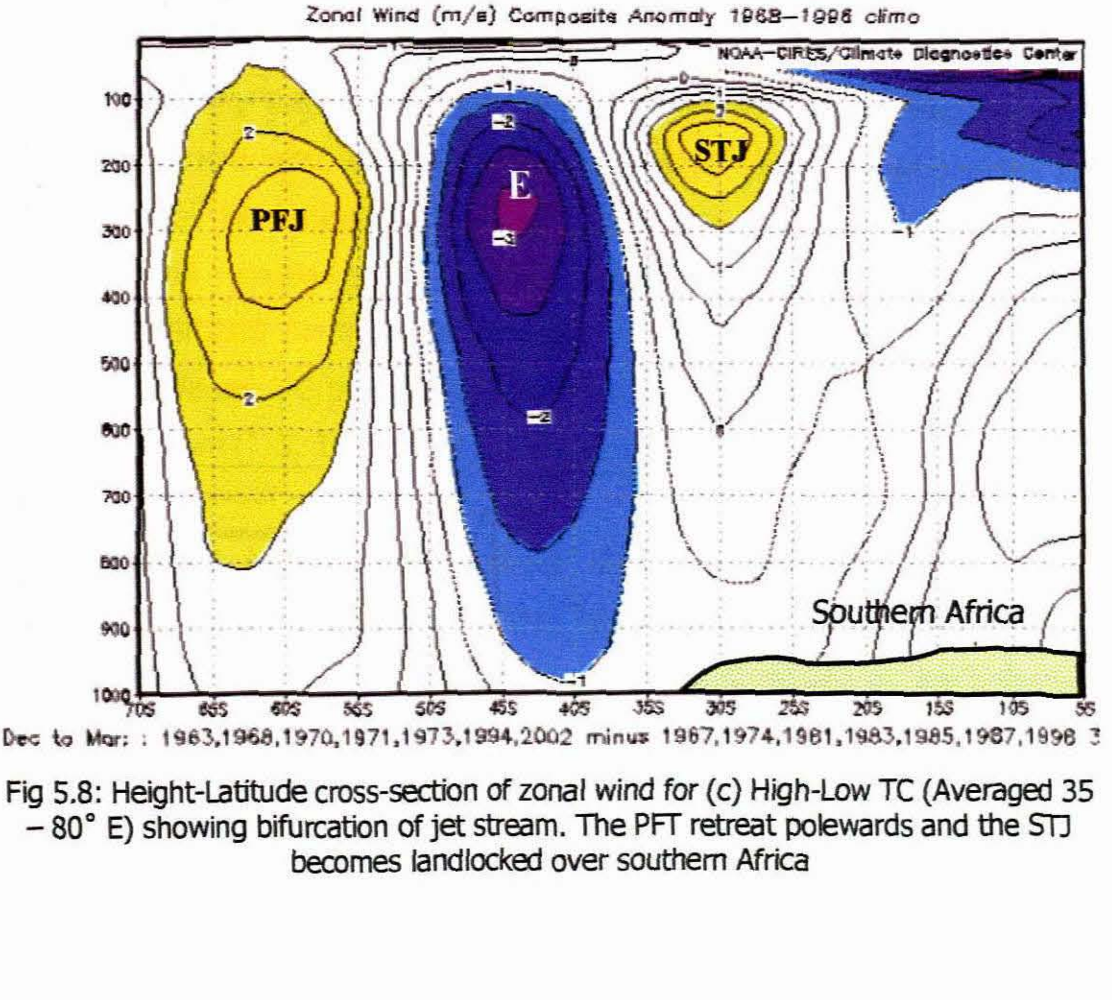

Fig 5.8: Height-Latitude cross-section of zonal wind for (c) High-Low TC (Averaged 35 – 80° E) showing bifurcation of jet stream. The PFT retreat polewards and the STJ becomes landlocked over southern Africa

Fig a

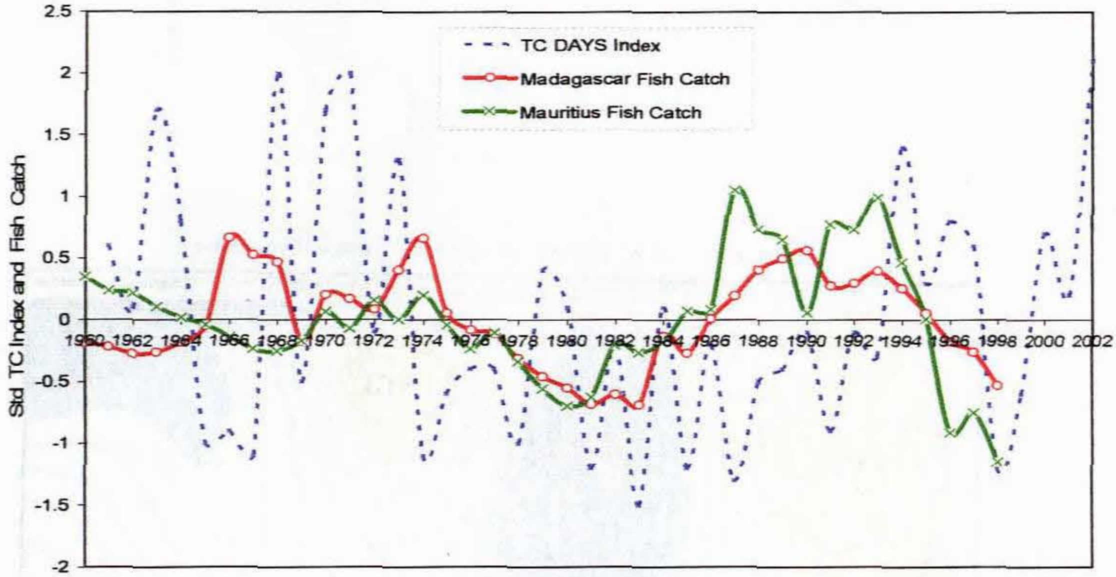

Fig b

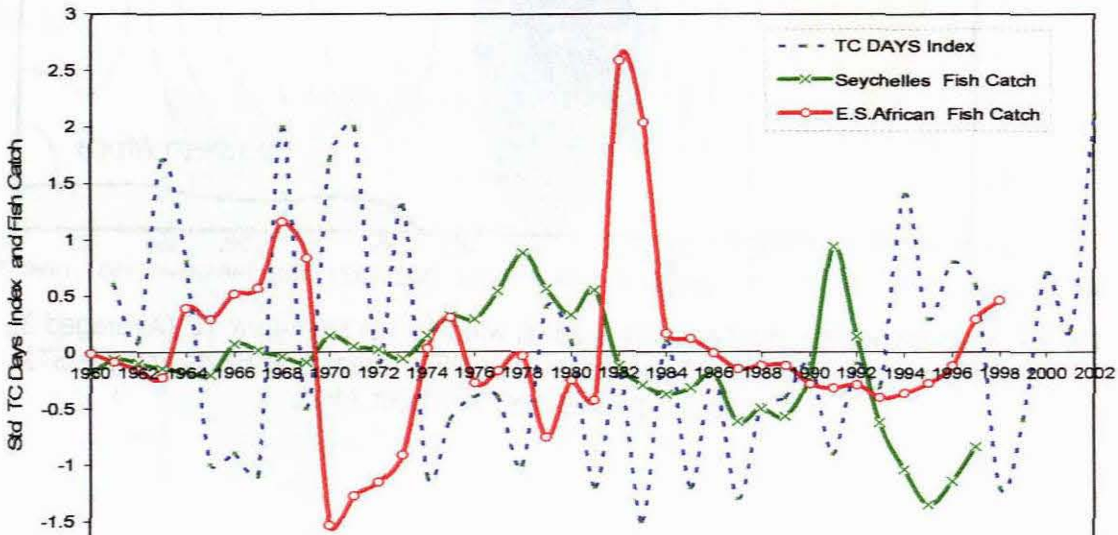

Fig 5.9: Detrended fish catch (polynomial of degree 2) for (a) Mauritius, Madagascar and (b) Seychelles and E.S Africa

Chapter 6

Evolution of The Circulation For Intense Tropical Cyclones Distinguished by Track

6.1.0 Introduction

The composite structure and evolution of the circulation associated with intense TC with different trajectories is analyzed using the NCEP daily data. Cyclones are grouped into west, southwest and southward trajectories around the time of maximum intensity. The TC composites are constructed to study the structure and evolution of the circulation surrounding the cyclones between T-4 to T+2 around the maximum intensity at T- 0 and contrasts are made between different TC trajectories. In most cases the T-4, T-1, T-0 and T+2 days are shown (T-3, T-2 and T+1 are omitted in the presentations).

Only the most important atmospheric fields are presented and discussed although a number of other fields have been analyzed. Detailed data analysis and presentation is done for southwest-moving TC where as the west and southward-moving TC only few graphs are presented. Table 6.1, 6.2 and 6.3 shows the name of cyclones, date and mean position of westward, southwestward and southward-moving TC. It is recalled that TCs were selected on the criteria that they are relatively co-located with the eye not more than 400 km from a central point at maximum intensity (T- 0). Cyclones should also reach peak intensity before 20° latitude. In addition the day of maximum intensity T- 0 is the day the cyclone reaches maximum surface wind speed following official declaration of TC strength with the eye visible from satellite imagery coupled with sustained wind speed of greater than 45 m s^{-1}.

Name	Date	T-4	T- 0	T+2
Hudah	Mar-Apr 2000	29 (16.1 S,73.5 E)	2 (16.1 S,54.1 E)	4 (14.9 S,44.4 E)
Nadia	Mar 1994	18 (12.2 S, 68.8 E)	22 (12.8 S,55.4 E)	24 (14.6 S, 43.2 E)
Kamisy	Apr 1984	5 Nill	8 (13.2 S,55 E)	10 (13.1 S, 47 E)
Andre	Dec 1983	5 (10.4 S,65.2 E)	9 (11S,52.6 E)	11 (13.2 S, 46.4 E)
Blanche	Feb 1969	7 (7 S,76 E)	11 (10.8 S,58.5 E)	13 (10 S, 49 E)

Table 6.1: Dates, and mean centre of westward-moving TCs

Name	Date	T-4	T- 0	T+2
Dina	Jan 2002	15 Nill	20 (18 S,64.1E)	22 (19.6 S, 56.7 E)
Bonita	Jan 1996	4 (12.8 S,70.6 E)	8 (18.1 S,56.6E)	10 (17.8 S, 50.3 E)
Geralda	Dec-Jan 1994	27 (13 S,68.6 E)	31 (14.9 S,55.5 E)	2 (18.4 S,48.4 E)
Hollanda	Feb 1994	6 (11.3 S,69.6 E)	10 (20 S,57.6 E)	12 (27.2 S,53.1 E)
Edwina	Jan 1993	22 (13.4 S,78.7E)	26 (16.7 S,63.3 E)	28 (24.8 S,59.6 E)
Firenga	Jan 1989	25 (11.7 S,64.3E)	29 (19.8 S,56.8 E)	31 (24.7 S,51.8 E)
Erinesta	Jan - Feb 1986	31 (12 S, 63.3 E)	4 (15.5 S,54.5 E)	6 (18.6 S, 52.5 E)
Honorinina	Mar 1986	9 (13 S,72.7 E)	13 (15.9 S,56.3 E)	15 (17.7 S, 51 E)

Table 6.2: Dates, and mean centre of Southwestward-moving TCs

Name	Date	T-4	T - 0	T+2
Gerry	Feb 2003	9 (13.5 S,54.7 E)	13 (19.4 S,58.5 E)	15 (28 S,67 E)
Crystal	Dec 2002	23 (12.1 S,65.8 E)	27 (18.5 S,59.8 E)	29 (27.7 S, 64.4 E)
Anacelle	Feb 1997	7 (12.8 S,63.6 E)	11 (19.7 S,58.9 E)	13 (29 S,64.4 E)
Edisoana	Mar 1989	1 (13.7 S,67.2 E)	5 (18.3 S,61.2 E)	7 (26 S, 62.2 E)
Ariane	Nov 1972	25 Nill	29 (16 S,56 E)	1 (20.9 S,61.5 E)

Table 6.3: Dates, and mean centre of Southward-moving TCs

6.1.1 Daily Composite of Southwestward - Moving TC

6.1.2 Sea Level Pressure

A high pressure anomaly is initially located around 35°S, 70° E. A low pressure anomaly develops in the area 10-15°S, and 65-75°E at T- 4 (fig 6.1). The low pressure anomaly deepens significantly and is centered at 17°S and 60°E at T-1. The southwestward-moving TC displays tight and concentric isobars throughout the sequence from T-1 to T+2. The TC passes just to the northwest of Mauritius and Reunion islands two days after peak intensity at T+2 and *affects the east coast of Madagascar. A high pressure anomaly persists in the* extreme southern SWIO.

6.1.3 Vector Wind at 200 hPa

The vector wind field anomaly shows a weak anti-cyclone south of 30° S and east of 75°E (fig 6.2). East-north-easterly winds dominate the SWIO basin at T-4. A sudden burst of easterlies is observed at 5-10□ S, 75□ E associated with the birth and development of TC at T-4. The anti-cyclonic circulation strengthens at 25-30°S, 55-65°E by T-1. At peak intensity the anti-cyclone generates strong southerly wind anomalies towards the equator on the eastern flank of the composite TC at 70-75°E. The atmospheric structure is maintained even up to two days after peak intensity. Meanwhile, in the northern hemisphere a strong easterly wind anomaly at 200 hPa propagates westward across the Arabian Sea from T- 4 to T+2. After TC peak intensity, the easterly wind anomaly increases over Somalia. The easterly wind anomaly has displaced

2000 km in just six days and represents a retreat of the northern subtropical jet stream.

6.1.4 Cross Section of Zonal wind

There is rapid strengthening of westerly wind anomaly to the immediate south of the equator between 0-15° S latitude one day before peak intensity (T-1) from surface to 200 hPa (fig 6.3 a, b). A strong easterly wind anomaly is confirmed between the middle and upper level. The easterly wind anomaly extends at upper levels into the southern subtropical region at 20° S.

6.1.5 Velocity Potential Field

The upper velocity potential field shows a marked negative anomaly over south India at T-4 (fig 6.4). The negative velocity potential extends southwards and dominates the central Indian Ocean. At T-1 the velocity potential field forms an organized circulation with a center just to the northeast of the Seychelles. At peak intensity the velocity potential center displaces slightly northwest of the equator at 5 - 10°N, 55 - 60°E. After peak intensity the negative velocity potential circulation splits into two with one center in the north and another in the south. The temporal displacement and spatial pattern of the velocity potential field is in phase with the propagation of the easterly wind anomaly over Arabian Sea and the TC in the SWIO.

6.1.6 Omega Field

The omega field for southwestward moving TC shows descending motion at 25°S and 15° N from surface to 200 hPa. Ascending motion is centered at 5°S four days before peak intensity (fig 6.5 a, b). As the TC moves southwestward the ascending motion shifts southwards to 15-20°S at T-1. At this time the descending motion is reduced in the north but increases in the subtropical region. At peak intensity there is descending motion from the equator to 8°S, while the descending limb in the southern subtropical region has weakened considerably from T-4 to T+2. Two days after peak intensity the ascending motion is broader and centered at 20°S. The vertical rising motion associated with the composite TC shifts polewards a few degrees per day.

6.1.7 Wind Field and CMAP Precipitation Rate

Figure 6.6 (a) shows strong westerly winds converging into the cyclonic center between latitudes 5-10° S and equally strong easterly flow between 18-20° S at T-2 and T-1. The westerly wind anomaly gradually veers to northwesterly north of 10° N at T+1 as the cyclone moves south west (fig 6.6 b). The TC maintains strong cyclonic circulation even at T+2. The precipitation rate anomaly displays a symmetrical rain band around the TC center between 5-12° S, 50-65° E and 12°-18°S, 60-80° E. The maximum precipitation ($kgm^{-2}s^{-1}$) in both bands is located behind the region of maximum converging zonal winds. The northern rain band undergoes a 45 degree rotation in 72 hours from T-2 to T+1. The southern rain band does not change significantly during the sequence. As the cyclone intensifies the rain band contracts and becomes more convectively active. There is excess rainfall over Seychelles before TC peak intensity and deficit rainfall over Africa during and after peak cyclone intensity.

Figures (6.7 a, b) and (6.8 a, b) are 1000 hPa wind field and CMAP precipitable rate ($kgm^{-2}s^{-1}$) anomalies for south and westward-moving TCs respectively for illustrating spatial and temporal characteristics and impacts around peak intensity.

6.2 Discussion of Differences In Structure Dependent on Trajectory

In this section the differences in thermodynamic and kinematic structure for west, southwest and southward-moving TC are discussed.

In the case of southwestward-moving TC a high pressure anomaly shifts south eastward at the surface. In the upper troposphere the winds shift gradually from east to NNE. This is the main reason for the cyclone to move southwestward especially after peak intensity. Most important and remarkable feature associated with the southwestward TC composite is the development and propagation of a core of pronounced easterly wind anomaly over the Arabian Sea linked with the northern subtropical jet stream. Sadler (1976), Holland and Merrill (1984), Kaplan, (1987), Molinari and Vollaro (1990) found interactions between TC and upper tropospheric troughs, but from the same hemisphere. The SW-moving TC maintains its intensity almost throughout the sequence due to enhanced kinematic and thermodynamic processes. The symmetrical rain band around the center prior to peak intensity is a remarkable observation. Internal forces have been investigated by a couple of researchers such as Barnes et al (1983) where they have suggested that rain band affects TC intensity through thermodynamic modification of low-level inflow.

The main causes of a westward trajectory are the presence of a strong persistent anticyclone in the central SWIO causing mid-level easterlies in a core region between 10 - 20°S, 35–65°E. These results are consistent with similar findings by the following researchers (Beven, 1993; Elsberry, 1993; Naerra and Jury, 1997; Parker and Jury 1999). With landfall over Madagascar, winds are forced upwards and precipitation increases in agreement with Nassor and Jury (1997). Excess rainfall is observed over Seychelles one to two days before peak TC intensity (T-2) while dry conditions prevail thereafter (fig 6.7). Dry conditions are observed over Africa. The westward-moving TC suffers from a lack of NW monsoon inflow intensity due to the blockage by Madagascar highlands.

The *southward-moving* TC is characterized by rapid change in the kinematic and thermodynamic processes during the sequence. Weakening is caused by cool air advection and increased wind shear anomaly. These findings are consistent with previous work of Jury and Parker (1999). The cyclone experiences rapid evolution in its structure as it moves southeastward. It rapidly drags the core of the maximum rainfall south causing dry conditions near the equatorial region of SWIO from T- 2 to T+1(fig 6.8 a). The southward moving TC does not show prominent rain bands compared to the other tracks. The interesting feature of the southward moving TC is the rapid formation of the Intertropical Convergence Zone (ITCZ) soon after TC peak intensity (fig 6.8 b). The formation of the ITCZ may be the result of rapid kinematic changes soon after the TC starts to re-curve southeastward. The southward-moving TC causes dry conditions (surface divergence) before peak intensity and wet conditions (rapid formation of ITCZ) soon after in the near equatorial SWIO. The other trajectories are characterized by wet conditions before peak intensity and dry conditions after

Figure 6.9 (a) and 6.9 (b) shows the pressure cross-sectional analysis of zonal wind for west and southward moving TC respectively in the SWIO at peak intensity (T-0). Refer to figure 6.3 (b) for Southwestward-moving TC. The westward-moving TC lacks easterly wind anomalies over the Arabian Seas while the southwest and southward-moving TCs are associated with strong easterly wind anomalies there. The main difference between the Southwest and southward-moving TCs is the presence of upper level westerlies in the case of southward-moving TCs. These results suggest possible interaction between the northern subtropical jet stream and the TCs in the SWIO. The northern subtropical jet stream weakens in phase with the movement of the TC in the SWIO. Simultaneously, enhanced equatorial outflow is observed in phase with the weakening of the jet. From the mechanism of Kinetic energy transfer of potentially warm air, driven by latent heat release ascends into the TC. The upward branch moves air polewards in the troposphere where it cools by long-wave radiation and then descends in the subtropical latitudes. The equatorial troposphere maintains the circulation, thus available potential energy is converted to KE. So KE is gained from the Hadley circulation.

An assessment of the vertical motion at 500 hPa by track during the evolution of the TC is computed using a composite system following method for various lags over the TC center. The average stream function is also computed in a grid box to evaluate the inflow in the TC from the northern hemisphere.The result shows that the southward-moving TC has initially greater vertical motion, but declines rapidly compared to the other tracks (fig 6.10). The SW-moving TC has greater vertical motion after peak intensity. The SW-moving TC has greater cyclonic shear compared to the other tracks up to one day after peak intensity while the westward-moving TC is lacking cyclonic shear at T-4 to T-1 (fig 6.11). However, there is a relatively rapid increase in cyclonic shear after T+1 possibly due to the re-curving action of the composite TC in the Mozambique Channel.

The forthcoming chapter focuses on daily marine-weather and TC impacts in the SWIO by comparing direct and indirect methods of observation.

Parameter	West – moving TC	Southwest-moving TC	South-moving TC
SLP	TC develops near 12°S, 73° E. Strong positive SLP anomaly centered near at 25-35° S, 50-80°E from T-4 to T+2. Trough over west Madagascar before T-0 *TC over Modagascar at T- 0*	TC develops near 12°S, 70°E. Anti-cyclone south-east (35° S, 85° E) before T-0. Anticyclone south at 40°S, 30-60° E after T-0 *TC to the NW of Mauritius at T-0*	TC develops near 12° S, 55° E at T-4. Low pressure/trough south of SWIO before T-0. Lack of Anti-cyclone in the basin. TC re-curve SE at T+1
Vector Wind 200hPa	Anti-cyclone fairly stationary near 30°S, 50° E. Easterly to southeasterly wind anomaly around T-0 between 10S-25°S, 40-65° E. Strong southeast wind anomaly at 65°E on the eastern flank of anti-cyclone after T-0. Weak easterly anomaly over Arabia	Anti-cyclone moves from near 27°S, 60° E to 20° S, 60° E *before and after T-0.* Burst of easterlies at 5-10S,75 E signals the birth of TC NE wind between 10-20°S, 50-60°E from T-4 to T+2. Strong Southerly anomaly at 70° E after T-0. Easterly wind anomaly propagates from west Indian to Somali from T-4 to T+2	Anti-cyclone moves from 20°S, 70° E to 23°S, 70°E *before and after T-0.* Strong NW wind anomaly 20 - 30°S, 45-65° E on the southern side of anti-cyclone and eastern side of trough. Deep tilting trough southern Madagascar. Easterly Wind anomaly over Arabia Sea after T-0
Zonal Wind-Latitude Averaged 45-75 E	Weak westerly wind anomaly. Moderate easterly wind anomaly peaking at 200 hPa at 10-25°S	Westerly wind anomaly increasing before T-0 at 5-15°S, 40-60° E peaking at 900 hPa. Peak easterly wind anomaly at *200 hPa extending from 12° N* to 20° S	Westerly anomaly peaking at 850 hPa before T-0. Westerly Wind anomaly increasing at 25-30° S peaking at 200 hPa. Peak easterly wind anomaly at 200 hPa extending from 15° N to 15° S
Air Temperature	Cool air advection from *southern latitude*	Significant warming in the low *levels between 15-20° S*	Significant warming in the low *levels between 15-20° S* before T-0

Table 6. 4: Summary of the Kinematic and thermodynamic differences of TC distinguished by track.

Parameter	Westward –moving TC	Southwestward-moving TC	Southward-moving TC
0.21 Sigma Velocity Potential (VP)	Center of negative VP develops at T-1 north of Mahe (Seychelles) extending southwestward towards Madagascar	Large negative VPI anomaly shifts from south India (5°N, 75°E) to eastern Somali (10°N 55° E) before T-0. VP center north and south of the equator after T-0	Large negative VP similar to SW moving TC but extends South east after T- 0
Omega Field	Descending motion decreasing significantly near 25-30° S. Ascending motion near 10-15° S beforeT-0. Descending motion near 0-8°S after T-0	Ascending motions at 5° S at T-4 shifting to 15° S at T-1 Descending motion at 25° S before T-0. Descending motion decreases at 25° S and increases at 5° S	Ascending motion at 15° S decreasing after T-0 and increasing at 10° S. Descending motion increases between 20-25°S up t0 T-0 Descending motion increasing north of 5°N
Surface Wind	Stationary anti-cyclone near 27°S, 55-70° E. Strong westerly anomaly near 5-10°S, 55-65° E and easterly wind anomaly at 12-20°S, 60-75°E before T-0. Weak W-NW after T-0	Strong westerly wind anomaly 5-10°S, 50-65 E and strong easterly wind anomaly 15-25 °S, 60- 75° E before T-0.	Anti-cyclone at 25°S, 65° E. Strong NW throughout the sequence from 5-15° S, 50-70°E. Strong southerly winds at 55-60° east after T-0 south of 15 °S
Rain Band Precipitation	Moderate rain band before peak intensity (4-10° S). Excess rainfall near equatorial *SWIO up to T-0 between 4-* 10° S (Seychelles) and dry after. Rainfall anomalies over north Madagascar close around T-0. Below normal rainfall over Ethiopia, Kenya, Tanzania, Mauritius, Reunion from T-4 to T+2	Strong Symmetrical rain band before T-0. Excess rainfall near equatorial *SWIO up to T-0 between 4-* 12°S(Seychelles) and dry after Rainfall anomaly increasing near Mauritius and Reunion after T-1 and maximum at T-0.	Poor rain band pattern. Rain clouds dragged south rapidly. Dry condition near Seychelles *from T-4 to T+1 but wet* condition after T+1 between 5-12°S caused by the rapid formation of ITCZ.

Table 6.4: Summary of the Kinematic and thermodynamic differences of TC distinguished by track.

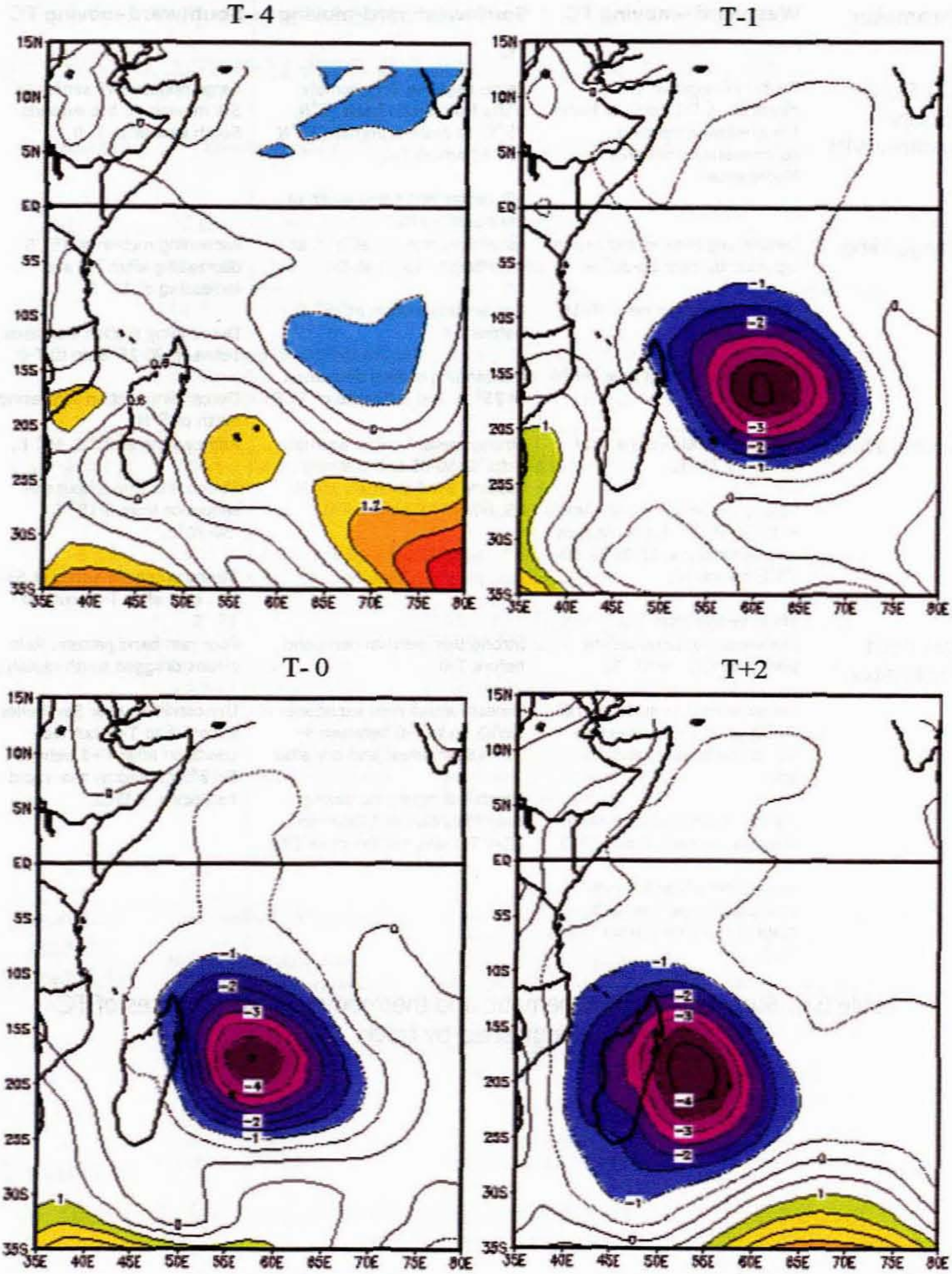

Fig 6.1: Mean sea level pressure for SW–moving TC
T-4 is shown to illustrate pattern close to cyclogenesis.

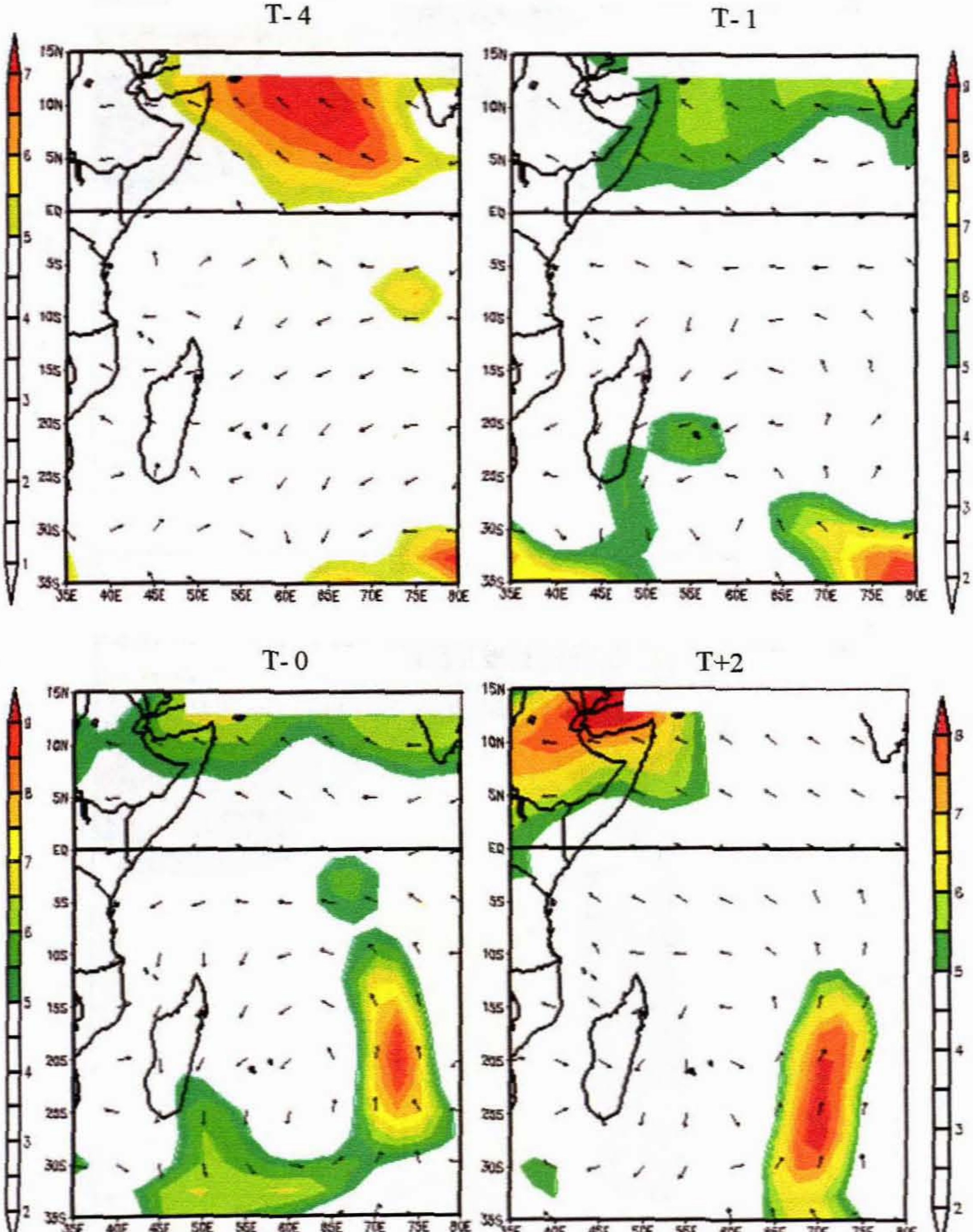

Fig 6.2: Vector wind at 200 hPa for SW-moving TC

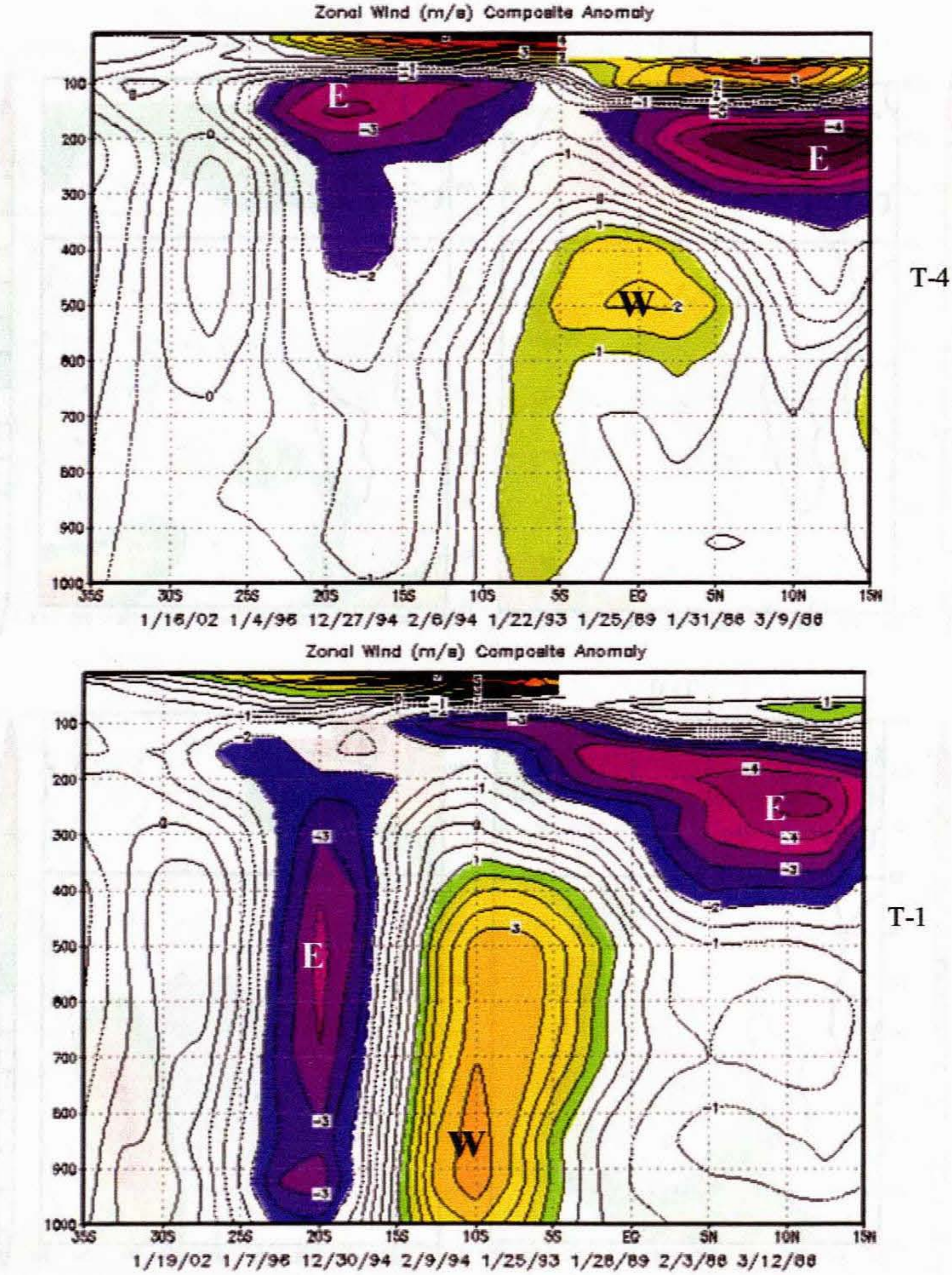

Fig 6.3: Height-Latitude cross section of zonal wind (Averaged 40-75° E) for SW-moving TC at (a) T-4 and T-1

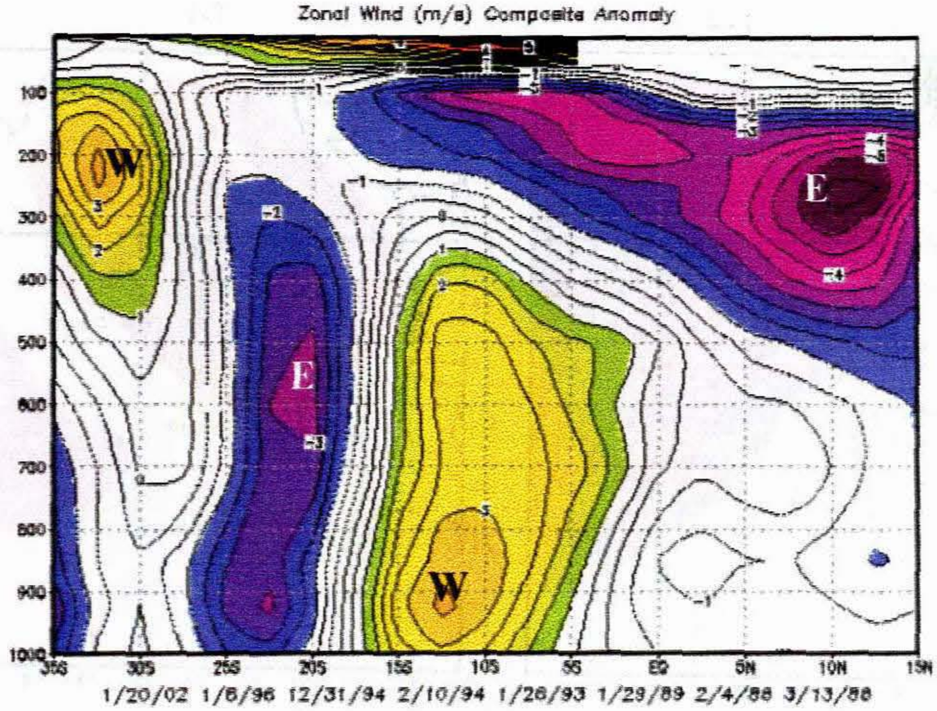

T-0

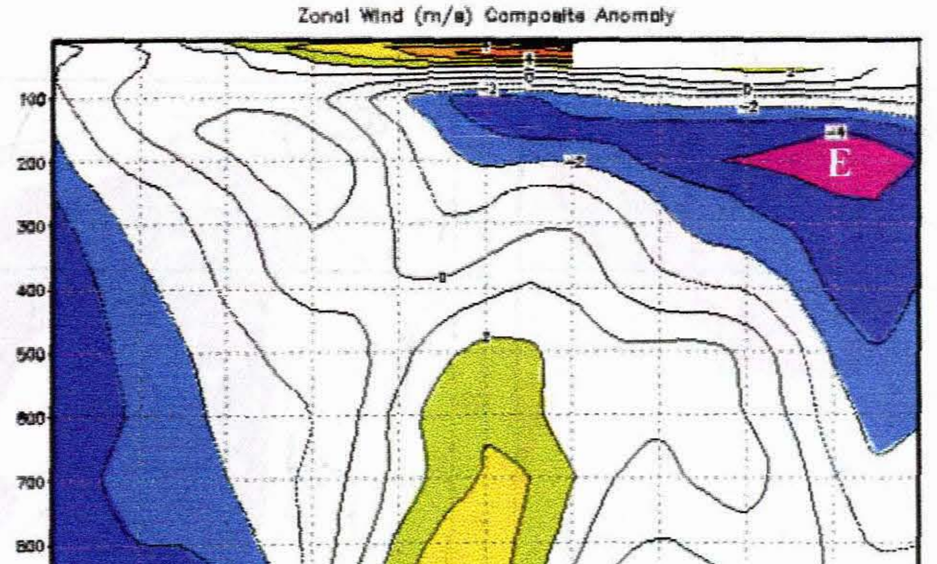

T+2

Fig 6.3: Height-Latitude cross section of zonal wind (Averaged 40-75° E) for SW-moving TC at (b) T-0 and T+2

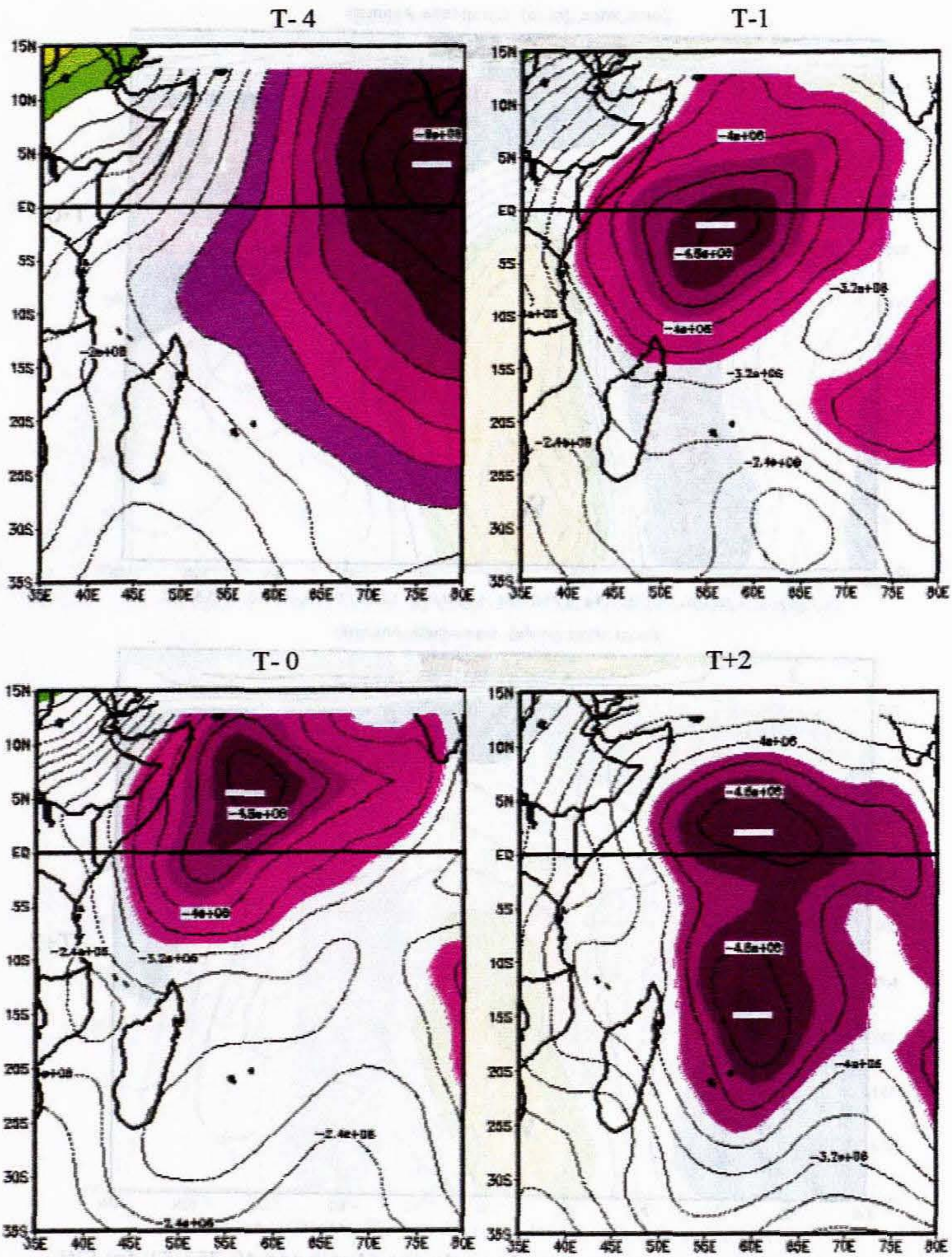

Fig 6.4: Velocity potential at 0.210 sigma level for SW-moving TC

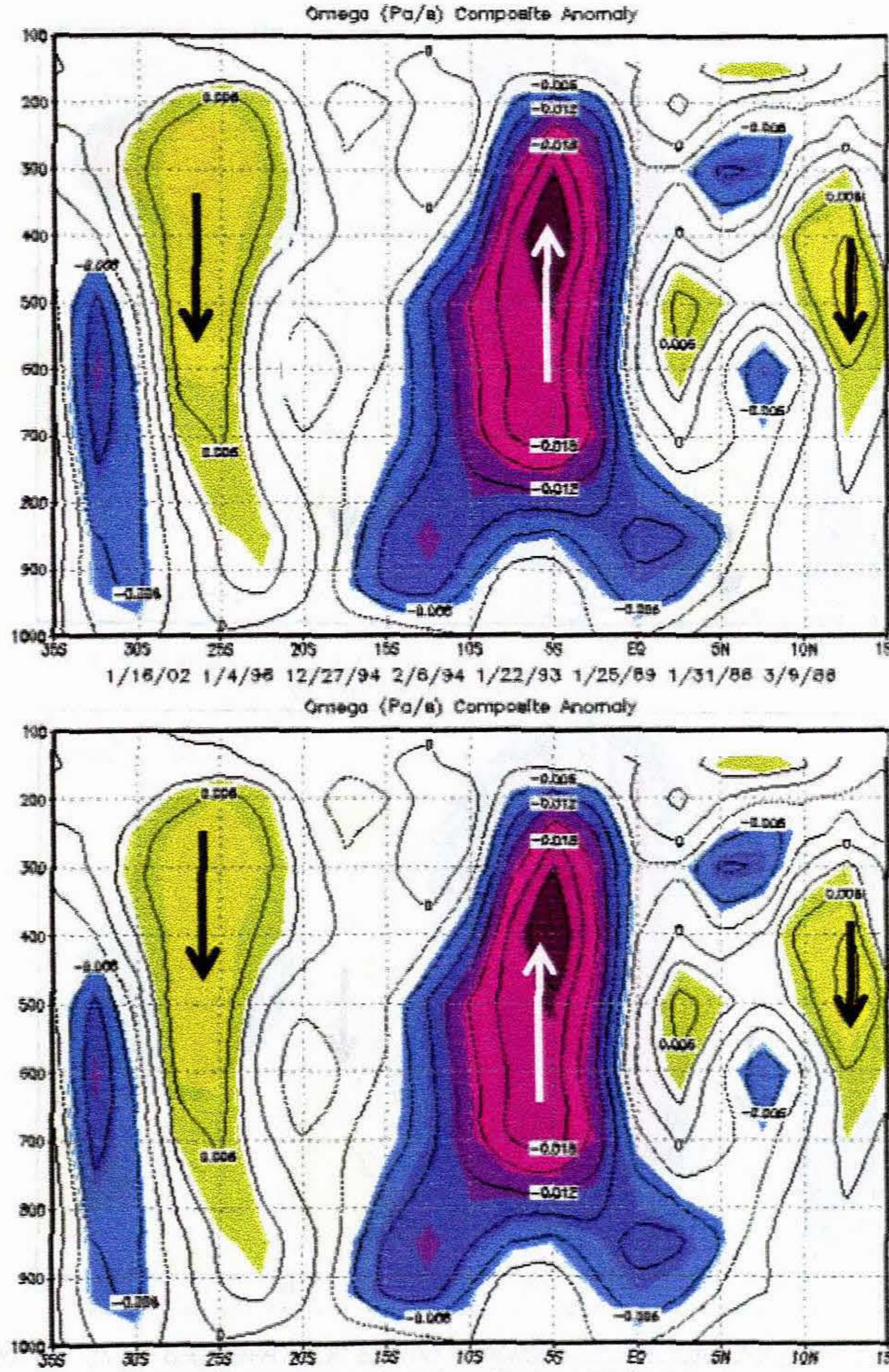

T-4

T-1

Fig 6.5: Height-Latitude cross section of omega field (Averaged 40-75° E) for SW-moving TC at (a) T-4 and T-1

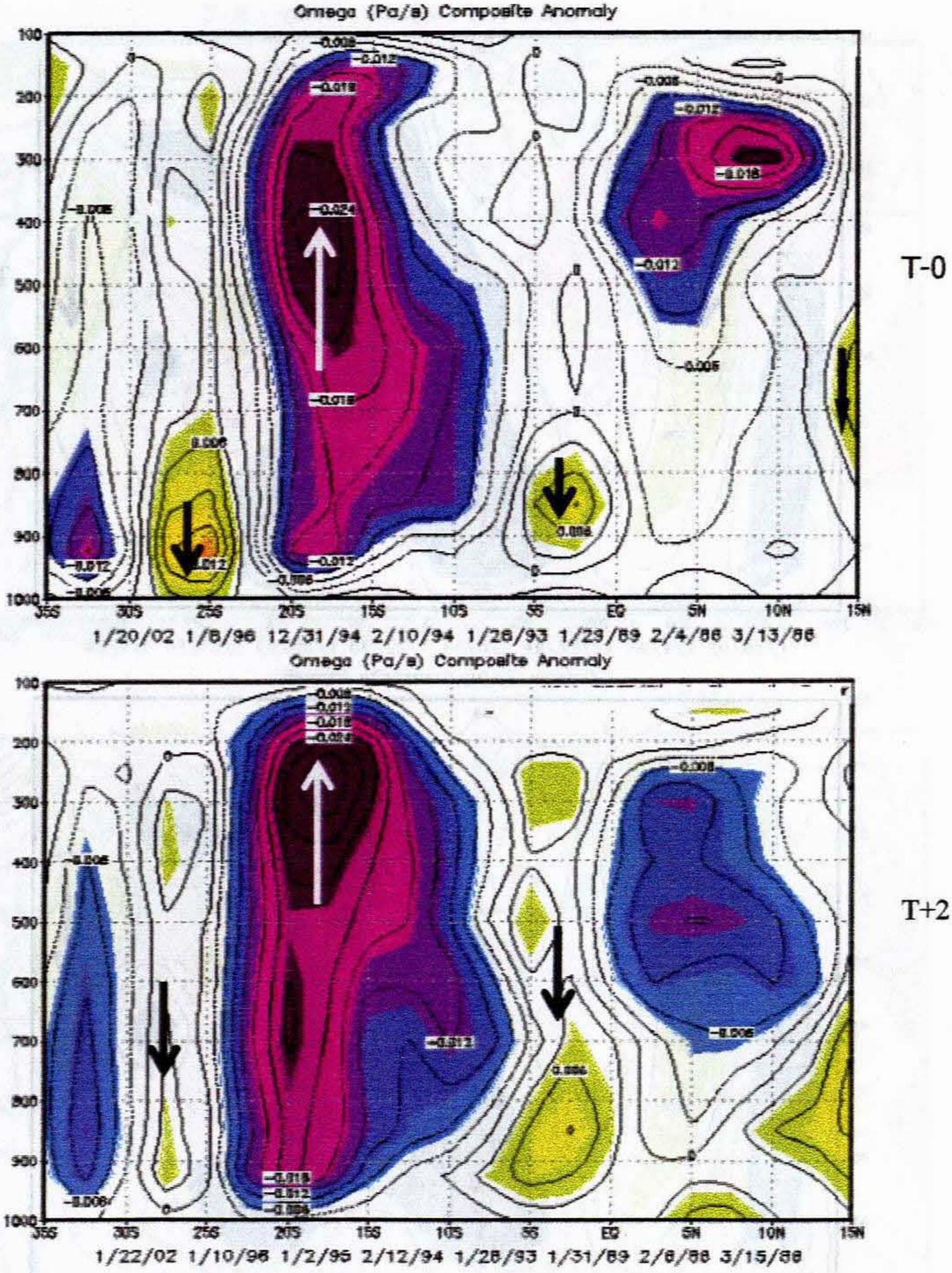

Fig 6.5: Height-Latitude cross section of omega field (Averaged 40-75° E) for SW-moving TC at (b) T-0 and T+2

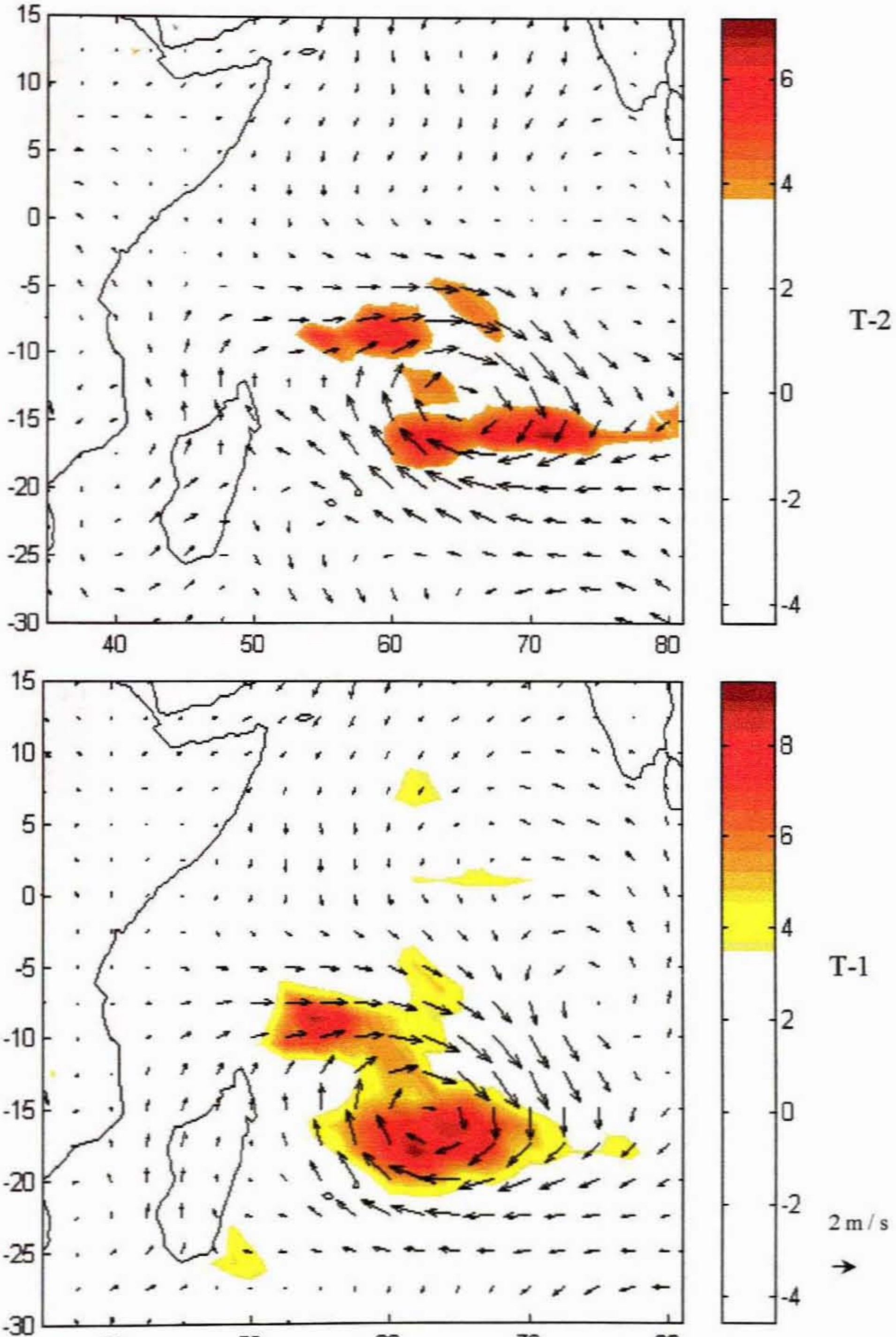

Fig 6.6: Wind flow at 1000 hPa and CMAP precipitation rate anomalies for SW-moving TC at (a) T-2 and T-1.

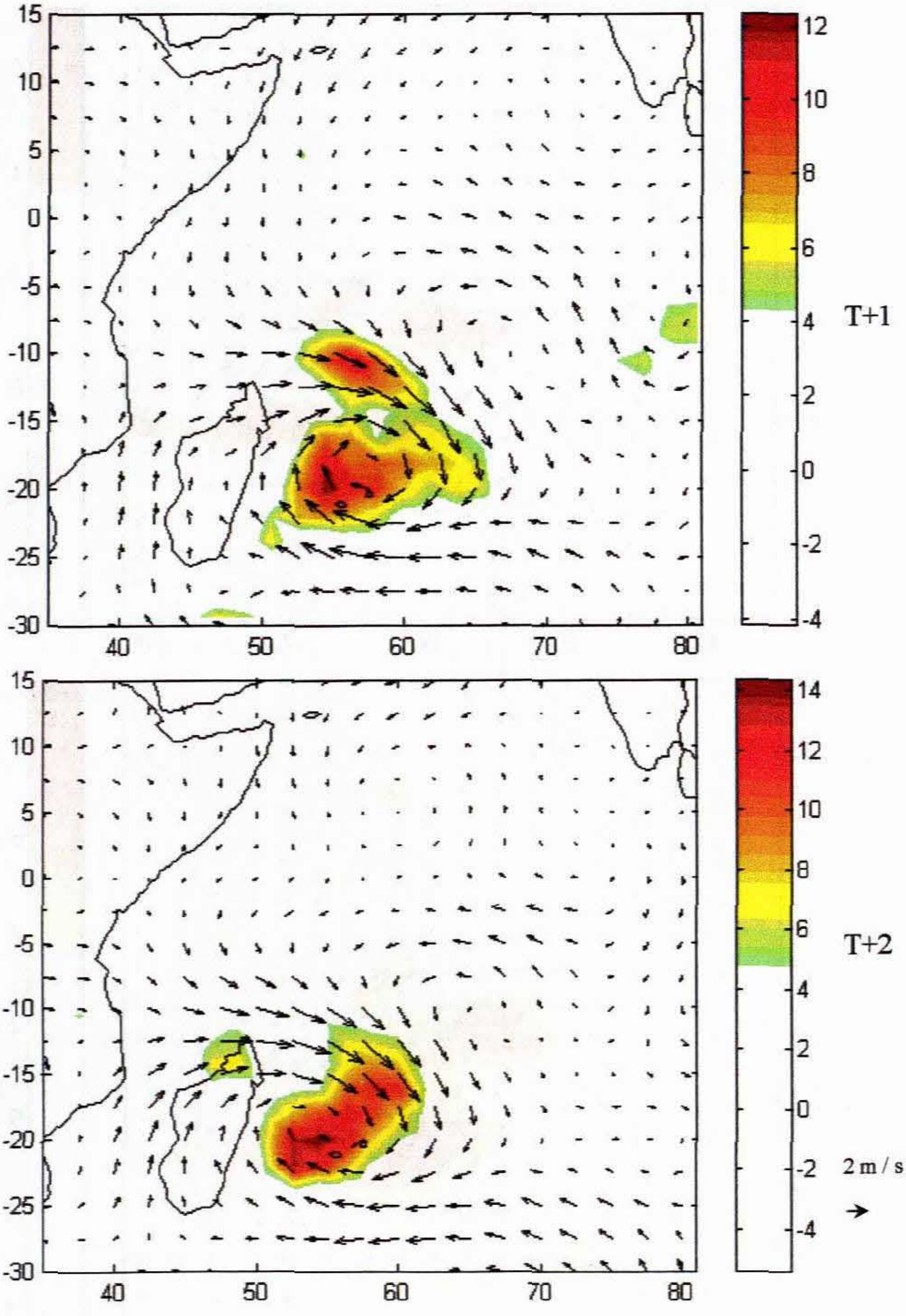

Fig 6.6: Wind flow at 1000 hPa and CMAP precipitation rate anomalies for SW-moving TC at (b) T+1 and T+2.

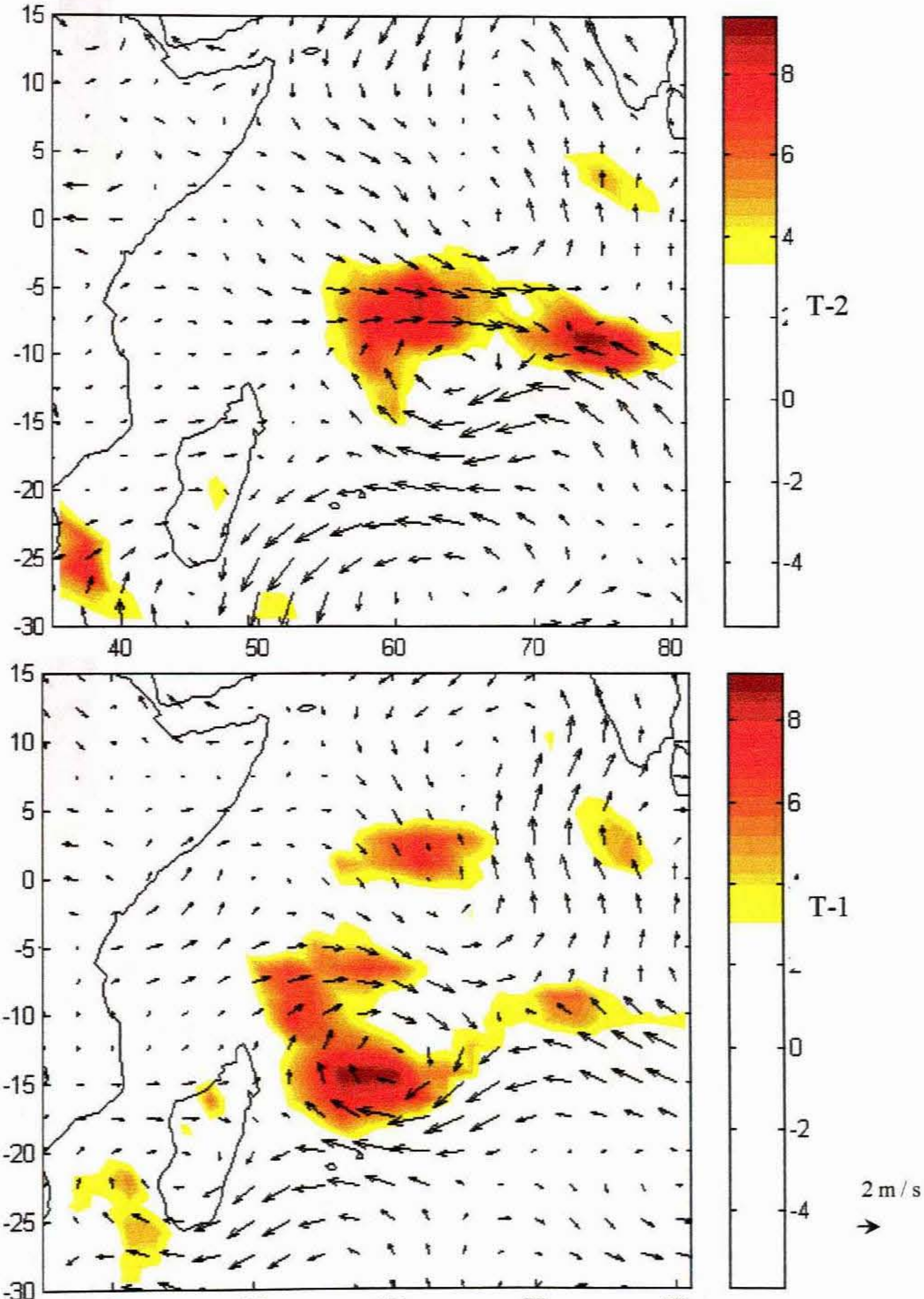

Fig 6.7: Wind flow at 1000 Hpa and CMAP precipitation rate anomalies for West-Moving TC at (a) T-2 and T -1

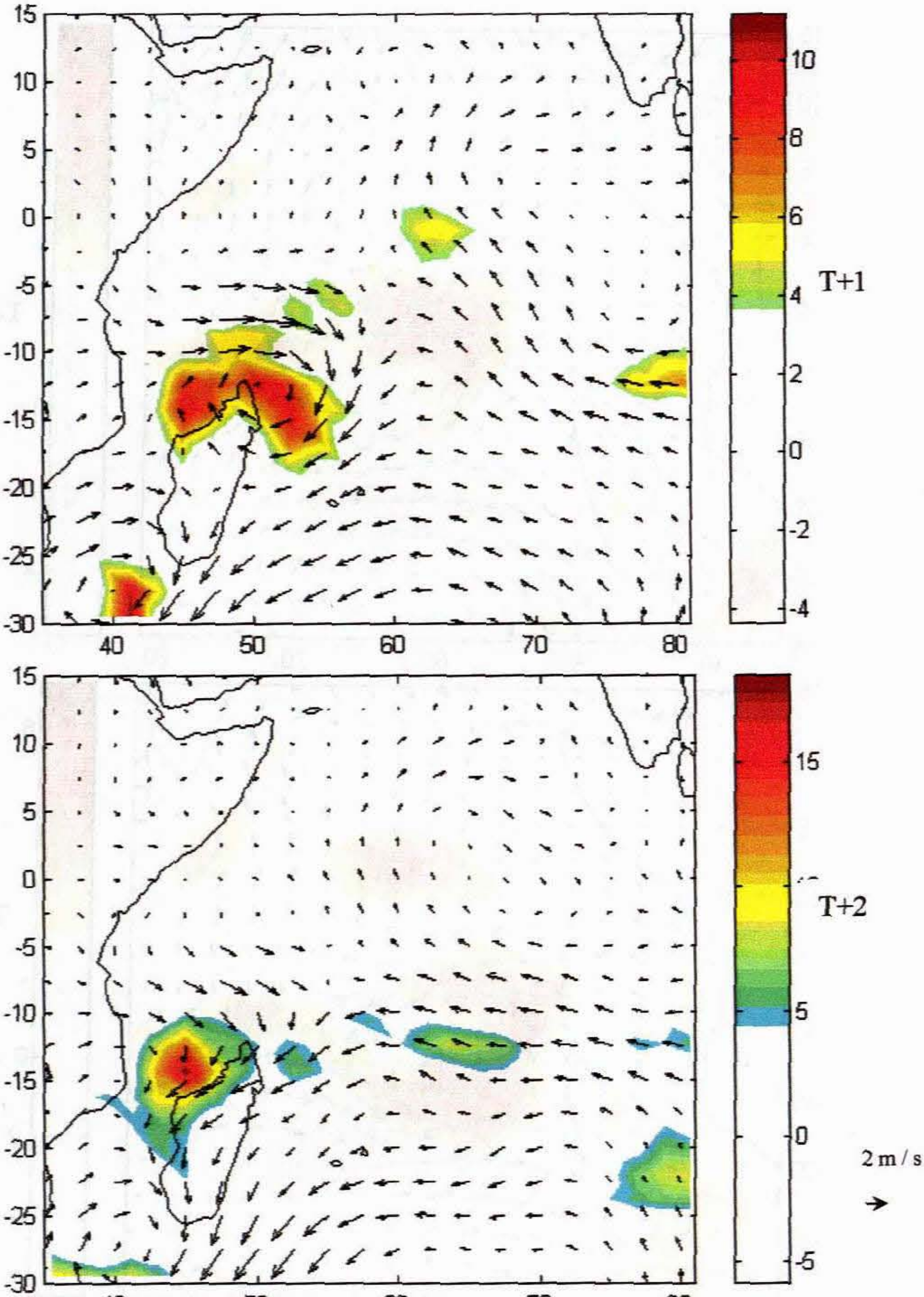

Fig 6.7: Wind flow at 1000 hPa and CMAP precipitation rate anomalies for West-moving TC at (b) T+1 and T +2

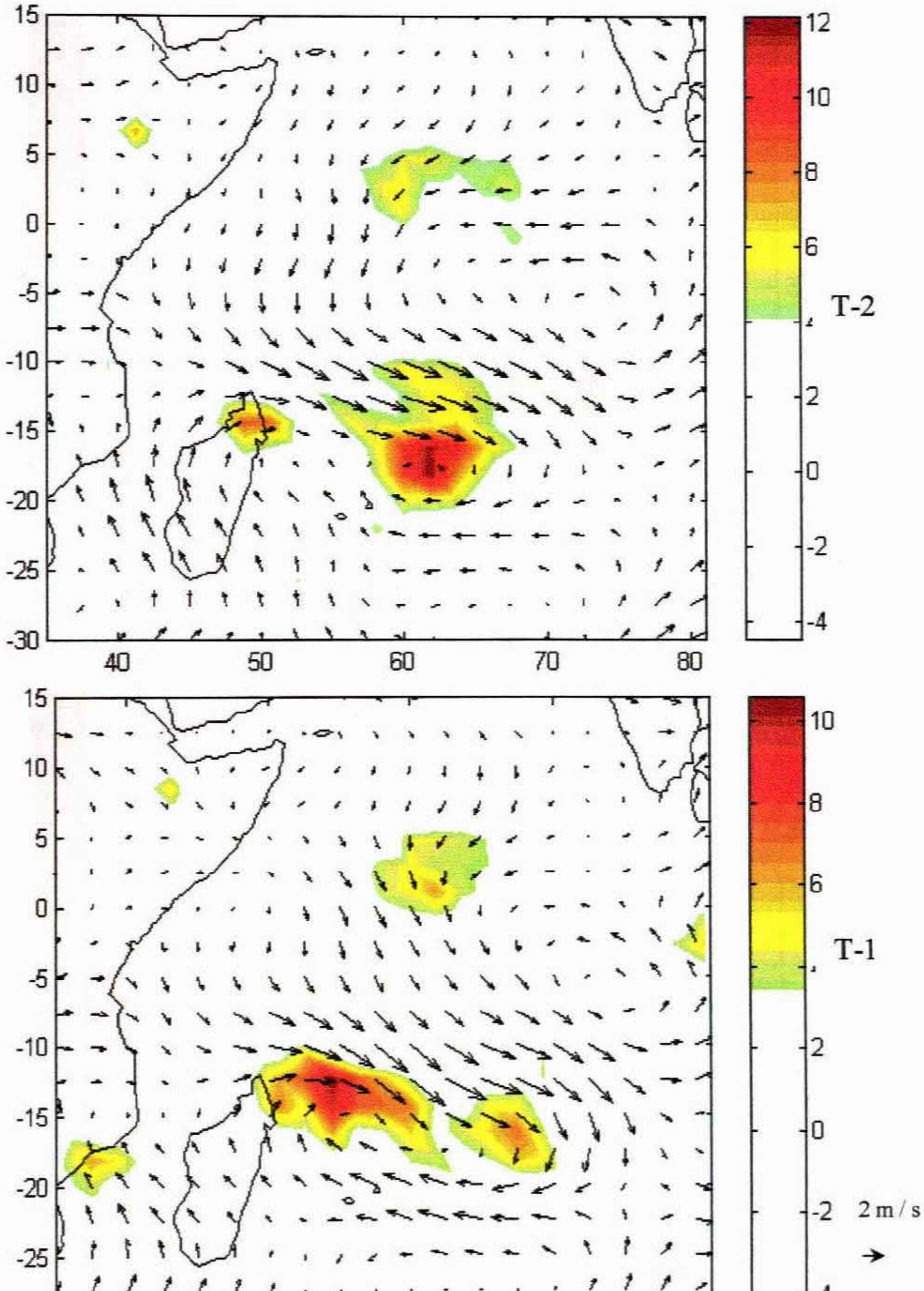

Fig 6.8: Wind flow at 1000 hPa and CMAP precipitation rate anomalies for South-moving TC at (a) T-2 and T-1

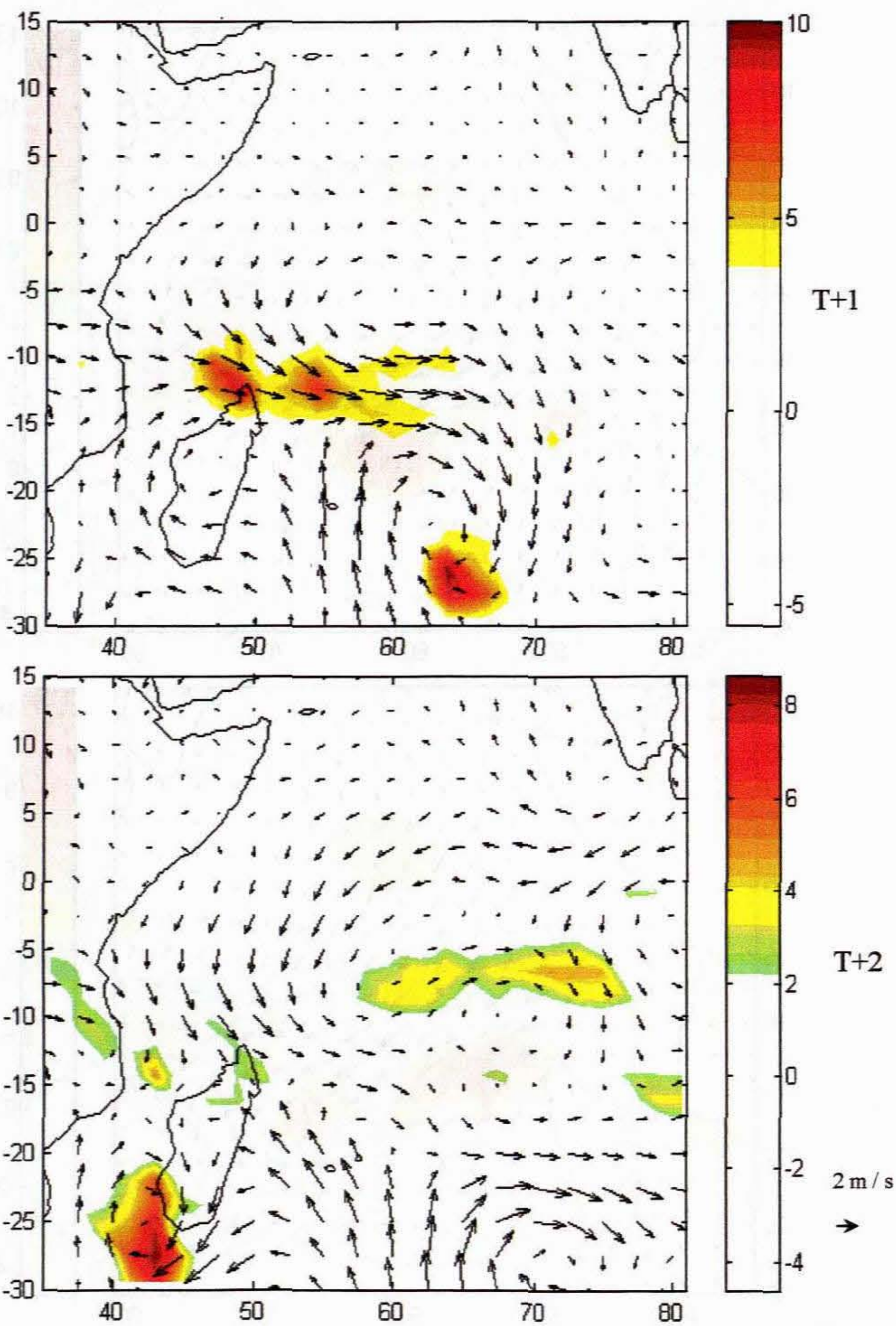

Fig 6.8: Wind flow at 1000 hPa and CMAP precipitation rate anomalies for South-moving TC at (b) T+1 and T+2.

Fig a

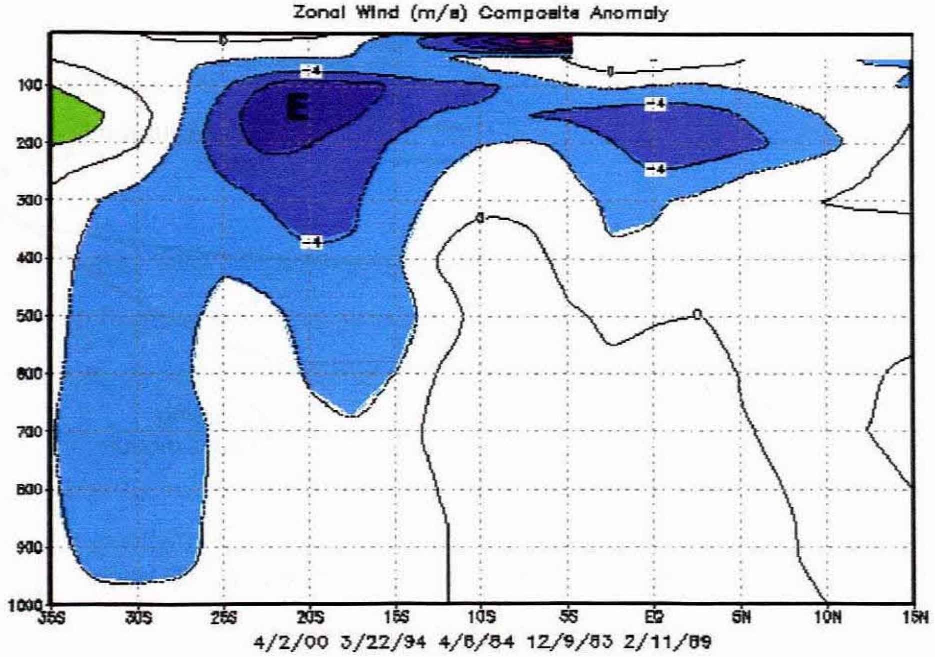

Fig b

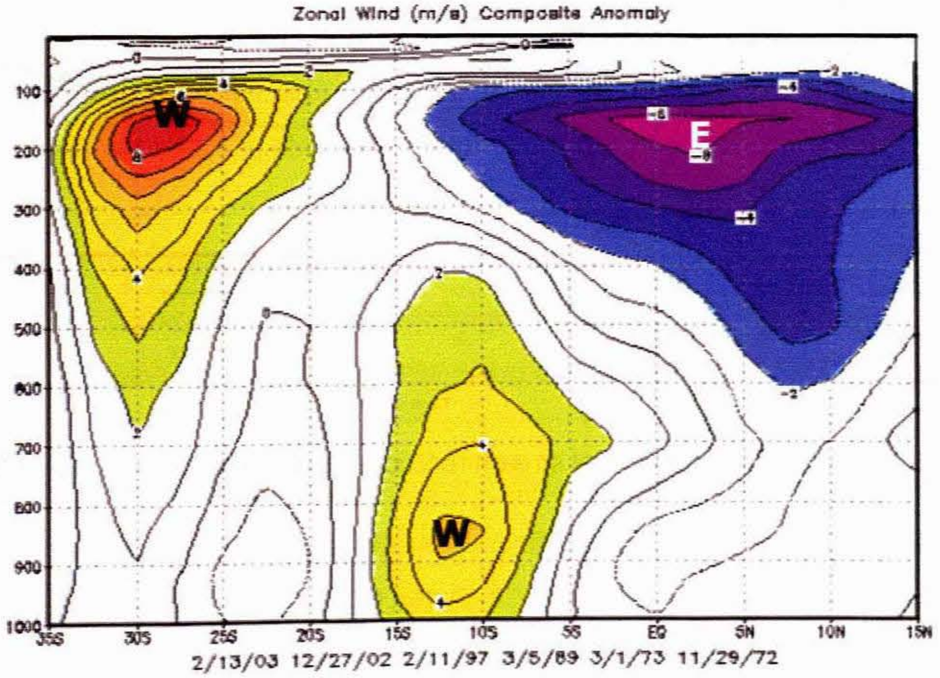

Fig 6.9: Height-Latitude cross section of zonal wind (Averaged 40-75° E) for (a) Westward and (b) Southward-moving TC at peak intensity (T-0).

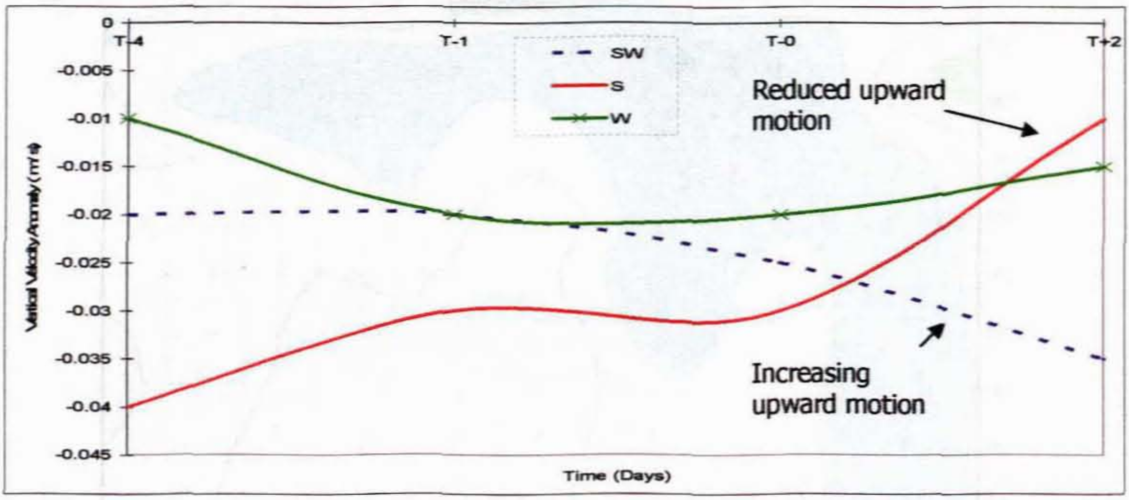

Fig 6.10: Evolution of 500 hPa vertical velocity by TC track

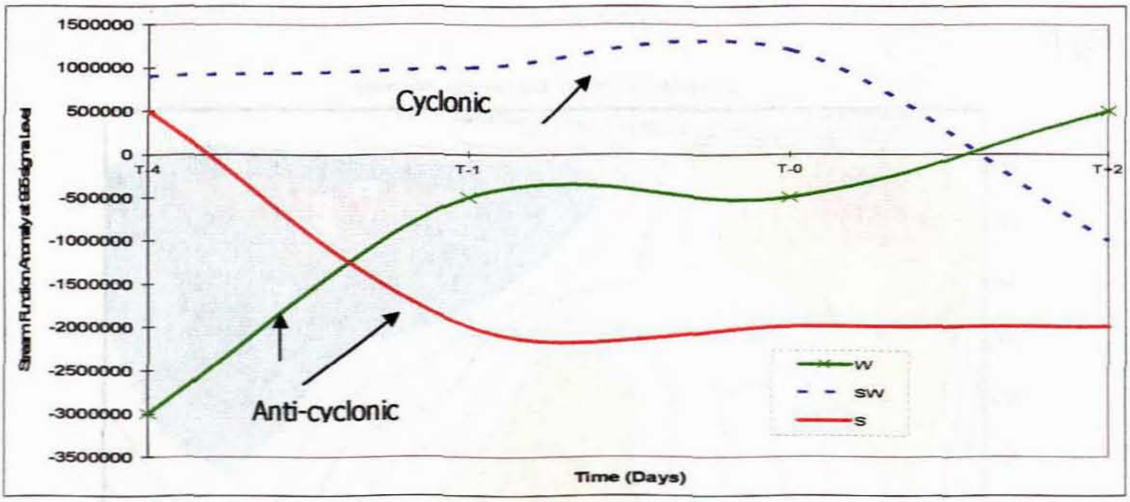

Fig 6.11: Evolution of low level stream function by TC track (5-10°S, 45-55°E)

Chapter 7

Marine Weather Impacts In The SWIO

7.0. Introduction

Intense TCs and their impacts are the main focus of this chapter. Cyclones at sea generate huge waves and swells that are hazardous to shipping. At landfall cyclones produce not only intense rain, flooding and strong winds but are often accompanied by a storm-surge that is devastating to the coast and human livelihood. Here, an evaluation of impacts is done by comparing direct and indirect methods of observation.

Scatterometer wind fields around TCs have strong differences when compared to numerical weather prediction (NWP) models. Comparison is made between QuikSCAT and NCEP winds in a 300 km radius around case study TCs. The swells and storm surges estimated by QuikSCAT and NCEP driven winds are compared. Comparison is also made with observed swell data.

The error in TC position and intensity is assessed for a number of TCs from 1999 - 2004. Comparison is made between the US Navy predicted (12, 24, 36 and 48 hours) and observed TC location and intensity (Meteo France-Reunion).

Snap shoot comparison between model estimated and observed rainfall of TC Eline and Hudah are done. Recent impacts of TC Harry and Gafilo are assessed by comparing satellite IR and TRMM (TMI) microwave estimates of rainfall in the northern part of the spiral rain band of selected cyclones. The NCEP/NCAR Wave Watch 3 marine model products offer a unique opportunity to evaluate the potential impacts of TC Gafilio that generated swell and storm surge in 2004.

7.1.0 Comparison Between NCEP And QuikSCAT Wind Field Across TC Center

Figures 7.1 (a) and (b) show QuikSCAT and NCEP wind fields for TC Eline. The wind speed across NS and EW cross sections for a number of TC is digitized from similar maps.

(a) QuikSCAT Winds for TC Eline on 15th Feb 2000 (b) NCEP Estimated Winds for TC Eline on 15th Feb 2000

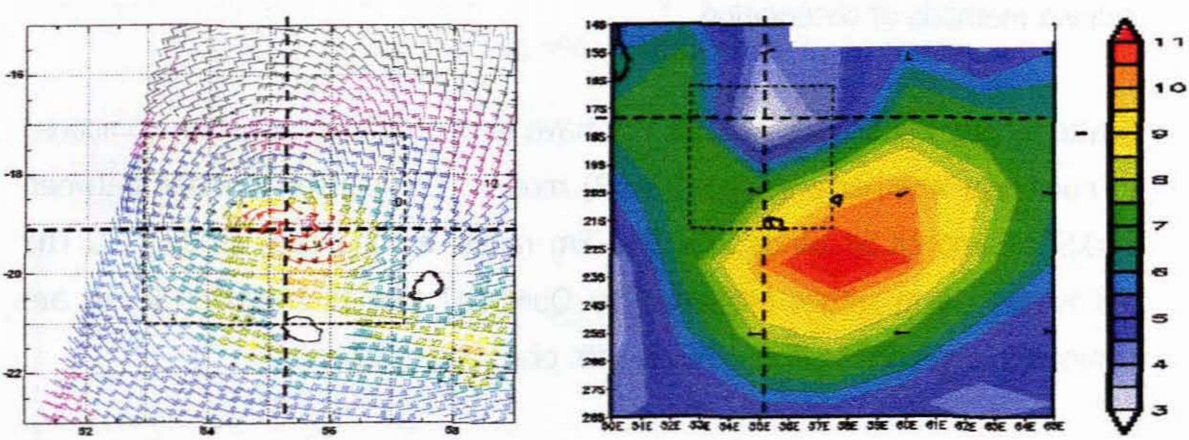

Fig 7.1: (a) QuikSCAT and (b) NCEP winds for TC Eline

Fig 7.1: (a) QuikSCAT and (b) NCEP winds for TC Eline

Figure 7.2 represents the digitized wind speeds from NCEP and QuikSCAT products in (a, b) north - south and (c, d) east - west cross-section across a number of TCs. Figure 7.1 (e) shows the composite map of wind speed across all case study TCs. The QuikSCAT winds in the 300 km radius of the TC are consistently higher than the NCEP winds in both NS-EW cross-sections.
The ratio of the two areas under the graphs from 1 - 3° (~100 km - 300 km) radius across the composite TC was calculated to be 2.2. It is noted that a similar result was obtained by comparing the average wind speed in the fetch area of the TC. This implies that NCEP is underestimating wind speed by a factor of two around the 300 km radius of the TC compared to scatterometer winds.

Figure 7.3 (a) to (d) are some of the QuikSCAT wind fields for intense TC Eline and figure 7.4 (a) to (d) for Hudah used to compute and compare swell and storm surges with the NECP model estimated winds.

Fig a

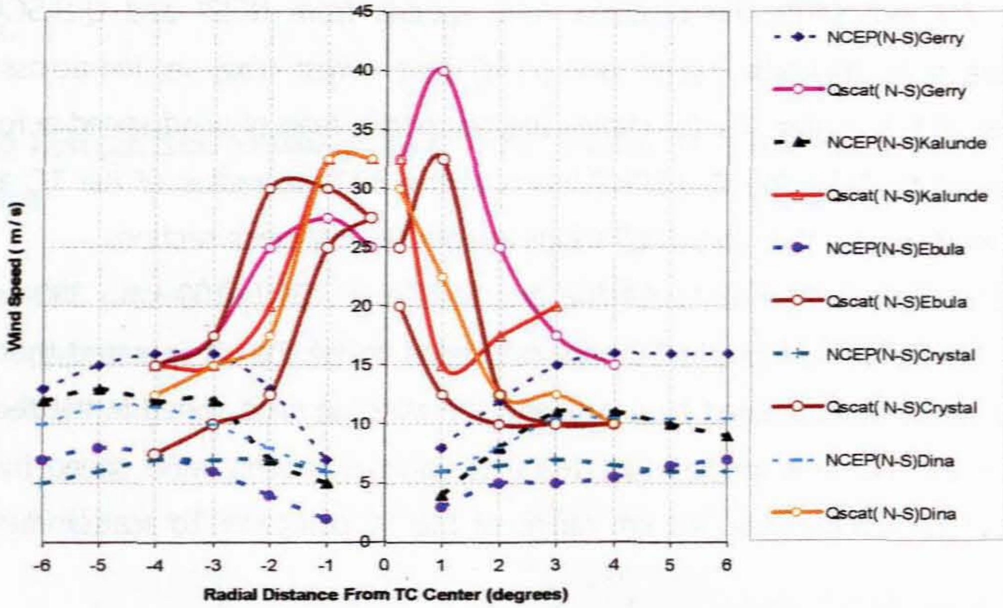

Fig b

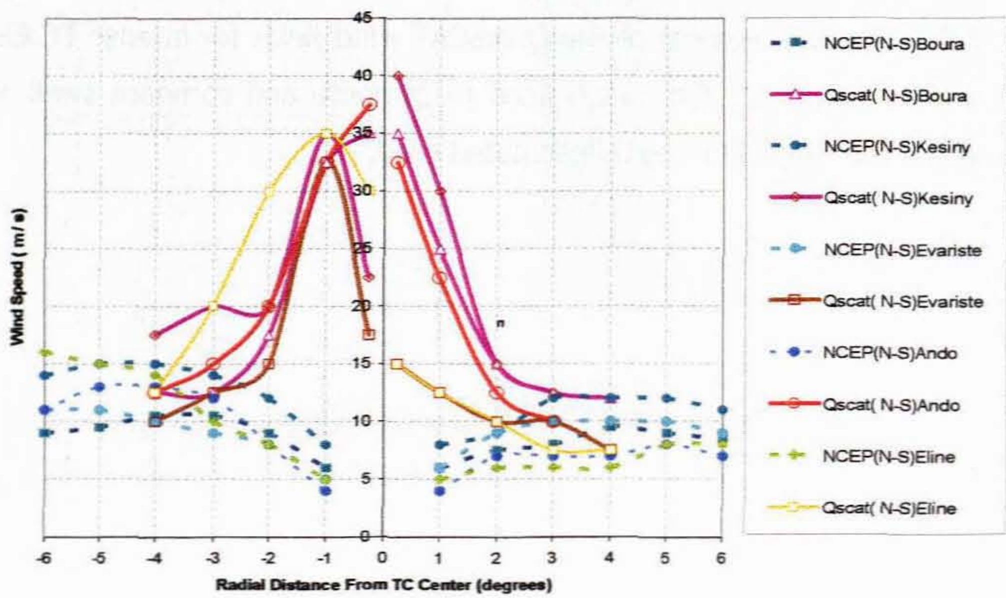

Fig 7.2 (a) and (b): Comparison Between NCEP and QuikSCAT wind field across N-S TCs

Fig c

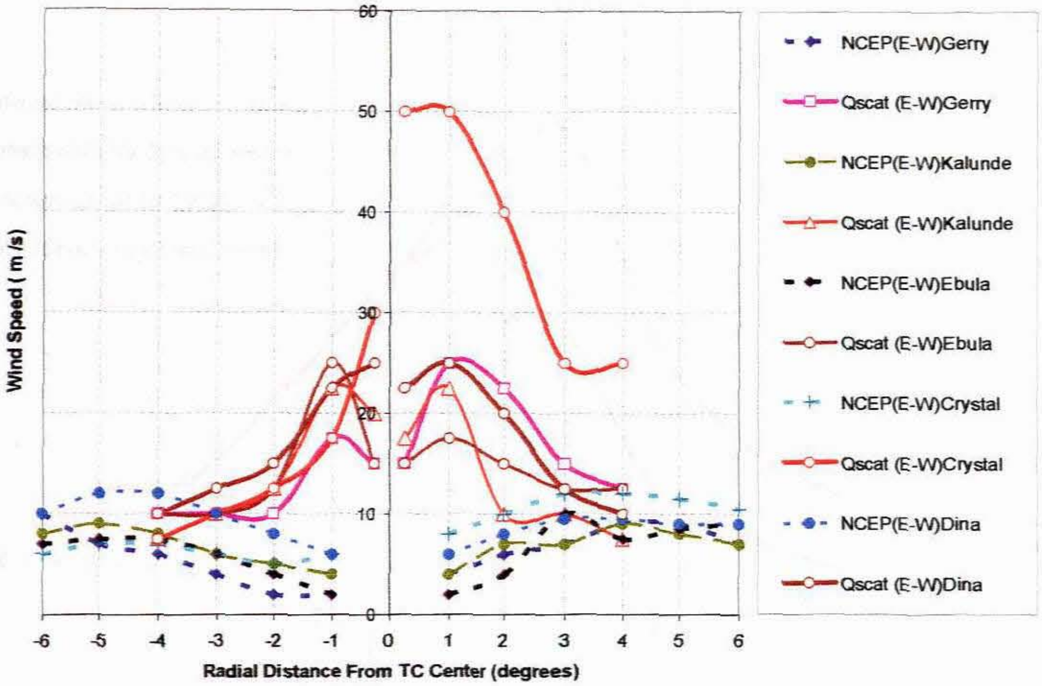

Fig d

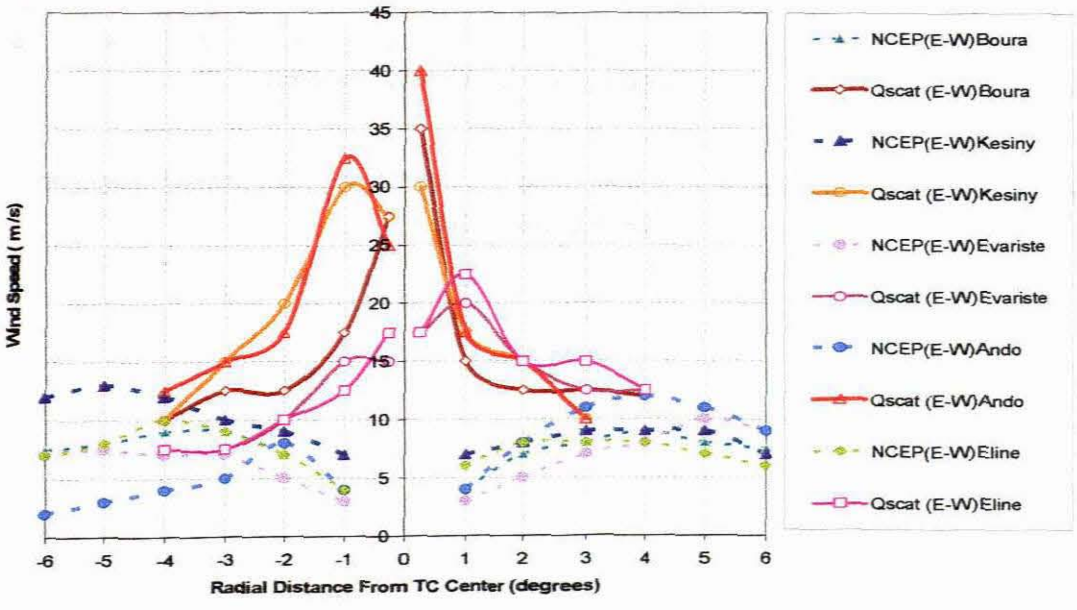

Fig 7.2 (c) and (d): Comparison between NCEP and QuikSCAT wind field across E-W TCs

Fig e

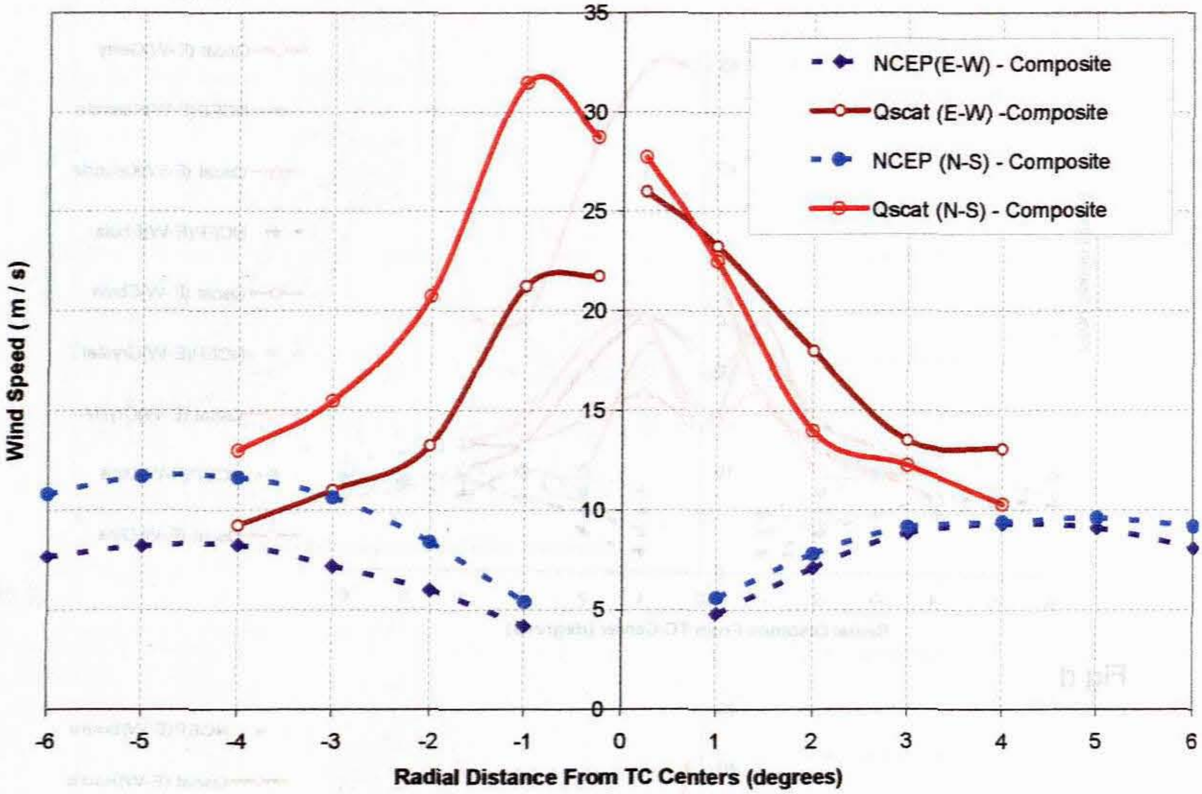

Fig 7.2 (e): Composite wind speed across NS and EW TC (Radial Distance) between NCEP and QuikSCAT

Fig a

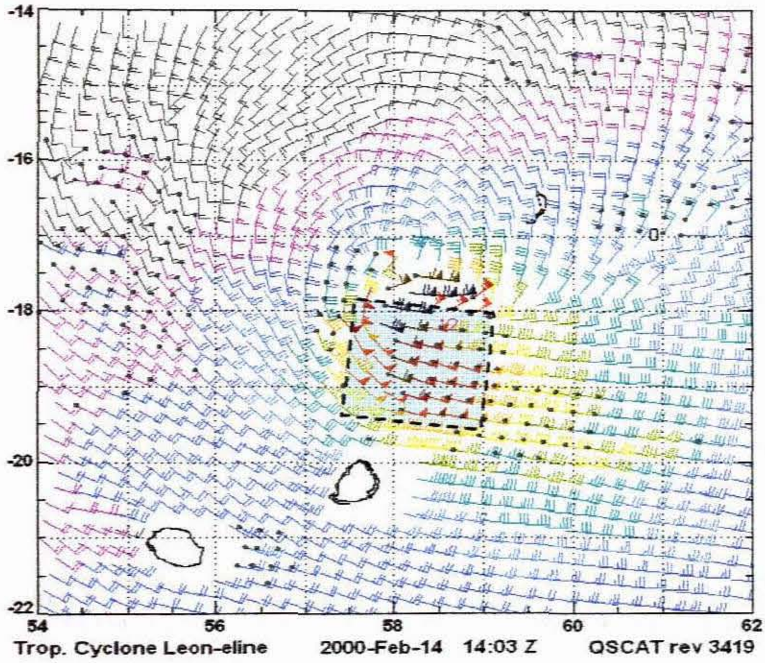

Fig b

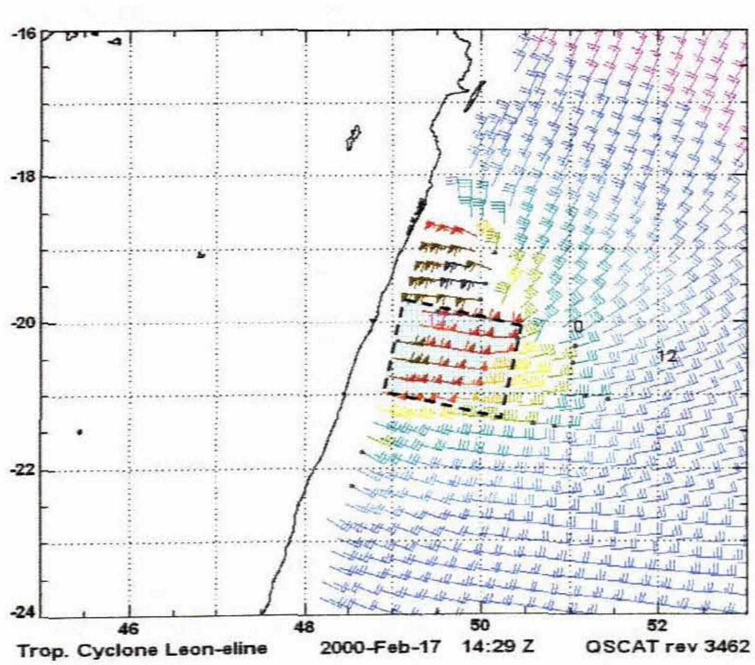

Fig 7.3: (a) TC Eline on 14 Feb northeast Mauritius (b) Tamatave, Madagascar on 17th Feb 2000

Fig c

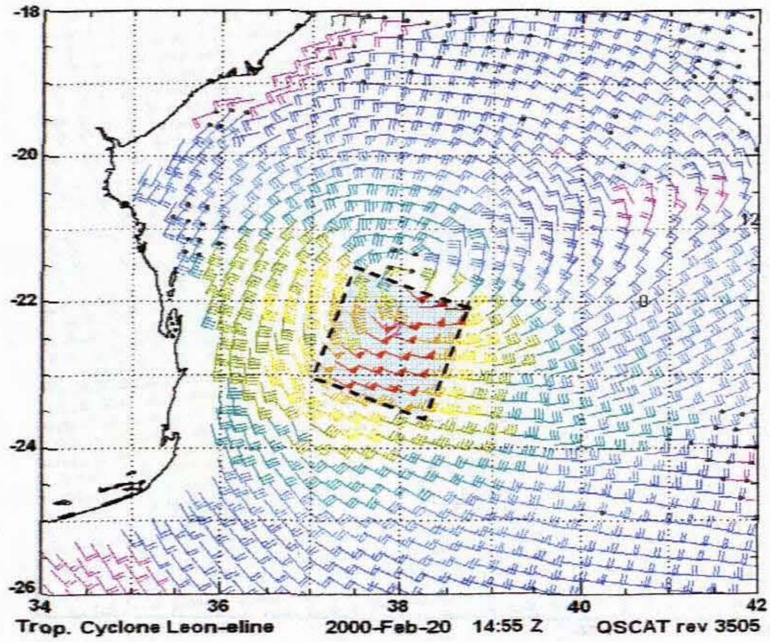

Fig d

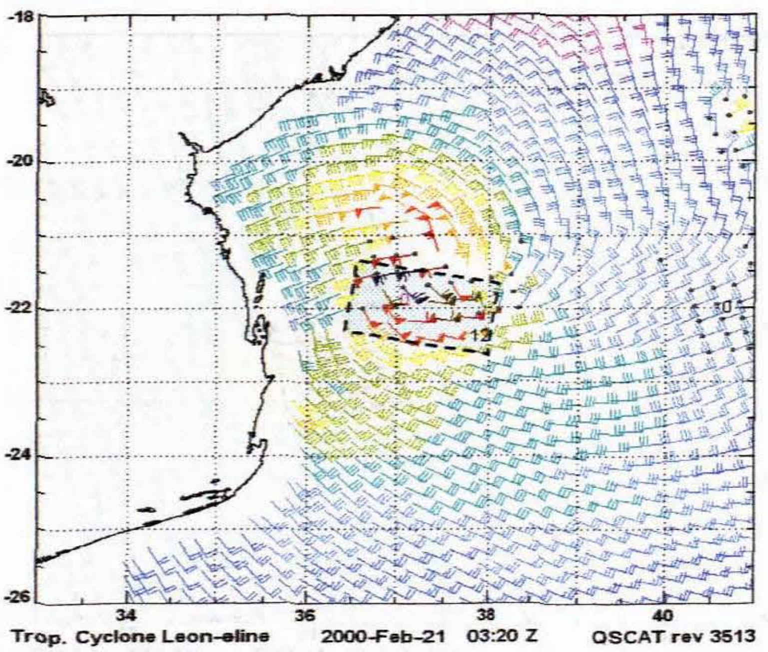

Fig 7.3: (c) TC Eline on 20 Feb 2000 in Mozambique Channel (d) landfall over South Mozambique on 21 Feb 2000

Fig a

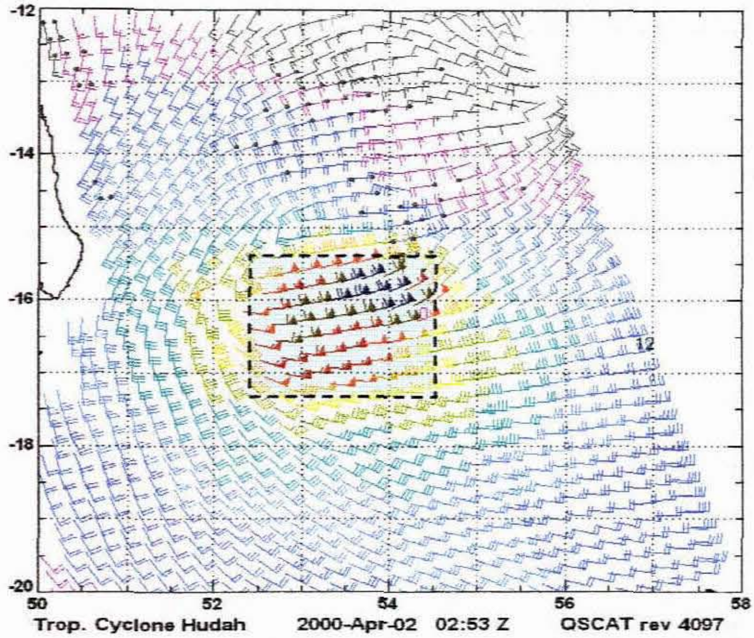

Fig b

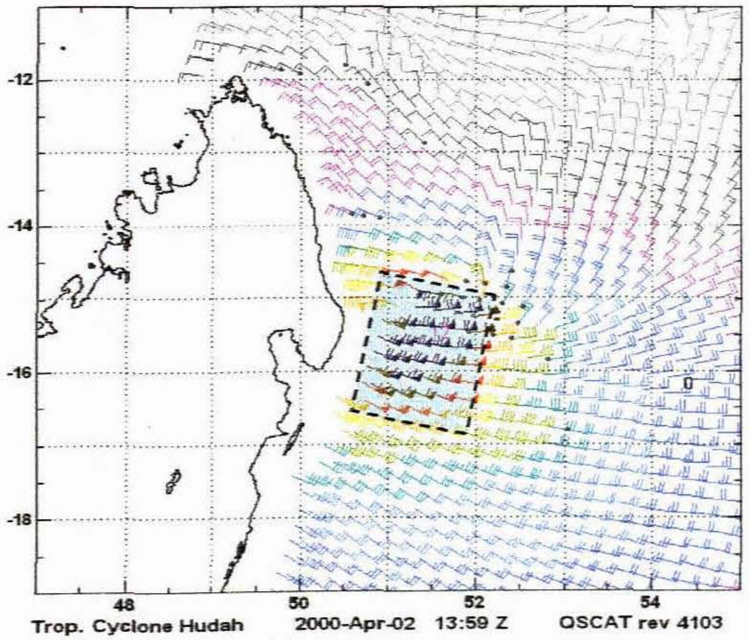

Fig 7.4: (a) TC Hudah on 2 April 2000 north east Madagascar (b) landfall over Tamatave on 2 April 2000

Fig c

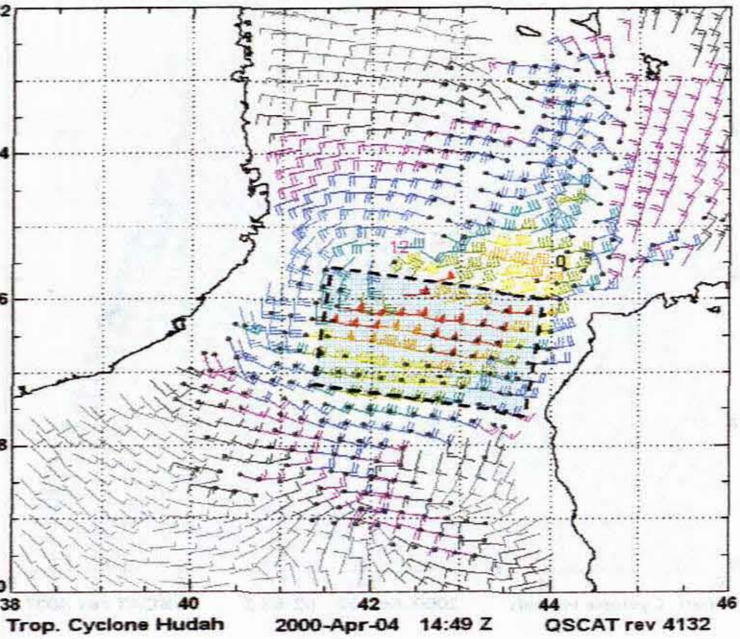

Fig d

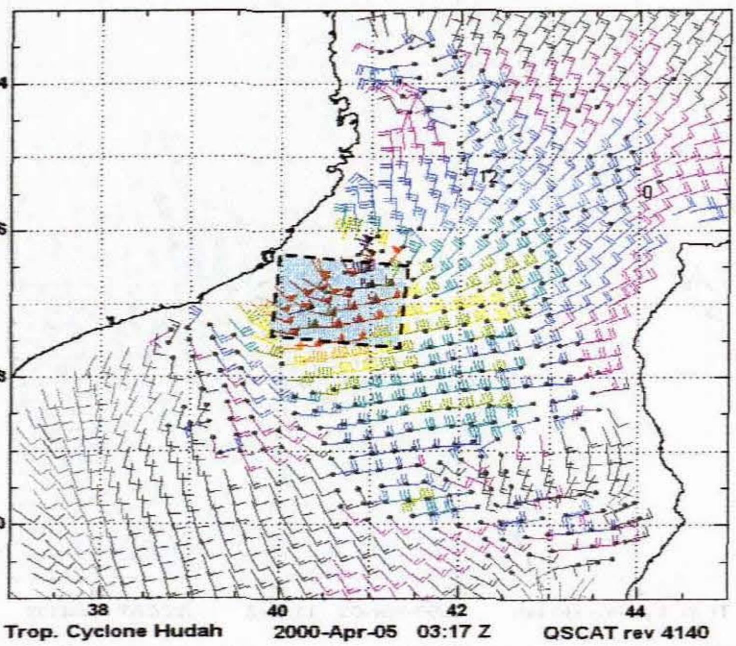

Fig 7.4: (c) TC Hudah on 4 April 2000 in north Mozambique channel (d) landfall over north Mozambique on 5 April 2000

7.1.1 Comparison of NCEP and QuikSCAT Cyclonic Generated Swells

Table 7.1 (a) to 7.1 (c) give swell properties computed using QuikSCAT and NCEP winds respectively. Although NCEP underestimates wind speed in the 300 km radius of TC it is observed that NCEP overestimates the average fetch area by three times. As a result the wave height and wave period are underestimated by only 1.7 and 1.1 times respectively. The estimated travel time is consequentially longer for NCEP data.

TC Name	**Day (TO)**	**U** *QScat* **($m\,s^{-1}$)**	**Fetch Width (km)**	**Distance From Landfall (Km)**	**H** *s* **at Landfall (m)**	**Wave Period T(s)**	**Travel time** t_S **(hrs)**
Hudah	22/4/2000	35.0	1167	556 1111	6.8 (Antalaha 5.3 (Toamasina)	13 s 13 s	1.5 7.5
Ando	6/1/2001	15.0 25.0	1296 1111	4482 5593	3.8 (Reunion) 3.5 (Toamasina)	12 s 12 s	13.5 16.5
Leon-Eline	15/2/2000 15/2/2000 21/2/2000	27.5 30.0 30.0	833 1685 1111	2222 8408 1685	2.4 m (Reunion) 3.0 (Madagascar) 3.0 (Mozambique)	10 s 13 s 11 s	8.0 24.0 6.0

Table 7.1 (a): Estimated swell significant wave height (Hs), wave period (Ts), and arrival time (t s) using QuikSCAT wind speed.

TC Name	Day (T0)	U_{NCEP} ($m\,s^{-1}$)	Fetch Width (Km)	Distance From Landfall (km)	H_S at Landfall (m)	Wave Period T(s)	Travel time t_S (hrs)
Hudah	22/4/2000	12.5	3334	556 1111	2.5 (Antalaha) 2.3 (Toamasina)	9 s	2.0 h 4.0 h
Ando	6/1/2001	14.0 14.0	3334 242	4482 5593	2.0 (Reunion) 2.4 (Toamasina)	10 s 11 s	16.0 h 18.0 h
Leon-Eline	15/2/2000 15/2/2000 21/2/2000	12.0 12.5 14.0	4482 5593 4241	2222 8508 1685	2.0 (Reunion) 1.0 (Madagascar) 2.2 (Mozambique)	9 s 12 s 13 s	9.0 h 25.0 h 5.0 h

Table 7.1(b): Estimated swell significant wave height (Hs), wave period (Ts), and arrival time (ts) using NCEP wind speed.

Parameter	$\frac{U_{QScat}}{U_{NCEP}}$	$\frac{X_{QSCat}}{X_{NCEP}}$	$\frac{Hs_{QScat}}{Hs_{NCEP}}$	$\frac{T_{QScat}}{T_{NCEP}}$	$\frac{t_{QScat}}{t_{NCEP}}$
Ratio	2.2	0.3	1.7	1.1	0.9

Table 7.1 (c): Comparison of area average wind speed (U), width of fetch area (X), estimated significant wave height (H_s), wave period (T_s) and travel time (t) for QuikSCAT and NCEP wind.

7.1.2 Comparison Of Model Estimated Wave Height With Real Observed Data

It was highlighted at the beginning that in-situ oceanographic data is lacking in the IO. Currently, only Meteo France-Reunion is measuring and reporting wave height. Comparing swell model data and observed data is difficult because only a few isolated swell heights are observed and reported.

The significant swell heights using QuikSCAT winds are underestimated by 0.6 m and 1.6 m compared to insitu - observation at Reunion Island for TC Eline and Ando respectively. The significant wave heights are underestimated by 1 m and 3.4 m when using NECP winds respectively. The NCEP /NOAA Wave Watch 3 wave model is also underestimating the significant wave height and wave period for TC Eline, Hudah and Ando (table 7.1 d).

In a case study, Meteo France simulated TC Ando generated swells. The simulated wave height near Reunion was 6.0 m. The observed wave height was actually 5.4 m.

TC Name	WW 3 Hs (m) 1.25°	NWW3 T_s(s) 1.25°	MeteoFrance Wave Model Hs (m)	Observed Hs (m)
Hudah	0.9 m (02/4/2000) 0.6 m (07/4/2000)	10 s 9 s		
Ando	1.2 m (06/2/2001)	10 s	6.0	5.4 (Reunion)
Eline	1.2 m (15/2/2000) 1.2 m (21/2/2000)	10 s 10 s		3.0 (Reunion)

Table 7.1 (d): Wave Watch 3 (WW3), Meteo-France wave model output and measured swell height

However, recently the NCEP/NOAA WW3 model predicted the swell generated by TC Gafilo reasonably well. Figure 7.5 shows the simulated wave heights and peak wave direction fields for 5, 6, 7 and 9 of March 2004 at T+ 00, T+24, T+ 48 and T+72 respectively. The predicted significant wave height for T+ 00 is 4.5 m and directed towards the eastern Madagascar coast. The 24 hour forecast shows swells directed towards the southern tip of Madagascar coast only. In the 48 hour forecast swells grow to an average height of 6 m. However, the peak swell direction is towards the south rather than being perpendicular to the Madagascar coast. The swells decays on 9 March but the decayed swells diffract around southern Madagascar. Since the swells were predicted to be traveling parallel instead of perpendicular to the coast the impacts were less.

The swells generated by Gafilo (2004) are compared to swells predicted for TC Ando (2001), Eline and Hudah (2000) (table 7.1 d). The model differences could be the result of either improvement in physical wave modeling or superior input data such as QuikSCAT winds.

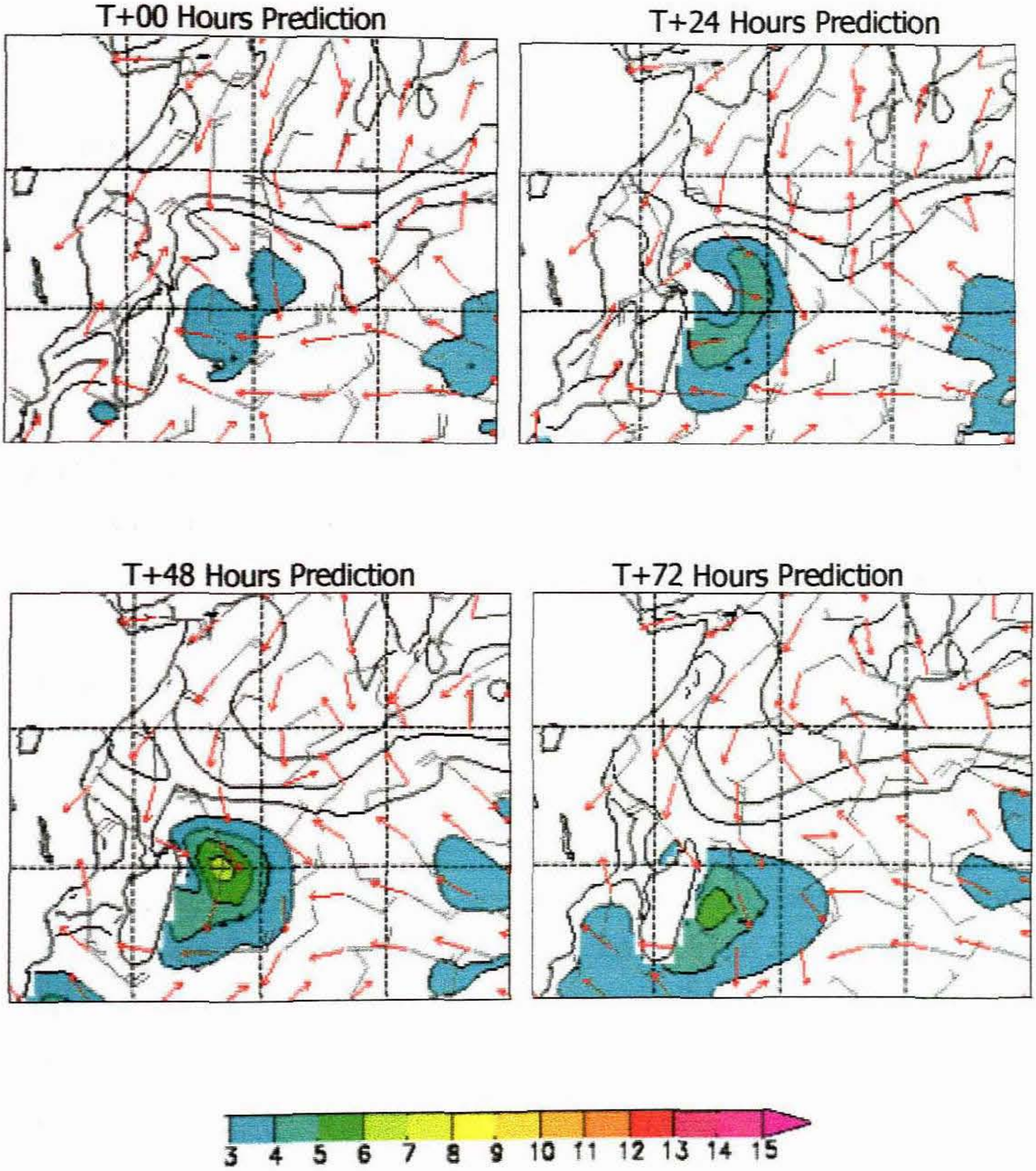

Fig 7.5: TC Gafilo predicted (NCEP/NCAR WW3) wave height (shaded m), wind speed (barbs, knots) and peak wave direction (vector, not scaled) for 00, 24, 48 and 72 hours on 5th March 2004

7.1.3 TC Generated Storm Surge Using NCEP and QUIKSCAT Winds

When a TC makes landfall there is often a rise of sea level that moves inland. It is dependent on the fetch area and winds, local pressure, open sea waves astronomical tides and local coastal features. This inland-moving water can have huge impacts on the coastal environment and habitat. A 2-D numerical model of storm surge is used to simulate and compare how much the sea level rises when driven by scatterometer (QuikSCAT) and NCEP winds at landfall over the Madagascar coast. The total storm surge is then estimated by summing up the effect of the surge, astronomical tide and inverse barometric pressure. The two TC studied are Eline and Hudah. The premise for choosing TC Eline and Hudah is that they were among the top killer cyclones in the SWIO according to the data extracted from Meteo-France Reunion annual review publications (table in appendix). Both intense TC landed on Madagascar and traversed the Mozambique Channel to make a second landfall over Mozambique.

Figure 7.6 (a) shows the 2-D analytical model output for the first three hours. It clearly illustrates that NCEP driven winds underestimate the sea level rise. The total storm surge estimated by NCEP and QuikSCAT winds are shown in figure 7.6 (b). The error bars indicate the tidal range. Large differences are indicated in the total potential storm surge height when using NCEP and QuikSCAT winds. The total potential storm surge is underestimated by a factor of 4 with NECP wind compared to QuikSCAT winds.

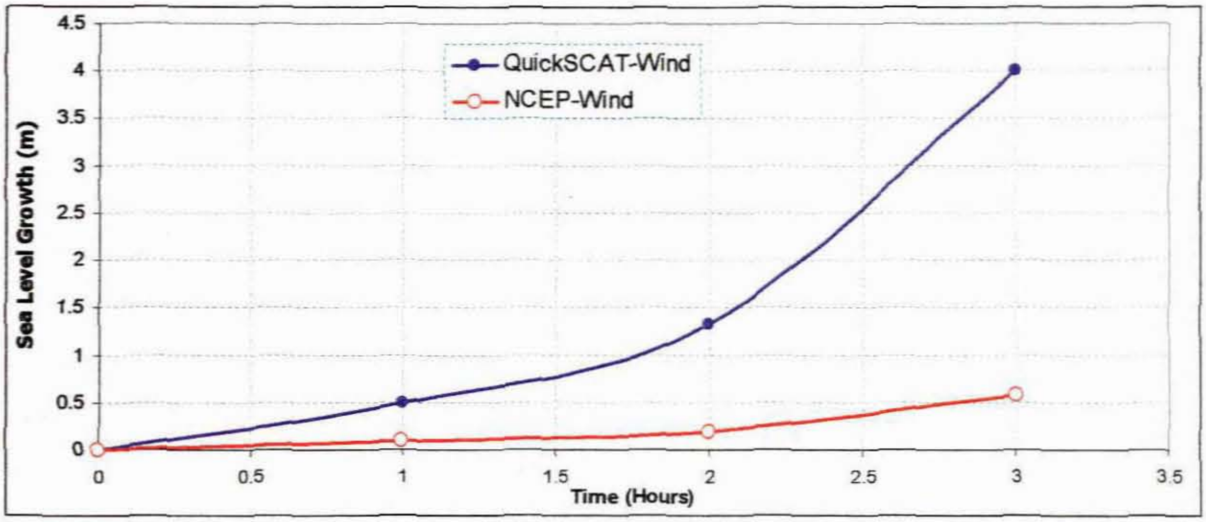

Fig 7.6 (a): Estimated ensemble sea level rise for QuikSCAT and NCEP winds of TC Hudah and Eline on landfall over Madagascar

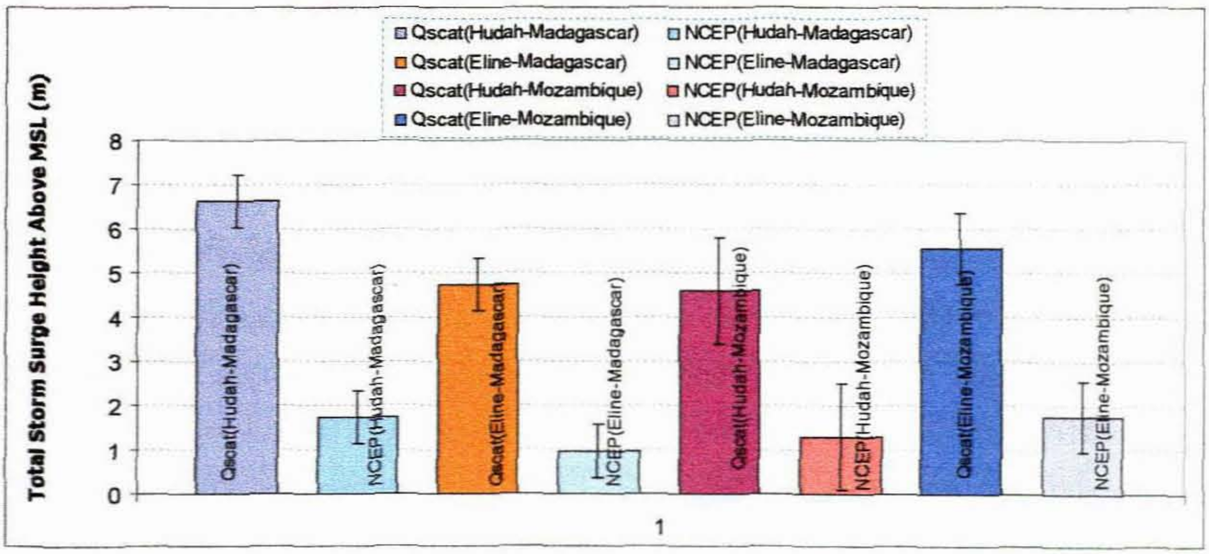

Fig 7.6 (b): Estimated total storm surge with mean location tidal range as error bar

7.2 Comparison of Satellite, Modeled and Measured Rainfall

It is important to make comparison between direct and indirect methods of estimating rainfall. This practice is particularly useful when there are few rain gauge stations. Similar research has focused on continental Africa, while very few have paid attention to the SWIO. Therefore, although limited in data, comparison is made between satellite IR, TMI microwave, model estimates of rainfall and insitu-measured values, particularly in the TC spiral rain band. The results indicate the level of performance between the different methods of rainfall measurement and serve as an initial benchmark for assessing rainfall impacts of TC spiral bands in the SWIO. Table 7.2 summarizes the case study TC rainfall. Note that presentation of TMI measured rainfall is for studying the TC spiral rain band near the equatorial SWIO only.

The estimated rainfall intensity maps for TC Eline and Hudah are shown in figures 7.7 (a) - 7.7 (d) and 7.8 (a) to 7.8 (d) respectively. On 14 February TC Eline had a spiral rain band over the equatorial SWIO. The model estimated rainfall intensity ranged from 20 to 100 mm per day (fig 7.7 a). The rainfall intensity increased to a maximum of 150 mm per day on 17 February when Eline crossed the coast of Madagascar. Similar rainfall intensity was observed over south Mozambique even when Eline was still over Madagascar (fig 7.7 b). Widespread flooding was reported over southern Mozambique. TC Eline re-intensified as it entered the Mozambique Channel (fig 7.7 c). The model estimated rainfall at landfall of TC Eline over southern Mozambique on 21 February ranged from 50-150 mm per day (fig 7.7 d). The arrival of TC Eline and its intense rainfall had a double impact causing the worst disaster in the SWIO since 1951. The maximum reported wind was 62.5 m s^{-1} and observed rainfall was 149 mm reported at Chipinge, Mozambique on the 21 February.

Three day total rainfall at Levebu from 22-25th February was 502 mm while the total monthly rainfall was 1212 mm (table 7.2). Comparison between daily model estimated and measured maximum rainfall is in close agreement although model rainfall is slightly higher. The reported number of deaths in Mozambique was 700, while 76 died in Madagascar and Zimbabwe. In Mozambique alone there were a total of 800,000 disaster victims and the total estimated disaster cost was 0.5 billion US dollars (table in appendix).

On the other hand intense TC Hudah had model estimated rainfall intensity (figures 7.8) less than 100 mm per day during its trajectory over Madagascar and north Mozambique from 2 to 5 May 2000. However, the reported maximum rainfall over Madagascar (Antalaha) was 161 mm while 171.6 mm along the northern Mozambique coast at Quelinane (table7.3). In this case the model estimated rainfall is lower than observed. This difference could be attributed to the enhancement of rainfall due to local orograpghy as discussed earlier in chapter 6. The maximum surface wind reported was 45 m s^{-1} causing 111 deaths and 300,000 disaster victims in Antalaha, Madagascar.

As was stated in the objectives of the research the spiral rain band associated with the revolving TC is also of interest. In chapter 6, the daily evolution of the CMAP precipitation pattern two days before and after peak cyclone activity was analyzed and it was concluded that there were large spatial and temporal variability distinguished by TC track. However the CMAP precipitation resolution of 250 km is low in resolving a spiral rain band of order 50 km. Its structure is studied by comparing infrared (CMAP), microwave measurement (TMI) and observed station rainfall intensity.

Figure 7.9 (a) and 7.9 (b) are TMI maps for TC Harry in March 2003. It should be noted that these images are the only two TMI maps available in the RSS data base. The TMI images show rainfall intensity in millimeters per hour in contrast to the satellite-modeled (GLOBE) rainfall which gives rainfall intensity per day.

From the TMI data it is clear that on 7 March 2003 (fig 7.9 a) the spiral rain band was located south of 5° S and on the early morning of the 8^{th} the spiral rain band crosses over the main islands of the Seychelles (fig 7.9 b). Deep patches of embedded convective clouds are revealed within the spiral rain band with maximum precipitation rates of 30 mm per hour. These rain rates although isolated, are equivalent to rain rates around the inner core of the TC. The satellite - model rainfall for TC Harry estimates rainfall of 30 - 40 mm per day over Mahe, Seychelles. NCEP model estimated rainfall is around 20 mm per day while the station measured rainfall on Mahe, Seychelles was 96.2 mm in 24 hours on 8 of March 2003.

TC Gafilo (Feb 2004) was also monitored for its rainfall impacts as it moved across northern Madagascar. Comparison between TMI and model estimated daily rainfall cannot be made because of lack of data. Figure 7.10 (a) and 7.10 (b) shows modeled estimated rainfall associated with the spiral rain band. Rainfall intensity ranged from 50-100 mm per day over Seychelles (Mahe) for TC Gafilo on 4 to 5 March 2004. Station observed rainfall (Mahe, Seychelles) was 48 mm and 73 mm on 4 and 5 March, respectively. Widespread flooding was reported over the island. Dry conditions followed immediately thereafter (fig 7.10 d and 7.10 e). TC Gafilo spiral rain band development and evolution agrees well with the results in chapter 6 for the composite precipitation pattern of west-ward moving TC. On landfall over north Madagascar Gafilo model estimated rainfall intensity on 8 March ranged from 100-250mm per day. The local orography in northern Madagascar plays an important role in enhancing rainfall. As a consequence 18 people were killed by widespread flooding and over 50,000 were left homeless.

TC Name	Location	Model Estimated mm/day	TMI mm/ hour	Observed Daily mm/day	Observed 3-Day Average
Eline	Madagascar Mozambique (Chipinge) Mozambique (Levebu)	150 (17 Feb 2000) 50-150 (21 Feb 2000) 50-150 (21 Feb 2000)	- - -	- 149 -	-- - 502
Hudah	Madagascar (Antalaha) Mozambique (Quelinane)	50-100 (2 Apr 2000) 50-100 (5 Apr 2000)	- -	161 171.6	- -
Harry	Seychelles (Mahe)	30-40 (8 Mar 2003)	30	96.2	-
Gafilo	Seychelles (Mahe) Northerm Madagascar	50-100 (5 Mar 2004) 100-250 (8 Mar 2004)	- -	73 -	- -

Table 7.2: Summary of case study TC rainfall

Fig a

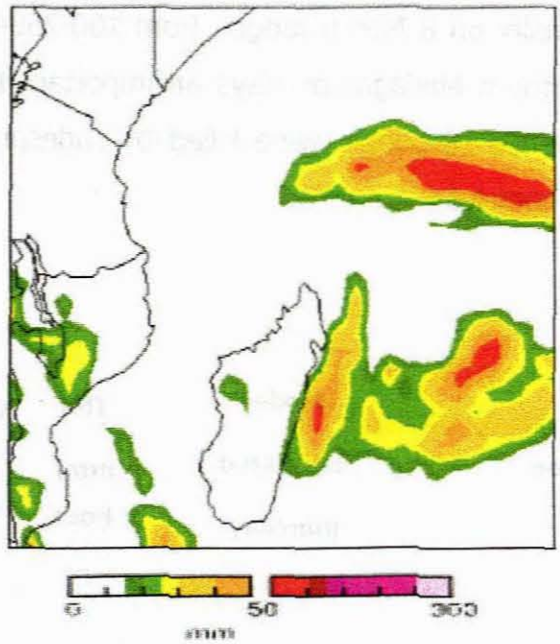

Fig 7.7 (a): Model estimated rainfall for TC Eline on 14 February 2000

Fig b

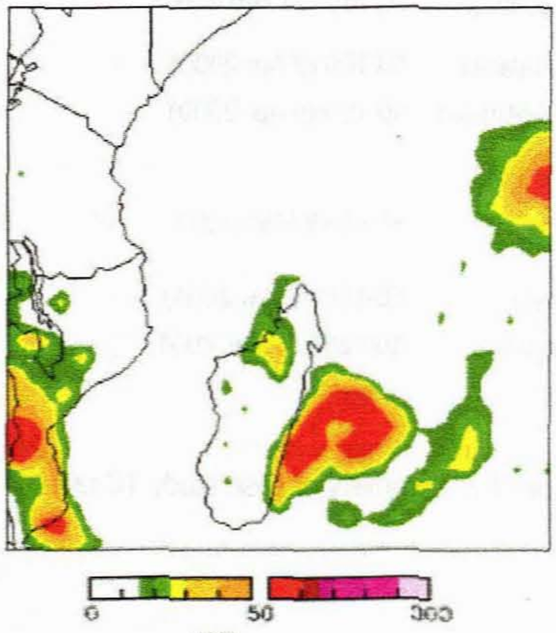

Fig 7.7 (b): Model estimated rainfall for TC Eline on 17 February 2000

Fig c

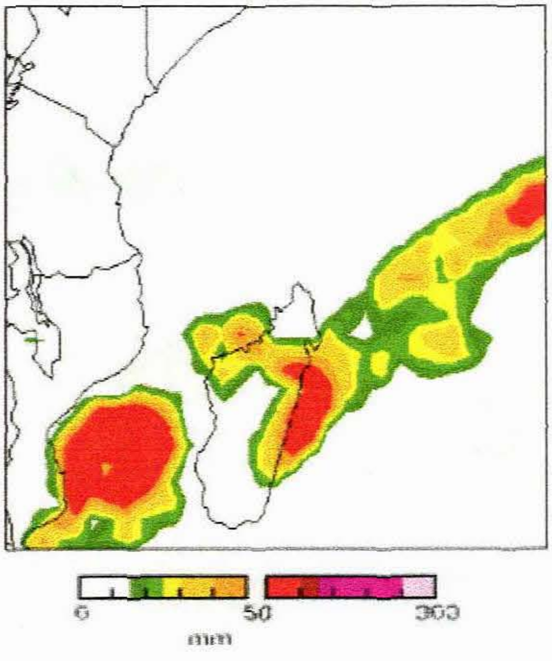

Fig 7.7 (c): Model estimated rainfall for TC Eline on 20 February 2000

Fig d

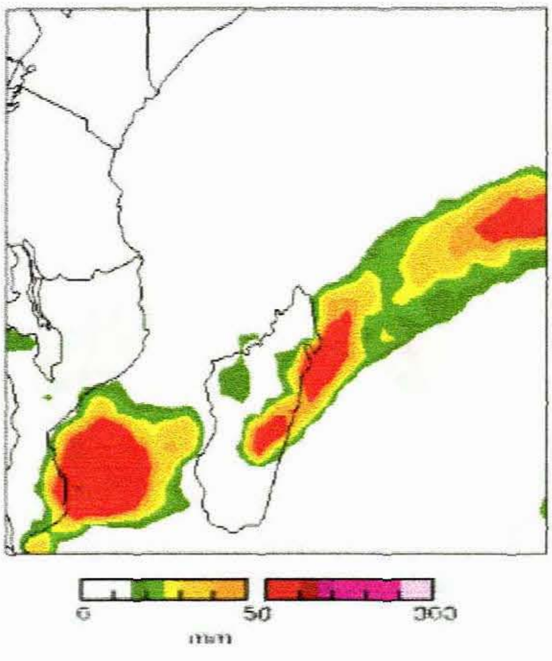

Fig 7.7 (d): Model estimated rainfall for TC Eline on 21 February 2000

Fig a

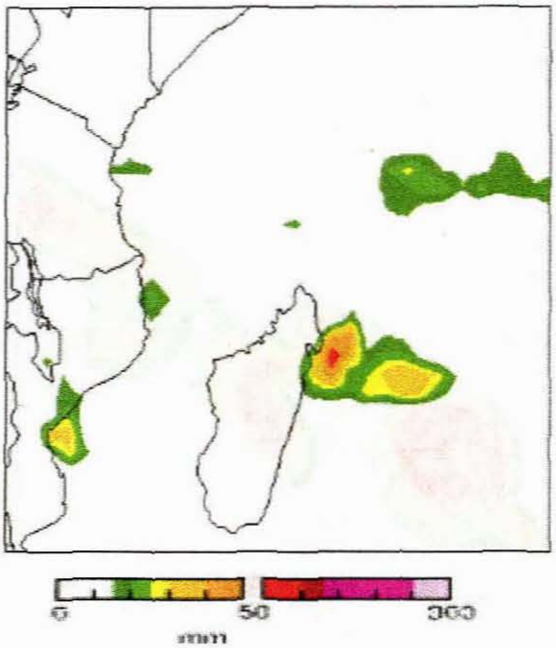

Fig 7.8 (a): Model estimated rainfall for TC Hudah on 2 April 2000

Fig b

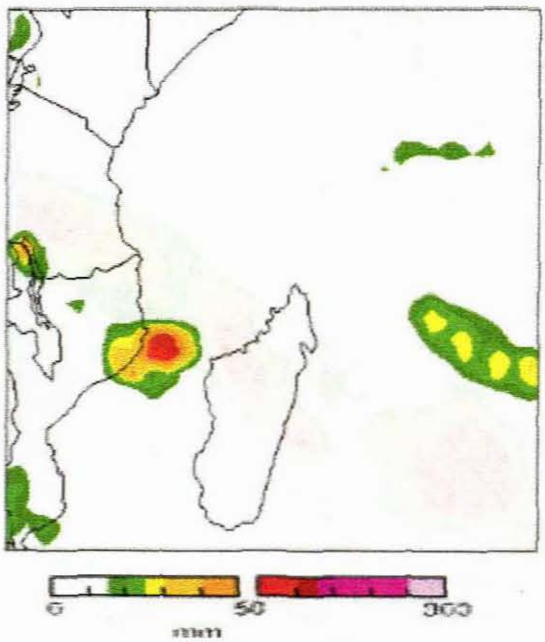

Fig 7.8 (b): Model estimated rainfall for TC Hudah on 5 April 2000

Fig a

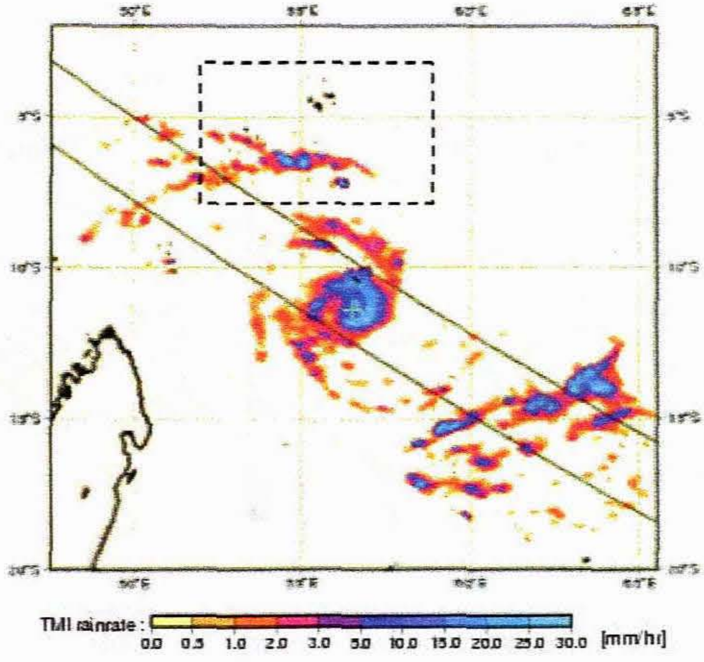

Fig b

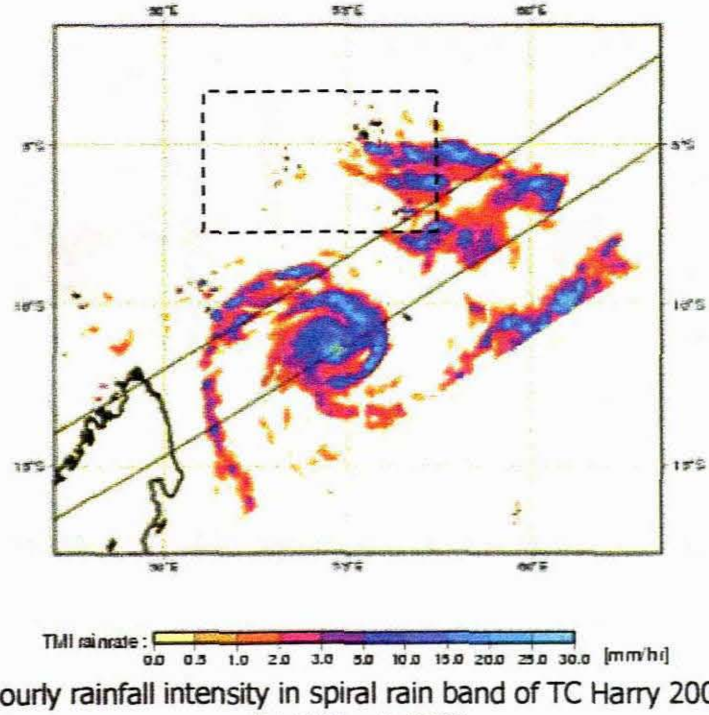

Fig 7.9: TMI hourly rainfall intensity in spiral rain band of TC Harry 2002 on (a) 7 and (b) 8 March 2003.

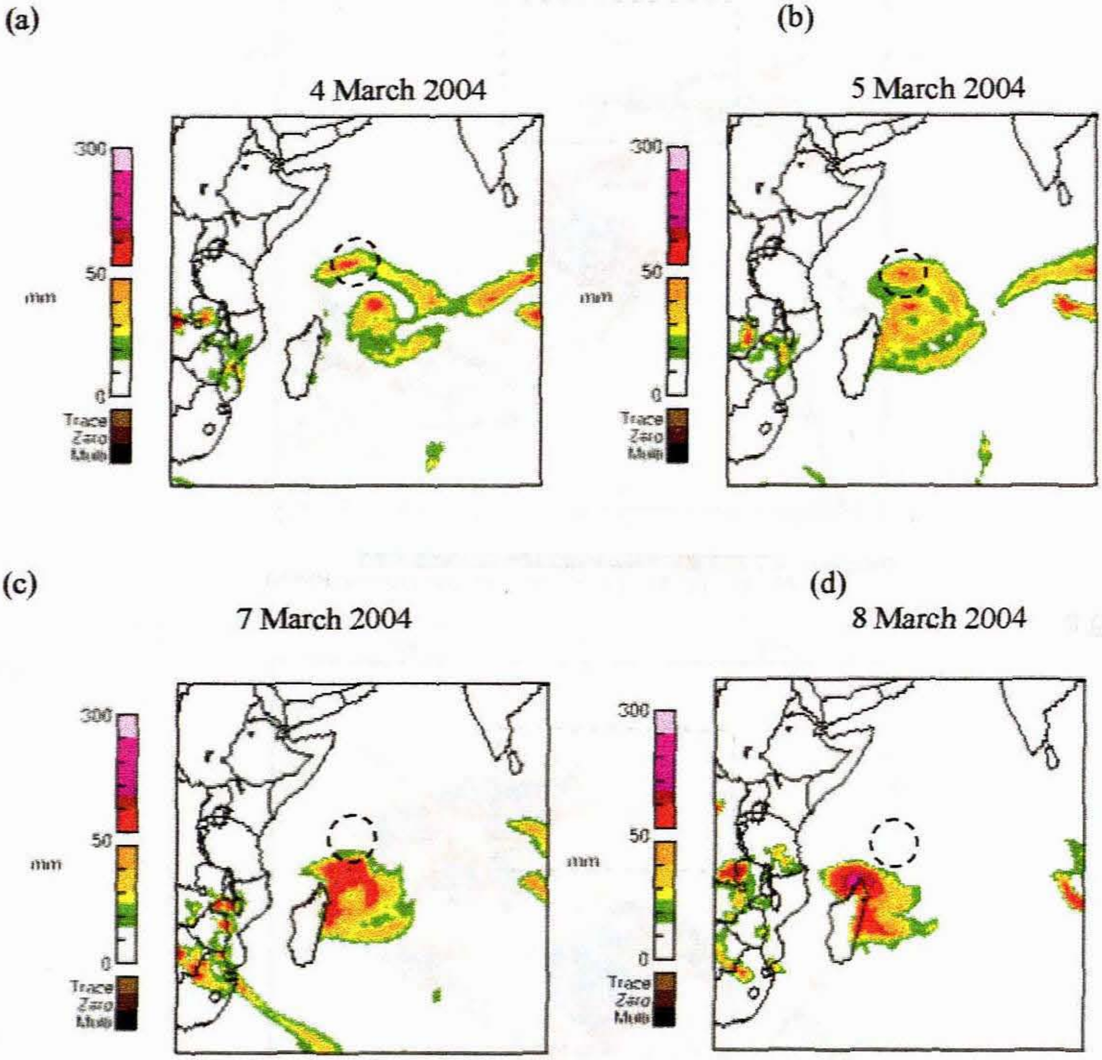

Fig 7.10: Satellite and model precipitation of TC Gafilo March 2004

7.3 Comparison Between Predicted and Observed TC position and Intensity

A total of 18 cyclones from 1999-2004 with a total of 48 prediction advisories from US Navy were used to access the predicted TC center and intensity in the region 45-60° east. Comparison was made with the official position and intensity of the Reunion tropical cyclone center for the SWIO. Figure 7.11 (a) shows that the error in the latitude is positive and increasing from 0.1 to 0.3 degrees on average from 12 to 48 hours prediction. The longitude error is increasing negatively from almost zero at 12 hour forecast to 0.6 degree at 48 hour forecast. This suggests that cyclones are predicted to move too much south compared to observed position. The results also suggest that TCs are predicted to move slowly than observed. Figure 7.11 (b) shows the standard deviation between the predicted and observed TC center for the 12, 24, 36 and 48 hours forecast. The graph shows the standard deviation increasing significantly with time from 0.9, 1.2, 2.1 and 2.8 degrees respectively. There is a 32 % deterioration in TC center from 12 to 48 hours forecast which is equivalent to about 215 km error in terms of distance. These results are consistent with the UK meteorological services mean error in TC position from 1999 - 2004 (fig 7.11). The mean error in TC positions are 50, 150, 200, 280, 410 and 550 km at T+ 0, T+24, T+ 48, T+ 72, T+ 96 and T+ 120 hours prediction, respectively. The mean error in TC position has decreased since the 1990's, but is higher during strong ENSO years such as 1991-1992 and 1997-1998.

On the other hand, there is consistent overestimation in both the 10 minutes maximum wind speed and maximum gust by 7.5 m s^{-1} and 10-12 m s^{-1} respectively (fig 7.11 d). This suggests that TC intensity is overestimated by the US Navy prediction model compared to the Meteo-France Reunion tropical cyclone center observations. The causes of such differences are likely to be found in the interaction of the steering flow and the TC circulation.

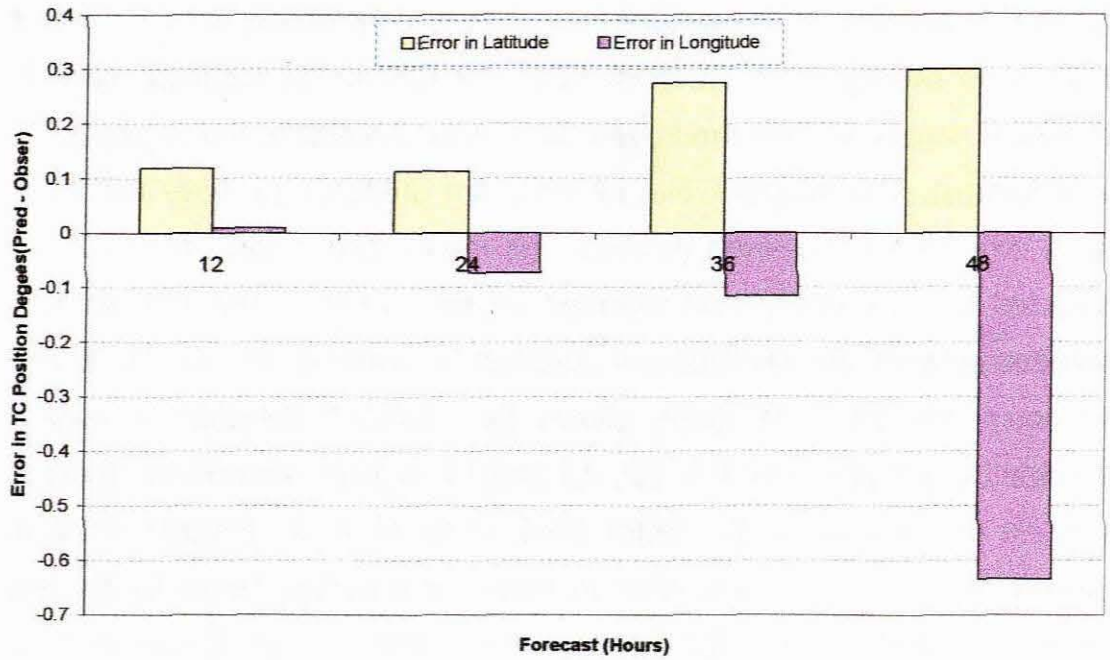

Fig 7.11(a): Error (Difference between predicted and observed position) in latitude, longitude.

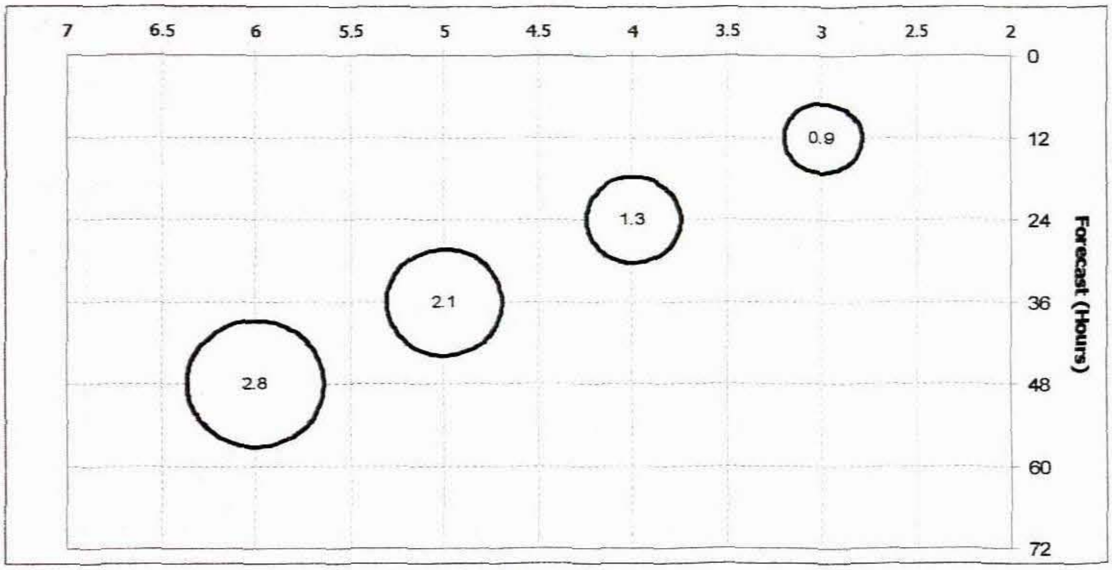

Fig 7.11 (b): Modulus ($Z = \sqrt{(STDlat)^2 + (STDlon)^2}$) of standard deviation of the TC position with increasing forecast Time

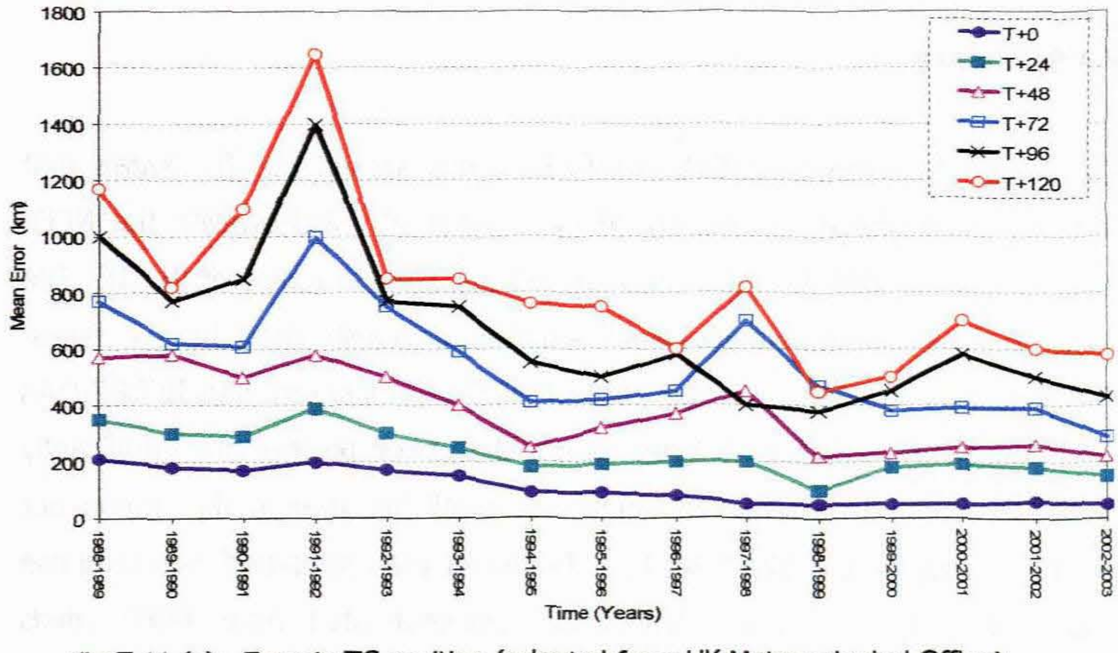

Fig 7.11 (c): Error in TC position (adapted from UK Meteorological Office)

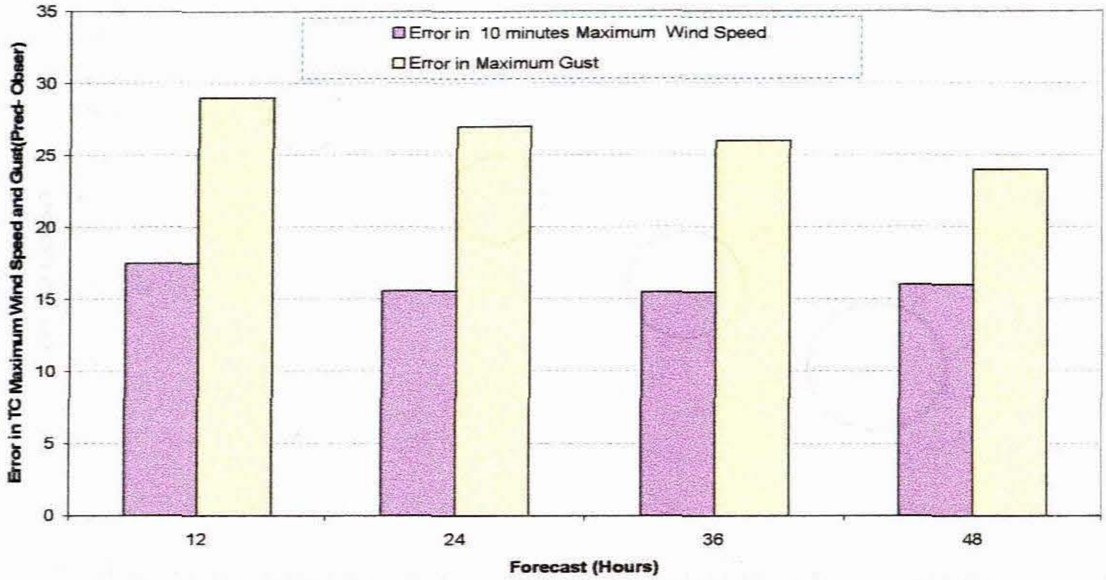

Fig 7.11(d): Error (Difference between predicted and observed) in 10 minutes maximum wind and maximum gust.

7.4 Summary

Comparison between QuikSCAT and NCEP winds around the TC reveals that NCEP is underestimating wind speed by a factor of 2.2. However, the NCEP model overestimates the fetch area around the 300 km radius of the TC. The computed cyclone generated swell height is underestimated by 1.7 times. Travel time is also longer in the case of NCEP. Comparison with NCEP/NOAA wave height for selected cyclones shows that swell heights are significantly underestimated. Real observed heights of swell are rare in the region but isolated comparisons indicate swells to be higher than computed. Sea level rise and total storm surge is significantly underestimated from NCEP winds compared to QuikSCAT winds. Total surge is about 4 times lower using NCEP winds. A comparison between US Navy predicted TC location and observed center from Meteo-France Reunion shows that the predicted cyclone is biased to move southwards. It is also revealed that cyclones are predicted to move more slowly compared to its observed speed. There is a 32% deterioration in predicted cyclone center location for 12 to 48 hours forecast, which is equivalent to about 200 km distance error.

TMI high - resolution data reveals high intensity rainfall associated with the spiral band in the SWIO. The rainfall intensity in the spiral rain band in the vicinity of Seychelles is as much as 30 mm per hour. Comparison is made with satellite and modeled data. It is shown that the rainfall intensity per day in the spiral rain band can range from 50 to 100 mm per day.

Wave height and peak wave direction fields predicted by NCEP/NOAA using the Wave Watch 3 model shows realistic wave height and peak wave direction generated by TC Gafilo. Although only a case study, this suggests NOAA/NCEP wave model to be performing better than in the case of TCs Hudah and Eline in the early 2000. The improvement may be largely associated with the availability of higher resolution wind field data from QuikSCAT. Cyclonic generated swells, storm surges and spiral rain band rainfall have important impacts in the SWIO. The comparison between various methods of data measurement and prediction schemes has offered a unique opportunity of impact assessment of cyclonic daily weather for only a few cases. A greater sample size would be necessary to draw firm conclusions.

The next chapter summarizes the results, and provides a discussion, conclusion and recommendation from this research.

Chapter 8

Conclusions and Recommendations

8.1 Introduction

In this chapter the main findings are summarized and a discussion is given to synthesize the main results and contributions of the research.
Recommendations are put forward to improve data bases and research on tropical cyclone prediction, impacts and mitigation strategies in the SWIO.

8.2 An Overview of Data Problems in the SWIO

A TC days index is the main basis for this work, but is formulated in a subjective way that imposes limitations. The TC days index has a correlation of less than 0.7 with local in-season field variables. The analysis of daily circulation around TC exposes some problems of data in the SWIO. Available grided re-analysis data are low in resolution, while higher resolution data (QuikSCAT, TMI) are only recently available and have gaps. The near equatorial region of the SWIO is indirectly influenced by TC and is somewhat neglected because TC activities are located further south. Fish catch data is subject to external factors (political and economical) while disaster data is somewhat lacking.

The human and resource capacity for these type of studies is lacking according to WIOMAP (Western Indian Ocean Marine Application Project), GOOS Africa (Global Ocean Observing System Africa), IO-GOOS (Indian Ocean Global Ocean Observing System) Science Implementation Plans.

8.3 Summary of Results

Chapter 3

The decade of 1960-69 was the most active in terms of intense tropical cyclone days while 1980-99 was the least active in SWIO. The ocean and atmospheric fields for high minus low cases of intense TC has revealed the potential climate signals influencing TC variability in the SWIO. The composite pattern shows the Atlantic zonal overturning. The composite analyses reveal a dipole-like pattern in the upper level velocity potential, OLR, Specific humidity and precipitation between South America and Indian Ocean. The South America signal is much stronger than the Indian Ocean signal. Another important pattern is revealed in the GPH with a dominant low centre in the southeast Pacific. It has a zonal wave number 3 structure particularly in SON. The oceanic parameters (HCA and subsurface temperature) reveal an east-west dipole in the Indian Ocean induced by a coupled propagating Rossby wave that impacts TC in the SWIO. In phase with this coupled Rossby wave is a westward-moving cyclonic circulation which increases north westerly monsoon flow to the north of Madagascar and easterly trade winds in the cyclone season.

Chapter 4

The south Pacific Geopotential height has the strongest association with the TC days index in the SON season. Other results suggest that ENSO plays a key role in TC variability in the SWIO by transmitting a signal through the Atlantic Zonal Circulation. The South America climate seems to operate in anti-phase association with the west Indian Ocean in respect of high and low TC days.

Anomalous OLR (drought /flood)) over the Amazon is linked with TC variability in SWIO. The zonal overturning is in fact an integral part of the global ENSO as indicated in the correlation and CWT analyses. La Nina conditions are favorable for TC development. The Atlantic Zonal Circulation leads the processes compared to the relatively slow eastward propagation of oceanic fields. Ocean-atmosphere interaction in the Indian Ocean plays a secondary role in developing the zonal overturning. Statistical analysis shows that the southeast Indian Ocean SST is significantly associated with the variability of TC days. There is coupling between the sub-surface and surface ocean temperature.

The intense TC index shows biennial (~2.4 yr) and decadal (~10 yr) cycles. The biennial cycle is modulated by the stratospheric quasi-biennial oscillation (QBO). It is suggested that the Atlantic Zonal Circulation (AZC) and SST in the eastern Pacific are conspiring in the decadal variability of TC days as revealed by low frequency data analyses. The AZC lags Nino 3 SST at decadal cycle unlike at inter-annual time scale.

Chapter 5

In this chapter multivariate models were developed for the prediction of TC days in the SWIO at various lead times. The models performances at 3, 6 and 9 months lead time are 48 %, 38 % and 33 % respectively. Newly uncovered predictors have significantly improved the seasonal prediction of TC in the SWIO. The new predictors are the south east Pacific geopotential height, SST in the southeastern Indian Ocean and the OLR over South America. Cross-validation technique suggests 90 % and 70 % operational reliability when the first and last decades of the data are removed respectively. The predictors such as GPH and OLR are characterized with interannual (2-3 yr) and decadal (10 yr) temporal variability. The south East Indian Ocean SST has 3 - 4, and 6 year cycle and is associated with the coupled transient Rossby wave. The Southeast Pacific GPH leads the rest by around 5 months, while the southeast Indian Ocean SST lags predictors of the Pacific. The interannual stability of the predictors is not always guaranteed. Monthly analysis of the model predictors (GPH, SST, and OLR) for TC days suggests predictability is optimal in certain months (fig 5.7).

An anti-phase association is found between South America and Indian Ocean particularly during ENSO years. The propagation of a zonal wave three pattern in GPH in the southern hemisphere determines the downstream oscillation and bifurcation of the subtropical jet stream which modulates westerly wind shear over the SWIO.

The fish catch of the region are negatively associated with TC days. More TC days implies less fish catch. In contrast, the South east African fish catch is positively linked with the southeast Pacific GPH propagation.

Chapter 6

This chapter looks at composite daily variability of TCs according to track. TCs are steered westward by the presence of a strong persistent and quazi-stationary anticyclone in the southern SWIO. The westward-moving TC suffers from a lack of NW monsoon flow due to the Madagascar high lands. On the otherhand, TCs are steered southwest by the high pressure anomaly which shifts southeastward at the surface after peak TC intensity. In the upper troposphere the winds shift gradually from east to NNE. An important feature associated with the southwestward TC composite is the development and propagation of a core of pronounced easterly wind anomalies across the Arabian Sea, linked to the northern subtropical jet stream. The SW-moving TC maintains its intensity almost throughout the sequence due to enhanced kinematic and thermodynamic processes.

The southward-moving TC is characterized by rapid changes in the kinematic and thermodynamic processes *during the sequence around peak intensity*. The TC circulation weakens rapidly due to increased cool air advection and increased wind shear.

The southwest-moving TC has an enhanced symmetrical rain band compared to the other trajectories. The southward-moving TC is lacking a rain band. It is associated with dry conditions up to peak intensity and wet conditions after in the equatorial SWIO due to the rapid formation of the ITCZ. The other tracks are characterized with wet conditions up to peak intensity and dry conditions after.

Chapter 7

In chapter 7, the focus is laid on TC impacts at daily time scales. Comparison between QuikSCAT and NCEP winds around case study TCs reveals that the NCEP model underestimates winds by a factor of 2.2. The computed swell height is underestimated by a factor of 1.7. Comparison with NCEP/NOAA wave height for selected TCs shows that swell heights are significantly underestimated. Storm surge is also significantly underestimated by 4 times using NCEP winds compared to QuikSCAT winds. Wave height and peak wave direction fields predicted by NCEP/NOAA Wave Watch 3 model suggests significant improvement in marine weather prediction probably as a result of high resolution wind data inputs.

A comparison between US Navy predicted and observed TC locations show that cyclone is predicted to re-curve too early and move too slowly. The mean error from the 12 to 48 hours forecast is about 200 km. TRMM satellite products reveal high intensity rainfall associated with a spiral rain band in the SWIO. The rainfall intensity in the spiral rain band in the vicinity of Seychelles is as much as 30 mm per hour, totalling 50-100 mm per day.

8.4 Synthesis and Discussion

The predictability of TC days has improved significantly for the following reasons. Firstly, new predictors have temporal (biennial to decadal) variability similar to TC days. The biennial cycle of TC days is modulated by the phase of the QBO and the transient coupled Rossby wave which modulates SST and enhances cyclonic circulation in the SWIO (fig 3.15). Jury et al (1999) found an association between SST in the south East Indian Ocean and TC days. However, their model algorithm did not to capture this predictor. The coupled ocean Rossby wave connection with cyclone prediction was then suggested by Xie et al., (2001). However, the ocean-atmosphere interactions in the Indian Ocean play a secondary role in predicting TC days variability.

The other driving force of SWIO TC variability is the anti-phase association with convection over the Amazon particularly during ENSO years. The physical mechanism is through the Atlantic zonal circulation as shown in figure 8.1.

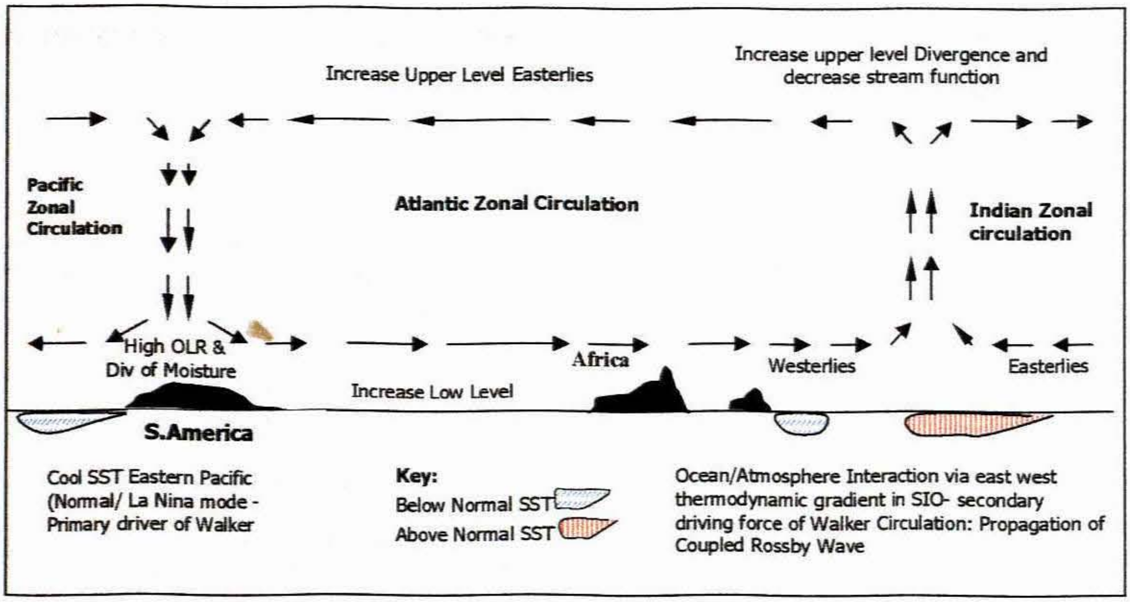

Fig 8.1: Conceptual model of the tropical Ocean-Atmosphere system before Intense TC season in SWIO

An important cause of TC variability is associated with the dominant zonal wave number 3 in GPH which foretells the downstream oscillation and bifurcation (splitting) of the southern subtropical jet stream modulating wind shear over the SWIO. We recall and note that Rakotondrafara (2001) found that named tropical cyclones were surprisingly found to be positively correlated with the vertical wind shear over the TC development area during the TC season, thus casting suspicions on the accuracy of the upper level wind data (1966 to 1998).

Figure 8.2 shows the propagation of the jet stream in the southern hemisphere prior to and during cyclone season. The number and positions of the major Rossby long waves and slight changes in amplitude/longitude position have major repercussion downstream. The schematic diagram shows the slow eastward propagation of the trough in the southeastern-Atlantic ocean to center over Mozambique Channel during the cyclone season. Dry/wet areas before and during TC season are over Amazon and Zimbabwe/ equatorial Africa respectively.

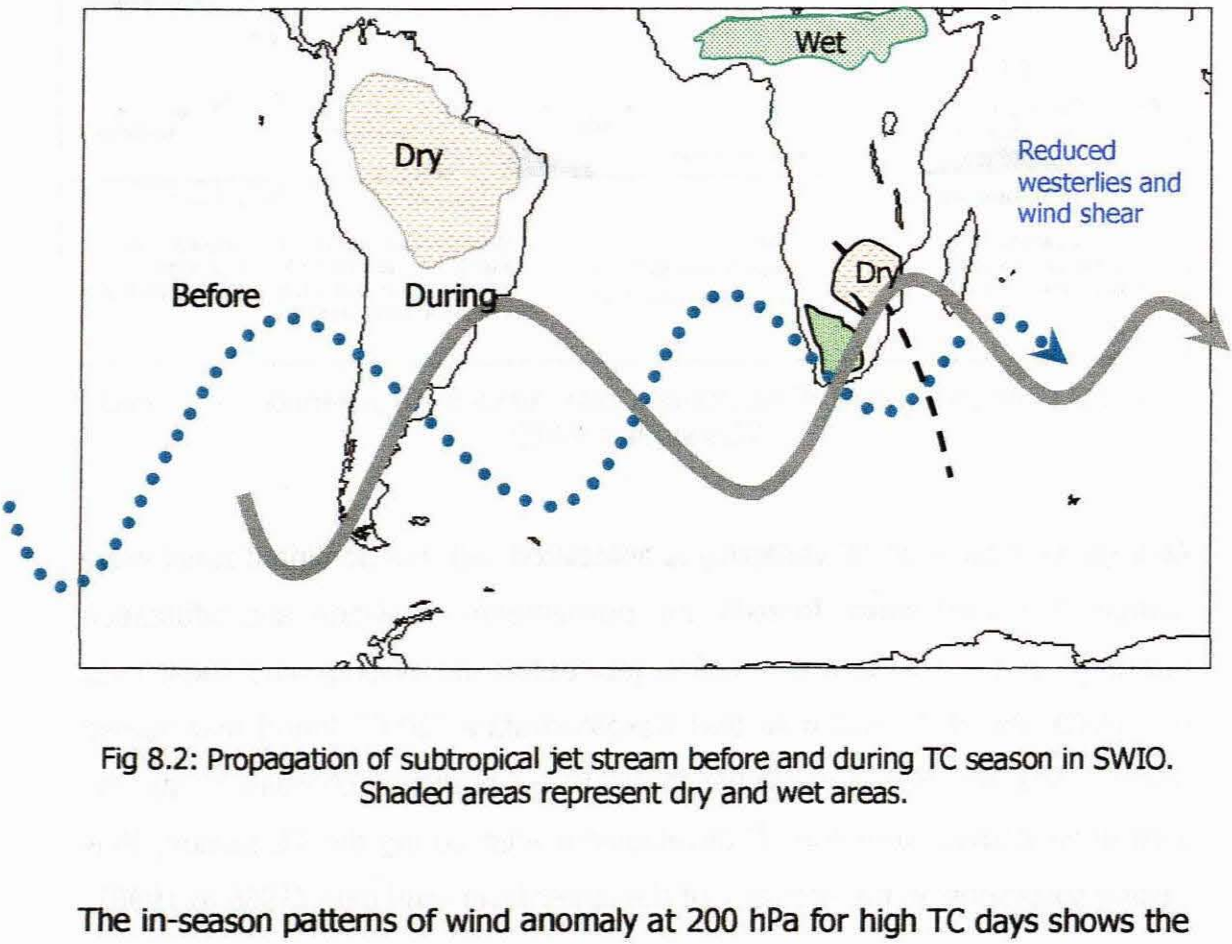

Fig 8.2: Propagation of subtropical jet stream before and during TC season in SWIO. Shaded areas represent dry and wet areas.

The in-season patterns of wind anomaly at 200 hPa for high TC days shows the subtropical jet stream over southern Africa and increased wind speed at the exit of the trough over the Mozambique Channel. A notable duct pattern is found in the equatorial SWIO (fig 8.3 a).

In the case of low TC days the wind anomaly pattern is characterized with an intense zonal STJ at 40-45°S (fig 8.3 b) with an upper level cyclonic flow polewards of the jet. Anti-cyclonic flow is found over southeastern Africa.
The in-season patterns of wind anomaly at 200 hPa for the difference in fields (high-low TC days) suggest bifurcation or splitting of jet between polar front jet (PFJ) and subtropical jet (STJ) (fig 8.3 c). The PFJ retreats and shifts pole wards, while the STJ is locked over southeastern Africa. The air speeds up (confluent pattern) on leaving trough just to the south of Madagascar causing anti-cyclonic development on the cold side/rearward of the trough axis and cyclonic development on the warm side/forward of the trough axis. The trough over Mozambique Channel acts as an attractor for TC to move west as indicated in the composite evolution of TC distinguished by track.

Another important pattern revealed in the difference in field is the duct flow pattern in the near equatorial SWIO which promotes positive vorticity anomalies of $+6.0X10^{6}s^{-1}$ over the equatorial SWIO (Seychelles) and negative vorticity of $-2.0X10^{6}s^{-1}$ northwest of Madagascar and central SWIO as shown in figure 8.4. Consequently convergence anomaly in the central SWIO cyclone basin increases to $-1.X\ 10^{-6}\ s^{-1}$ while cyclonic circulation (stream function) increases to $+1.2X10^{6}s^{-1}$. This agrees with earlier results of Rakotondrafara (2001) who found substantial differences in the low-level vorticity between active and inactive years of named TCs.

Meandering of jet stream occurs when north-south temperature gradient are less pronounced compared to winter when the flow is stronger in winter. It is not clear what may cause jet stream to block, split and shift polewards. When jet stream has meridional characteristics the pattern become locked in one geographical area giving persistent weather depending on location of trough/ridge of the loop. Orlanski (1998) found that the bifurcation of jet could be the effect of baroclinic eddies which exert a cyclonic forcing at the western poleward side of the Pacific storm and anti-cyclonic forcing at the eastern equatorward side of the storm track and is consistent with the trough-ridge system. The jet streams vary in strength and direction due to feedback mechanisms such as injection of energy from tropical disturbances, distribution of SST anomalies and temperature gradient.

Figure 8.5 (a) summarizes schematically the causes and mechanisms of intense TC variability in SWIO. It should be noted that this work can explain only 48 % of the TC variability. Therefore, more than 50 % of the TC variance is unaccounted. Perhaps chaotic processes could explain some of the unaccounted variance.

Figure 8.5 (b) is a schematic diagram showing how TC days may increase or decrease in the SWIO. For instance TC days are likely to increase by the following combinations:

- normal to La Nina type of mode in eastern Pacific Ocean (influences southeast Pacific GPH and Amason convection etc)
- low GPH in the southeast Pacific (decreases wind shears)
- increased SST in the southeast Indian Ocean (extra energy for TC development and intensification)
- dry Amason monsoon (enhances direct zonal circulation)
- a westerly phase of QBO

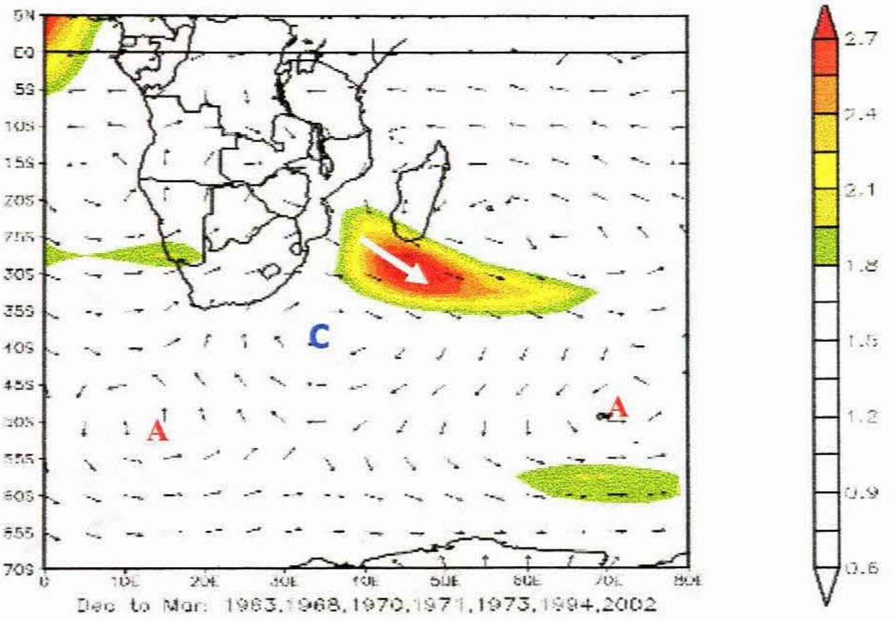

Fig 8.3 (a): 200 hPa wind anomaly pattern for high TC days showing STJ over the southern Africa, increase wind speed south of Madagascar and duct pattern near the equatorial SWIO

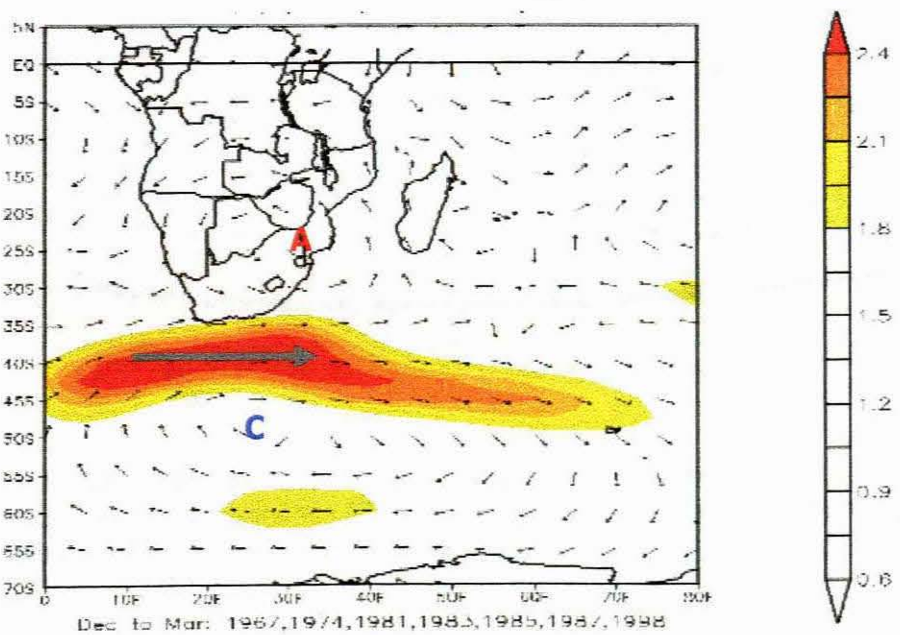

Fig 8.3 (b): 200 hPa wind anomaly pattern for Low TC days showing intense zonal jet south of Afica. Extratropical-cyclone polewards of the jet and anti-cyclonic flow over southeastern Africa

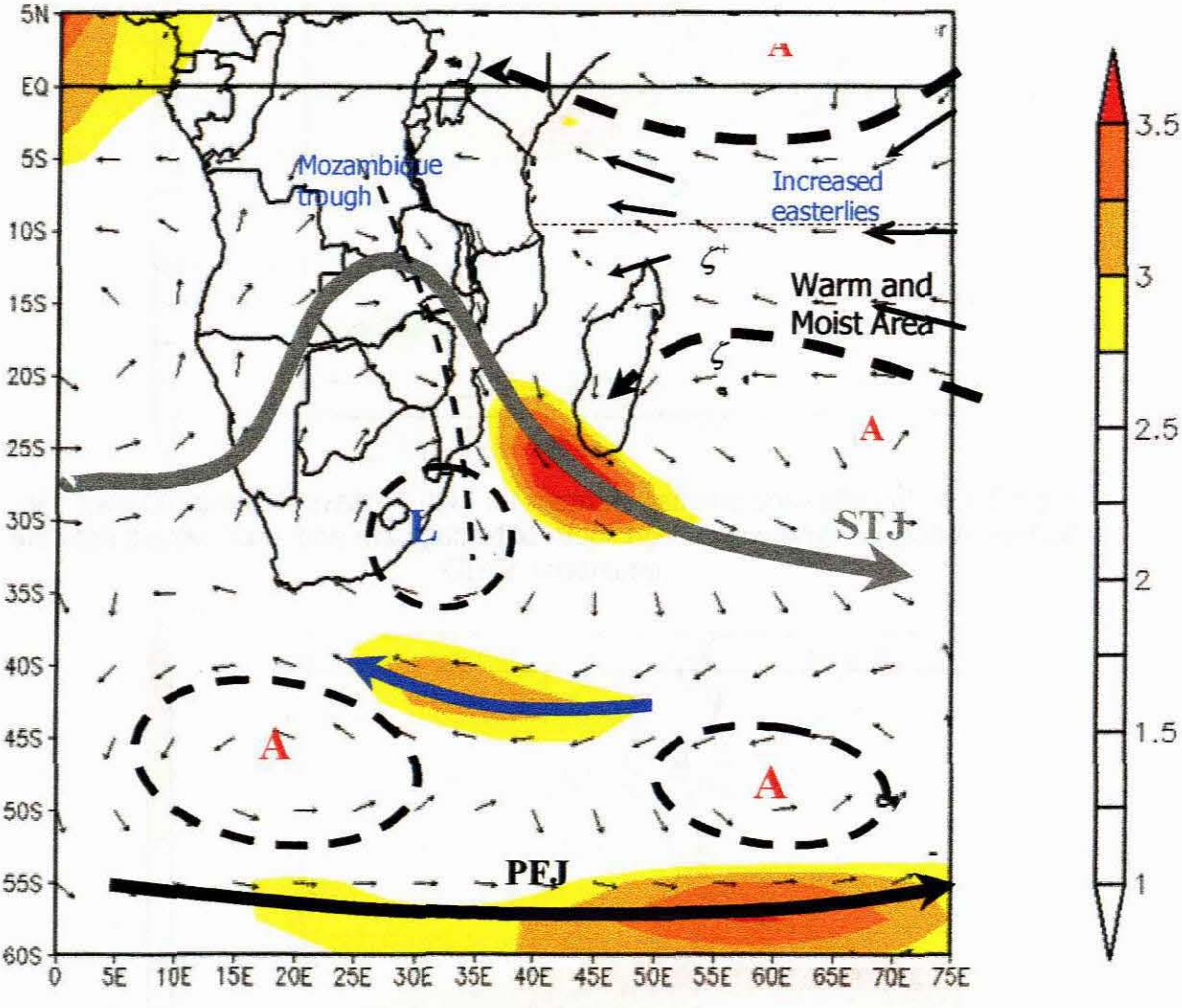

Fig 8.3 (c): 200 hPa wind anomaly pattern for high-low TC days showing biffurcation of jet streams. PFJ shift westerlies polewards and STJ confining westerlies southwest of Madagascar modulating wind shear locally.Reamarkable duct pattern near the equatorial SWIO promoting cyclonic vorticity developments over SWIO

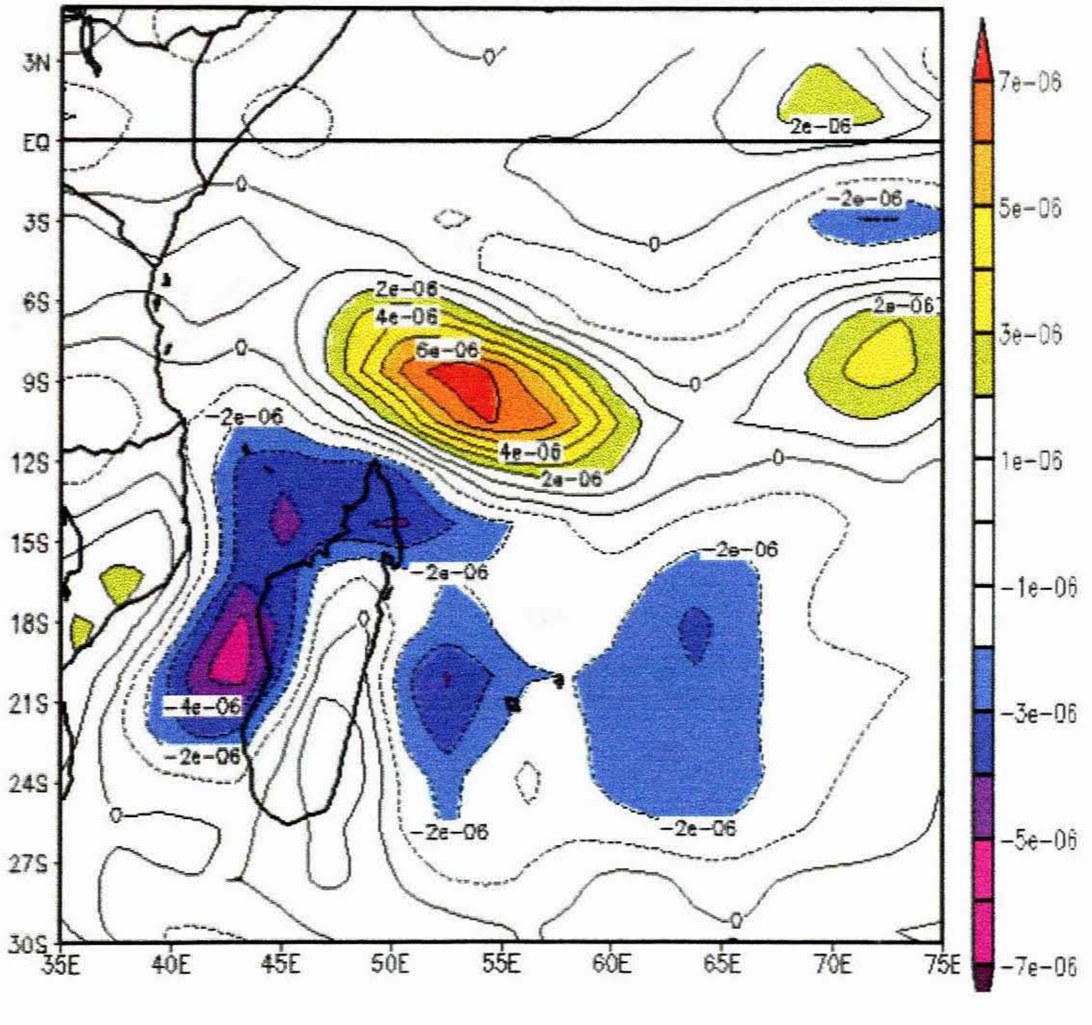

Fig 8.4: Enhanced cyclonic /anti-cyclonic vorticity at low level south/north of SWIO during TC season

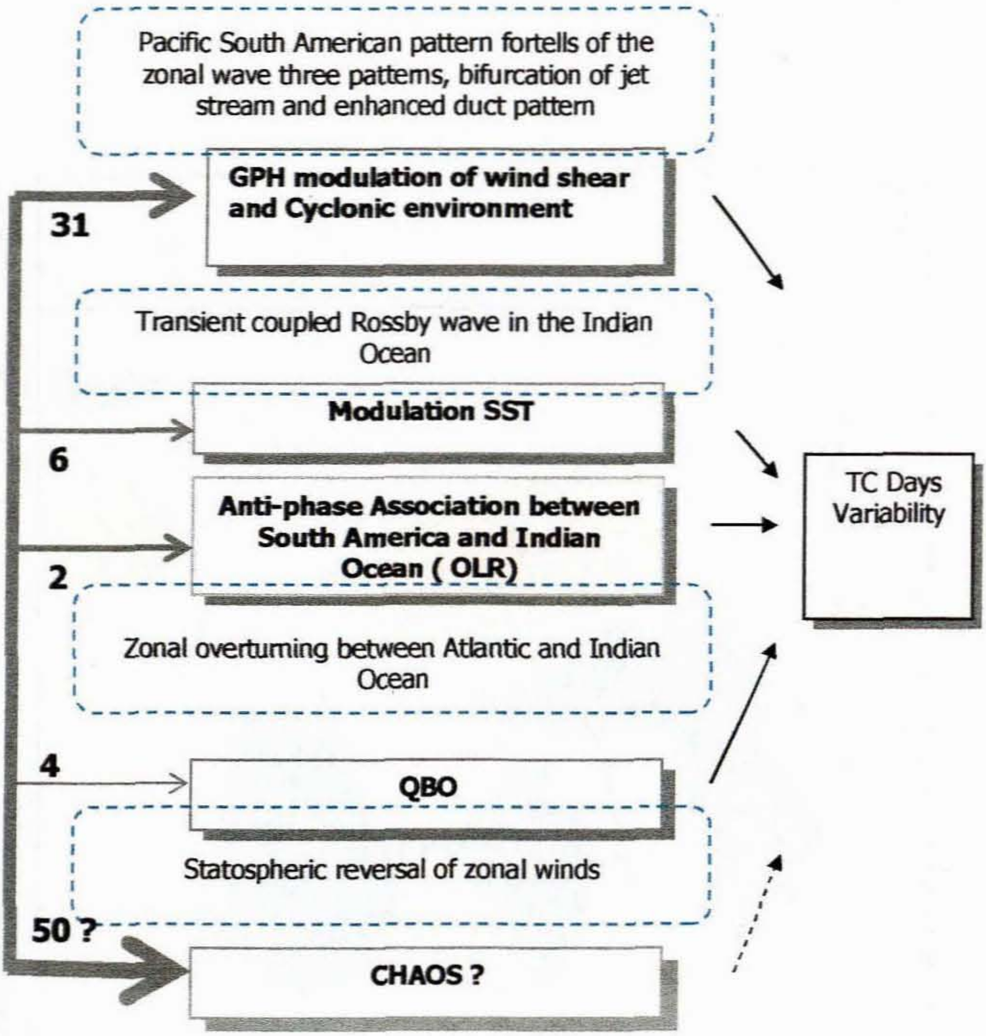

Fig 8.5 (a): Schematic diagram showing factors and mechanisms conspiring in TC days variability. Values indicate variance explained in TC days variability in SWIO.

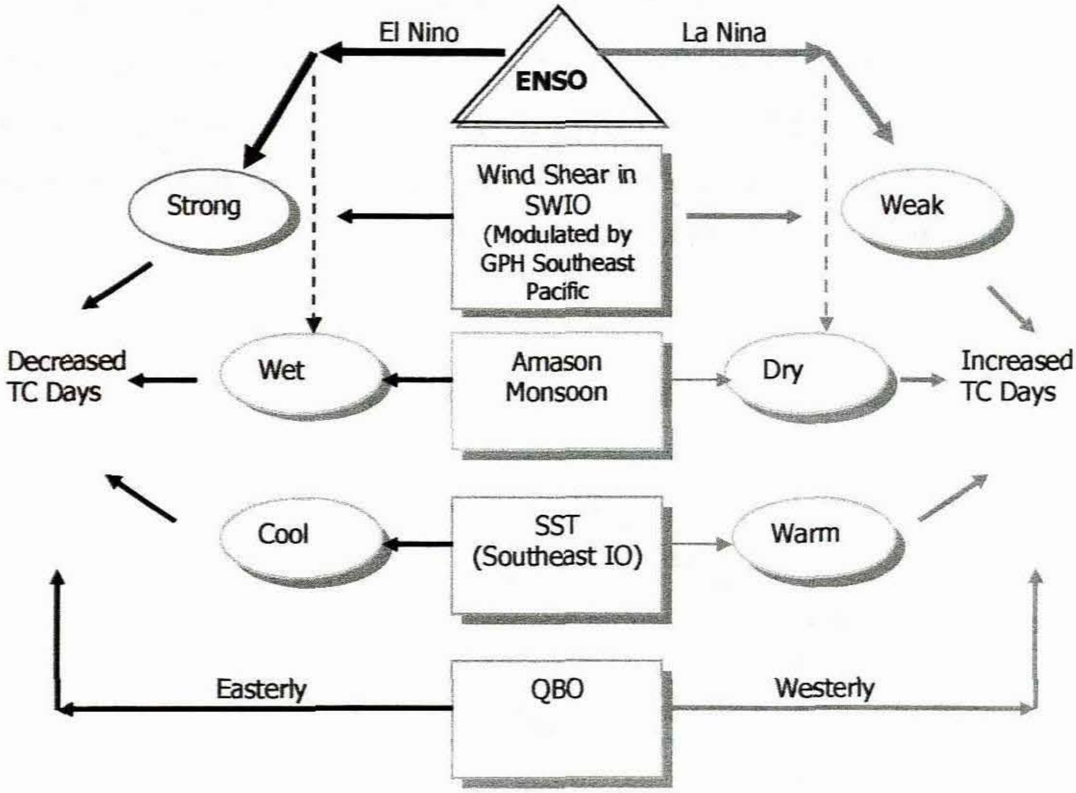

Fig 8.5 (b): Schematic diagram showing how TC Days increases / decreases in SWIO

The interaction of the northern sub-tropical jet stream is remarkable in the case of TC moving southwestward, while non-existent for westward-moving TC. The southward-moving TC shows a similar pattern but is contrasted by westerly wind anomalies in the southern sub-tropical region. The interaction of the sub-tropical jet stream increases equatorial tropospheric outflow (divergence) and increase inter-hemispheric inflow ($-\nabla \bullet (vk)$) which may cause TC to intensify (gain in KE) with help from the Hadley circulation. Figure 8.6 illustrates how TC intensity and track may be affected by the weakening/strengthening of the northern subtropical jet stream.

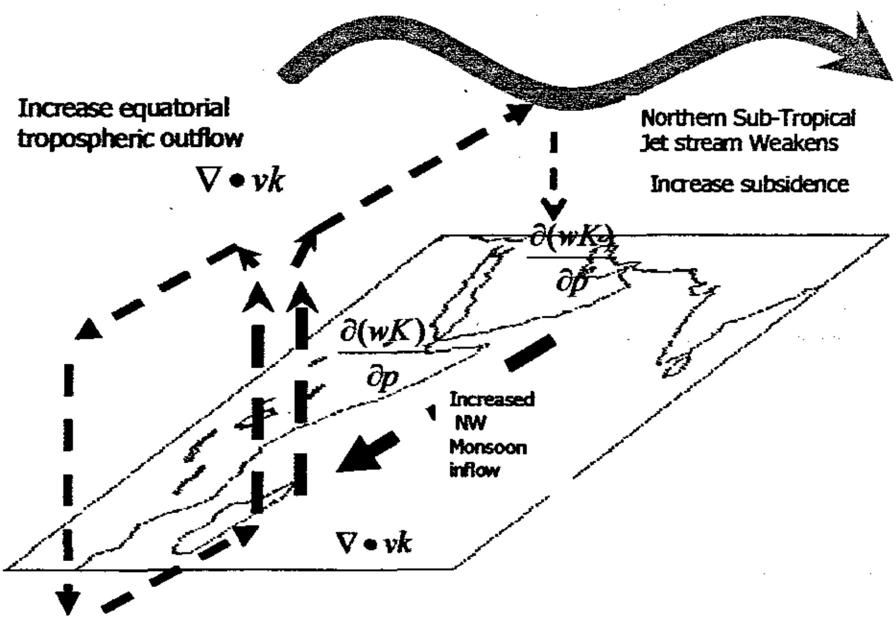

Fig 8.6: Interaction of northern sub-tropical Jet stream with TC in SWIO.

8.5 Conclusion

The intense TC index is characterized with biennial to decadal cycles that may be related with the QBO (Jury et al 1999) and the ocean thermohaline circulation respectively. It is found that the decade 1960-69 was the most active (STD +0.3) while 1980-89 was the least active (STD -0.7) in terms of intense tropical cyclone days in SWIO.

In general, the in-season analysis results agrees well with earlier findings of Rakotondrafara (2001) who found substantial differences in SST, the low-level vorticity and wind circulation between active and inactive years of named TCs. An improved multivariate model has been developed for prediction of TC days in the SWIO region (48 % of TC days variability explained). The model has improved by about 42 % compared the predecessor model (Jury et al 1999).

The dominant factor controlling TC days variability is the geopotential height zonal wave number 3 pattern that foretells of reduced wind shear over SWIO through the mechanisms of bifurcation of jet stream and enhanced tropical upper easterlies /lower westerlies and cyclonic vorticity over SWIO. This mechanism may also be related to the variability of intense cyclones in the east Australian basin.

A related mechanism is the anti-phase association between the South American monsoon and SWIO TC days through the Atlantic zonal circulation particularly during ENSO years. Decadal variability in TC days is influenced by the Atlantic Zonal circulation and SST in the Pacific Ocean.

The role of the transient coupled Rossby wave and its associated westward co-propagating cyclonic circulation is of importance to TC days prediction and fish resources of the region. Fish catch is negatively associated with TC days. The East-African fish catch responds to the GPH zonal wave three patterns.

The interaction of the northern sub-tropical jet stream is suggested to influence the intensity and track of TC in the SWIO. The southwest-moving TC maintains its intensity compared to the other tracks. There exist large temporal and spatial variability of rainfall distinguished by tracks. Intense rainfall of up to 30 mm h^{-1} is observed in spiral rain bands in the near equatorward region of SWIO.

The circulation around 300 km radius of TC is poorly resolved in NWP by a factor of 2 compared to space borne and insitu-measurements causing marine-weather and cyclonic impacts to be often underestimated.

8.6 Recommendations

a) Data and Observation

Recently the Indian Ocean has gained much interest due to its unique climate such as the Indian Ocean dipole, monsoon variability and its potential in marine resources etc. There has been a number of proposals and developing projects (GOOS-Africa, WIOMAP, IO-GOOS) that is expected to enhance data and observation in the Indian Ocean. Here, a few points are highlighted flowing from this research.

- Satellite data access should be extended to researchers and should include peripheral zones of TCs.
- Seychelles (Adabra atoll) and northern Madagascar needs to be further equipped to monitor cross hemispheric flow.
- There is a need to implement insitu data observation in SWIO as recommended in WIOMAP, GOOS-Africa, IO-GOOS Science Plans.
- There is a need to verify the link between the geopotential height zonal wave number 3 pattern with the east Australian basin intense tropical cyclone days

Modeling

(i) There is a need to carry out numerical modeling on the geopotential height zonal wave number 3 pattern that foretells of reduced wind shear over SWIO through the mechanisms of bifurcation of jet stream.

(ii) Model the northern subtropical jet stream and its sensitivity to daily TC intensity and track. The important question is:

- How does the variability of the Arabian Sea jet stream influence TC intensify and track in the SWIO ?

c) Assessing and Mitigation strategies

Public institutions face thousands of risks every day, ranging from minor issues to catastrophes. Effective management of these risks allows the institution to continue functioning, even when the unexpected happens. The same steps of risk management can be applied to a wide array of risks. The two main steps are: assess and mitigate. Assessing risk involves determining ones exposure to a risk. Mitigation are steps taken to reduce the threat, reducing vulnerability to the threat, reducing the likelihood of the risk, or reducing the impact of the threat. This could be achieved through the following:

(ii) Daily circulation characteristics of TC could be made of useful by implementing the following:

- Meteorological centers may use circulation around TC as a guide in predicting intensity, track and evaluating impacts distinguished by track.
- Aviation and marine users may use circulation maps as climatology for navigation guides.

(iii) Meteorological/marine centers should be aware and make adjustment to:

- the operational numerical weather predictions of wind analysis (NCEP, ECMWF) around 300 km radius of TC and related marine weather impacts (swell-driven storm surges).
- differences in estimating rainfall intensities by indirect methods (CMAP Infrared), TMI- high resolution passive microwave and model rainfall).

(iv) There is a need to improve disaster monitoring in the SWIO. This could be achieved by:

- RA1 (SWIO) cyclone committee to introduce or reinforce a regional benchmark in disaster evaluation.
- Annual review publication of TC by Meteo-France Reunion needs to extend presentation to include disaster statistics.

The study of the underlying causes, mechanisms, prediction of intense tropical cyclone days variability, and the daily circulation climatology surroundings TC distinguished by track has proved to be worthwhile. The comparison between various methods of data measurement and prediction schemes has offered a unique opportunity for impact assessment of daily cyclonic marine-weather in the SWIO.

References

Abdullah, A. J., 1966: The 'Musical sound' emitted by a tornado. *Mon. Wea. Rev.*, **94**: 213-220.

Arpe, K., L. Dumenil, and M. A. Giorgetta, 1998: Variability in the Indian Monsoon in the ECHAM3 model: Sensitivity to sea-surface temperature, soil moisture, and the stratospheric quazi-biennial oscillation. *J. Climate*, **11**: 1837-1858.

Asnani, G. C., 1993: *Tropical Meteorology*, **9**: 770-777.

Barnes, M. G.: Rainband influence on Hurricane intensity, University of Hawaii. 21st Conference on hurricanes and tropical meteorology, 611-612.

Barnes, G. M., E. J. Zipser, D. Jorgensen, and F. Marks, Jr., 1983: Mesoscale and convective structure of a hurricane rainband. *J. Atmos. Sci.*, **40**: 2125-2137.

Barnes, G. M., and M. D. Powell, 1995: Evolution of the inflow boundary layer of Hurricane Gilbert (1988), in press, *Mon. Wea. Rev.*

Baines, P. G., and W. Cai, 2000: Analysis of an interactive instability mechanism for the Antarctic circumpolar wave. *J. Climate*, **13**: 1831-1844.

Barnston, A. G., and C. F. Ropelewski, 1992: Prediction of ENSO episodes using canonical correlation analysis. *J. Climate*, **5**: 1245-1316.

Behera, S. K., P. S. Salvekar, and T. Yamagata, 1999: Simulation of Interannual SST Variability in the Tropical Indian Ocean, *Amer. Meteorol. Soc.*, **13**: 3487-3498.

Beven. L. J.: Tropical cyclone-environmental interactions in Hurricane Florence, National Hurricane Center, Coral Gables, Florida, USA. 21st Conference on hurricanes and tropical meteorology, 491-493.

Beven, J. L., 1993: Tropical cyclone environmental interactions during recurvature. Extended abstracts: 20th Conf. on Hurricanes and Tropical Meteorology San Antonia, *Amer. Meteorol. Soc.*, 38-41.

Bowden, K. F., 1983: Physical oceanography of coastal waters. 124-161.

Cai, W., and P. G. Baines, 2001: Forcing the Antarctic circumpolar wave by El-Nino – Southern Oscillation teleconnections. *J. Geophys. Res.*, **106** (C5): 9019-9038.

Cambelin, P., S. Jaincot, and I. Poccard, 2001: Seasonal and atmospheric dynamics of the teleconnection between African rainfall and tropical sea-surface temperature: Atlantic vs. ENSO. *Int. J. Climatol.*, **21**: 973-1005.

Cardone, V. J., W. J. Pierson, and E. G. Ward, 1976: Hindcasting the directional spectra of hurricane generated waves. *J. Pet. Technol.*, **28**: 385-394.

Cardone, V. J., and K. C. Ewans, 1992: Validation of the hindcast approach to the specification of wave conditions at the Maui location off the west coast of New Zealand. Preprints of the third International Workshop on Wave Hindcasting and Forecasting, May 19-22, Montreal, Quebec, 232-247.

Carleton, A. M., 1988: Sea-ice atmosphere signal of the southern oscillation in the Weddell Sea, Antarctica. *J. Climate*, **1**: 379-388.

Carril, A. F., and A. Navarra, 2001: Low – frequency variability of the Antarctic circumpolar wave. *Geophys. Res. Lett.*, **28**: 4623-4626.

Chelton D. B., 2000: Scatterometer-Based Assessment of surface wind field analysis from the European Center for Medium Range Weather Forecast, College of Oceanic and Atmospheric Science, Oregon State University, Corvallis, OR 97331-5503.

Christoph, M., T. P. Barnett, and E. Roeckner, 1998: The Antarctic circumpolar wave in a coupled ocean-atmosphere GCM. *J. Climate*, **11**: 1659-1672.

Clark, O. C., E. J. Cole, and J. P. Webster, 1999: Indian Ocean SST and Indian summer rainfall: Predictive relationship and their decadal variability, *J. Climate*.

Conkright, et al., 1998, World Ocean Database 1998: Documentation and Quality Control. NODC Internal Rep. 14, NOAA/NESDIS, Maryland, 43 pp.

Cox, A.T. and V.J. Cardone., 2000: Operational System for the Prediction of Tropical Cyclone Generated Winds and Waves. 6th International Workshop on Wave Hindcasting and Forecasting November 6-10, Monterey, California.

Das, P. K., M. C. Sinha, and V. Balasubramanyam, 1974: Storm surges in the Bay of Bengal. *Quart. J. Roy. Meteorol. Soc.*, **100**: 437-449.

Daubenchies I., 1992: Ten lectures on wavelets. SIAM Philadelphia.

Delprat N., B. Escuide, P. Guillemain, R. Kronland-Martnet, P. Tchamitchian and Torresan, 1992: Asymptotic wavelets and Gabor analysis: Extraction of instantaneous frequencies. IEEE transaction on information theory, **38**(2): 644-664.

Dennet, M. D., 1978: Variations of rainfall and seasonal forecasting in Mauritius. *Arch. Met. Geoph. Biokl.* B., **25**: 359-370.

Derber, J and Rosati, A, 1989, A global oceanic data assimilation system, *J. Phys. Oceanogr.*, **19**: 1333-1347.

Elsberry, R. L., 1993: Advances in dynamical Predictions and Modelling of tropical cyclone motion. Technical Report NPS-MR-93-002, Naval Postgraduate School, Monterey , CA 93943, 86 pp. And 35 pp appendix.

Flierl, G. R., and A. R. Robinson, 1972: Deadly surges in the Bay of Bengal, Dynamics and storm tide tables. *Nature*, **239**: 213-215.

Folland, C. K., T. N. Palmer, and D. E. Parker, 1986: Sahel rainfall and world-wide sea surface temperature. *Nature*, **320**: 602-607.

Folland, C. K., J. A. Owen, M. N. Ward, and W. Colman, 1991: Prediction of seasonal rainfall in the Shael region using empirical and dynamical methods. *J. Forecasting*, **10**: 21?6.

Foufoula-Georgiou, E., and P. Kumar, Eds, 1995: Wavelets in Geophysics. *Academic Press*, 373 pp.

Freilich, M. H., and R. S. Dunbar, 1999: The accuracy of the NSCAT-1 vector winds: Comparisons with National Data Bouoy Center buoys. *J. Geophys. Res.*, **104**: 11231-11246.

Freilich, M. H., and B. A. Vanhoff, 2001: Characterization of sea winds on QuikSCAT vector wind accuracy. In preparation.

Fujita, T. T., T. Izawa, K. Watanabe, and I. Imai, 1967: A model of typhoons accompanied by inner and outer rain bands. *J. Appl. Meteorol.*, **6**: 3-19.

Ghosh, S. K., 1977: Prediction of storm surges on the east coast of India. *Ind. J. Met. Hydrol. Geophys.*, **28**: 157-168.

Gloersen, P., 1995: Modulation of hemispheric sea ice cover by ENSO events. *Nature*, **373**: 503-506.

Goldenberg, S. B., and L. J Shapiro, 1995: Physical mechanisms for the relationships between El Nino, West African rainfall, and North Atlantic major hurricanes. *J. Climate*, (in press).

Gray, W. M., 1968: Global view of the origin of tropical disturbances and storms. *Mon. Wea. Rev.*, **96**: 669-700.

Gray, W., 1984a: Atlantic seasonal hurricane frequency. Part1: El Nino and 30 mb quasi-biennial oscillation influences. *Mon. Wea. Rev.*, **112**: 1649-1668.

Gray, W., 1984b: Atlantic seasonal hurricane frequency. Part II: Forecasting its variability. *Mon. Wea. Rev.*, **112**: 1669-1683.

Gray, W. M., J. D. Sheaffer, and C. W. Lansea, 1997: Climate trends associated with multi decadal variability of Atlantic hurricane activity. Hurricanes, climatr and socioeconomic impacts, edited by H. F. Diaz and R. S. Pulwarty, Springer, Berlin, 15-53.

Hastenrath, S., 1985: Climate and Circulation of the Tropics. Doordrecht, D. Riedel Pub., 455 pp.

Hastenrath, S., A. Nicklis, and L. Greischer, 1993: Atmospheric-hydrospheric mechanisms of climate anomalies in the western Indian Ocean. *J. Geophys. Res.*, **98**: 20219-20235.

Hastenrath, S., L. Greischer, and Van Heerden, 1995: Prediction of summer rainfall over South Africa. *J. Climate*, **8**: 1511-1518.

Hastenrath, S., 2001: In search of zonal circulations in the equatorial Atlantic sector from the NCEP-NCAR re-analysis, *Int. J. Climatol.*, **21**: 37-47.

Hirst, A. C., and J.S. Godfrey, 1994: The Response to a sudden change in Indonesian throughflow in a global GCM.*J. Phys.* Oceanogr., **24**,1895-1910.

Hoarau, K., 1999 : La frequence des cyclones tropicaux intenses dans le sud-ouest de l'ocean indien (1970-1999). *Publications de l'Association Internationale de Climatologie*,**12**: 405-413.

Holland, G. J., and R. T. Merrill, 1984: On the dynamics of tropical cyclone structural changes. *Quart. J. Roy. Meteor. Soc.*, **110**: 723-745.

Hsu, C. S., and W. T. Liu, 1995: Tropical Cyclone Intensity from scatterometer winds. Jet Propulsion Laboratory, California Institute of Technology Pasadena, California. 21st Conference on hurricanes and tropical meteorology, 286-288.

Huang, B., and J.L. Kinter III, 2002: Interannual variability in the tropical Indian Ocean. *J. Geophy. Res.*, **107** (C11), 3199, doi:10.1029/2001JC001278.

Jacobs, G. A., and J. L. Mitchell, 1996: Ocean circulation variation associated with the Antarctic circumpolar wave. *Geophys. Res. Lett.*, **23**: 2947-2950.

Jupp, P. E., and K. V. Mardia, 1980: A general correlation coefficient for directional data and related regression problems. *Biometrika*, **67**: 163-173.

Jury, M. R., and B. Pathack, 1991: A study of Climate and Weather variability over the Tropical Southwest Indian Ocean. *Meteorol. Atmos. Phys.*, **47**: 37-48.

Jury, M. R., B. Pathack, G. Campbell, B. Wang, W. Landman, 1991a: Transient convective waves in the tropical SW Indian Ocean. *Meteorol. Atmos. Phys.*, **47**: 27-36.

Jury, M. R., 1992: A climate dipole governing the interannual variability of convection over the SW Indian Ocean and SE African region. Trends *Geophys. Res.*, **1**: 165-172.

Jury, M. R., 1993: A preliminary study of climatological associations and characteristics of tropical cyclones in the SW Indian Ocean. *Meteorol. Atmos. Phys.*, **51**: 101-115.

Jury, M. R., B. Pathack, B. B. Wang, M. Powell, and N. Raholijao, 1994: A destructive tropical cyclone season in the SW Indian Ocean: January-February 1984. *S. A. Geogr. J.*, **72**: 53-59.

Jury, M. R., H. Mulenga, S. J. Mason, and A. Brandao, 1997: Development of objective statistical system to forecast summer rainfall over southern Africa. *WRC Report* No. 672/1/97.

Jury, M. R., 1998: Forecasting water resources in South Africa. Water resources variability in Africa during the XXth century (Proceeding of the Abijan '98 Conference held at Abijan, Cote d'Ivoire).

Jury, M. R., 1999: Interannual variability of Africa river flows and associated climate structure. Preprint volume of the Eight Conference on climate variation, 13-17 September 1999, Denver, Co. by the AMS, Boston, MA.

Jury, M. R., H. M. Mulenga and S. J. Mason, 1999: Exploratory long-range models to estimate summer climate variability over South Africa. *J. Climate*, **12**: 1892- 1899.

Jury, M. R., and B. A. Parker, 1999: Synoptic environment of composite tropical cyclones in the South-West Indian Ocean. *S. A. J. Marine Sci.*, **21**: 99-115.

Jury, M. R., B. Pathack, and B. Parker, 1999: Climatic determinants and statistical prediction of tropical cyclone days in the south west Indian Ocean. *J. Climate*, **12**: 1738-1746.

Jury, M. R., 2001b: Development of optimum statistical long-range forecast models of summer climate and hydrological resources over Southern Africa. A report to the Water Research Commission, based on research in the period 1997-2002.

Jury, M. R., D. B. Enfield, and J. Melice, 2002: Tropical monsoons around Africa: Stability of El-Nino-Southern oscillation associations and links with continental climate. *J. Geophys. Res.*, **107**(C10): 3151-3168.

Jury, M. R., and N. D. Mwafulirwa, 2002: Climate variability in Malawi, Part 1: Dry summers, statistical associations and predictability. *Int. J. Climatol.*, **22**: 1289-1302.

Kalnay, E., M. Kanamitsu, R. Kistler, W. Collins, D. Deaven, L. Gandin, M. Iredell, S. Saha, G. White, J. Woollen, Y. Zhu, A. Leetmaa, R. Reynolds, M. Chelliah, W. Ebisuzaki, W. Higgins, J. Janowiak, K. C. Mo, C. Ropelewski, J. Wang, R. Jenne, D. Joseph, 1996: The NCEP/NACR reanalysis 40-year project. *Bull. Amer. Meteor. Soc.*, **77**: 437-471.

Kaplan. J., 1987: An examination of the role of large-scale forcing on the rapid intensification of Hurricane Emily(1987), Hurricane Research Division, AOML Miami, FL33149. 21st Conference on hurricanes and tropical meteorology, 332-334.

Kelly, M. A. and D. A. Randall, 2001: A Two-Box Model of a Zonal Atmospheric Circulation in the Tropics. *J. Climate.*, **14**: 3944-3964.

Kurihara, Y., 1976: On the development of spiral bands in a tropical cyclone. *J. Atmos. Sci.*, **33**: 940-958.

Kumar, P., and E. Foufoula-Georgiou, 1993: A new look at rainfall fluctuations and scaling properties of spatial rainfall using orthogonal wavelets. *J. Appl. Meteorol.*, **32**: 209- 222.

Landsea, C. W., and W. M. Gray, 1992. The strong association between western Sahel monsoon rainfall and intense Atlantic hurricanes. *J. Climate*, **5**: 435-453.

Landsea, C. W., W. M. Gray, P. W. Mielke, K. J. Berry, 1992: Long term variations of Western Sahelian Monsoon rainfall and intense US landfalling hurricanes. *J. Climate*, **5**: 1528-1534.

Latif, M., and T. Barnett, 1995: Interactions of the tropical oceans. *J. Climate*, **8**: 952-964.

Ledley, T. S., and Z. Huang, 1997: A possible signal in the Ross Sea. *Geophys. Res. Lett.*, **24**: 3253-3256.

Ligda, M. G. H., 1955: Hurricane squall lines. *Bull. Amer. Meteorol. Soc.*, **36**: 340-342.

Lindesay, J. A., and M. R. Jury, 1991: Atmospheric circulation controls and characteristics of a flood event over central South Africa. *Int. J. Climatol.*, **11**: 609-627.

Liu, W. T., H. Hu, and S. Yueh, 2000: Interplay between wind and rain observed in Hurricane Flyod. *Eos, Trans. Of AGU*, **81**: 253 & 257.

Liu, W. T., T. Song, and W. Tang: Improvement of Scatterometer wind vectors-Impacts on Hurricane and coastal studies. Jet Propulsion Laboratory, California Institute of Technology, Pasadena, CA 91109, USA.

Makarau, A., and M. R. Jury, 1997: Predictability of Zimbabwe summer rainfall. Int. *J. Climate*, **17**: 1421-1432.

Mason, S. J., 1995: Sea-surface temperature-South African rainfall associations. 1910-1989. Int. *J. Climatol.*, **15**: 119-135.

Mason, S. J., 1998: Seasonal forecasting of South African rainfall using a non-linear discriminant analysis model. *Int. J. Climatol.*, **18**: 147-164.

Masumoto, Y. and Meyers, G., 1998: Forced Rossby waves in the southern tropical Indian Ocean. *J. Geophys. Res.*, **103**: 27589-27602.

Matitu, M. R., 2001: Response of tropical African rainfall to zonal circulations over adjacent oceans, *MSc Thesis*, University of Zululand, 133 pp.

Mathur, M. B., 1975: Development of banded structure in a numerically simulated hurricane. *J. Atmos. Sci.*, **32**: 512-522.

Meyers, G. J. R. Dongug, and R. K. Reed, 1986: Evaporative cooling of the western equatorial Pacific Ocean by anomalous winds. *Nature* (London); **323**: 523-526.

Meyers, S. D., B. G. Keley, and J. J. O'Brien, 1993: An introduction to wavelet analysis in oceanography and meteorology: with application to the dispersion of Yanai waves. *Mon. Wea. Rev.*, **121**: 2858-2866.

Meyers, G. J, 1996: Variation of Indonesian throughflow and the El- Nino-Southern oscillation. *J. Geophys. Res.*, **101**: 1255-12263.

Molinari, J., and D. Vollaro, 1989: External influences on hurricane intensity. Part I: Outflow layer eddy angular momentum fluxes. *J. Atmos. Sci.*, **47**: 1093-1105.

Molinari, J., and D. Vollaro, 1990: External influences on hurricane intensity. Part II: Vertical structure and responses of the hurricane vortex. *J. Atmos. Sci.*, **47**: 1902-1918.

Mooley, D. A., B. Parthasarathy, and G. B. Pant, 1986: Relationships between Indian summer monsoon rainfall and location of the ridge at the 500-mb level along 757E. *J. Climate Appl. Meteor.*, **25**: 633-640.

Morlet, J., 1983: Sampling theory and wave propagation. NATO Series, FI, Springer, 233-261.

Mpeta, E. J., 2002: Mechanisms of inter-annual rainfall variability over tropical highlands of Africa and its predictability potential. *PhD Thesis*. Department of Geography and Environmental studies. University of Zululand, 188 pp.

Murtugudde, R., and A. J. Busalacchi, 1999: Interannual variability of the dynamics and thermodynamics of the tropical Indian Ocean. *J. Climate*, **12**: 2300-2326.

Naerra, M., and M. R. Jury, 1997: Tropical cyclone composite structure and impacts over eastern Madagascar during January-March 1994, *Meteorol. Atmos. Phys.* (in press).

Nassor, A., 1994: monsoon surges, tropical cyclones and extreme rainfall in NW Madagascar. *Msc Thesis*. University of Cape Town, South Africa.

Nassor, A., M. R. Jury, 1997: Intra-seasonal climate variability of Madagascar. Part 2: Evolution of flood events. *Meteorol. Atmos. Phys.*, **64**: 243-254.

National Climate Data Center (NCDC), 1999: Global tropical cyclone data set (1967-1999), Asheville, North Carolina.

National Hurricane Center (NHC), 1999: Best track and intensity estimates of tropical cyclones in the North Atlantic (1944-1999) and the East Pacific (1950-1999), Miami, Florida

Nicholls. M. E., and R. A. Pielke: A numerical investigation of the effect of vertical wind shear on tropical cyclone intensification, Department of Atmospheric Science, Colorado State University, Fort Collins, CO 80523. 21st Conference on hurricanes and tropical meteorology, 339-341.

Oberhuber, J M, 1988, An atlas based on the COADS data set: budgets of heat buoyancy and turbulent kinetic energy at the surface of the global ocean, Rep 15, Max-Planck Inst fur Meteor., Hamburg, Germany, 199 pp.

Ogallo, L. J., 1988: Relationship between seasonal rainfall in east Africa and the Southern Oscillation. *J. Climate*, **8**: 34-43.

Orlanski, I., 1998: On the poleward deflection of storm tracks. *J. Atmos. Sci.*, **55**: 128-154.

Palmer, T. N., 1986: Influence of the Atlantic, Pacific and Indian oceans on Sahel rainfall. *Nature*, **322**: 251-2653.

Palmer, T. N., C. Brankovic, P. Viterbo and M. J. Miller, 1992: Modelling interannual variations of summer monsoons. *J. Climate*, **5**: 399-417.

Peterson, R. G., and W. B. White, 1998: Slow oceanic teleconnections linking the Antarctic circumpolar wave with the tropical El-Nino – Southern Oscillation. *J. Geophys. Res.*, **103**(C11): 24573-24583.

Pfeller, R. L., and Challa, 1981: A numerical study of the role of eddy fluxes of momentum in the development of Atlantic hurricanes. *J. Atmos. Sci.*, **38**: 2393-2398.

Philander, S G H, Hurlin, W J, and Seigel, A D, 1987, A model of the seasonal cycle in the tropical Pacific Ocean, *J. Phys. Oceanogr.*, **117**: 1986-2002

Qiu, B., and F. F. Jin, 1997: Antarctic circumpolar waves: an indication of ocean-atmospheric coupling in the extra tropics. *Geophys. Res. Lett.*, **24**: 2585-2588.

Rakotondrafara, M.L,2001: Interannual variability of tropical cyclone occurrences in the southwest Indian Ocean, MSc Thesis, University of Hawaii, 93 pp.

Reason, C. J. C., and H. M. Mulenga, 1999: Relationship between South African rainfall and SST anomalies in the SW Indian Ocean. *Int. J. Climatol.*, **19**: 1651-1673.

Reed, R. J., 1965: The present status of the 26-month oscillation. *Bull. Amer. Meteor. Sci.*, **46**: 374-387.

Reihl, H., 1950: A model of Hurricane formation. *J. Appl. Phys.*, 917-925.

Reynolds, R.W. and Smith, T M, 1994: Improved global sea surface temperature analyses using optimal interpolation. *J. Climate*, **7**: 929-948.

Reverdin, G., D. Cadel, and D. Gutzler, 1986: Interannual displacements of convection and surface circulation over the equatorial Indian Ocean. *Quart. J. Roy. Meteorol. Soc.*, **112**: 43-67.

Ropelewski, C. F., M. S. Halpert, and X. Wang, 1992: Observed tropospheric Biennial variability and its relationship to the southern oscillation. *J. Climatol.*, **5**: 594-616.

Rosati, A., and K. Miyakoda, 1988: A general circulation model for the upper ocean circulation. *J. Phys. Oceanogr.*, **18**: 1601-1626.

Rouault, M., S. A. White, and J. R. E. Lutjeharms, 1998: Studying rainfall events over South Africa and adjacent oceans using the TRMM satellite.

Sadler, J., 1976: A role of the tropical upper tropospheric trough in early season typhoon development. *Mon. Wea. Rev.*, **104**: 1266-1278.

Saji, N. H., B. N. Goswami, P. N. Vinayachandran, and T. Yamagata, 2001: A dipole mode in the tropical Indian Ocean. *Nature*, **401**: 360-363.

Schroeder, A. T., and Z. Yu: Interannual variability of central Pacific Tropical cyclones. 21st Conference on hurricanes and tropical meteorology, 437-439.

Shapiro, L. J., 1987: Month-to-month variability of the Atlantic tropical circulation and its relationship to tropical storm formation. *Mon. Wea. Rev.*, **115**: 2598-2614.

Shapiro, L. J., 1989: The relationship of the quasi-biennial oscillation to Atlantic tropical storm activity. Mon. Wea. Rev., 117: 1545-1552.

Simmonds, I., and T. H. Jacka, 1995: Relationships between the interannual variability of Antarctic sea ice and the Southern oscillation. *J. Climate*, **8**: 637-647.

Simpson, R. H., 1954: Structure of an immature hurricane. *Bull. Amer. Meteorol. Soc.*, **35**: 335-350.

Simpson, R. H., and Reihl, 1981: The Hurricane and its Impacts. *LSU Press*, 398 pp.

Slutz, R. J., S. L. Lubker, J. D. Hiscox, D. D. Woodruff, R. L. Jenne, D. H. Joseph, P. M. Steurer, and J. D. Elms, 1985: COADS: The Comprehensive Ocean-Atmosphere Data Set. CIRES. 39.

Thompson, E. F., and V. J. Cardone, 1996: Practical modeling of hurricane surface wind fields. ASCE J. of Waterway, Port, Coastal and Ocean Engineering. **122**: 195-205.

Torrence, C., and G. P. Compo, 1997: A practical guide to wavelet Analysis, *Bull. Amer. Meteorol. Soc.*, **79**(1): 61-79.

Tourre, Y. M., and W. B. White, 1997: Evolution of the ENSO signal over the Indo-Pacific domain. *J. Phys. Oceanogr.*, **27**: 683-696.

Venegas, S. A., 2003: The Antarctic circumpolar wave: a combination of two signals?. *J. Climate*, **16**: 2509-2525.

Venzke, S. M., M. Latif, and A. Villwock, 2000: The coupled GCM ECHO-2. Part II: Indian Ocean response to ENSO. *J. Climate*, **13**: 1371-1387.

Vermulen, J. H., M. R. Jury, 1992: Tropical cyclones in the south west6 Indian Ocean-track prediction and verification. 1989-991. Meteorol. Mag., 121: 186-192.

Veryard, R. G., and R. A. Ebdon, 1961: *Meteor. Mag.*, **90**: 125-143.

Vinayachandran, P. N., S. Iizuka, and T. Yamagata, 2002: Indian ocean dipole mode events in an ocean general circulation model. *Deep-sea Res.*, **49B**: 1573-1596.

Walker, N. D., 1990: Links between South African summer rainfall and temperature variability of Agulhas and Benguela current systems. *J. Geophys. Res.*, **95**(C3), 3297-3319.

Walsh, R. P. D., 1993: Climate of the Seychelles, 39-58pp.

Ward, N. M., 1998: Diagnosis and short lead time prediction of summer rainfall in tropical North Africa at inter-annual and multi-decadal time scales. *J. Climate*, **11**: 3167-3191.

Ward, N. M., 1992: Provisionally corrected surface wind data, world-wide ocean-atmosphere surface fields and Sahelian rainfall variability. *J. Climate*, **5**: 454-475.

Webster, P. J., A. M. Moore, J. P. Loschning, and R. R. Leben, 1999: Coupled ocean-atmosphere dynamics in the Indian Ocean during 1997-1998, *Nature*, **401**: 356-360.

Wexler, H., 1947: Structure of Hurricanes as determined by radar. Ann. N. Y. *Acad. Sci.*, **34**: 1028-1039.

White, W. B., and R. G. Peterson, 1996: An Antarctic circumpolar wave in surface pressure, wind, temperature and sea-ice extent. *Nature*, **380**: 699-702.

White, W. B., and Y. M. Tourre, 2003: Global SST/SLP waves during the 20th century. *Geophys. Res. Lett.*, **30**: NO. 12, 1651.

Williams, J. B., 1990: Some temporal and regional variations of climate in Madagascar, Tech. Rep. Overseas Devep. Nat. Res. Inst., Chatham Marine, Kent, pp 144.

Willoughby, H. E., 1977: Inertia-buoyancy waves in hurricanes. *J. Atmos. Sci.*, **34**: 1028-1039.

Willoughby, H. E., 1978: A possible mechanism for the formation of hurricane rainbands. *J. Atmos. Sci.*, **35**: 838-848.

Xie, S. P., H. Annamalai, F. A. Schott, and J. P. McCreary, 2002: Structure and mechanisms of South Indian Ocean climate variability. *J. Climate*, **15**: 864-878.

Yeshanew, A. B., 2004: Mechanisms and prediction of climate variability in tropical North Africa. PhD Thesis. Department of Geography and Environmental studies. University of Zululand, 317 pp.

Yuan, X., and D. G. Martison, 2000: Antarctic sea-ice variability and its global connectivity. *J. Climate*, **13**: 1697-1717.

Appendix

Date	TC Name	Weather	Location	Disaster (Death/Cost/Victims)
2000 1 Jan- 29 Feb	Eline	Max 250 km/ h 131mm/ 24 hrs Swell<3m(Reunion) floods (worst since 1951)	Mozambique Madagascar (Mahanoro) Zimbabwe	700 dead 800,000 disaster victims 0.5 Billion USD. 64 dead 10,000 homeless 0.5million disaster victims 80 % damage. 12 dead 250,000 disaster victims
1994 26 Jan- 9 Feb	Geralda	Violent winds/ torrential rains/ flooding	Madagascar (Joa-Masina)	231 dead 73 unaccounted 267 injured 40000 homeless 13000 cattle problems Toamasina destroyed (80 %) Estimated cost (10 m USD)
2000 24 Mar- 8 Apr	Hudah	Max 180 km/ h Vioent winds Storm surge/swell	Madagascar Antalaha	111 deaths. 300,000 disaster victims. 90 % homes destroyed
1972 5 Feb	Eugenie		Madagascar (Morafenobe)	91 dead 50 lost, 30 injured 4114 homeless
2000 27 Feb- 10 Mar	Gloria	Max 93 km/ h 150 mm/ 24 hrs 500 mm/ 3 Days	Madagascar Madacascar (Mananjary,Sambava)	84 dead 1000's homeless Malaria-Cholera
1977 25 Jan- 10 Feb	Emilie	106.6mm/24 hrs max 140 km/ h	Madagascar (Mananjary)	36 dead 18,000 homeless
1996 3-15 Jan	Bonita		Madagascar/Mozam (Foui Point Fenerice)	25 dead 5000 homeless
1991 2 Apr	G2	220.7mm/ h 91 km/ h	Madagascar (Tamatave)	18 dead
1972 3 Mar	Hermione	204 mm/ 24 hrs	Madagascar (Majunga)	11 dead 7 lost,5 injured 5310 homeless

Disaster Data extracted from Annual Cyclone Review publication in SWIO: Order according to worst disasters from 1972-2002.Shading indicates case studies.

1973 24 Jan	Hortense		Andlamena	11 dead 7 injured 434 homeless
1987 27-30 Jan	Georgia		Madacascar	10 dead 12,800 homeless
1993 2-9 Mar	Ionia	flooding	Madagascar (Sambirano)	8 dead 3644 homeless slight structural Damage
1994 16 Mar- 1 Apr	Nadia		Mozambique (Nampula)	8 dead 128 injured 85 % homeless 75 % crop damage
1979 22-23 Dec	Claudette		Mauritius	4 dead 47 injured,5600 victims 11000 homeless
1972 15 Feb	Isis	246mm / 24 hrs	Madagascar (Diego-squarez)	2 dead 300 homeless
2001 30 Dec- 13 Jan	Ando	Max 108 km/h Swell (5.4 m) Possesion's Bay	Reunion	2 dead damage to Agriculture cattle died
1980 27-28 Jan	Hyacinthe	Heavy rains	Reunion	2 dead
1973 10 Jan	Dorothee		Madagascar (Morondava)	1 dead 2 injured 373 homeless
2000 24 Jan- 2 Feb	Connie		Reunion	1 death 40,000 households deprived of electricity damage to agriculture
1973 3 Jan	Challotte		Madagascar (Majunga)	1 dead 1 injured
1989 30 Mar -9 Apri	Krissy			8 injured 339 homeless estimated Damage 800
1986 10-18Jan	Delfinina	Ship 675 km from center v= 55km/h Swells 3 m(11S,82E)		
1993 16-24 Jan	Dessilia	Swell 3-4m		

Disaster Data extracted from Annual Cyclone Review publication in SWIO: Order according to worst disasters from 1972-2002.Shading indicates case studies.